Long-term effects of creep and shrinkage on the structural behavior of balanced cantilever prestressed concrete bridges

Emilia Antonia Andrade Borges

Long-term effects of creep and shrinkage on the structural behavior of balanced cantilever prestressed concrete bridges

by

Emilia Antonia Andrade Borges

Thesis submitted in Partial Fulfillment of the Requirements for the Degree of

Master of Science

at the Delft University of Technology

Faculty of Civil Engineering and Geosciences

Student number:	5504341	
Project Duration:	January, 2023 - December, 2023	
Thesis committee:	Dr. ir. Y. Yang	TU Delft
	Dr. ir. G. Ye	TU Delft
	Dr. ir. A.T. Slobbe	TNO
	Dr. ir. G.J.A.M. Eumelen	TNO
	ir. B. van den Broek	Rijkswaterstaat

TU Delft TNO

Acknowledgements

Reflecting on my time as a MSc student at TU Delft, I would like to express my gratitude to those who have supported me throughout this journey.

First, I would like to thank my committee for their support during my thesis. Guang Ye and Bart van den Broek for their keen interest and invaluable feedback. My chair, Yuguang Yang, for his guidance throughout my academic journey, which has been truly encouraging.

I am especially grateful to my supervisors, Arthur Slobbe and Gijs Eumelen, for their support and mentorship through this challenging yet rewarding project. Thank you for sharing your knowledge, experience, and endless enthusiasm with me. I feel honored to have had the opportunity to work with you this past year.

To the concrete team at TNO, for their continuous encouragement. I have deeply enjoyed working alongside you all these months. I want to express special gratitude to Huibert, for his guidance and for sharing his passion for forensic engineering with me.

My thanks also go to Eva Lantsoght for her mentorship, which started during my studies at USFQ and continued throughout my journey here at TU Delft. Her unwavering dedication to her work has been a constant source of inspiration for me, and her support has been instrumental in helping me reach where I am today.

To my wonderful friends who have made Delft my second home, thank you for being there for me through both good and challenging times. You all inspire me every day.

Above all, my deepest appreciation goes to my family: gracias por cuidar de mí y por su apoyo incondicional. Ma y pa, cada día me enseñan el valor de la honestidad y el trabajo diario. Gracias por apoyar mis metas, todo lo que he logrado hoy es gracias a ustedes.

Emilia Antonia Andrade Borges
Delft, November 2023

Abstract

This thesis addresses the topic of ongoing (excessive) deformations observed in balanced cantilever prestressed concrete bridges all over the world. Many authors attribute this behavior to the time-dependent phenomena of creep and shrinkage. Balanced cantilever bridges are classified as creep-sensitive structures, and for that reason, a detailed analysis of the long-term structural behavior, such as deformations and prestress losses, is recommended. However, during the design of these bridges, commonly used code-based models generally tend to underestimate the long-term creep and shrinkage effects. Additionally, various (simplifying) assumptions are made when modeling these bridges, making their actual creep and shrinkage behavior unclear.

This work aims to investigate whether the long-term effects of creep and shrinkage are indeed a plausible explanation for the excessive and ongoing deflections detected in a specific balanced cantilever bridge in the Netherlands: the Rooyensteinse Brug. This bridge, inaugurated in 1977 in Zoelen, currently exhibits a deflection at midspan of 0.43 m, more than two times what was anticipated in bridge design. To investigate this behavior, a detailed two-and-a-half-dimensional finite element model was developed, incorporating a time-dependent phased analysis accounting for the construction phases. Creep and shrinkage effects were incorporated into the concrete material model through creep compliance and shrinkage strain curves.

A sensitivity study is conducted to analyze the impact of: (i) different code-based models for creep and shrinkage, (ii) accounting for the large creep and shrinkage model uncertainties, (iii) different maturities on the creep compliance curve, and (iv) considering cross-sectional variability in the drying characteristics. The main findings showed that commonly used code-based models, including the current standard Eurocode 2, significantly underestimate the long-term (multi-decade) deflections observed in the Rooyensteinse Brug by 30%. Notably, only the RILEM B4 model (B4), considered the most theoretically grounded creep and shrinkage model, was able to capture the long-term deflection trend reasonably well. Further, acknowledging the inherent uncertainties in B4 significantly widened the range of potential deflections and prestress losses. Using the bounds of the 90% credible interval, the midspan deflections after 60 years range between 0.514 m and 2.91 m, compared to a mean of 0.895 m. The prestress losses range between 18% and 30% in the shear-critical zone, against a mean of 23%. Additionally, accounting for the cross-sectional variability in drying characteristics led to an improvement in both the short-term (first 10 years of service life) and long-term (multi-decade) deflection prediction when comparing the results to in-situ measurements, with differences of 14% and 6.1%, respectively. Based on these predictions, it is expected that the current deflection trend of the Rooyensteinse Brug will continue to decrease linearly (log-scale) for the next two decades.

This study demonstrates that a detailed finite element model incorporating time-dependent phased analysis, in combination with the RILEM B4 model and accounting for cross-sectional variability, can explain the observed behavior in the Rooyensteinse Brug. The results support the hypothesis that the long-term effects of creep and shrinkage are the cause of the ongoing trend of excessive deformations in this balanced cantilever prestressed concrete bridge.

Contents

1

Introduction

1.1. Motivation

The construction of box-girder prestressed concrete bridges using the balanced cantilever method is recognized as one of the most efficient methods for the construction of bridges with spans ranging from 90 to 200 m [1, 2]. This efficiency is attributed to its self-supporting structure that eliminates the need for falsework and a prestressing layout that is well aligned with the moment diagram. Initially adopted in the 1950s in Germany and subsequently in France, balanced cantilever prestressed bridges have become widely accepted in bridge construction over the past decades [1, 3]. However, an unexpected behavior, unaccounted for during the design phase, has surfaced.

The monitoring data of various existing balanced cantilever prestressed concrete bridges all over the world has shown considerable deformations. A study on 69 large-span prestressed bridges revealed that most of them exhibit excessive deflections, requiring, in some cases, retrofitting and closing [4]. The collapse of the Koror-Babeldaob Bridge in 1996 has only fueled safety concerns. Despite the collapse being triggered by an unsuccessful retrofitting, measurements revealed a mid-span deflection of 1.61 m and a prestress loss of 50% after only 18 years [5, 6].

In the Netherlands, there are 36 balanced cantilever bridges, with the oldest one, the Maasbrug Wessem, dating back to 1964 (see Figure 1.1). A recent study analyzed the measurement data from 21 of these bridges, all older than 30 years [7]. The findings revealed 9 bridges with deformations greater than 1/600L, and 3 greater than 1/400L. As a reference, a deflection-span relation of 1/800 is considered to be within serviceability limits [8]. These observations have raised concerns about the serviceability, durability, and overall safety of these structures [9, 10].

Comparative studies throughout the years have attributed the ongoing deformations observed in

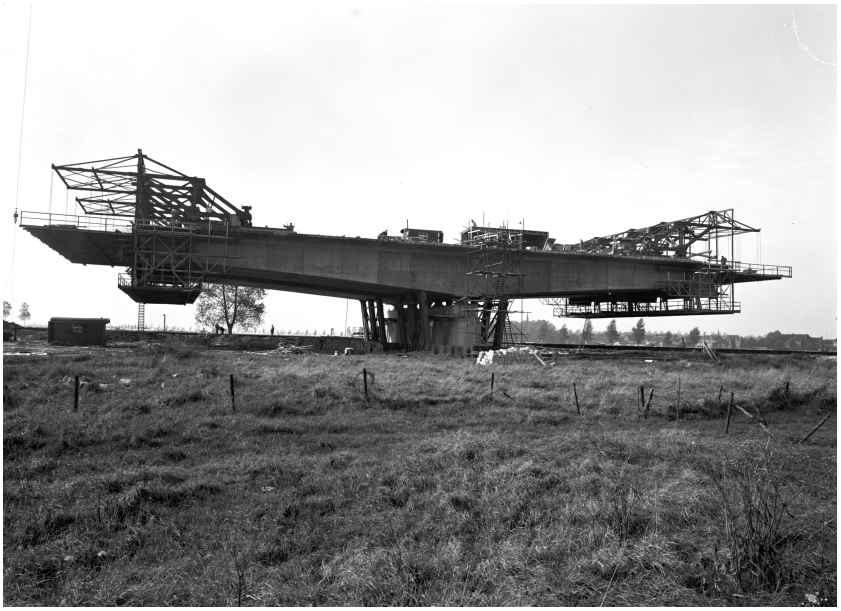

Figure 1.1: Construction of the Maasbrug near Wessem, the first balanced cantilever concrete bridge in the Netherlands [11].

balanced cantilever bridges to the time-dependent phenomena of creep and shrinkage [5, 10, 12, 13, 14, 15, 16]. More specifically, the underestimation of these effects by code-based models, which are characterized by practical calculation processes and a series of simplifying assumptions. These bridges, classified as creep-sensitive structures, require a detailed analysis to assess the impact of time-dependent deformations in their bearing capacity [17]. However, the suitability of commonly used creep and shrinkage models remains unclear. Further, other common practices in bridge assessment within the Netherlands include: (i) using a simplified beam element model; (ii) omitting explicit modeling of construction phases; (iii) assuming a certain % for time-dependent prestress losses; (iv) considering a single average creep coefficient derived from the current standard for the entire bridge; (v) treating this average creep coefficient as a deterministic parameter; and (vi) using this coefficient for ultimate limit state (ULS) moment verification [18]. Consequently, there is a notable disregard for the substantial uncertainties inherent in creep and shrinkage models, a lack of consideration for the impact of construction phases, an oversight of maturity effects, and neglect to incorporate state-of-the-art insights regarding creep and shrinkage models. Then a question emerges, can the application of these substantial simplifications be justified when performing Serviceability Limit State (SLS) and Ultimate Limit State (ULS) verifications for existing balanced cantilever bridges?

1.2. Research Questions

This study aims to improve the understanding of the time-dependent behavior of balanced cantilever prestressed concrete bridges. It investigates whether long-term creep and shrinkage effects are a plausible explanation for the excessive and ongoing deformations, while also evaluating the impact of several modeling decisions. The main research question is proposed as follows:

What are the long-term (i.e. multi-decade) effects of creep and shrinkage on the structural behavior of balanced cantilever prestressed concrete bridges?

The sub-questions that will help address the main research question are:

- *Which code-based models for creep and shrinkage are suitable to describe the long-term behavior of balanced cantilever prestressed concrete bridges?*
- *What are the important aspects to be considered for an accurate modeling of long-term creep and shrinkage effects in balanced cantilever prestressed concrete bridges, and how can they be addressed in a finite element model?*
- *What is the impact of long-term creep and shrinkage effects on the deformation, prestress losses, and moment redistribution in balanced cantilever prestressed concrete bridges?*
- *To what extent can time-dependent structural finite element analysis help to investigate the hypothesis of long-term effects of creep and shrinkage causing the excessive deformations of balanced cantilever prestressed concrete bridges in the Netherlands?*

1.3. Approach

The research presented here is divided into three stages. First, a literature review on balanced cantilever bridges, creep and shrinkage of concrete, and code-based models for creep and shrinkage is conducted. Next, a series of minimal examples are developed to test and validate the implementation of different functionalities in the finite element modeling of the bridge. Finally, a finite element model of the Rooyensteinse Brug is developed, see Figure 1.2. This bridge built between 1975 and 1977 was chosen based on the following considerations:

1. The Rooyensteinse Brug is one of the prestressed concrete box-girder bridges constructed with the balanced cantilever method that shows a growing trend of excessive deflections.
2. Deflection measurement data is available for the Rooyensteinse Brug dating from August 1978 until April 2022.
3. Information is available regarding the material properties and geometry of the bridge.

To evaluate the long-term effects of creep and shrinkage on the behavior of the Rooyensteinse Brug, two levels are considered: a *structural analysis level*, involving the finite element method, to describe the time-dependent structural response; and a *material level* with reliable models to predict creep and shrinkage behavior [6, 19].

The structural analysis is conducted using a two-and-a-half-dimensional finite element (FE) model with shell elements. The FE model contains the box girder segments and all cantilever and continuity tendons are described individually. To accurately incorporate the effects of the construction process, a

Figure 1.2: The Rooyensteinse Brug.

time-dependent phased structural analysis is performed. Each main phase in this analysis describes the casting procedure of one segment.

Considering the material level, the concrete material behavior is described by means of linear viscoelasticity. The stresses are calculated from the strain history using the Boltzmann principle of superposition [20, 21]. The input for the viscous concrete material model is provided by creep compliance, $J(t, t_0)$, curves, and shrinkage strain, $\varepsilon_{cs}(t, t_0)$, curves. The different curves are obtained from creep and shrinkage models presented in various design codes.

The FE analyses on the Rooyensteinse Brug are performed with the commercial FE software DIANA FEA 10.7. To facilitate interaction with DIANA's Application Programming Interface (API) and ensure a parametric model description, the Python programming language is used [22]. Hence, with relatively limited effort the code can be used to analyze other balanced cantilever concrete bridges as well.

1.4. Scope and Limitations

This research follows a case study approach, offering the advantage of addressing a real-world problem and providing insights relevant to practical applications. However, it is important to recognize that the findings are context-dependent. Generalization and extrapolation of results have to be done carefully.

The material models follow from various design codes, which are, in part, semi-empirical rather than physical. Consequently, the predicted material response does not necessarily match the physical response. The main focus of this research is on the long-term behavior of creep and shrinkage. Even though relaxation is also a time-dependent phenomenon, it is considered in a simplified way. Furthermore, the interaction of creep and shrinkage with environmental fluctuations is not considered. Finally, real measurement data is employed for comparison with the finite element model results. It is assumed

that the influence of environmental conditions (e.g. daily temperature fluctuations) and settlements is negligible. Therefore, no corrections are applied to account for these effects.

In Chapter 6, the results from this case study will be placed within the context of other similar studies, including [5, 8, 10, 12, 15, 23, 16]. The correspondence in the type of construction method, the evaluated code-based models, and other modeling considerations help establish realistic comparisons between studies. Nevertheless, the conclusions of this research must be examined within the context of the case study from which they will originate.

1.5. Thesis Structure

This thesis is structured into seven chapters. Following the introductory chapter, Chapter 2 is dedicated to the literature review. This chapter includes a review of the balanced cantilever method for prestressed concrete bridges, followed by a description of the creep and shrinkage phenomena in concrete, and an overview code-based models. The impact of lightweight aggregate concrete on these time-dependent phenomena is also briefly discussed. Chapter 3 presents the Rooyensteinse Brug, including the geometry, material properties, phasing, and the measured deformation over the past 45 years. The FE modeling approach of the Rooyensteinse Brug is explained in Chapter 4, including geometry, material properties, boundary conditions, applied loads, and the phasing implementation. Chapter 5 presents the results from the FE model, further discussed in Chapter 6. The conclusions and recommendations for future work are presented in Chapter 7.

Additionally, Annex A provides the location of the reference points for the in-situ measurements of the Rooyensteinse Brug. Annex B presents further plots from the sensitivity study on input parameters for creep and shrinkage discussed in Chapter 2. Annex C is dedicated to presenting the minimal examples, while Annex D contains tables with information on the phasing and load cases. Annex E is the Excel sheet used for notional size calculation, and Annex F presents the results for the Reference Analysis with the new symmetry conditions, as mentioned in Chapter 4.

2

Literature review

This chapter provides an introduction to balanced cantilever prestressed concrete bridges in Section 2.1. Section 2.2 discusses creep and shrinkage, both from a material point of view, as well as from a structural point of view. Section 2.3 provides a brief historical overview of how creep and shrinkage models have been developed in different codes. Only the main equations are presented. For a detailed explanation of the formulation, the reader is referred to the corresponding original documentation. Finally, Section 2.4 briefly discusses the influence of lightweight aggregate concrete in creep and shrinkage in contrast to the provisions from code-based models.

2.1. Balanced cantilever prestressed concrete bridges

The use of prestressed concrete to build bridges is a well-established technique that is widely used around the world. The combination of the tensile strength of the prestressing tendons and the compressive strength of the concrete allows the creation of a balanced structure with many advantages, including slenderness and long spans [24]. Prestressed concrete bridges are used for different functions (e.g. for pedestrians, bicycles, or cars), can have different cross-sectional shapes (e.g. inverted T-beam, box girder), and can be constructed using different construction methods (e.g. incremental launching, balanced cantilever).

The design of these bridges is highly dependent on the required span. For spans ranging between 40 m and 300 m, cast in situ single-cell box girders are preferred because they are considered an economical solution for both medium and long-span bridges [24]. For these types of bridges, the balanced cantilever method is considered a suitable and economical construction method for spans ranging between 90 and 200 m [25].

2.1.1. Bridge design and construction

The balanced cantilever method to construct bridges with single-cell box girders has proven to be useful for long-span structures, especially in situations where placing falsework becomes a complicated task, e.g. over waterways, gorges, or when traffic below cannot be interrupted during construction [1]. The construction starts with the permanent pier and the hammerhead on top. Then, with the help of traveling formwork, a section is cast on both sides of the hammerhead. The segments are then held together by post-tensioning longitudinal prestressing tendons. By maintaining symmetry, large unbalancing moments in the hammerhead are avoided and the structure is self-supporting throughout all construction stages [1, 24]. Nevertheless, small moments do arise during the construction stage, requiring temporary support for the hammerhead. A schematic overview of the construction process is shown in Figure 2.1. Segmental casting is a process that typically lasts one week. Table 2.1 provides an overview of a typical casting week, which is a common practice all over the world [15]. This construction method can be done with both cast-in-place and precast concrete segments.

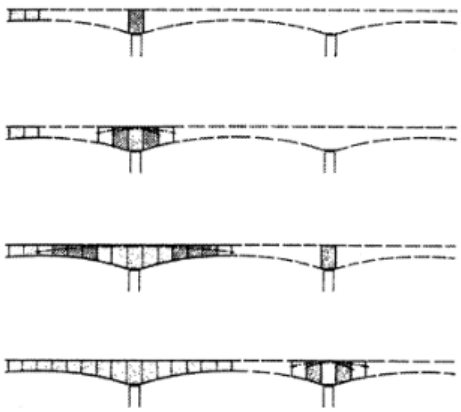

Figure 2.1: The balanced cantilever method [1].

Day	Activity
1. Monday	Move traveling formwork Install steel reinforcement
2. Tuesday	Install steel reinforcement
3. Wednesday	Install steel reinforcement
4. Thursday	Cast segment side 1
5. Friday	Cast segment side 2
6. Saturday	Prestress cantilever tendons
7. Sunday	No activities

Table 2.1: Weekly activities in segmental casting [15].

The static system of a balanced cantilever bridge undergoes changes upon completion (see Figure 2.2). During the segmental casting, the bridge behaves as a statically determined cantilever girder, with a moment diagram evolving as shown in Figure 2.2a. Upon completion and immediately after the stitching, the bridge exhibits a moment diagram represented by $M_{stitching}$ in Figure 2.2b. Even

though the static system is now statically indeterminate, the moment line resembles that of a cantilever girder. In the hypothetical situation where the bridge would have been constructed monolithically, the moment line would resemble $M_{monolithic}$. In reality, the moment $M_{t=\infty}$ evolves in time as a line between $M_{stitching}$ and $M_{monolithic}$ due to a redistribution of stresses [2, 25]. This redistribution is due to the time-dependent phenomena of creep and shrinkage.

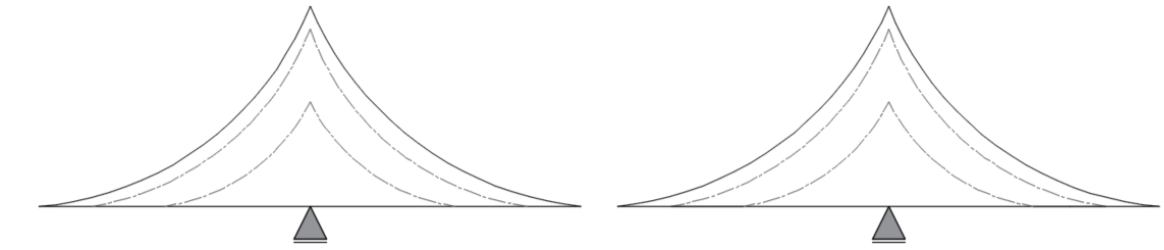

(a) The moment diagram at different stages of the construction process.

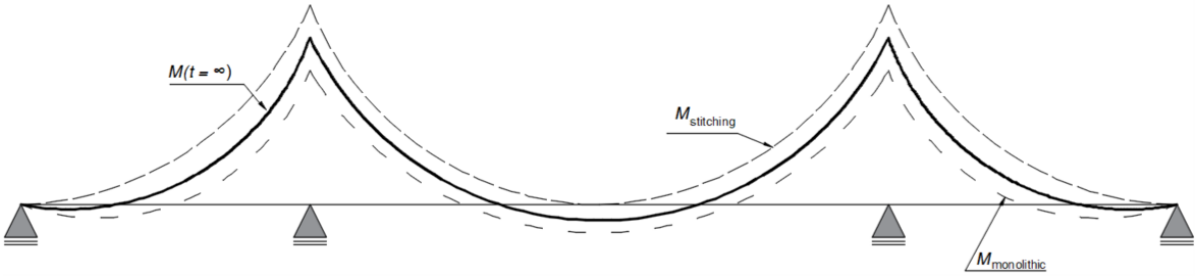

(b) Moment redistribution due to time-dependent phenomena during service life.

Figure 2.2: The evolution of moment diagram for different stages: construction and service life.

Typically, the height of the segments gradually changes along the longitudinal axis of the bridge, starting with relatively large segments near the hammerhead to small segments at the midspan. This aligns the longitudinal bridge geometry to the bending moment diagram, hence allowing for economical, practical, and aesthetic designs. There are specific requirements the cross-section must comply with for the balanced cantilever method. The deck slab geometry must be sufficient to accommodate the cantilever tendons [2]. The web thickness is primarily determined by the required design shear resistance, but it also depends on the concrete cover, presence of tendon conducts, and anchorage [1]. The haunch depends on the required space to accommodate the tendon ducts. The increasing bottom slab thickness is proportional to the required area to resist the compressive force due to flexure and shear, which reach a maximum at the supports [1, 2]. Figure 2.3 provides an illustrative example of a box girder cross-section.

2.1.2. Bridge in service: the problem of long-term deformations

The monitoring data of various existing balanced cantilever prestressed concrete bridges all over the world has shown considerable deformations [5, 8]. Research throughout the years has linked this unexpected behavior to creep and shrinkage effects. In reality, a precise understanding of creep and shrinkage is essential for an accurate prediction of the structural behavior of these structures [6].

Several case studies have contributed to the understanding of the deformation problem in balanced

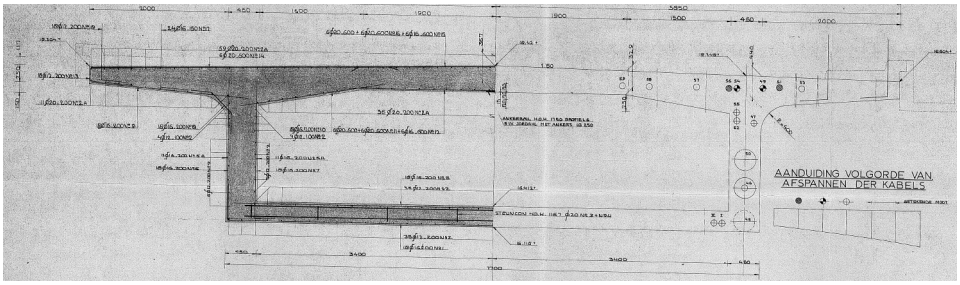

Figure 2.3: Example of a box girder cross-section [18].

cantilever bridges, particularly in the context of the underestimation of these phenomena by commonly used code-based models. This literature review selects a set of these case studies, briefly presented in Table 2.2, to investigate how their findings relate to the results of this research. In this section, a brief overview of the main conclusions of each case study is presented.

Takács [10] conducted a comparative analysis using a 2D beam model using creep and shrinkage models from both the CEB-FIP Model Code 1990 (MC90) and the RILEM B3. In the short term, B3 predicted smaller deflections, while in the long term, it surpassed the prediction by MC90. In comparison with the in-situ measurements from the first 8 years of service life, MC90 showed better agreement. Takács also explored the impact of cross-sectional variability with a 2 1/2D model, indicating that the uniform analysis slightly overestimates deflections in contrast to the non-uniform analysis [10]. With a similar model as Takács, Louman [15] compared the results obtained with the creep and shrinkage models of Eurocode 2 (EC2), MC90, and the modified version of MC90 (mM90) with the in-situ measurements from the first 6 years of service life of the Tweede Stichtse Brug. While he encountered difficulty in determining the most suitable model due to the distortion of deflection trends in one of the in-situ measurements, the other two data points indicated a closer alignment with EC2.

Bažant et al. [5] employed a 2 1/2D model of the Koror-Babeldaob Bridge to compare the deflection prediction of five code-based creep and shrinkage models: ACI, JSCE, GL, mMC90, and B3 with in-situ measurements. Their primary finding was that all models underestimated the deflection of this bridge. However, B3 was the only model capable of capturing the deflection trend observed in the in-situ measurements. Additionally, their study also accounted for cross-sectional variability, concluding on the importance of a non-uniform analysis for accurately capturing the initial deflection history [5]. This aligns with the observations made by Malm and Sundquist [26], who found notably larger deflections within 2 years when employing a non-uniform analysis with EC2, in contrast to a uniform analysis.

Tong et al. [12] adopted a comprehensive approach in their 3D model, considering not only static creep but also cyclic creep, damage, and concrete softening. When comparing the predictions of this model with the creep and shrinkage models from the fib Model Code 2010 (MC10) and RILEM B4 against in-situ measurements from the first 8 years, one of the main conclusions was that neglecting these additional factors resulted in an underestimation of deflections by both code-based models. Jia et al. [23] also used a 3D model to study the impact of uncertainty propagation on deflection predictions. Subsequently, they updated the numerical model using in-situ measurement data from the initial 8

years of service life of the bridge. This refinement led to the narrowing of the 95% confidence limit bounds, addressing the underestimations caused by the deterministic model with B3 [23]. In Chapter 6, these case studies will serve as reference points to contrast and further explore the implications of the findings from this research.

Reference	Case study	Deflection data	Type of FE model and analysis	Creep and shrinkage models	Sensitivity studies
[10]	Støvset Bridge (1993), Norway.	Yes (8 years)	2 1/2D model with shell elements, and 2D beam model. Time-dependent phased analysis with construction process.	MC90, B3	Different creep and shrinkage models, and cross-sectional variability.
[15]	Tweede Stichtse Brug (1997), the Netherlands.	Yes (6 years)	2D beam model. Time-dependent phased analysis with construction process.	MC90, mMC90, EC2	Different creep and shrinkage models.
[5, 27]	Koror-Babeldaob Bridge (1977), Palau.	Yes (18 years)	2 1/2D model with shell elements. Time-dependent phased analysis with construction process.	ACI, JSCE, GL, mM90, B3	Different creep and shrinkage models, and cross-sectional variability.
[12]	Humen Bridge (1997), China.	Yes (6 years)	3D model. Time-dependent phased analysis with construction process.	MC10, B4	Different creep and shrinkage models.
[26]	Gröndal bridge (1967), Sweden.	No	2 1/2D model with shell elements. Time-dependent phased analysis with construction process.	MC90 (creep), EC2 (shrinkage)	Cross-sectional variability.
[23]	Unknown.	Yes (8 years)	3D model. Time-dependent phased analysis with construction process.	B3	Propagation of uncertainty.

Table 2.2: Brief overview of case studies on the deformation problem of balanced cantilever bridges.

2.2. Creep and shrinkage of concrete

Concrete is the most widely used construction material in the world [28]. Composed primarily of cement, sand, aggregates, and water, it is a heterogeneous mixture with complex properties. The combination of external (e.g. loading, temperature, and exposure conditions) and internal (e.g. composition and hydration process) factors will define not only its resistance but also its behavior over time. The time-dependent behavior of concrete is governed by two phenomena: creep and shrinkage. This section aims to introduce these phenomena, discussing them on the material level and the structural level.

2.2.1. Mechanisms and contributing factors

Creep is defined as the slow further increase in deformation observed in a loaded concrete specimen after the instantaneous deformation has occurred [29]. This mechanical property of concrete can be divided into two components: basic and drying creep. Basic creep takes place when no moisture movement is involved while drying creep occurs when the element is exposed to drying [20]. Shrinkage is defined as a gradual reduction in the volume of unloaded concrete at a constant temperature [30]. This reduction usually happens because of water loss during a drying process and is considered a gradual process. Several types of shrinkage can occur in concrete, with autogenous and drying shrinkage governing the time-dependent behavior. Autogenous shrinkage results from cement hydration in the absence of moisture exchange, while drying shrinkage occurs when specimens lose moisture due to exposure to the environment [6].

Creep and shrinkage significantly impact the strain behavior in concrete, as shown in Figure 2.4. This example considers a specimen exposed to drying conditions at time t_0, and subsequently loaded at time t_p. The figure highlights a key distinction between creep and shrinkage: while creep-induced strains are initiated by applied stresses, shrinkage-induced strains are stress-independent.

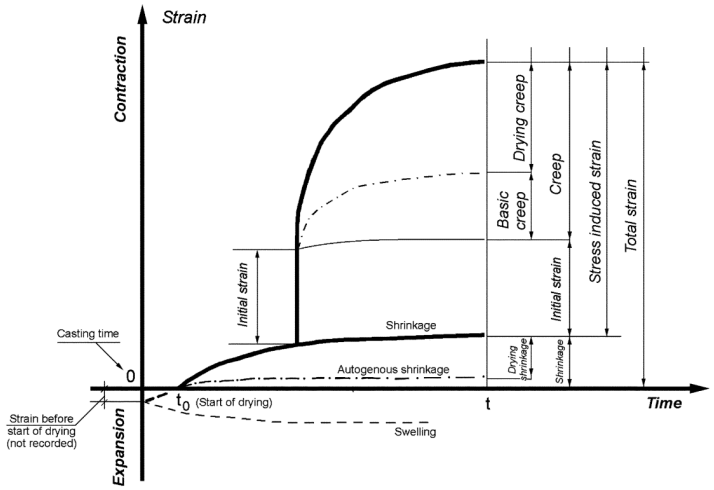

Figure 2.4: Schematic drawing of creep and shrinkage effects in time [31].

Creep and shrinkage are an integral part of successfully describing the behavior of concrete. Through-

out the years, progress has been made in understanding the physical mechanisms behind these properties [32, 33, 34]. However, despite these developments, a complete and comprehensive understanding of these phenomena remains a subject of ongoing research [35].

The mechanism behind basic creep can be classified into short-term and long-term. Short-term basic creep results from a stress-induced redistribution of capillary water in the hardened cement paste [33]. In contrast, long-term basic creep is caused by the displacement of gel particles under tension [15]. Contrary to short-term creep, the mechanism for long-term creep is more complex due to various factors, including non-uniform stress distribution, moisture content, and age of loading [33]. Similarly complex is the mechanism of drying creep, the subject of multiple explanatory theories including micro-cracking [32].

Multiple factors influence creep. Over the years, experiments have attempted to isolate variables in controlled settings to clarify the extent of their influence on creep [32, 33]. However, due to the significant interdependence among variables, discerning direct effects from indirect ones remains complex. The challenge increases when factoring in the applied stress level at a specific time of loading [31]. The factors influencing creep can be divided into intrinsic and extrinsic.

- *Intrinsic factors*

  The cement paste and aggregates are considered the main material-related factors for the creep behavior of the concrete. The cement paste is where the actual creep mechanism occurs. For example, increasing the water-to-cement ratio (*w/c*) has been shown to increase both basic and drying creep behavior [31]. The aggregates, on the other hand, show a restraining effect on the creep behavior of the concrete, because of their low susceptibility to creep [31, 36]. This also explains why concrete made with lightweight aggregates is on average, more prone to creep [37, 38]. Additional factors such as slump, air content, and admixtures are mentioned in the literature to also affect the creep behavior of the concrete, thereby indicating that nearly all properties of hardened concrete influence its creep behavior [39].
- *Extrinsic factors*

  Extrinsic factors come into play after the concrete is cast. Locally, an extended curing period reduces permeability and increases the modulus of elasticity, diminishing basic and drying creep [31]. The age of loading also plays an important role. Applying loads at a later stage reduces both basic and drying creep due to the influence of maturity effects. Externally, an important factor influencing drying creep is relative humidity. Environments characterized by lower relative humidity levels increase creep effects. Additionally, drying creep is affected by the size and shape of specimens. As thickness increases, the drying rate is slower, thereby leading to a decrease in creep [36].

The mechanism of shrinkage, attributed to induced capillary forces during drying, is widely understood and generally accepted [31]. Both autogenous and drying shrinkage share this common underlying mechanism, but their development has some differences. Autogenous shrinkage results from a

chemical reaction within the cement paste due to a reduction of internal moisture during cement hydration [40]. This type of shrinkage occurs during the initial days after casting. In contrast, drying shrinkage initiates when concrete is exposed to drying conditions, making it more sensitive to environmental conditions and specimen size [34]. Unlike autogenous shrinkage, drying shrinkage can continue affecting concrete for years. As was the case for creep, the influencing factors can be categorized into intrinsic and extrinsic.

- *Intrinsic factors*

  Both autogenous and drying shrinkage depend on concrete composition. A lower *w/c* ratio is associated with an increase in autogenous shrinkage, while it reduces drying shrinkage [41]. The quantity, grading, and elastic modulus of the aggregates results in a restricting effect, similar to what is observed for creep [31]. Other factors include the type of cement and the use of admixtures.
- *Extrinsic factors*

  While both autogenous and drying shrinkage are affected by the concrete composition, only drying shrinkage can be controlled by external factors. A higher relative humidity will result in a lower drying shrinkage. Furthermore, the drying rate decreases in thicker specimens.

2.2.2. Influence in concrete structures

The influence of creep and shrinkage on a structural level depends on the type of structure. According to [17], structures are classified into five levels based on their susceptibility to creep and shrinkage. Levels one to three, which include reinforced and prestressed beams, slabs, and medium-span bridges, are generally considered less sensitive. In contrast, structures categorized as levels four and five, such as long-span and record-span bridges, cooling towers, and large roof shells, are regarded as sensitive. For these sensitive structures, a detailed creep and shrinkage analysis is recommended [17].

Primarily, creep and shrinkage reduce the stiffness in concrete structures, which is reflected in the time-dependent deformations [42]. In prestressed elements, these phenomena cause shortening of the section, thus leading to prestress losses [30]. Additionally, creep and shrinkage will have an impact on the stresses of statically indeterminate structures [42]. In a scenario where concrete elements of different ages interact in a structure, the action effects on the elements with a higher creep rate will be redistributed to the ones with a lower creep rate [30]. Additionally, statically indeterminate structures have constraints that may result in imposed deformations. For example, the settlement of the pier of a continuous bridge will result in imposed stresses which are proportional to the system's stiffness. Creep diminishes these stresses by reducing the stiffness of the structure.

The influence of creep and shrinkage is generally evaluated in the Serviceability Limit State (*SLS*), specifically the limit state of deflection and cracking [19]. The recurrent problems encountered with creep and shrinkage include:

- Excessive deflections
- Loss of prestressing force
- Stress redistribution due to differential creep
- Stress redistribution due to changes in statical systems

2.3. Modelling of creep and shrinkage

2.3.1. Code-based models for creep and shrinkage

Creep and shrinkage are among the most uncertain properties of concrete [10]. The complex mechanisms and the variability in the contributing factors add complexity to their study. Consequently, accounting for these effects in structural design becomes a challenging task. The importance of accounting for creep and shrinkage in design gained recognition from several international organizations like ACI, CEB, and FIP, starting in the 1960s [6]. The task of these groups was to develop semi-empirical models that strike a balance between accuracy and practicality. This led to the development of multiple code-based models for design codes and guidelines, such as Eurocode 2 and *fib* Model Code for Concrete Structures. Furthermore, models rooted in more substantial theoretical principles, like the RILEM B3 and B4 models, were developed to provide more accurate predictions for creep-sensitive structures.

Code-based models are typically formulated based on simplifying assumptions. One of the main assumptions is that creep and shrinkage are independent and additive [6]. This allows for a convenient formulation that treats these two effects separately. Moreover, an aging linear viscoelastic material model for concrete is assumed (see Section 2.3.3) [20]. This assumption, which implies the applicability of the superposition principle, aligns well with experimental data for stresses lower than 40% of the concrete compressive strength [10]. Nevertheless, deviations from this principle happen when strain reductions occur, such as during unloading [43]. Furthermore, under higher stresses, non-linear behavior can occur due to micro-cracking and stress-induced aging [44]. Another prevalent assumption encountered in code-based models is that creep and shrinkage strains are uniformly distributed along the cross-section. Yet, this assumed uniformity has been proven to be inadequate for box girder bridges, due to the large difference in shrinkage between top and bottom slabs [16].

fib Model Code for Concrete Structures

The Fédération internationale du béton *fib* was formed in 1998 through the merger of Comité européen du béton CEB and Fédération internationale de la précontrainte FIP. Their collaboration led to the publication of the CEB-FIP Model Code for Concrete Structures in 1978 (MC78), which became a reference for design standards like Eurocode 2 [45].

The MC78 recommends two approaches for incorporating creep and shrinkage effects in concrete structures. The first approach provides mean values for the creep coefficient $\varphi(t_\infty, t_0)$ and the shrinkage strain $\varepsilon_{cs}(t, t_0)$, and is suitable when great accuracy is not required. They depend on relative

humidity, notional size, and age of concrete [43]. The second approach addresses the time-dependent behavior of concrete. For creep, it introduces a creep function $\phi(t, t_0)$, which represents the total deformation of concrete over time under constant unit stress. This function requires the calculation of the creep coefficient $\varphi(t, t_0)$ with a summation model that accounts for rapid initial strain, delayed elastic strain, and delayed plastic strain (flow) [46]. Regarding shrinkage, the strain curve $\varepsilon_s(t, t_0)$ is formulated as the product of a final shrinkage coefficient and a function describing the evolution of shrinkage over time [19].

Revisions to the MC78 resulted in the publication of the CEB-FIP Model Code for Concrete Structures 1990 (MC90). MC90 introduces the concept of a creep compliance function $J(t, t_0)$, which represents the total stress-dependent (i.e. elastic + creep) strain per unit stress [44]. The creep coefficient, denoted now as $\phi(t, t_0)$, undergoes a major change by adopting a linear product model instead of the previous summation model. This new model expresses creep as the product of two functions: one describing the effect of age at loading, and another describing the development of creep over time under load [19]. Regarding the total shrinkage strain $\varepsilon_s(t, t_s)$, the basis of the product formulation from MC78 is maintained while incorporating certain improvements [44].

Twenty years after the publication of MC90, the current version *fib* Model Code for Concrete Structures 2010 (MC10), was introduced. The product model for creep, as introduced by MC90, is refined in MC10. Notably, in recognition of the dominance of micro-structural mechanisms in high-strength concrete. A new formulation for shrinkage is introduced, distinguishing autogenous shrinkage $\varepsilon_{cas}(t)$ and drying shrinkage $\varepsilon_{cds}(t, t_s)$ [47].

In June 2023, the *fib* Model Code for Concrete Structures 2020 (MC20), was approved, with the official release planned for the last quarter of 2023 [48]. The notable change introduced by MC20 is now focused on the creep coefficient $\varphi(t, t_0)$, introducing a distinction between basic and drying creep. The shrinkage formulation from MC10 has some minor improvements in intermediate calculations for this edition [21]. This improvement acknowledges that the physical mechanisms behind basic and drying creep are different. This is complemented by the fact that, while the hyperbolic function describing drying creep approaches an asymptotic value at a time t_∞, the chosen function for basic creep is logarithmic and does not approach a finite value [21].

Eurocode 2: Design of Concrete Structures

Released in 2004, Eurocode 2 (EC2) is the current standard for the design of concrete structures [49]. In the context of shrinkage effects, EC2 considers two components: drying and autogenous shrinkage strains. For creep, no distinction is made between basic and drying creep [50]. Given the significant variability in creep and shrinkage values, this code acknowledges the need for experimental assessments of these effects in creep-sensitive structures. Annex B (of the Eurocode) provides a procedure for incorporating experimental data into the formulation.

The work towards the development of a second generation of Eurocodes started in 2016. Although the expected release is scheduled for 2026, selected draft versions have been made available for infor-

mational purposes, as is the case of Eurocode 2 [51]. This final preliminary release (fprEC2) introduces significant revisions to the original model for creep and shrinkage. The previously established general approach is now applicable only to plain concrete structures with a maximum design life of 50 years. For a more accurate prediction, the now normative Annex B (of the Eurocode) should be used. The new model is similar to MC20, with only minor differences in specific coefficients for intermediate calculations. A notable refinement of fprEC2 compared to its predecessor EC2 is the subdivision of creep into two components: basic creep and drying creep [51].

B-Models

The series of *B* models, initially developed at Northwestern University and later endorsed as a RILEM recommendation, are widely recognized as the most theoretically grounded models for predicting creep and shrinkage effects in concrete structures. The first model, known as the BP Model, was introduced in 1978 to address the need for a more sophisticated and theoretically justified approach for creep-sensitive structures. The BP model characterizes time-dependent deformations by four main principles: a square-root hyperbolic law for shrinkage, a double power law for creep, a diffusion-type size dependence of humidity effects, and an additive drying creep term related to shrinkage [52]. In 1991, an updated version was presented as the BP-KX model. This model incorporated the latest knowledge, at that time, regarding the physical mechanisms and mathematical formulations governing creep and shrinkage in concrete [53].

Due to their theoretical and mathematical background, both the BP and BP-KX models were naturally more complex than other code-based models available at the time. A simpler yet theoretically well-justified version was presented as the third major update, known as the Model B3. The refinements of this model include simplified expressions as a result of sensitivity studies, and the introduction of a theoretically derived expression for drying creep [54]. Additionally, creep is presented as a compliance function accounting for both aging basic creep and drying creep effects [55]. The refinement of this model was the result of a calibration based on a large dataset comprising approximately 15000 data points [54]. Notably, this model also provides a methodology to improve creep and shrinkage estimations based on short-term tests.

The dataset used for the calibration of Model B3 was further extended for the calibration of Model B4, incorporating the multi-decade deflection data of 69 large-span prestressed bridges [17]. Six of these bridges are from the Netherlands: Maastricht, Grubbenvorst, Wessem, Empel, Ravenstein, and Heteren [56]. The updated database led to refinements in the expressions for concrete strength, cement, and aggregate types, and a new formulation for autogenous shrinkage, based on new data from high-performance concrete. The formulation proposed by Model B4 is a product model that distinguishes basic and drying creep, as well as autogenous and drying shrinkage. Creep behavior is characterized by a creep compliance function $J(t, t')$, while shrinkage effects are described by a strain curve $\varepsilon_{sh,total}(t, t_0)$. Further, to capture the relationship between creep and shrinkage, and other influencing factors, such as the water/cement ratio (*w/c*) or cement type, semi-empirical parameters q_1 through q_5

are introduced in the model [17].

2.3.2. Formulation and sensitivity of input parameters

Section 2.3.1 introduced various code-based models for creep and shrinkage. This study specifically employs four models: MC78, EC2, fprEC2, and B4. The main equations for each model are presented below. For the complete formulation, the reader is referred to the original documentation of each respective model. For MC78, the creep coefficient $\varphi(t, t_0)$ and shrinkage strain $\varepsilon_s(t, t_0)$ are calculated with Equations (2.1) and (2.2), respectively [46].

$$\varphi(t, t_0) = \beta_a(t_0) + \varphi_d \beta_d(t, t_0) + \varphi_f[\beta_f(t) - \beta_f(t_0)] \tag{2.1}$$

where:

$\beta_a(t_0)$ is the coefficient depending on the compressive strength of concrete at t_0 and ∞

φ_d is the delayed modulus of elasticity

β_d is the function for the delayed elasticity

φ_f is the flow coefficient

β_f is the function of the delayed plasticity

t_0 is the age of the concrete at the time of loading

$$\varepsilon_s(t, t_0) = \varepsilon_{so}[\beta_s(t) - \beta_s(t_0)] \tag{2.2}$$

where:

ε_{so} is the basic shrinkage coefficient

$\beta_s(t)$ is the change of shrinkage in time t

$\beta_s(t_0)$ is the change of shrinkage at the time of exposure t_0

MC78 has additional provisions for the calculation of the modulus of elasticity, the creep coefficient, and the shrinkage strain to account for the use of lightweight aggregate concrete (LWAC) [46]. The modulus of elasticity of LWAC can be assumed equal to the value for normal weight concrete (NWC) multiplied by a coefficient η_2 (see Equation (2.3)). The creep coefficient can also be assumed equal to the value for NWC multiplied by the same coefficient η_2. Additionally, MC78 recommends multiplying the creep strain by a factor that may vary from 1.0 to 1.2. The shrinkage strain for LWAC is equal to NWC multiplied by a factor as high as 1.5.

$$\eta_2 = (\frac{\rho}{2400})^2 \tag{2.3}$$

where:

ρ is the oven-dry density of LWAC

For EC2, the creep coefficient $\varphi(t, t_0)$ and shrinkage strain ε_{cs} are calculated with Equations (2.4) and (2.5), respectively [50].

$$\varphi(t, t_0) = \varphi_0 \cdot \beta_c(t, t_0) \tag{2.4}$$

where:

φ_0 is the notional creep coefficient

β_c is the coefficient describing the development of creep in time

t_0 is the age of the concrete at the time of loading

$$\varepsilon_{cs} = \varepsilon_{cd} + \varepsilon_{ca} \tag{2.5}$$

where:

ε_{cd} is the drying shrinkage strain (see Equation (2.6))

ε_{ca} is the autogenous shrinkage strain (see Equation (2.7))

$$\varepsilon_{cd}(t) = \beta_{ds}(t, t_s) \cdot k_h \cdot \varepsilon_{cd,0} \tag{2.6}$$

where:

$\beta_{ds}(t, t_s)$ is a function describing the time development of drying shrinkage

k_h is the coefficient dependent on the notional size

$\varepsilon_{cd,0}$ is the nominal unrestrained drying shrinkage

$$\varepsilon_{ca}(t) = \beta_{as}(t) \cdot \varepsilon_{ca,\infty} \tag{2.7}$$

where:

$\beta_{as}(t)$ is a function describing the time development of autogenous shrinkage

$\varepsilon_{ca,\infty}$ is the final value of autogenous shrinkage

For EC2, the modulus of elasticity and the creep coefficient for LWAC can also be assumed equal to NWC multiplied by a coefficient η_E (see Equation (2.8)) [50]. The creep strains should be multiplied by a factor η_2, equal to 1.3 for strength classes LC16/18 and lower, and equal to 1.0 for strength classes LC20/22 and higher. The final drying shrinkage strain for LWAC is equal to NWC multiplied by a factor η_3, equal to 1.5 for strength classes LC16/18 and lower, and equal to 1.2 for strength classes LC20/22 and higher. EC2 notes that its formulation for autogenous shrinkage in NWC does not consider water

supplied by the aggregate. Consequently, the model predicts maximum values for LWAC. If LWAC aggregates are partially or fully saturated, it is expected that autogenous shrinkage in LWAC is lower.

$$\eta_E = (\frac{\rho}{2200})^2 \tag{2.8}$$

where:

ρ is the oven-dry density of LWAC.

For fprEC2, the creep coefficient $\varphi(t, t_0)$ and shrinkage strain $\varepsilon_{cs}(t, t_s)$ are calculated with Equations (2.9) and (2.12), respectively [51].

$$\varphi(t, t_0) = \varphi_{bc}(t, t_0) + \varphi_{dc}(t, t_0) \tag{2.9}$$

where:

φ_{bc} is the basic creep coefficient (see Equation (2.10))

φ_{dc} is the drying creep coefficient (see Equation (2.11))

t_0 is the age of concrete at the time of loading

$$\varphi_{bc}(t, t_0) = \beta_{bc,fcm} \cdot \beta_{bc,t-t_0} \tag{2.10}$$

where:

$\beta_{bc,fcm}$ is a function to describe the effect of concrete strength on basic creep

$\beta_{bc,t-t_0}$ is a function to describe the time development of basic creep

$$\varphi_{dc}(t, t_0) = \beta_{dc,fcm} \cdot \beta_{dc,RH} \cdot \beta_{dc,t_0} \cdot \beta_{dc,t-t_0} \tag{2.11}$$

where:

$\beta_{dc,fcm}$ is a function to describe the effect of concrete strength on drying creep

$\beta_{dc,RH}$ is a function to describe the effect of relative humidity and notional size on drying creep

β_{dc,t_0} is a function to describe the effect of the adjusted concrete age at loading on drying creep

$\beta_{dc,t-t_0}$ is a function to describe the time development of drying creep

$$\varepsilon_{cs}(t, t_s) = \varepsilon_{cbs}(t) + \varepsilon_{cds}(t, t_s) \tag{2.12}$$

where:

$\varepsilon_{cbs}(t)$ is the basic shrinkage (see Equation (2.13))

$\varepsilon_{cds}(t, t_s)$ is the drying shrinkage (see Equation (2.14))

t_s is the time at the beginning of drying

$$\varepsilon_{cbs}(t) = \varepsilon_{cbs,fcm} \cdot \beta_{bs,t} \cdot \alpha_{NDP,b} \tag{2.13}$$

where:

$\varepsilon_{cbs,fcm}$ is the notional basic shrinkage coefficient

$\beta_{bs,t}$ is the function describing the time development of basic shrinkage

$\alpha_{NDP,b}$ is a coefficient dependent on the National Annex

$$\varepsilon_{cds}(t, t_s) = \varepsilon_{cds,fcm} \cdot \beta_{RH} \cdot \beta_{ds,t-t_s} \cdot \alpha_{NDP,d} \tag{2.14}$$

where:

$\varepsilon_{cds,fcm}$ is the notional drying shrinkage coefficient

β_{RH} is the coefficient to consider the effect of relative humidity

$\beta_{ds,t-t_s}$ is the function describing the time development of drying shrinkage

$\alpha_{NDP,d}$ is a coefficient dependent on the National Annex

Similarly to EC2, fprEC2 provides a coefficient $\eta_{lw,Ec}$ for the LWAC modulus of elasticity and the creep coefficient (see Equation (2.15)) [51]. For strength classes equal or lower to LC16/18, an additional factor of 1.3 is also multiplied to the creep coefficient. The total shrinkage strain is obtained by multiplying the values for NWC with 1.5 for strength classes LC16/18 and lower, and equal to 1.2 for strength classes LC20/22 and higher.

$$\eta_{lw,Ec} = (\frac{\rho_c}{2200})^2 \tag{2.15}$$

where:

ρ_c is the oven-dry density of LWAC

The creep compliance function $J(t, t_0)$ for MC78, EC2, and fprEC2 is written as shown in Equation (2.16).

$$J(t, t_0) = \frac{1}{E_c(t_0)} + \frac{\varphi(t, t_0)}{E_{c28}} \tag{2.16}$$

where:

$\varphi_(t, t_0)$ is the creep coefficient

$E_c(t_0)$ is the modulus of elasticity of the concrete at the time of loading t_0

E_{c28} is the modulus of elasticity of the concrete at 28 days

B4 calculates the creep compliance function $J(\hat{t}, \hat{t'})$ with Equation (2.17) [17]. The creep coefficient $\phi(t, \hat{t'})$ can be derived from this function with Equation (2.18). Additionally, the shrinkage strain $\epsilon_{sh,total}(\tilde{t}, \tilde{t_0})$ is obtained with Equation (2.19). B4 does not have additional provisions for LWAC. However, its calibration database does encompass LWAC concrete specimens [56]. Moreover, the formulation includes an aggregate-dependent parameter for shrinkage. This parameter allows the selection of materials such as Limestone, which may exhibit lower particle density than aggregates typically used for NWC.

$$J(\hat{t}, \hat{t'}) = q_1 + R_T C_0(\hat{t}, \hat{t'}) + C_d(\hat{t}, \hat{t'}, \tilde{t_0}) \tag{2.17}$$

where:

q_1 is the instantaneous compliance

R_T is a factor that accounts for the effects of temperature

$C_0(\hat{t}, \hat{t'})$ is the compliance function for basic creep

$C_d(\hat{t}, \hat{t'}, \tilde{t_0})$ is the additional compliance due to simultaneous drying

$$\phi(t, \hat{t'}) = E(\hat{t'}) J(t, \hat{t'}) - 1 \tag{2.18}$$

where:

$E(\hat{t'})$ is the modulus of elasticity at loading age $\hat{t'}$

$$\epsilon_{sh,total}(\tilde{t}, \tilde{t_0}) = \epsilon_{sh}(\tilde{t}, \tilde{t_0}) + \epsilon_{au}(\tilde{t}, \tilde{t_0}) \tag{2.19}$$

where:

$\epsilon_{sh}(\tilde{t}, \tilde{t_0})$ is the drying shrinkage (see Equation (2.20))

$\epsilon_{au}(\tilde{t}, \tilde{t_0})$ is the autogenous shrinkage (see Equation (2.21))

$\tilde{t}$ is the temperature corrected exposure duration

$\tilde{t_0}$ is the temperature corrected age at exposure

$$\epsilon_{sh}(\tilde{t}, \tilde{t_0}) = \epsilon_{sh\infty}(\tilde{t_0}) \cdot k_h \cdot S(\tilde{t}) \tag{2.20}$$

where:

$\epsilon_{sh\infty}(\tilde{t_0})$ is the shrinkage correction for the effect of aging on the elastic stiffness

k_h is a factor that accounts for the relative humidity

$S(\tilde{t})$ is the time curve

$$\epsilon_{au}(\tilde{t},\tilde{t_0}) = \epsilon_{au\infty}[1 + (\frac{\tau_{au}}{\tilde{t}+\tilde{t_0}})^{\alpha}]^{r_t} \tag{2.21}$$

where:

$\epsilon_{au\infty}$ is the final autogenous shrinkage

τ_{au} is the autogenous shrinkage halftime

α is a factor dependent on the type of cement and the water-to-cement ratio

r_t is a factor dependent on the type of cement

As explained before, the B4 model is the most theoretically grounded model for creep and shrinkage. Consequently, this model requires the most input. Table 2.3 illustrates the input variables for each code-based model.

Parameter	MC78	EC2 / fprEC2	B4
Age at loading	X	X	X
Age at drying	X	X	X
Mean Compressive Strength	X	X	X
Cement Type	X	X	X
Aggregate Type	X	X	X
Relative Humidity	X	X	X
Temperature of Environment	X	X	X
Temperature of Environment during curing	X		X
Notional Size	X	X	X
Cement Content			X
Water/Cement Ratio			X
Aggregate/Cement Ratio			X
Mass Density of Concrete			X
Specimen Type			X
Activation Energy			X

Table 2.3: Input for different code-based creep and shrinkage models.

Propagation of uncertainty

The code-based models used to incorporate creep and shrinkage effects on structural designs show significant uncertainty due to various factors. First and foremost, the underlying mechanisms governing creep and shrinkage phenomena are still not fully understood [57]. Additionally, the available databases used to calibrate models exhibit a notable degree of scatter. There is not sufficient experimental data on the long-term effects of creep and shrinkage, so predictions are based on extrapolations [10]. Furthermore, discrepancies between the characteristics of the specimens used in tests and real-world structural elements, such as differences in size, further contribute to the uncertainty associated with these models.

Guidelines provide clear warnings regarding the potential prediction errors associated with creep and shrinkage effects [21, 47]. They emphasize the importance of adopting a probabilistic approach to

account for the uncertainty. For instance, MC10 provides mean coefficients of variation for the creep model ($V_c = 20\%$) and shrinkage model ($V_s = 35\%$), as well as correction factors to the mean creep coefficient and shrinkage strain values to obtain the corresponding 5th or 10th percentiles. Similarly, Models B3 and B4 also recommend a statistical analysis with an estimation of the 95% confidence interval limits for creep-sensitive structures (e.g. long-span prestressed box girder bridges). This recommendation is accompanied by uncertainty factors for each model parameter to determine the deviations for the mean [17]. Consequently, it is important to analyze the structural response as a statistical variable rather than a deterministic value. An approach accounting for the statistical variation will provide more realistic results.

Alongside the inherent uncertainties within the creep and shrinkage models discussed above, there exists additional uncertainty in their respective inputs. To explore the influence of specific parameters on the creep compliance function and shrinkage strain curves, a sensitivity analysis was conducted. This analysis focused on three key parameters: environmental temperature *T*, relative humidity *RH*, and mean compressive strength f_{cm}. The selection of *T* and *RH* for this study was motivated by their daily and annual variations, while f_{cm} may introduce uncertainty due to a lack of exactness in its value. Only the most relevant results of this sensitivity analysis are presented in this section. The remaining results are included in Annex B.

The selected values for *T* are 15, 20, and 25°C. For the creep compliance function, two times of loading *t'* were selected, 28 and 250 days. The most influenced model by the variation of 5°C is B4, as seen in Figure 2.5. This results in an approximately 10% difference in the creep response after 100 years, irrespective of *t'*. For the remaining models, MC78, EC2, and fprEC2, the influence of *T* is minimal for creep. The behavior of B4 and MC78 regarding shrinkage strain exhibits minimal variation. Notably, the formulation governing shrinkage in EC2 and fprEC2 models does not incorporate the parameter *T*.

The variations for relative humidity *RH* are 70, 80, and 90%. For creep, MC78 shows the most pronounced sensitivity to a 10% increase in *RH*, exhibiting an approximate 15% difference after 100 years (see Figure 2.6). In contrast, the influence of *RH* on B4, EC2, and fprEC2 models is minimal. Additionally, all models show significant sensitivity to *RH* for shrinkage, as illustrated in Figure 2.7. On average, the 10% variation results in roughly 25%, 40%, 30%, and 35% differences for B4, MC78, EC2, and fprEC2, respectively.

The mean compressive strength f_{cm} was arbitrarily set at a central value of 38 $\mathrm{N/mm^2}$, with by two additional values representing an approximate 10% increase and decrease, equal to 34 $\mathrm{N/mm^2}$ and 42 $\mathrm{N/mm^2}$. The models most affected by these variations are EC2 and fprEC2, as shown in Figure 2.8. However, in both cases, the observed differences remain within 10%. Regarding shrinkage, the influence of f_{cm} remains minimal for MC78, EC2, and fprEC2, and with no impact for B4.

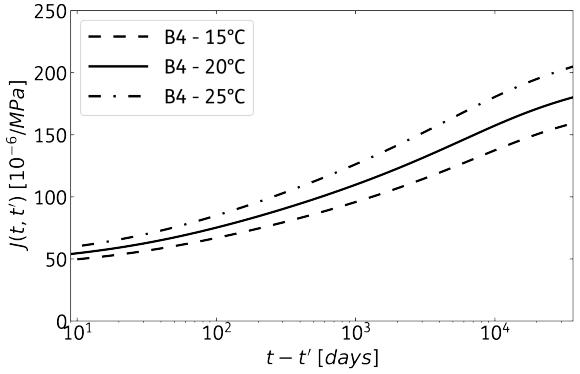

(a) Comparison of creep compliance curves for B4 at *t'* of 28 days.

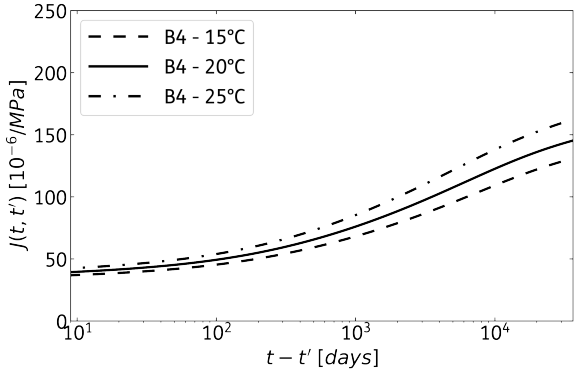

(b) Comparison of creep compliance curves for B4 at *t'* of 250 days.

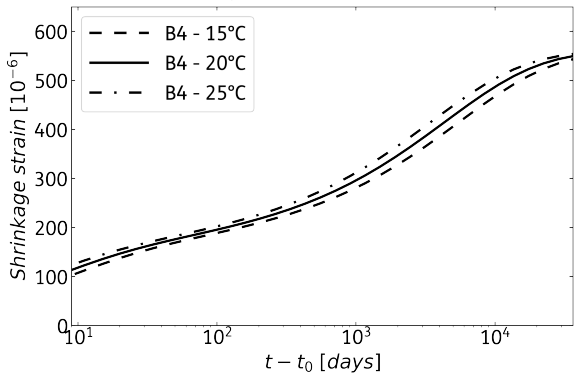

(c) Comparison of shrinkage strain curves for B4.

Figure 2.5: Impact of temperature (*T*) in the creep compliance and shrinkage strain curves of B4. The chosen values for *T* are 15, 20, and 25°C. The chosen times of loading (*t'*) for creep are 28 and 250 days.

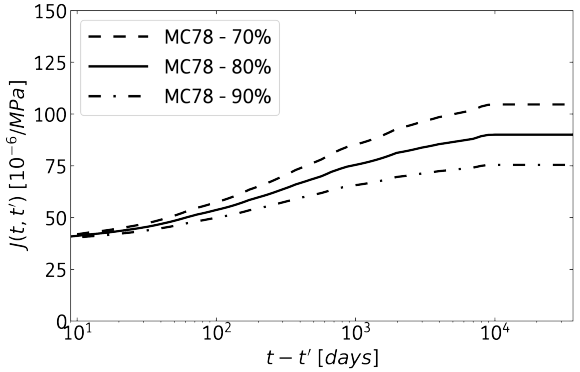

(a) Comparison of creep compliance curves for MC78 at *t'* of 28 days.

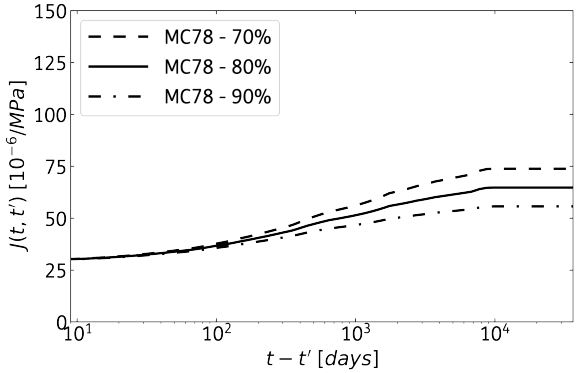

(b) Comparison of creep compliance curves for MC78 at *t'* of 250 days.

Figure 2.6: Impact of relative humidity (*RH*) in the creep compliance curves of MC78. The chosen values for *RH* are 70, 80, and 90%. The chosen times of loading (*t'*) are 28 and 250 days.

2.3.3. Calculation procedure

Concrete can be modelled as an aging linear viscoelastic material. With viscoelasticity, the material has memory, so the strain history affects the current stresses [58]. The time-dependent strain $\varepsilon(t)$ in concrete due to constant stress $\sigma(t_0)$ can be calculated with Equation (2.22).

$$\varepsilon(t) = \sigma(t_0) \cdot J(t_0, t) \tag{2.22}$$

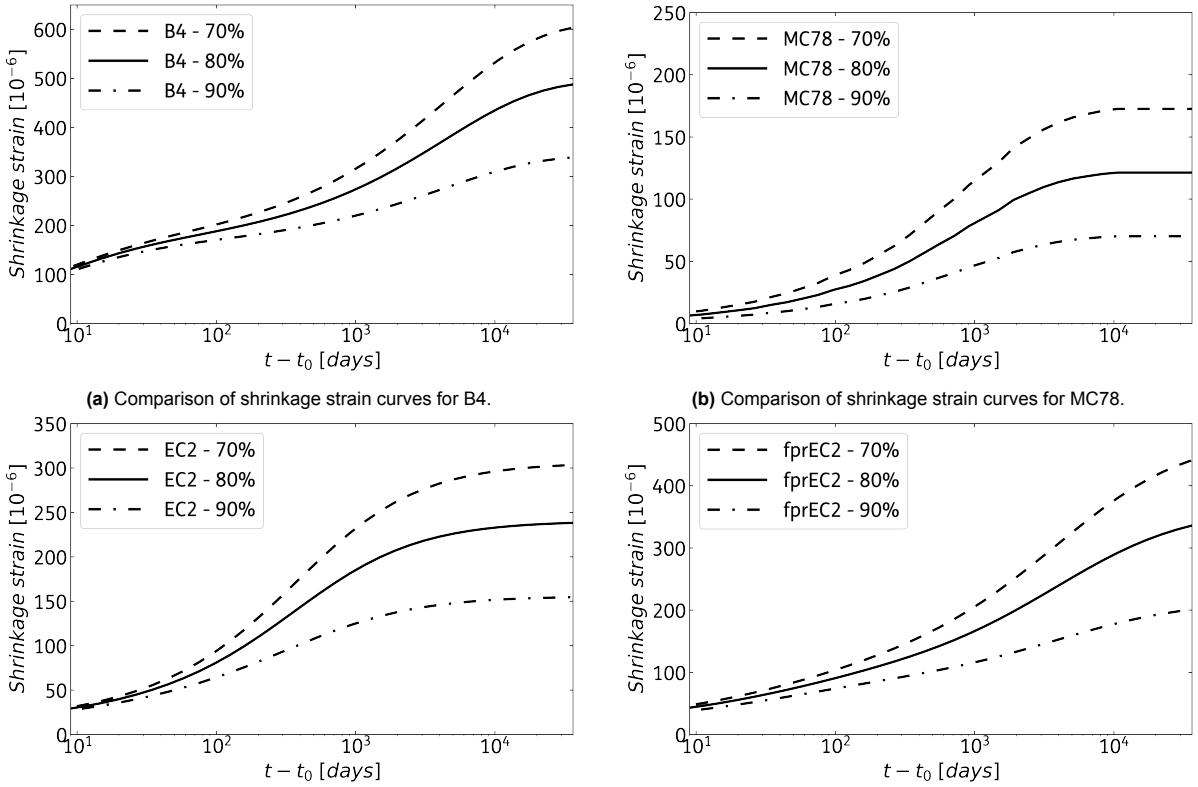

(a) Comparison of shrinkage strain curves for B4.

(b) Comparison of shrinkage strain curves for MC78.

(c) Comparison of shrinkage strain curves for EC2.

(d) Comparison of shrinkage strain curves for fprEC2.

Figure 2.7: Impact of relative humidity *RH* in the shrinkage strain curves of B4, MC78, EC2, and fprEC2. The chosen values for *RH* are 70, 80, and 90%.

where:

$J(t_0, t)$ is the creep compliance function

The stress history of a structure such as a balanced cantilever bridge is complex, especially during the construction stage. To account for the variation of stress conditions, the principle of superposition is used. The principle of superposition states that the strain caused by a stress history $\sigma(t)$ can be obtained by decomposing the history into small increments $d\sigma(t)$ applied at different times τ_i (see Figure 2.9) [6, 59]. This allows $\varepsilon(t)$ to be calculated by Equation (2.23) [6]. The principle of superposition is valid under certain conditions: (i) the stresses are lower than 40% of the strength, (ii) deloading does not occur, (iii) the change in moisture content during creep is negligible, and (iv) there is no sudden stress increase long after the initial loading [59].

The formulation presented in Equation (2.23) has the disadvantage that each strain increment is calculated based on the entire stress history [10]. The memory requirements for such calculation make this approach unfeasible for Finite Element Analysis (FEA) on real-world bridges. A solution is to reformulate the integral stress-strain relation into a differential counterpart [6]. With a differential-type equation, the stress history is replaced by state variables, which are updated for each time step [10, 6]. This is the formulation used in DIANA FEA [58].

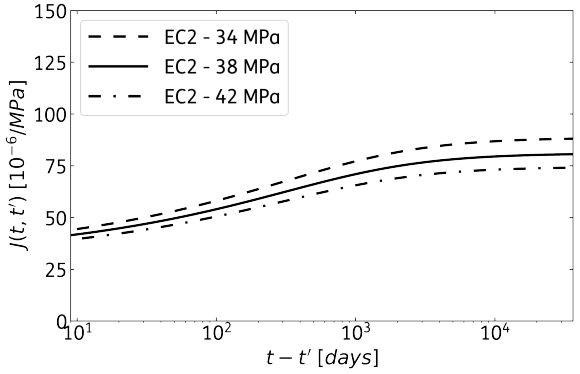

(a) Comparison of creep compliance curves for EC2 at *t'* of 28 days.

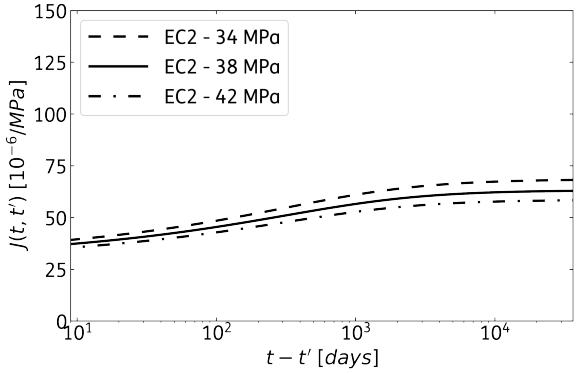

(b) Comparison of creep compliance curves for EC2 at *t'* of 250 days.

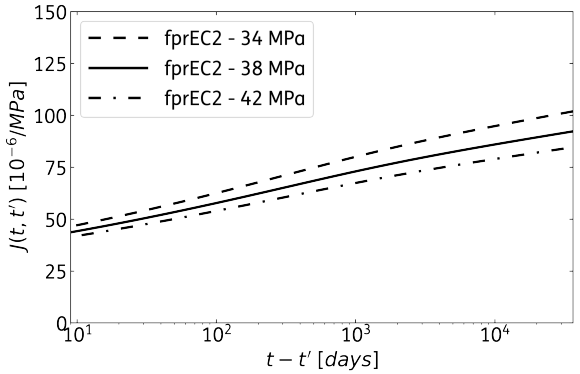

(c) Comparison of creep compliance curves for fprEC2 at *t'* of 8 days.

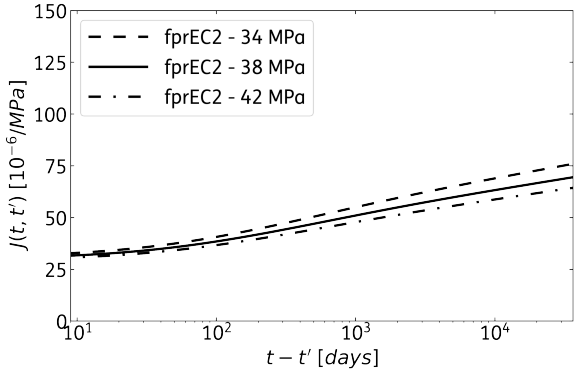

(d) Comparison of creep compliance curves for fprEC2 at *t'* of 250 days.

Figure 2.8: Impact of mean compressive strength *fcm* in the creep compliance curves of EC2 and fprEC2. The chosen values for *fcm* are 34, 38, and 42 N/mm^2. The chosen times of loading (*t'*) are 28 and 250 days.

$$\varepsilon(t) = \sigma(t_0) \cdot J(t_0, t) + \int_0^t \frac{d\sigma(\tau)}{dt} \cdot J(\tau, t)\, d\tau \tag{2.23}$$

where:

$\frac{d\sigma(\tau)}{dt}$ is the stress rate

2.4. Creep and shrinkage in lightweight aggregate concrete

Code-based models commonly used for analyzing creep and shrinkage incorporate additional provisions for lightweight aggregate concrete (LWAC) in concrete design. These provisions modify the modulus of elasticity, creep coefficient, and shrinkage strain, all originally calculated for normal-weight concrete (NWC) [46, 50, 51]. These modifications, explained in Section 2.3.2 for MC78, EC2, and fprEC2, can be summarized into three main concepts: (i) LWAC has a lower modulus of elasticity compared to NWC, (ii) the time-dependent response in the creep compliance function is the same for LWAC and NWC, and (iii) shrinkage is expected to be higher in LWAC when compared to NWC. It is worth noting that Model B4, while not explicitly addressing lightweight aggregate, includes LWAC test data within its calibration database [17].

Even though creep occurs in the cement paste, aggregates have a restraining effect in concrete

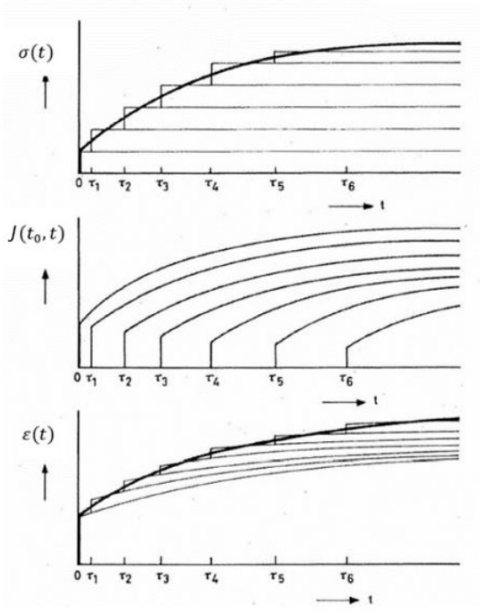

Figure 2.9: Decomposition of the stress history for the calculation of the time-dependent strain with the superposition principle [6].

due to their low susceptibility to creep [37]. The lower modulus of elasticity in LWAC diminishes this restraining effect, which is why creep and shrinkage in LWAC are expected to be higher than NWC for a similar concrete compressive strength [38]. Nevertheless, MC10 mentions that the higher creep tendency of LWAC due to the lower stiffness in the aggregates is compensated by the lower creep capability of the stiffer cement paste matrix [47]. This is reflected in the creep compliance formulation for LWAC, which assumes a time-dependent response equal to NWC, and a reduced initial elastic response due to a lower modulus of elasticity.

Evaluating whether the provisions for LWAC in code-based models are conservative is essential. The study on creep in LWAC by Best and Polivka [60] concluded that creep in LWAC resulted equal and in some cases lower than for NWC of comparable strength and that the difference in the response comes only from the elastic response due to the lower modulus of elasticity of LWAC. Furthermore, a study by Szydlowski and Labuzek [61] in LWAC beams showed that, compared to the prediction by EC2, the tested specimens exhibited a lower creep and shrinkage response. Wang et. al. [62] also compared creep in LWAC with the prediction from EC2, concluding that observed creep strains were lower than the prediction by EC2. The main conclusion from this 30-year-long experiment is that, by accounting for the provisions for LWAC in the standards, the formulation from EC2 can be applied and remain conservative for LWAC creep prediction.

In contrast to creep, the shrinkage strain for LWAC is increased by a certain percentage by code-based models like EC2. However, research suggests that drying shrinkage is lower in LWAC than in NWC. This is due to internal curing, which is the ability of a lightweight aggregate to absorb, retain, and release water, to provide concrete mixes with a post-hardened water supply [63]. The capacity of LWAC to store water in the porous aggregates and result in internal curing has proven to reduce drying

shrinkage in LWAC [64, 63, 65, 60]. This effect creates a denser cement matrix and has also been proven beneficial for reducing creep deformation [66]. But Takács [10], who compared experimental results with the prediction for creep and shrinkage by EC2 and MC90 found a delayed rate increase for creep and shrinkage, which resulted in final values surpassing the prediction by the code-based models. Similarly, Labbé and Lopez [67] concluded that internal curing does not reduce drying creep and shrinkage, but delays it.

The conservative nature of the provisions in code-based models when considering LWAC remains inconclusive due to the conflicting research findings. Further long-term research on creep and shrinkage is needed to gain a deeper understanding of the delay effect caused by internal curing, as it may initially appear that the provisions in code-based models are conservative, but subsequent behavior shows a reversal in the rate of deformations.

3

The Rooyensteinse Brug

This chapter describes the main characteristics of the Rooyensteinse Brug. Sections 3.1 and 3.2 explain the geometry and materials of the bridge, respectively. The construction process is discussed in Section 3.3. Finally, the results of a long-term, non-continuous monitoring campaign are presented in Section 3.4.

The Rooyensteinse Brug is a box girder prestressed concrete bridge located in Zoelen. This bridge was built with the balanced cantilever method between 1975 and 1977 (see Figure 3.1). The Rooyensteinse Brug spans over the Amsterdam Rijnkanaal and is part of the N835 highway, which serves as a distributor road.

3.1. Geometry

The Rooyensteinse Brug is a prestressed concrete box girder bridge. It has three spans, a main span of 150.5 m and two side spans, each extending 78.75 m [68]. This bridge has a total of 84 segments, each with a 3.5 m length (see Figure 3.2). The substructure comprises two intermediate piers and two bank seats. Upon completion of both sides of the bridge, a closing piece connected them monolithically, making the deck hyperstatic.

The cross-section is a box girder with a total width of 11.70 m and a height that varies between 2.12 m in the bank seats and 6.42 m at the intermediate piers [68]. The deck or top flange follows a tapered shape (1:50) with a thickness of approximately 0.37 m at the center. The cantilever part of the deck has a length of 2 m, and a variable thickness between 0.44 m on the web and 0.25 m at the end. The haunch has a length of 1.50 m and a height of 0.25 m. The webs have a thickness of 0.45 m and vary in height between 1.30 m and 4.87 m. Finally, the bottom flange varies in thickness between 0.20 m

(a) A side view.

(b) The spherical bearings located at the intermediate supports.

Figure 3.1: The Rooyensteinse Brug: side view and view of one of the piers.

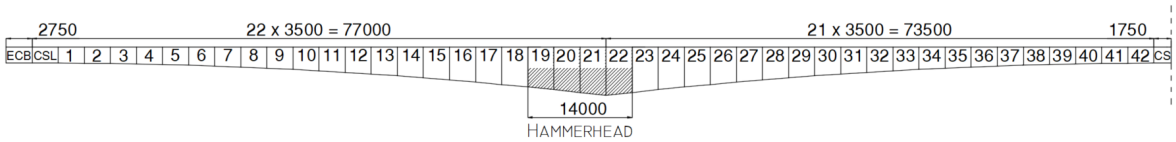

Figure 3.2: Overview of the segments comprising half of the Rooyensteinse Brug.

and 1.18 m and has a width of 7.70 m. Figure 3.3 shows the smallest and largest box-girder sections of this bridge.

The prestressing layout in the Rooyensteinse Brug is categorized into three groups. Groups 1 and 2 are continuity tendons, added to the design to resist the positive moment at mid-span and near the bank seat, respectively. Group 1 comprises a total of 12 prestressing tendons, 6 on each bridge end at the bank seat. This set of tendons extends from the webs towards the bottom flange of the initial 6 segments of the bridge (see Figure 3.4). Group 2 has a total of 42 prestressing tendons in the bottom flange of the 17 segments at the center of the mid-span of the bridge (see Figure 3.5). Group 3 consists of the cantilever tendons. A total of 236 tendons, 118 on each half of the bridge, are positioned within the top slab and sequentially anchored at the end of each segment. Figure 3.6 illustrates the layout of

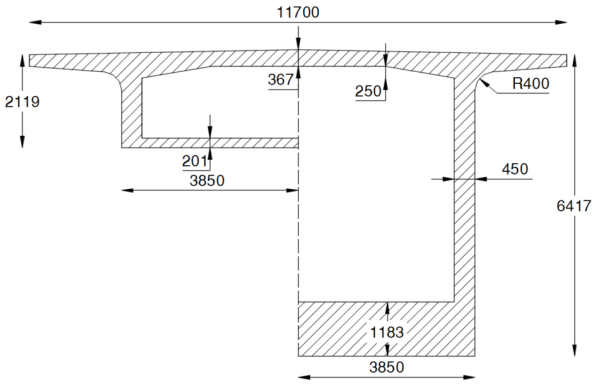

Figure 3.3: Dimensions of the smallest and largest cross-sections of the Rooyensteinse Brug (Segments 1 and 22, respectively). Dimensions are shown in mm.

the tendons present at the webs of Segment 17. The tendons labeled as 10, 11, and 22 are prestressed once this segment is cast. The figure also shows the progressive descent of tendons 12, 23, and 24 from the top flange. These tendons will be then anchored to segment 16. All other cantilever tendons, as indicated by the dashed lines, remain within the top slab until they are anchored at the webs of their respective segments.

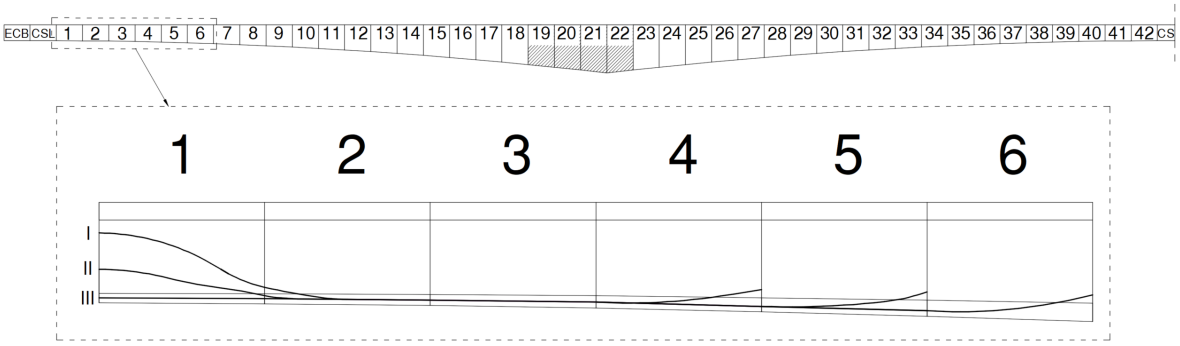

Figure 3.4: Side view of the continuity tendons of Group 1.

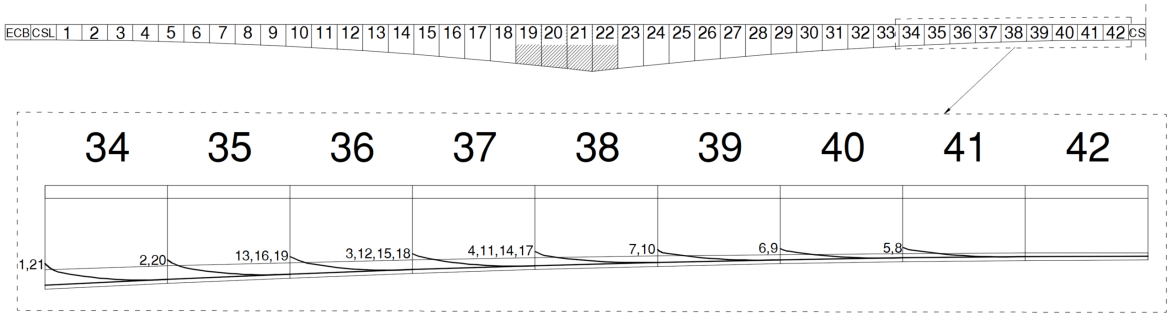

Figure 3.5: Side view of the continuity tendons of Group 2.

Groups 1, 2, and 3 are the longitudinal prestressing of the Rooyensteinse Brug, with a cross-sectional area of 1182 mm^2 per tendon. Additionally, in the hammerhead (i.e. segments 19-22),

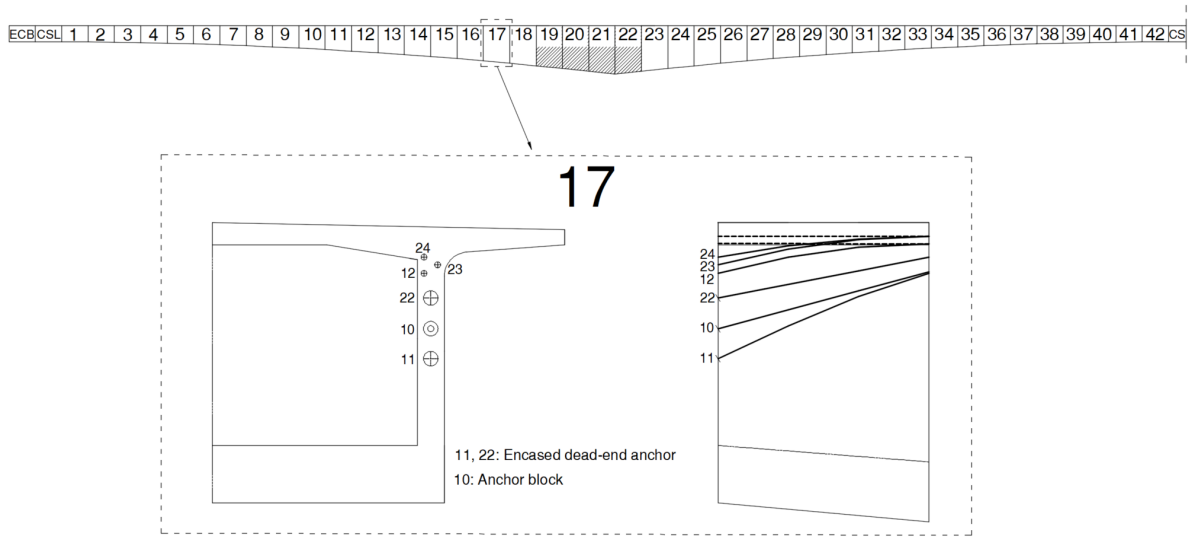

Figure 3.6: Front and side view of the cantilever tendons in the webs of Segment 17.

transversal prestressing is implemented using 28 tendons, each with an area of 530 mm^2. The applied tensioning stress is 1333 N/mm^2. While the specific grouting schedule for the Rooyensteinse Brug is not available, in practice it occurs approximately every two to three weeks. Details on the conventional reinforcement have been omitted since they are not utilized in the finite element model.

The Rooyensteinse Brug is supported by eight spherical bearings, with four of them positioned at the intermediate supports and the remaining four located at the bank seats. Spherical bearings allow for rotational movements, and the constraints on displacements are designed to accommodate thermal expansion and contraction. Figure 3.7 presents the specific boundary conditions for the Rooyensteinse Brug. During the construction process, temporary supports were added to the hammerhead to assist in mitigating the unbalanced moments that arise during the segment casting process.

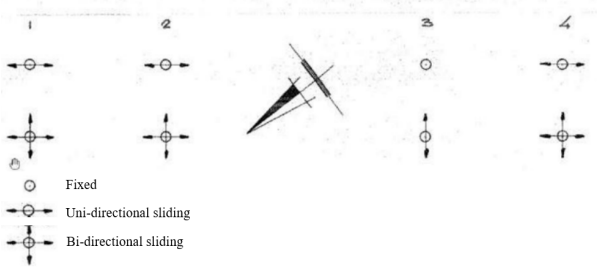

Figure 3.7: The constraints applied to the spherical bearings [18].

3.2. Material properties

The Rooyensteinse Brug is constructed with lightweight aggregate concrete. The information on the composition of this concrete mixture comes from three sources. [69] contains the specifications and conditions for the construction of the Rooyensteinse Brug, including the composition, preparation, processing, and finishing of the lightweight concrete mix. A summary of the relevant data is presented in

Table 3.1 [69].

Material Property	Value
Cube Compressive Strength (28 days) $f_{c,cube}$ [N/mm^2]	(minimum) 35
Cube Tensile Strength (28 days) $f_{t,cube}$ [N/mm^2]	(minimum) 3.5
Cube Compressive Strength (2 days) f_{cube} [N/mm^2]	(minimum) 24
Cement Type	Portland cement class B
Cement Content (per m^3) [kg]	360
Aggregate Type and Content (per m^3) [kg]	Dry Sand: 620 Dry loose poured Korlin A: 600
Mass Density Freshly Compacted Concrete ρ [kg/m^3]	Between 1730 and 1780

Table 3.1: Material properties of lightweight concrete, according to [69].

When casting the box-girder segments, cubes measuring 158 x 158 x 158 mm^3 were produced. Six cubes were cast per segment, amounting to a total of 252 cubes. These cubes were used to determine the concrete compressive strength after 28 days. As documented in [70], the results show a mean value of 44.7 N/mm^2 and a standard deviation of 3.0 N/mm^2.

In 2011, Rijkswaterstaat commissioned an investigation into the material properties of the Rooyensteinse Brug [71]. The focus was on evaluating the compressive and tensile strength of the concrete through core sampling. A total of 24 cores were extracted. Half of the cores were used to determine the compressive strength; the other half was used for the tensile strength. The results were subsequently used to calculate the characteristic compressive and tensile strength values. The mass density of the cores was also calculated. The main findings from this material investigation are presented in Table 3.2.

Material Property	Value
Characteristic Cylinder Compressive Strength f_{ck} [N/mm^2]	41.1
Characteristic Cylinder Tensile Strength f_{tk} [N/mm^2]	2.6
Average Mass Density Unreinforced Concrete Core ρ_{uc} [kg/m^3]	1759
Average Mass Density Reinforced Concrete Core ρ_{rc} [kg/m^3]	1766

Table 3.2: Main results from material investigation, according to [71].

The documentation for the Rooyensteinse Brug does not explicitly mention the water/cement ratio. However, based on similar bridge documentation, the expected value is 0.47. Additionally, the bulk density of Korlin A, the lightweight aggregate used for this bridge, is 1270 kg/m^3 [72]. The information concerning the steel quality of the tendons for this bridge is derived from the original calculations and the recalculation report [18, 68]. For the longitudinal prestressing, QP190 is utilized, with a characteristic tensile strength f_{pk} of 1864 N/mm^2. The transversal prestressing used QP170 steel, with a f_{pk} of 1670 N/mm^2.

3.3. Construction phases

The Rooyensteinse Brug was constructed with the balanced cantilever method. The construction began with the pier and bank seat, followed by the hammerhead. With the hammerhead ready, the traveling formwork was assembled and the weekly segmental construction began. Due to the size of the first 10 segments, only one segment was cast per week. Afterward, two segments were cast per week, one on each side of the hammerhead. The first half of the Rooyensteinse Brug was completed in 252 days, and the entire bridge was finished in approximately 484 days.

A general overview of the weekly construction cycle is discussed in Chapter 2. Some key moments in this process include the movement of the traveling formwork, the casting of a new segment, and the prestressing of the cantilever tendons. Figure 3.8 shows a schematic representation of these moments for segment 25. The cycle starts at day 1 with the movement of the traveling formwork. At day 4, the concrete casting of Segment 25 occurs. The prestressing of the cantilever tendons happens two days later. Finally, the movement of the traveling formwork will mark the start of a new week.

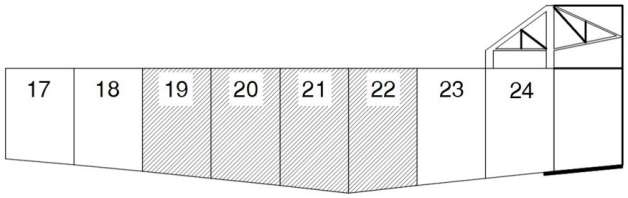

(a) Day 1: the moving of the traveling formwork to the corresponding position.

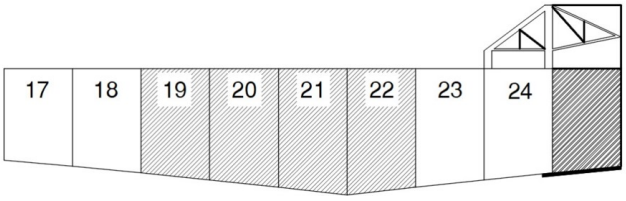

(b) Day 4: the casting of the new segment.

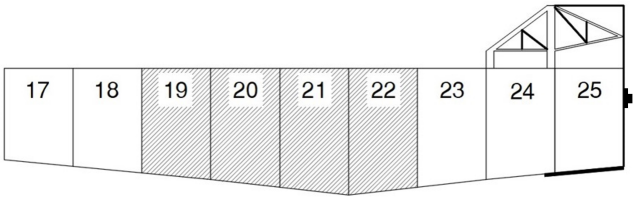

(c) Day 6: the prestressing of the cantilever tendons.

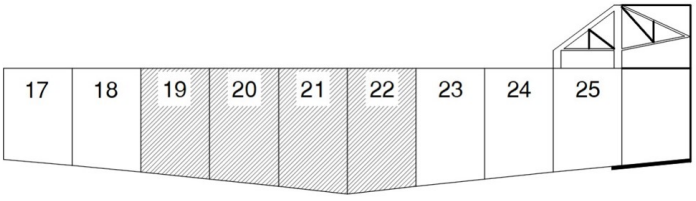

(d) New week, Day 1: the moving of the traveling formwork to the new position.

Figure 3.8: The weekly construction cycle for Segment 25. It starts at day 1 with the movement of the traveling formwork, (a). At day 4, the concrete casting of Segment 25 occurs, (b). The prestressing of the cantilever tendons happens two days later, (c). Finally, the movement of the traveling formwork will mark the start of a new week, (d).

3.4. Long-term, non-continuous monitoring of deflections

Upon the completion of the Rooyensteinse Brug, 22 brass bolts were positioned on the bridge deck to function as reference points for in-situ measurements (see Figure 3.9). These bolts are distributed on both sides of the bridge, along its entire length. For the precise locations of the reference points and the assigned numbering scheme, refer to Annex A.

Figure 3.9: Brass bolt located on the deck of the Rooyensteinse Brug.

Following the initial reference measurement taken in August 1978, a total of eight deflection measurements have been collected over a period of about 44 years, from 1980 to 2022. Figure 3.10 presents the measured deflections (i.e. the deformations in the vertical direction). The maximum negative deflection is registered at midspan, monitored by reference points 107 and 407. The maximum positive deflection occurs at the sidespans, registered by reference points 104 and 404 at one side, and 110 with 410 at the other. Table 3.3 provides an overview of the date, temperature of the structure and environment, and the average measured deflection at these locations. The difference in deflection between the left and right side spans is small, hence the deflections presented are measured by reference points 104 and 404.

Table 3.3 shows that the in-situ measurements have been conducted under varying environmental conditions over the years. Daily temperature fluctuations influence the behavior of the bridge, consequently, they may influence the measured values. The mean temperature of the environment was used to categorize the in-situ data into two groups: those taken between October and May, and those taken from June to September. Figure 3.11(a) and (b) show the deflection at midspan and one of the sidespans, respectively. The $\times$-marker indicates measurements taken between June and September and $\bullet$-marker indicates measurements taken between October and May. June-September includes data with a mean temperature of the environment above $10°C$, and October-May the data below this

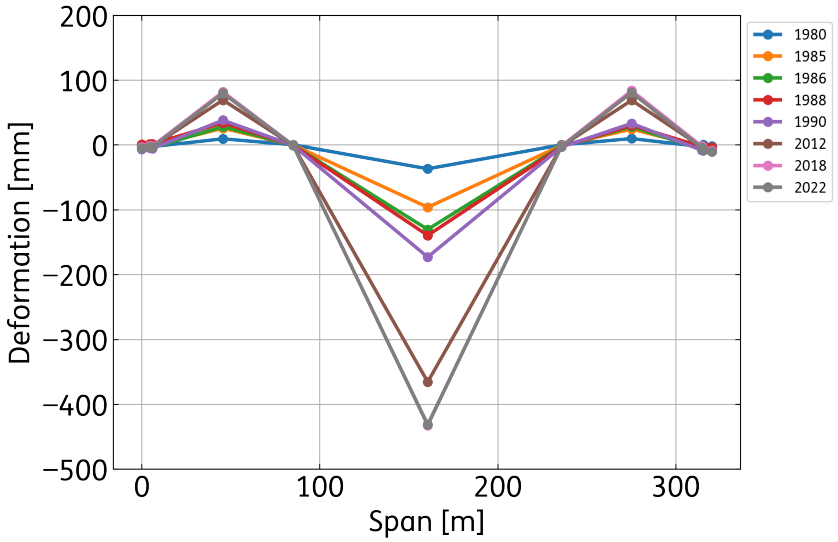

Figure 3.10: Averaged measured deflections along the full length of the bridge between 1980 and 2022.

Date of Measurement	Temperature Structure [$^{\circ}C$]	Mean Temperature Environment [$^{\circ}C$]	Deflection Midspan [mm]	Deflection Side span [mm]
23/08/1978	N/D	+17	0	0
24/09/1980	N/D	+10.8	-36.9	9.35
03/05/1985	N/D	+6.9	-96.3	25.6
20/06/1986	N/D	+16.8	-130.4	28.1
13/04/1988	N/D	+5.3	-139.6	34.15
20/06/1990	N/D	+15.8	-173.0	38.05
15/10/2012	+11	+10.4	-363.6	69.15
17/07/2018	+21	+20	-432.6	81.65
29/04/2022	+9	+8.8	-431.4	79.55

Table 3.3: Temperature and average deflection registered at the midspan and sidespan over time. For the midspan, the measurements are an average of the data from reference points 107 and 407. For the sidespan, the data is from reference points 104 and 404.

threshold. Further, the overall trend is plotted for the June-September measurements. Based on this trend line, the deflection at mid-span is expected to keep increasing in the future.

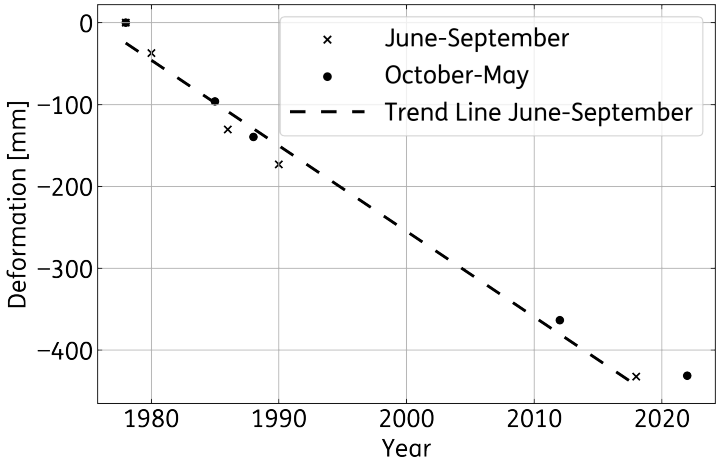

(a) In-situ deflection at the midspan in time: average of data from the reference points 107 and 407.

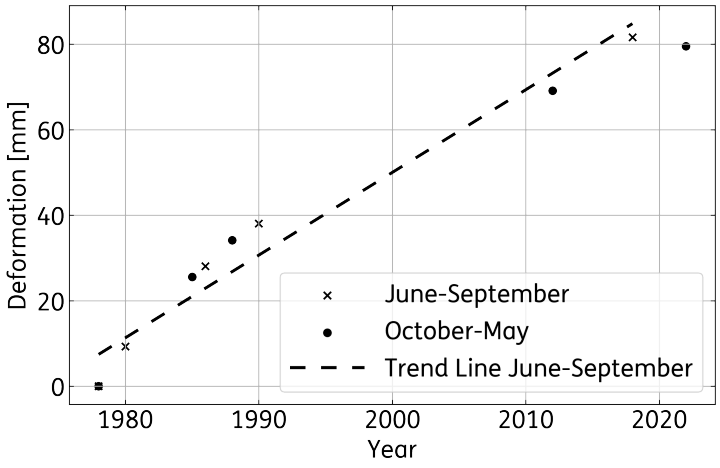

(b) In-situ deflection at the sidespan in time: average of data from the reference points 104 and 404.

Figure 3.11: Evolution of the in-situ deflection at the midspan and sidespan in (a) and (b), respectively. × indicates measurements taken between June and September, and ● indicates measurements taken between October and May. The dashed line indicates the trend line for the June-September measurements.

4

Finite Element Modelling Approach of the Rooyensteinse Brug

This chapter describes the approach used to model the Rooyensteinse Brug. It begins with an explanation of the main modeling assumptions in Section 4.1. This is followed by the implementation of geometry in Section 4.2. Subsequently, the material models are presented in Section 4.3, while the types of elements and the finite element mesh are covered in Section 4.4. The application of boundary conditions is outlined in Section 4.5, and the various loads included in the model are described in Section 4.6. The phased analysis is explained in Section 4.7. Moreover, Section 4.8 provides insight into the solution procedure, convergence criteria, and time increments. Finally, Section 4.9 summarizes key information regarding the parametric script created for the finite element model, whereas Section 4.10 presents the model checks, conducted to gain trust in the model.

4.1. Modeling assumptions

The finite element (FE) model of the Rooyensteinse Brug is a two-and-a-half-dimensional model with shell elements, and a time-dependent phased analysis is implemented to account for the construction stages, creep, and shrinkage effects. Given the bridge is symmetric, only half of the bridge was modeled to save computational time. Specifically, the FE model represents the second half of the Rooyensteinse Brug, with symmetry conditions applied at the midspan after activating the last segment. Solely the superstructure is modeled, whereas piers and bank seats are represented as supports, assuming no settlements occur at these points.

In the cross-section, all the bridge components (top slab, bottom slab, and webs) are modeled indi-

vidually with curved shell elements. The overheight corrections that are applied in practice to achieve the theoretical building line are not accounted for in the model. Consequently, permanent boundary conditions are applied to the deformed shape of the FE model (refer to Figure 4.1). Regarding material properties, concrete is modeled as a viscoelastic material. The non-linearity resulting from cracking is neglected, hence excluding the need for modeling ordinary steel reinforcement. Additionally, the relaxation of prestressing steel is not treated as a time-dependent phenomenon but is considered an initial loss for the prestressing force applied to the tendons. Finally, the impact of environmental fluctuations on the time-dependent behavior of the bridge is neglected. The FE model and the analyses are performed with DIANA FEA version 10.7.

Figure 4.1: Undeformed versus (scaled) deformed shape at the end of construction. The boundary conditions at the bank seat, and the symmetry conditions at the midspan, are applied to the deformed shape.

4.2. Geometry

The geometry of the finite element model is divided into two parts: the concrete box girder and the post-tensioned tendons. The modeling choices for each of these components are discussed in the following subsections.

4.2.1. Box girder

A box girder segment is formed by three components: top slab, bottom slab, and webs. All are modeled with curved shell elements, as shown in Figure 4.2a. As seen in Chapter 3, the thickness in the box girder cross-section of the Rooyensteinse Brug varies not only along the span but also along its width. To accurately account for these variations, spatial functions were created and assigned to the shape entities of the segment parts (see 4.2b).

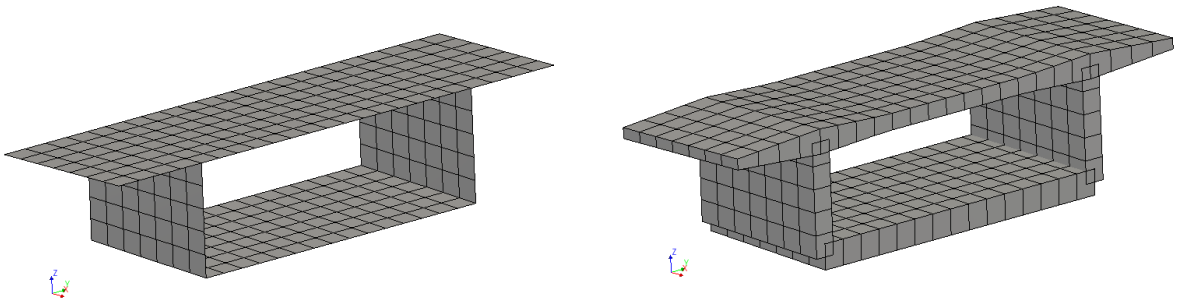

(a) Geometry and mesh of Segment 9.

(b) 3D render of Segment 9 showing the out-of-plane thickness of all the components.

Figure 4.2: 2D and 3D render of Segment 9 showing the components, mesh, and out-of-plane thickness.

The bridge has been modelled using curved shell elements, which may result in overlapping and

missing material at the connections of the segment components. Additionally, the shell elements are positioned at half-height of the out-of-plane thickness, meaning that the cross-sectional area and moment of inertia are approximations. Figure 4.3 compares the real cross-section for Segment 9, and the one implemented in the finite element model. The main requirements considered in the implementation of the geometry are to maintain: (i) the distance between the centroidal axis of the top slab and the bottom fiber of the section; and (ii) the distance between the centroidal axis of the top slab and the centroidal axis of the cantilever tendons at the hammerhead. Furthermore, the dimensions of the top slab were chosen to guarantee an area and moment of inertia as close as possible to the real section. This approach aims to achieve a bending stiffness that closely mimics the real cross-section. On average, considering the smallest and largest segments, the difference in area is approximately 2%.

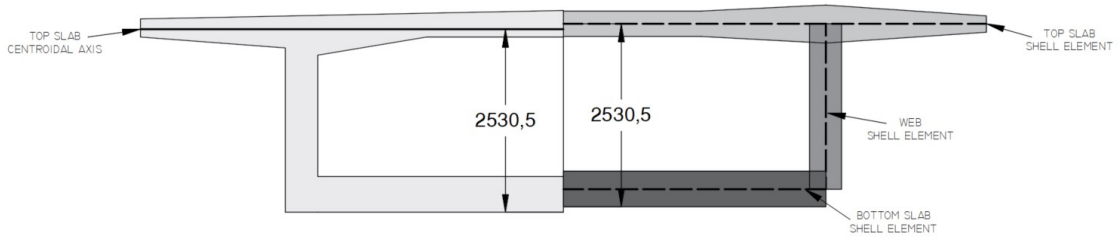

Figure 4.3: Real versus implemented cross-section for Segment 9.

The webs have a constant width on most of the bridge, except for Segments 21 and 22 at the hammerhead. In these specific segments, spatial functions were used to account for the localized increase in web thickness (see Figure 4.4). Additionally, spatial functions on the plane *x-y* (see coordinate system in Figure 4.2) were applied to the bottom slab of all the segments to incorporate the progressive increase in thickness in the model. This increase reaches its maximum at the hammerhead, where similarly as for the webs, there is also a local increase in bottom slab thickness for Segments 21 and 22. These spatial functions were also used to create anchorage blocks. These local thickness increases are for the anchorage of the continuity tendons (see Figure 4.5).

4.2.2. Prestressing tendons

All the prestressing tendons are modeled as embedded line reinforcement elements. The cantilever and continuity tendons are modeled individually and explicitly, corresponding as closely as possible to the actual layout of the prestressing reinforcement in the bridge (see Figure 4.6). The area of each tendon is 1182 mm^2. The transversal prestressing, originally conformed by 28 tendons, is modeled by 2 tendons located in the centroid of the full distribution. Therefore, an equivalent area accounting for 14 tendons is applied to each modeled reinforcement, equal to 7420 mm^2. Following the construction method, the prestressing tendons are initially not bonded to the concrete. In practice, the grouting process occurs every few weeks. This is accounted for in the phasing, where every three weeks, the activated tendons become bonded to the concrete.

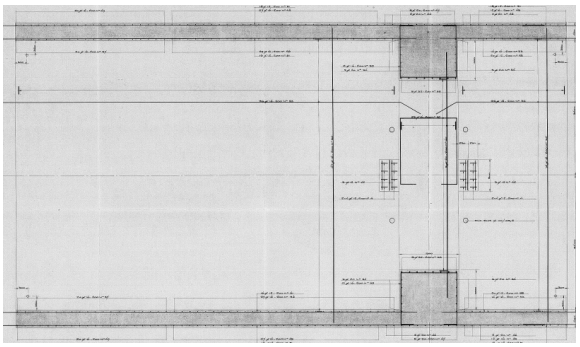

(a) Top view showing the local increase in web thickness [18].

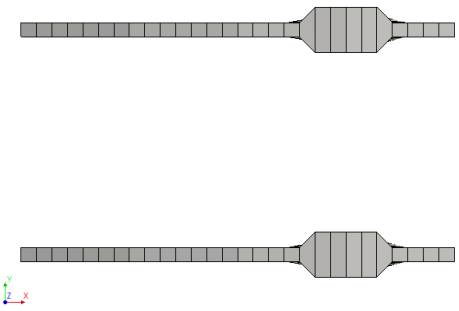

(b) Implemented cross-section in the FE model.

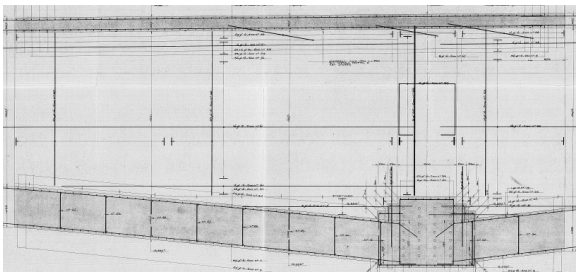

(c) Side view showing the local increase in bottom slab thickness [18].

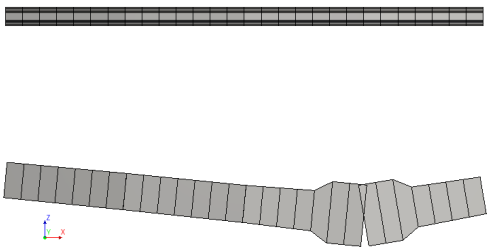

(d) Implemented cross-section in the FE model.

Figure 4.4: Local increase of the webs and bottom slab in the hammerhead, formed by segments (from left to right) 19, 20, 21, and 22. The increase is applied to segments 21 and 22.

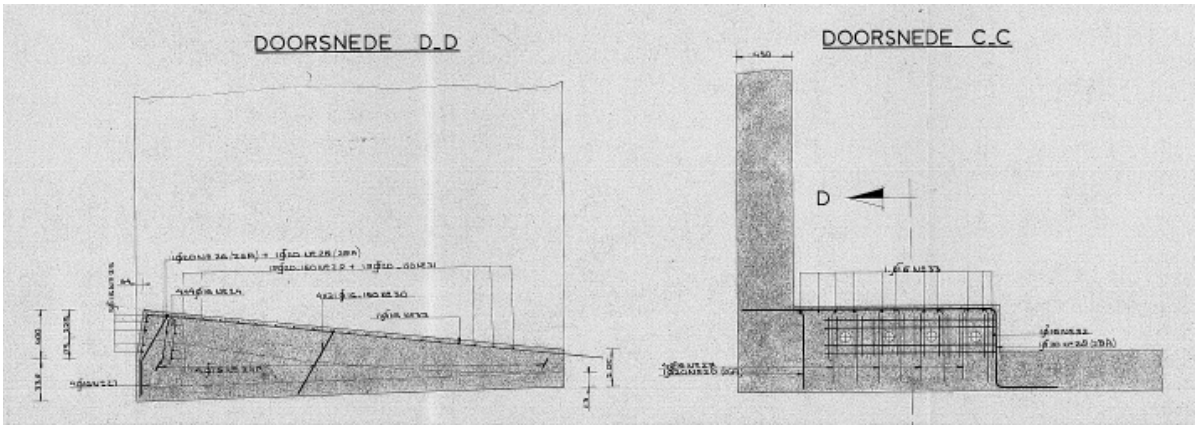

(a) Side and front view of the local increase in the bottom slab of segment 38, known as anchorage blocks [18].

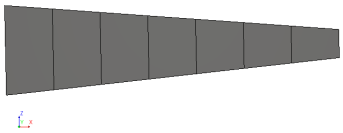

(b) Side view (plane *x*-*z*) of the implemented cross-section in the FE model.

(c) Front view (plane *y*-*z*) of the implemented cross-section in the FE model.

Figure 4.5: The implementation of anchorage blocks in the bottom slab of Segment 38. The function of this additional concrete area is to anchor the continuity tendons.

4.3. Material models and parameters

The model of the Rooyensteinse Brug requires three material models: concrete for the box girder segments, and unbonded and bonded prestressing steel for the prestressing tendons. All are discussed

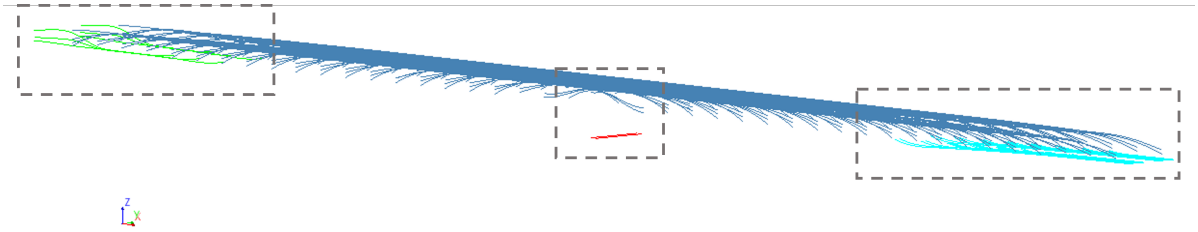

(a) The prestressing tendons, explicitly modeled in the FE model.

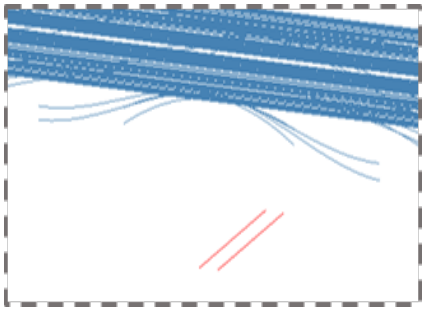

(b) The transversal prestressing is modeled as 2 tendons with an equivalent area.

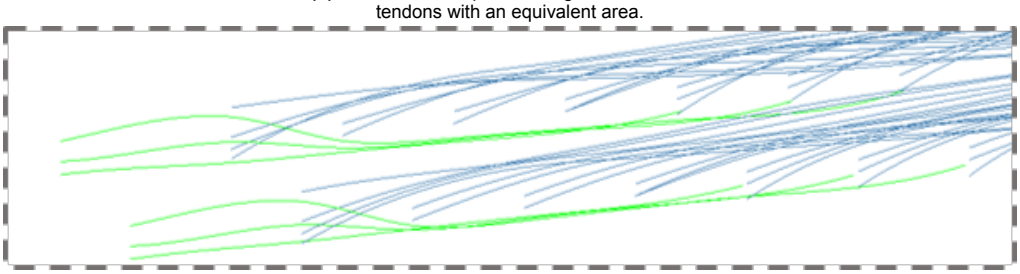

(c) The continuity tendons at the left cantilever arm. These tendons will resist the positive moment close to the bank seat.

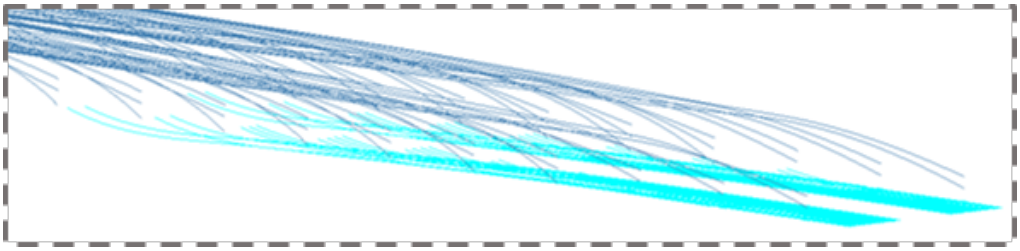

(d) The continuity tendons at the right cantilever arm. The tendons will resist the positive moment at midspan.

Figure 4.6: The explicitly modeled prestressing tendons: the cantilever tendons (dark blue), continuity tendons (green and light blue), and the transversal tendons (red).

in the subsections below.

4.3.1. Concrete

The concrete material behavior is modeled with a Maxwell/Kelvin chain viscoelasticity model, characterized by a Young's Modulus E_{cm} of 3.3×10^{10} N/m^2, a Poisson's ratio ν of 0.2, and a mass density ρ of 1859 kg/m^3. In the Reference Analysis, the RILEM B4 model (B4) was used for the creep and shrinkage formulation (see Section 5.2). The input is summarized in Table 4.1. The concrete-related parameters are based on available information previously presented in Chapter 3. Regarding the geometry-related parameters, the notional size of 0.471 m is an average value calculated for the entire bridge and used for all concrete bridge components (see Annex E for the calculation of the notional size). From this

point forward, this approach is referred to as a uniform analysis. The choice of infinite slab as the specimen type aligns with the type of model. Additionally, the activation energy of 4000 K is a recommended value from B4 in the absence of specific data [17]. For the temperature of environment *T* and the relative humidity *RH*, the chosen values were 20°C and 75%, respectively. Despite the selection of 20°C being relatively high compared to the average temperature in the Netherlands, the sensitivity study presented in Section 2.3.2 showed a minor impact of *T* on both creep and shrinkage. For simplicity, the same value was assumed for the temperature during curing. The study also showed that *RH* significantly influences the shrinkage strain, and 75% is considered a reasonable value for conditions in the Netherlands. Finally, the age of exposure of 3 days is based on the demoulding schedule.

The Reference Analysis accounts for maturity effects, which is the development of the concrete properties over time. Incorporating maturity effects in DIANA 10.7 is achieved by selecting a maturity-dependent creep compliance function as input for the viscoelastic chains. This approach allows the incorporation of several discrete creep compliance functions, each corresponding to a different time of loading. For the times of loading where no creep compliance functions are specified, values are obtained by linear interpolation. To accurately describe the creep effects, the specified times of loading (i) must cover the whole time period in which new loads are applied, and (ii) are densely specified in the young hardening stage of concrete wherein the creep properties rapidly change. For that reason, the creep compliance is defined using the times of loading at 1, 2, 3, 4, 7, 10, 14, 20, 28, 40, 60, 100, 140, 180, 220, 260, and 300 days. Figure 4.7a shows the maturity effects for a set of creep compliance curves incorporated in the FE model. Additionally, the shrinkage strain curve is shown in Figure 4.7b.

Concrete-related parameters	
Parameter	Value
Concrete Compressive Strength f_{cm} [N/m^2]	38×10^6
Mass density ρ [kg/m^3]	1759
Cement Type	R
Cement Content [kg]	360
Water/Cement Ratio [-]	0.47
Aggregate/Cement Ratio [-]	3.389
Aggregate Type	Limestone
Geometry-related parameters	
Parameter	Value
Notional size [m]	0.471
Specimen Type	Infinite slab
Activation Energy [K]	4000
Environment-related parameters	
Parameter	Value
Relative Humidity [-]	0.75
Temperature of Environment [°C]	20
Temperature of Environment during curing [°C]	20
Age at Start of Environmental Exposure [days]	3

Table 4.1: Material properties for the Model B4, used in the Reference Analysis.

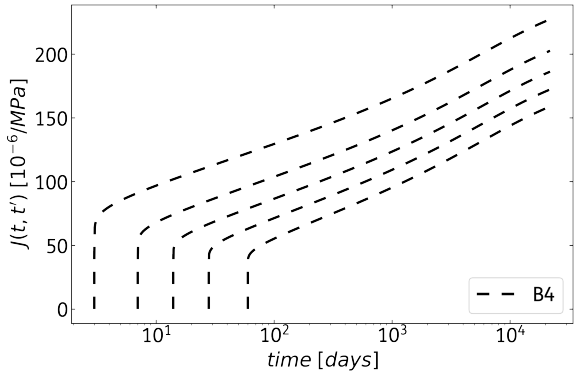

(a) Creep compliance functions for times of loading 3, 7, 14, 28, and 60 days.

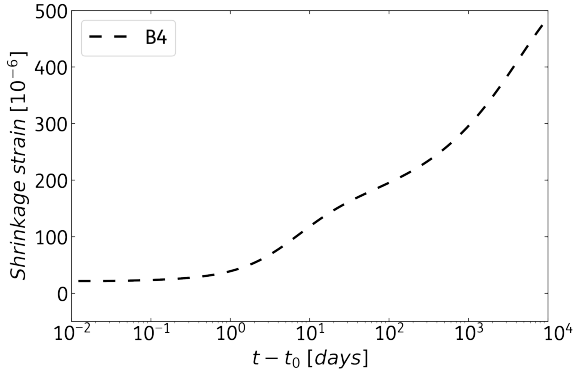

(b) Shrinkage strain curve.

Figure 4.7: Creep compliance and shrinkage strain curves for the Reference Analysis. To improve clarity, only a limited selection of creep curves is presented.

4.3.2. Prestressing steel

The prestressing steel is described using a linear elasticity model with a Young's Modulus E_p equal to 2×10^{11} N/m^2. The effect of relaxation on prestressing loss is accounted for in the initial prestressing force that is applied to the tendons. The calculation of the loss is based on a model from literature, see Equation (4.1) [73]. The σ_{p0} used was 1.33×10^9 N/m^2, and f_{py} was estimated as 90% of f_{pk}, equal to 1.68×10^9 N/m^2. Over a period of 60 years, this leads to a reduction in the prestressing force of 11.2%, corresponding to a prestressing force of 1399 kN. Figure 4.8 shows the full evolution of the prestressing loss due to relaxation in time.

$$\frac{\sigma_{pr}}{\sigma_{p0}} = -\frac{\log(\tau - \tau_0)}{10} \cdot \left(\frac{\sigma_{p0}}{f_{py}} - 0.55\right) \tag{4.1}$$

where:

$(\tau - \tau_0)$ is the time in hours after stressing

σ_{p0} is the initial stress immediately after stressing

f_{py} is the yield stress of prestressing steel

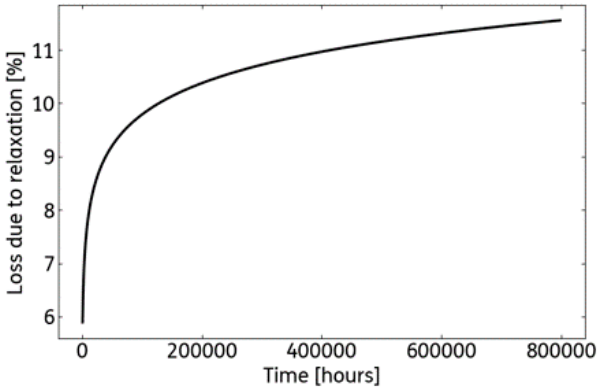

Figure 4.8: Prestressing loss due to relaxation in time, as proposed in [73].

4.4. Element types and finite element mesh

The finite element model of the Rooyensteinse Brug uses three different element types: curved shell elements, embedded line reinforcements, and composed line elements. The concrete has a structured mesh consisting of a four-node quadrilateral isoparametric curved shell element with a 2x2 Gauss quadrature and a 3-point Simpson integration scheme over the thickness. The Mindlin-Reissner theory is applied to these elements. The average element size is 0.5 m by 0.5 m (see Figure 4.9). In total, the concrete segments are discretized by 15534 elements. The prestressing tendons are modeled by embedded reinforcement elements. The integration scheme is derived from the mother element. The composed line elements are solely used to obtain the cross-sectional forces along the bridge; they do not have a physical contribution.

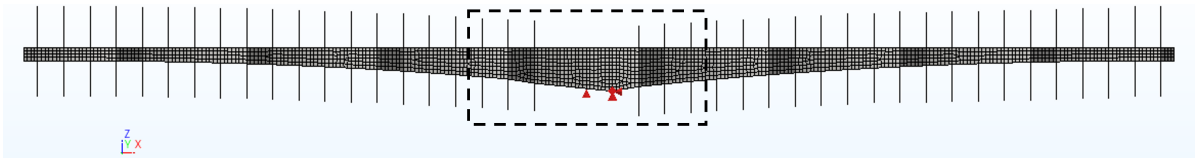

(a) Mesh on the full bridge.

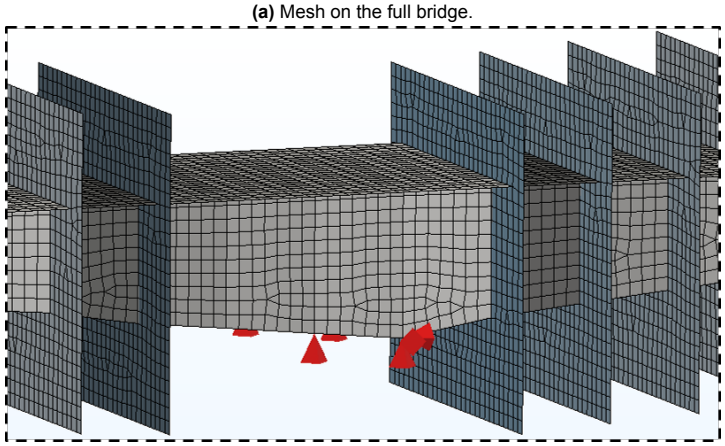

(b) Close-up of mesh in the hammerhead, including the dummy plates (see Section 4.6).

Figure 4.9: The mesh on the FE model, with an average element size is 0.5 m by 0.5 m.

4.5. Boundary conditions

Two types of support conditions are considered in the finite element model: *construction* and *permanent*. The *construction* support conditions, shown in Figure 4.10, consist of four supports, two point supports at the location of the piers (labeled A and B), and two acting as temporary supports (labeled C and D). Support A restricts all translational degrees of freedom, while B only constrains the *y* and *z* translations. Supports C and D restrict the translations in the *z*-direction only. The *permanent* support conditions are shown in Figure 4.11. Support E restricts translations in *y* and *z*. Supports F, G, and H, constrain displacements in *z*. Finally, Support I, the symmetry condition, restricts translations in *x*-direction[1]. This condition is applied to all edges of the closing piece.

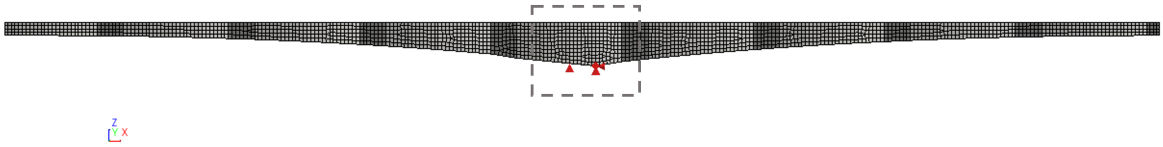

(a) The FE model with the construction boundary conditions.

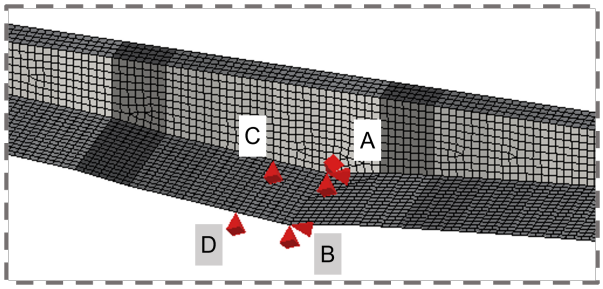

(b) Close-up to the boundary conditions.

Figure 4.10: The boundary conditions during the construction. They consist of four-point supports (A, B, C, and D).

4.6. Loads

Two load categories can be distinguished: *phased-independent* loads and *phased-dependent* loads. In the first category, the definition of the load case in the model does not change over the phases. Examples include construction loads, which will be present throughout the entire construction stage with a constant magnitude. The self-weight and the over-imposed dead loads are also considered phased-independent loads. In the second category, the definition of the load case does change over the phases. For instance. prestressing falls in this category since new tendons are added after each phase. The other phased-dependent loads are the fresh concrete, traveling formwork, and import deformations. All loads are explained in the following subsections. Additionally, Table D.3 in Annex D provides a complete overview of the defined load cases.

[1]The symmetry conditions should restrict both translations and rotations in all edges of the closing piece. The rotational restraints were omitted. We came across this at a late stage of the thesis project, and there was no time left to update all the results. However, a new Reference Analysis was conducted, revealing a local impact at midspan only. Annex F presents the results for this updated Reference Analysis.

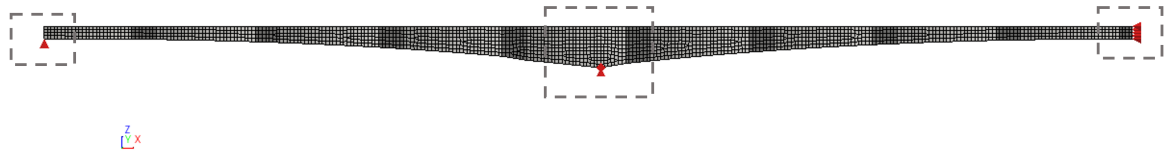

(a) The FE model with the permanent boundary conditions.

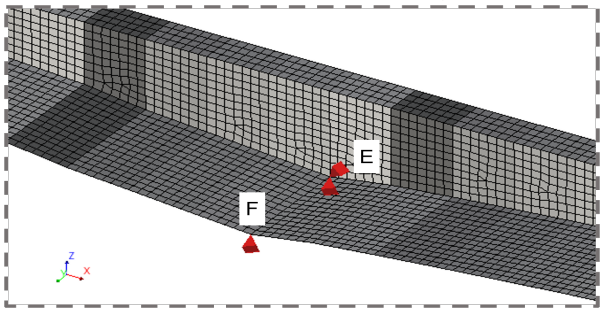

(b) Close-up to the boundary conditions at the hammerhead.

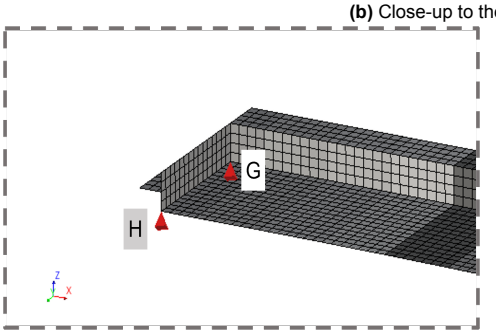

(c) Close-up to the boundary conditions at the bank seat.

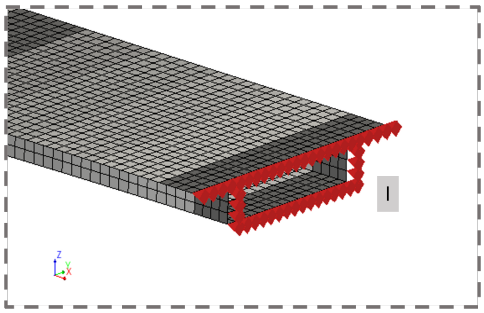

(d) Close-up to the symmetry conditions at the midspan.

Figure 4.11: The boundary conditions during the service life. They consist of four-point supports (E, F, G, and H) and symmetry conditions at midspan (I).

4.6.1. Self-weight

The self-weight is defined as a global load; therefore, it is recalculated in the phasing with each new active segment. The reinforcement is accounted for in the mass density of the concrete, with a total value of 1859 kg/m^3.

4.6.2. Prestressing

The prestressing is defined in the model with post-tensioning loads. Following the original tensioning method, the load is applied at one end. The nodal anchor force in the case of the transversal prestressing is 6042 kN. For the longitudinal prestressing (cantilever and continuity tendons) the applied force is 1399 kN. The immediate prestressing losses due to friction and anchorage slip are incorporated using an anchorage retention length of 0.007 m, a coulomb friction coefficient of 0.25, and a wobble factor of 0.007. The relaxation is incorporated through a reduction of 11.2% in the initial anchor force (see Section 4.3).

4.6.3. Fresh concrete

The fresh concrete is incorporated in the model as a point load and distributed moment applied to the bridge end. The loads depend on the geometry of the specific segment, and the density used for the calculation is 1759 kg/m^3, excluding the contribution of the reinforcement. These loads are introduced through temporarily present stiff dummy plates (see Figure 4.9), which are modeled as curved shell elements. These plates have a thickness of 0.25 m, with dimensions of 14 m in width and 12 m in height. The dimensions ensure the dummy plate covers the whole box girder cross-section for all segments. The center of gravity of each plate coincides with the one of the segment it is attached to, ensuring uniform distribution of the point loads and moments to the segments. The dummy plates are modeled with a linear elastic isotropic model, characterized by a Young's Modulus E_s is 1×10^{13} N/m^2, a Poisson's ratio ν of 0.3, and no mass density. The choice of a high E_s ensures the plates are sufficiently stiff to effectively transmit the loads.

4.6.4. Traveling formwork

The load coming from the traveling formwork is modeled in two different ways. Before the casting of a new segment, and during the hardening of the concrete, the traveling formwork is treated as a point load and uniformly distributed moment applied at the bridge end through the dummy plate. Once the concrete in the newly casted segment has hardened, it becomes a uniformly distributed load applied to the top slab. So, the way the load is applied depends on the stage in the weekly construction process, which is explained in detail in Section 4.7. With a total weight of 60000 kg, the loads corresponding to the traveling formwork are shown in Table 4.2. The sign of the moment will depend on the side of the bridge the segment is located at.

Property	Value
Uniformly distributed load [N/m^2]	-14.37
Point load [N]	-588600
Uniformly distributed moment [N/m]	$\pm$ 6131.25

Table 4.2: Loads for the traveling formwork effect in the FE model.

4.6.5. Construction loads

The construction loads reported in the original calculations are incorporated in the model as a uniformly distributed load equal to -686.7 N/m^2 [68].

4.6.6. Over-imposed dead loads

The over-imposed dead loads are added once the bridge is complete. The asphalt is represented by a uniformly distributed load over the deck equal to -3700 N/m^2, based on a minimum and maximum asphalt thickness of 140 and 230 mm [18]. The rails, curbs, lighting, and other non-structural elements

added to the edges are represented by two line loads. On the northwest side, the value is -13500 N/m, while for the southeast is -5700 N/m [18].

4.6.7. Import deformations

When a new segment is activated, it does not automatically incorporate the nodal displacements resulting from previous phases. Therefore, a type of load called import deformation is required. This load will impose translations and rotations from the last constructed segment end to the newly constructed segment (see Figure 4.12). For this, master and slave nodes are used to describe the connection between the existing and new segments.

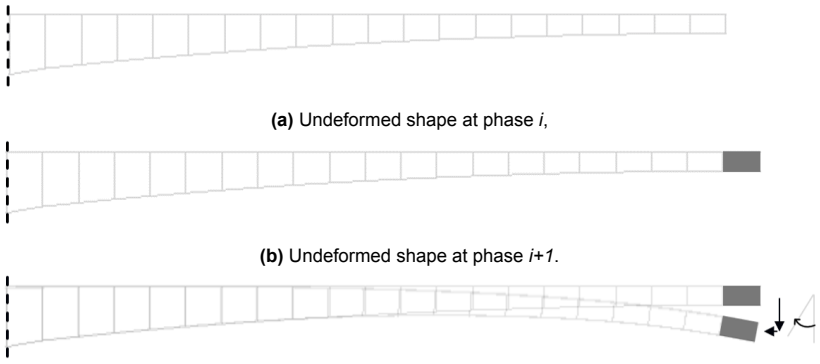

(a) Undeformed shape at phase *i*,

(b) Undeformed shape at phase *i+1*.

(c) Import deformation load applied to the new segment in phase *i+1*.

Figure 4.12: Illustrative example of the import deformation load. The segment activated in phase *i+1* will then follow the current deformed shape of the bridge.

4.7. Phased analysis

Chapter 2 provides an overview of the weekly construction process for balanced cantilever bridges. This section explains the implementation in the FE model. At the start, only the hammerhead is present, which corresponds to Segments 19 to 22. Then, on a weekly cycle, new segments and tendons are activated until the bridge is complete. The analysis has a total of 58 phases. From this total, 31 phases are time-dependent, while the remaining 27 are load-dependent. The load-dependent phases incorporate the import deformation loads into the model. The time-dependent phases represent the construction process of the balanced cantilever bridge. In the finite element model, each phase starts with the activation of a new segment and the corresponding prestressing (see Figure 4.13).

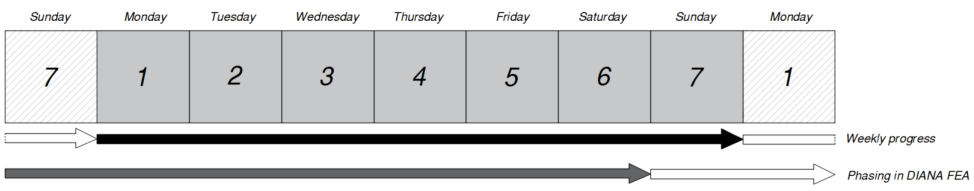

Figure 4.13: The weekly construction cycle: reality versus implementation.

To understand the implementation better, the weekly construction cycle for Segment 25 is presented

in Figure 4.14. The new phase starts at day 0 with the activation of Segment 17 and prestressing tendon 10. A distributed load represents the traveling formwork UDL_{TF}. Two days later, the traveling formwork is moved to its new position, represented as a point load P_{TF} and distributed moment M_{TF}. The casting of Segment 25 occurs five days later and is included as a point load P_{FC} and distributed moment M_{FC}. Finally, a new phasing starts seven days later with the activation of Segment 25 and tendons 7 and 9. The grouting of the tendons occurs every three weeks. Table D.2 in Annex D provides a complete overview of the phased analysis. Following the completion of the construction stage, the service life phase begins. The service life period for this analysis is 60 years, from 1978 to 2038. Therefore, the predictive window covers 15 years, from 2023 to 2038.

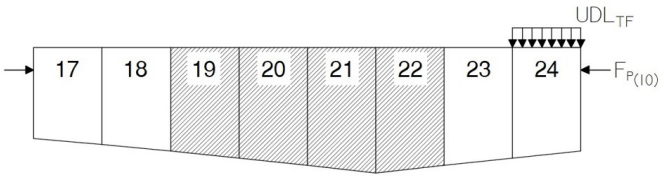

(a) Phase 11: Day 0.

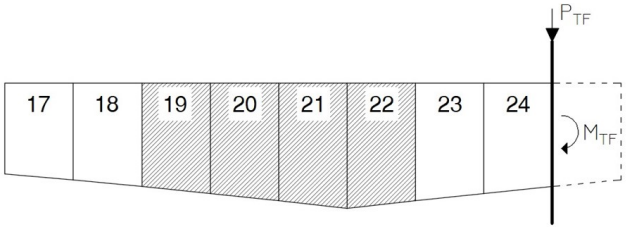

(b) Phase 11: Day 2.

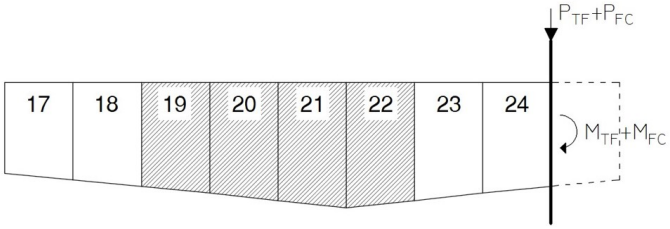

(c) Phase 11: Day 5.

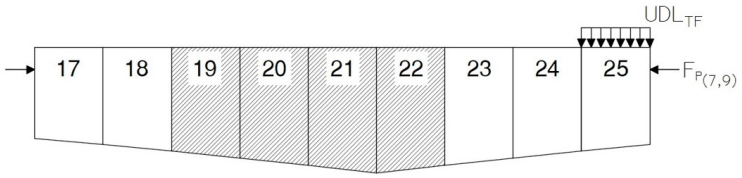

(d) Phase 13: Day 0.

Figure 4.14: The implemented weekly construction cycle for Segment 25.

4.8. Solution procedure, convergence criteria, and time increments

The analysis has a total of 58 phases, as explained in the previous section. In the construction phase, the defined time steps are 2 days, 5 days, and 7 days. These steps are such that they coincide with the application of phase-dependent loads (e.g. travelling formwork). For the service life phase, the time

steps begin with one step after four days, followed by 51 steps of one week, 40 steps of one month, and 55 steps of one year. The iterative method used is regular Newton-Raphson. Displacement and force norms with a tolerance of 0.001 and 0.01 respectively are used in the convergence criterion. Convergence is reached when one of the criteria is satisfied. The maximum number of iterations per time step is 30. The analysis is set to continue even when convergence criteria are not satisfied.

4.9. Parametric script

A parametric FE model of the Rooyensteinse Brug is built using the programming language Python. This means that the model can be implemented for other case studies with minimum effort. The developed code consists of three main scripts: input, modeling, and post-processing. The input script handles all the case-specific information, such as external Excel files for the geometry and the phasing of the bridge. This script also uses an external creep and shrinkage repository for code-based models, created by TNO. In the input script, all the information of the bridge will be prepared for the modeling script. The modeling script contains the code that will be run in DIANA FEA and has six main parts: geometry, material, boundary conditions, loads, finite element discretization, and phasing. The modeling script is general, which means that with the appropriate input, it can build a FE model of an arbitrary balanced cantilever bridge. The post-processing script includes functions to export the results and plot them. In total, the parametric model of the Rooyensteinse Brug consists of approximately 4000 lines of code, with 1400 required for the modeling script. This code shows the importance of good bookkeeping in the development of parametric models.

4.10. Model checks

A finite element model of a balanced cantilever bridge is complex to check. To guarantee the correct implementation of several procedures, minimal examples were developed. The first minimal example aimed to understand the correct implementation of a maturity-dependent creep compliance function in DIANA 10.7. For this, a single-cell element model was created and analyzed in terms of (i) the required input, (ii) the interpolation capabilities, and (iii) the impact of accounting for maturity effects. The second minimal example focused on simply supported prestressed beams to further investigate the implementation of maturity effects, now on a structural component level. Additionally, the propagation of uncertainty was explored by calculating the upper and lower bounds with B4. Finally, the third minimal example focused on the implementation of construction phases with a prestressed cantilever beam, learning that was later applied in the phasing of the FE model. For more information on these examples, refer to Annex C.

In addition to the minimal examples, a linear elastic analysis was performed on the FE model. The resultant internal forces from self-weight and prestressing of the cantilever tendons were compared with those that are reported in the original calculations and the recalculation report [68, 18]. The model in the linear elastic analysis has some different material properties, boundary conditions, and loads than

the model described in this chapter. These modifications were needed to make a fair comparison. For concrete, a linear elastic material model is used with the values indicated in Table 4.3. For prestressing steel, only immediate losses are considered. The applied boundary conditions are Supports A, B, C, D, G, and H (see Figures 4.10 and 4.11). The boundary conditions represent the moment immediately before stitching when all the segments, except for the closing piece at midspan, have been cast. The only loads included in the FE model are self-weight and the prestressing of the cantilever tendons. The reduction in the initial prestressing load due to relaxation is not included. Therefore, the applied force per cantilever tendon is 1575E3 N.

Parameter	Value
Young's Modulus E_s [N/m^2]	3.3×10^{10}
Poisson's ratio ν [-]	0.2
Mass Density ρ [kg/m^3]	1761

Table 4.3: Material properties for concrete in the linear elastic analysis.

Figure 4.15 compares the bending moment diagram due to self-weight for the numerical results and the original calculations. The difference in the maximum bending moment is 6.5%. This is due to the difference between the real and the implemented cross-section, discussed in Section 4.2. The observed difference is considered to be within acceptable limits. To complement this check, a comparison of reaction forces due to self-weight between the numerical results (32980E3 N) and the recalculation report (31704E3 N) was conducted [18]. The difference of 4.0% further confirms that the concrete geometry of the box girder bridge is correctly incorporated into the FE model.

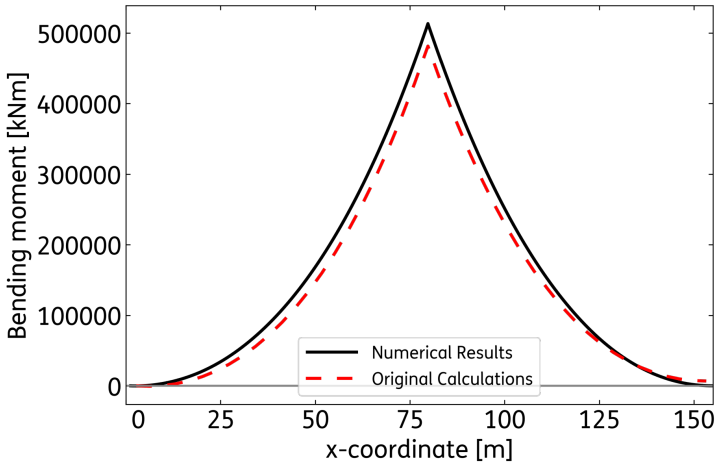

Figure 4.15: Bending moment due to self-weight: numerical results versus original calculations. The difference in the maximum bending moment is 6.5%.

The effects of the cantilever tendons were checked with the normal force and bending moment diagrams. The numerical results for normal force were compared with the original calculations in Figure 4.16. The difference in the maximum normal force is 1.7%. Figure 4.17 shows the bending moment diagram for the numerical results, the original calculations, and the recalculation report. The difference

in maximum bending moment between the original calculations and the numerical results is 7.3%. This difference appears at the location of the hammerhead. For the other parts of the bridge, the difference between the two curves is much smaller. In comparison with the recalculation report, the maximum bending moment has a difference of 1.2%. Similarly to the case for self-weight, the differences are considered to be within acceptable limits. Overall, these checks give confidence in the way the finite element model is generated.

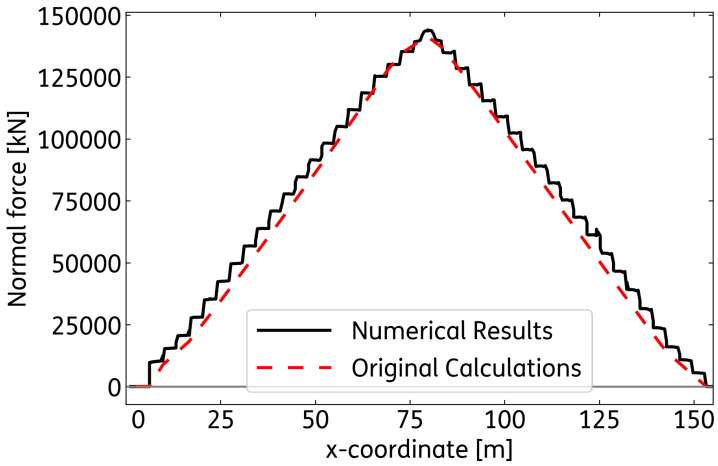

Figure 4.16: Normal force due to the prestressing of the cantilever tendons: numerical results versus original calculations. The difference in maximum normal force is 1.7%.

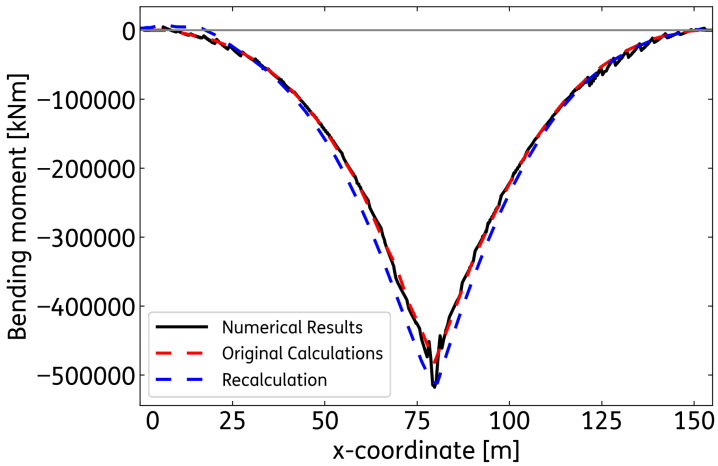

Figure 4.17: Bending moment due to the prestressing of the cantilever tendons: numerical results versus original calculations and recalculation report. The difference in maximum bending moment is 7.3% and 1.2%, respectively.

5

Analysis and results

This chapter presents the results of the time-dependent structural analyses of the Rooyensteinse Brug. Section 5.1 provides an overview of all the presented analyses. The results of the Reference Analysis, based on the finite element model discussed in Chapter 4, are presented and interpreted in Section 5.2. Sections 5.3 to 5.6 study the impact of several modeling aspects on the results. The available in-situ measurements (see Chapter 3) are incorporated for comparison with the numerical results.

5.1. Overview of analyses

Table 5.1 provides an overview of the analyses presented in this chapter. The variations considered for this sensitivity study are briefly explained below. The relevant information regarding each analysis is mentioned in the corresponding section.

- Creep and shrinkage model: to study the impact of several code-based models, the analyses in this thesis are performed with the models from RILEM B4 (reference), the CEB-FIP Model Code for Concrete Structures 1978 (MC78), the current Eurocode 2 (EC2), and the final preliminary release of the new Eurocode 2 (fprEC2) (see Section 2.3.1 in Chapter 2).
- Fractile: to explore how the uncertainty in the RILEM B4 creep and shrinkage model propagates into the structural response of the Rooyensteinse Brug, analyses are performed based on the mean (reference), an upper bound, and a lower bound creep and shrinkage curve. The upper and lower bounds are defined based on a 90% credible interval.
- Maturity effects: to study the impact of a maturity-based creep model (reference) compared to a maturity-independent creep model with a fixed age of loading.

- Cross-sectional variability: to investigate the relevance of accounting for differences in moisture diffusion (drying) of the box girder cross-sectional components, since the webs, top and bottom flanges have different thicknesses. In the Reference Analysis one creep and shrinkage model is used for the whole bridge, based on an average notional size, in analysis 8 we adopt a creep and shrinkage model per structural component.

Analysis	Creep and Shrinkage Model	Fractile	Maturity Effects	Cross-sectional variability	Section
1 (REF)	RILEM B4	Mean	Yes	Uniform	5.2
2	MC1978	Mean	Yes	Uniform	5.3
3	EC2	Mean	Yes	Uniform	5.3
4	fprEC2	Mean	Yes	Uniform	5.3
5	RILEM B4	Upper 90% CI	Yes	Uniform	5.4
6	RILEM B4	Lower 90% CI	Yes	Uniform	5.4
7	RILEM B4	Mean	No	Uniform	5.5
8	RILEM B4	Mean	Yes	Non-uniform	5.6

Table 5.1: Overview of the analyses presented in this chapter.

5.2. The Reference Analysis

The Reference Analysis serves as the benchmark for the comparison with the sensitivity analyses. Table 5.1 summarizes the main characteristics of this analysis. The RILEM B4 model is chosen because it is considered one of the most state-of-the-art models for predicting creep and shrinkage effects in concrete structures. Furthermore, mean values are adopted for the input of the creep and shrinkage model, and maturity dependency is considered in the creep response (i.e. the creep compliance depends on the age of loading). Although it is more realistic to account for differences in drying of the structural components, a simpler approach is employed where uniform shrinkage and creep compliance are assumed for all cross-sections of the box girder. The simulated structural behavior is analyzed by considering the following output: vertical deformations, bending moments and stresses in the concrete, and stresses in the tendons and their prestress losses. These results are presented in the following subsections.

5.2.1. Vertical deformations

The vertical deformations are analyzed at a specific point over time, and along the span at a specific time. The first way is referred to as the deflections over time, and the second way as the deflections along the span. There are two main locations of interest for the deflections in time, both shown in Figure 5.1. The first one is at the mid of the main span, which is where the maximum downward deflection is expected. The second one is at the mid of the side span, where the maximum upward deflection is expected. At both locations, in-situ measurements are available that can be used for comparison (the reference points 107 and 407, and 104 and 404 respectively, as indicated in Section 3 and Figure A.1).

From this point on, these two locations will be referred to as midspan and side span, respectively.

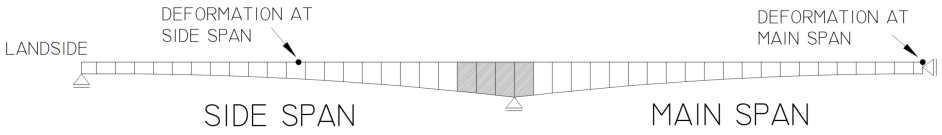

Figure 5.1: Location of the points of interest for the deflections in the vertical direction.

It should be noted that the two aforementioned monitoring locations are not present during the entire phased analysis. The midspan location appears once all construction stages in the phased analysis are finished (see Chapter 4), and the side span monitoring location is present after half the construction period. To get insight into the deflections over time during the construction stage, we make use of a moving measurement point that is located at the end of the cantilever arms until the point reaches its location as shown in Figure 5.1. This moving measurement point is illustrated in Figure 5.2.

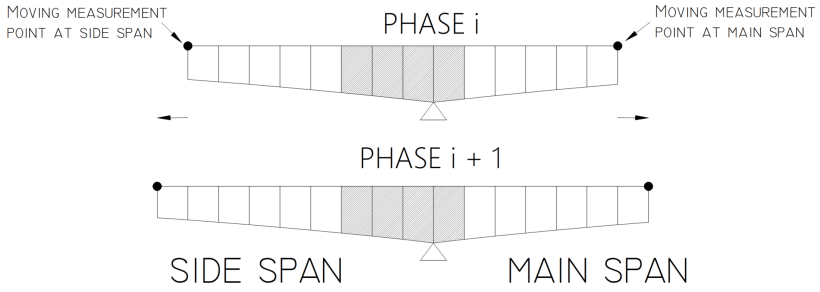

Figure 5.2: Representation of the moving measurement point at phases *i* and *i+1*. The point will keep moving towards the end of each new segment until it reaches its wanted location. For the side span, it will reach the final position with the casting of Segment 10. For the main span, with the casting of the closing piece.

Figure 5.3 shows the deflection over time (log-scale) at midspan. The analysis is performed for a period of 60 years. The graph indicates the periods when the deflections belong to the end of the cantilever arm (i.e. moving measurement point) and when they belong to the midspan location (i.e. fixed measurement point). For the midspan location, the transition from moving to a fixed measurement point coincides with the transition from the construction stage to service life. Figure 5.4 shows the deflection over time (log-scale) at the side span. Now, the moving point reaches its final position with the casting of Segment 10. Therefore, the transition from moving to a fixed measurement point happens 91 days before the end of construction.

The numerical results from Figure 5.3 can be analyzed for the two main stages: the construction stage, and service life. Apart from the over-imposed dead loads applied at the start of service life, no additional loads are considered in this second stage. Therefore, the increase in deflection is primarily attributed to creep and shrinkage effects. At the start of service life, the deflection at midspan is -0.200 m. After 60 years, the results show a midspan deflection of -0.895 m. So, the increase in deflection is 0.695 m, which corresponds to a difference of 347%. The side span deflections in Figure 5.4 reveal in absolute terms smaller deflections. At the start of service life, the deflection at the side span is -0.200 m, and after 60 years is -0.084 m. So, over this period the deflection decreases with 0.116 m, a difference

of 58.1%.

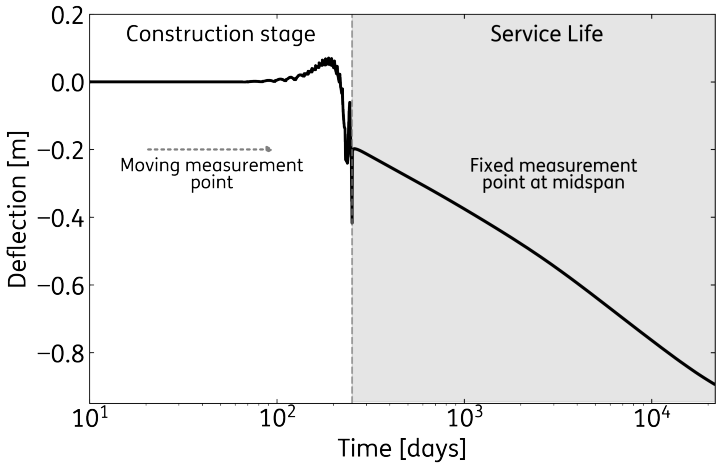

Figure 5.3: Deflection over time at the midspan for a period of 60 years (log-scale).

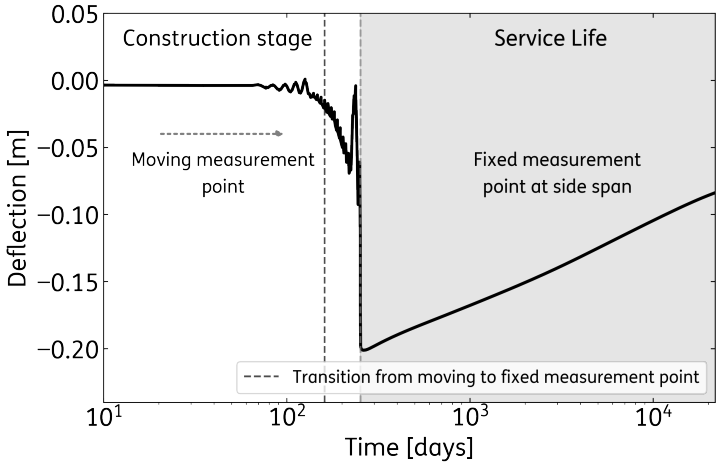

Figure 5.4: Deflection over time at the side span for a period of 60 years (log-scale).

Figure 5.5 aims to reveal more in depth what happens during the construction stage, by showing a zoomed-in view of Figure 5.3 in linear time scale. This stage lasts 252 days, and the evolution of the deflection in the main span can be divided into five zones, labeled A to E. Zone A relates to the casting of Segments 23 to 38. Throughout this first zone, the main span exhibits a positive deflection with a maximum of 0.068 m. Zone B, with the casting of Segments 39 and 40, shows the start of the descent for the deflection until it reaches zero. The deflections continue to decrease in Zone C, with the consecutive casting of Segments 41 and 42. As Segment 42 is activated, resulting in an equal number of segments on each span, the deflection reaches -0.238 m. The construction ends at Zone D. The deflection first increases to -0.061 m with the casting of Segments CSL (closing segment landside) and ECB (end cross-beam) at the side span. Then, the casting of Segment CS (closing segment) at the main span results in a decrease in deflection to -0.471 m. Zone E marks the removal of construction loads and the application of over-imposed dead loads for the service life analysis. This transition, especially the removal of the traveling formwork, induces a deloading effect. Subsequently, the deflection will

increase to -0.200 m. There are local peaks throughout the construction, especially in Zones A and B. These peaks result from the application of phased-dependent loads: prestressing, traveling formwork, and fresh concrete. Each weekly cycle begins with the prestressing of the cantilever tendons, lifting the main span. Then, the combined weight of the traveling formwork and the fresh concrete cause an opposing effect.

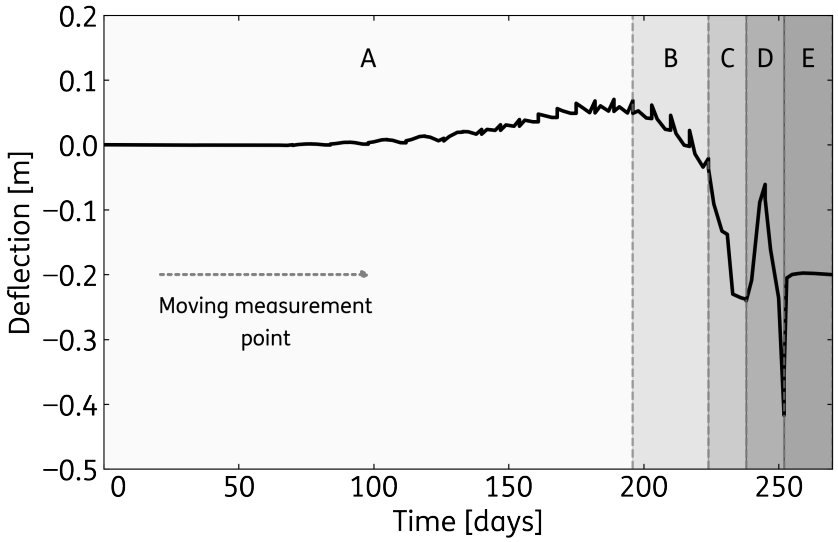

Figure 5.5: Maximum deflection over time at the midspan during the construction stage. Five zones are highlighted to divide the key moments.

A zoomed-in view of the construction stage in Figure 5.4, is presented in Figure 5.6. The evolution of the deflection in the side span can be divided into four zones, labeled A to D. Zone A is the casting of Segments 18 to 1. This means that, for most of the construction, the side span shows a negative deflection, reaching 0.065 m with the casting of Segment 1. No segments are cast in the side span in Zone B. The increase in deflection is due to the casting of Segments 41 and 42 at the main span. The deflection at the end of this increase is 0.004 m. Zone C starts with the casting of Segments CSL and ECB. This causes a decrease in the deflections. Then, an increase is caused by the casting of the CS at the midspan. The final drop in deflections in Zone D, reaching 0.200 m, is due to the deloading effect previously described for the midspan.

The evolution of the deflection at the midspan and side span during the construction is consistent with the expected behavior in the balanced cantilever method. The positive and negative deflections present for most of the construction, seen in Zone A of Figures 5.5 and 5.6, are related to the asymmetry of the hammerhead. The presence of, at least, one additional segment at the side span at all times causes small unbalancing moments that lift the main span. As the spans grow, and the asymmetry ends, the deflection at both spans is negative. The casting of the last closing segments is marked by representative variations in the deflection. This behavior shows the sensitivity of the bridge to phased-dependent loads when it is close to completion.

The deflection presented in Figures 5.3 and 5.4 does not include the overheight correction. In

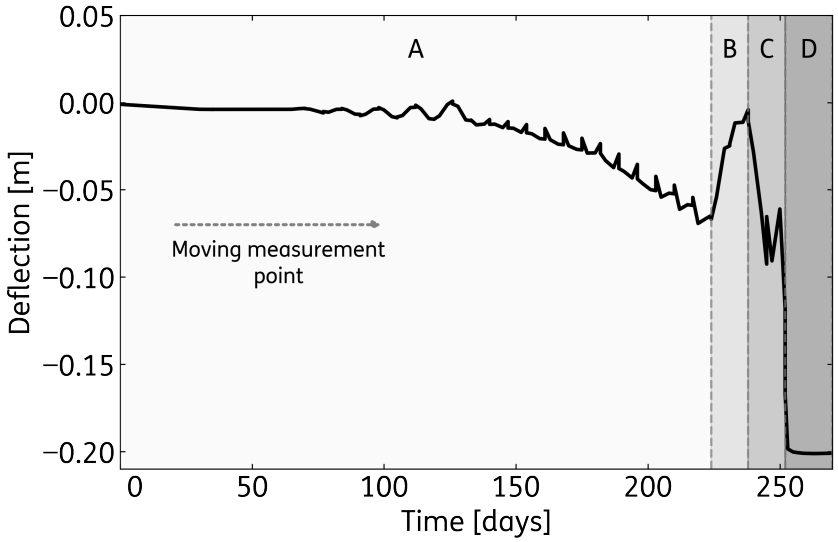

Figure 5.6: Maximum deflection over time at the side span during the construction stage. Four zones are highlighted to divide the key moments.

reality, upon completion, the deflection would follow the theoretical building line. This was not included in the FE model. Therefore, the in-situ measurements require a correction to ensure comparability with the numerical results. The exact opening date of Rooyensteinse Brug is uncertain, but in [74], it is suggested that the bridge was opened in the spring of 1977. It is assumed that the bridge officially began service in June 1977, with a three-month interval between the casting of the closing piece at the main span and the opening. Therefore, it is estimated that the construction time, which takes 252 days, was completed by March 1977. The first in-situ measurement was conducted in August 1978 (see Table 3.3). These two key dates, March 1977 and August 1978, are used to establish a reference time of 762 days. The corresponding deflection from the numerical results at 762 days is then added to all in-situ measurements taken from 1980 to 2022 for comparison purposes.

Figure 5.7 incorporates the corrected in-situ measurements at midspan for comparison with the numerical results. The percentage difference is presented in Table 5.2. On average, the Reference Analysis is overestimating the deflections at the midspan by 19.4%. A similar comparison, but for the side span, is shown in Figure 5.8. The percentage difference is presented in Table 5.3. On average, the Reference Analysis overestimates the deflections at the side span by 5.8%.

Year	1980	1985	1986	1988	1990	2012	2018	2022
Corrected in-situ measurements [m]	-0.376	-0.435	-0.469	-0.478	-0.512	-0.702	-0.772	-0.770
Numerical results [m]	-0.436	-0.559	-0.578	-0.611	-0.639	-0.812	-0.839	-0.850
Difference [%]	15.9	28.5	23.2	27.8	24.8	15.7	8.7	10.4

Table 5.2: Difference in percentage between the corrected in-situ measurements and the numerical results at midspan.

Analyzing deflections in the *z*-direction along the span at a specific time is a valuable approach for comprehending the deformed shape of the structure. The deflection along the span is shown in Figure 5.9. To illustrate the changes in the deformed shape, two key moments were selected: the

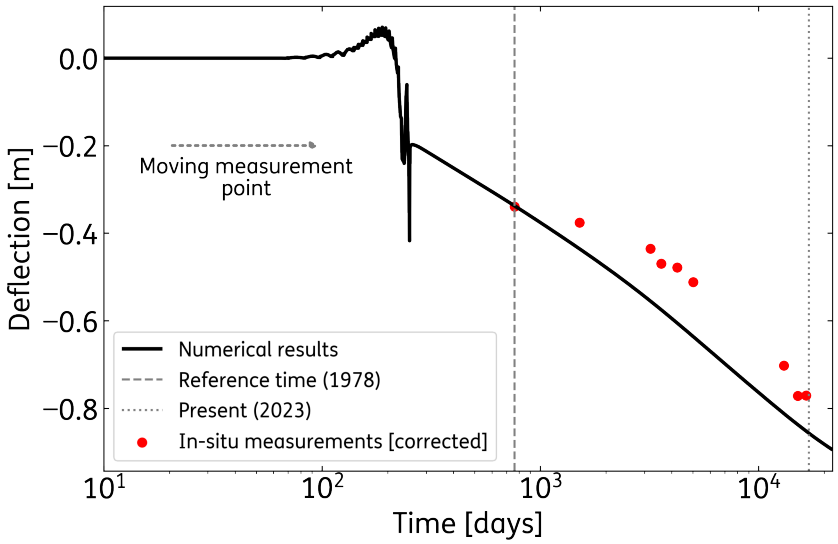

Figure 5.7: Comparison of the maximum deflection over time at midspan between the numerical results and the corrected in-situ measurements (log-scale). The in-situ measurements are corrected for a reference time of 762 days.

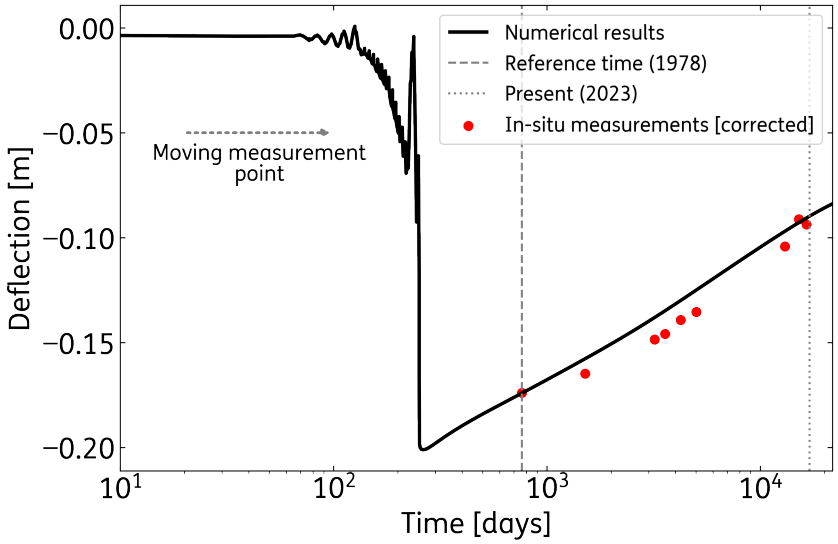

Figure 5.8: Comparison of the maximum deflection over time at the side span between the numerical results and the corrected in-situ measurements (log-scale). The in-situ measurements are corrected for a reference time of 762 days.

Year	1980	1985	1986	1988	1990	2012	2018	2022
Corrected in-situ measurement [m]	-0.165	-0.148	-0.146	-0.139	-0.135	-0.104	-0.091	-0.094
Numerical result [m]	-0.158	-0.137	-0.134	-0.129	-0.124	-0.097	-0.093	-0.091
Difference [%]	4.2	7.4	8.3	7.2	8.1	6.9	1.5	3.1

Table 5.3: Difference in percentage between the corrected in-situ measurements and the numerical results at side span.

start of service life and after 60 years. Each curve represents the maximum deflection obtained in the numerical results along the *x*-direction for that specific time. This figure also shows the previously mentioned absolute increase in deflection at the midspan, equal to 0.695 m, and at the side span, equal to 0.116 m.

Similarly to the deflections over time, the deflections along the span can also be compared with

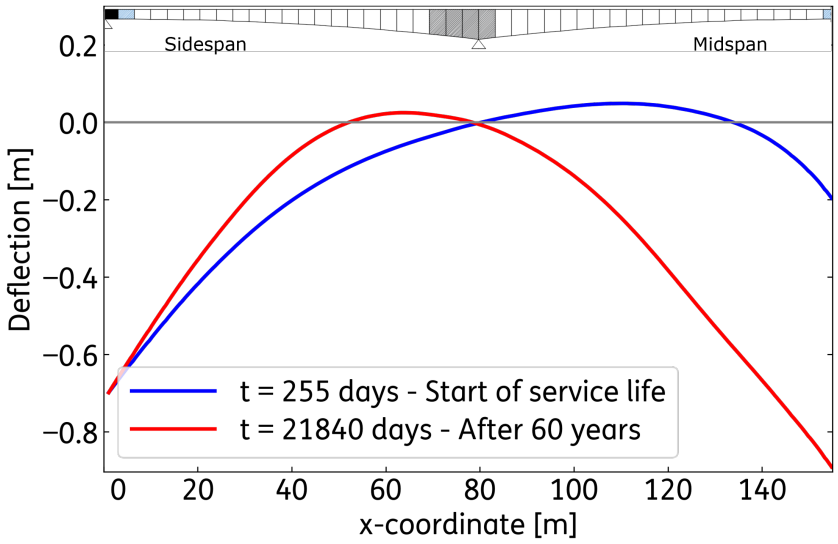

Figure 5.9: Maximum deflection along the span (*x*-direction) at the start (blue line) and end (red line) of service life.

the corrected in-situ measurements. Figure 5.10 shows the numerical results and the latest corrected in-situ measurements from April 2022. The in-situ measurements are collected from five pairs of reference points: 102-402, 103-403, 104-404, 105-405, and 107-407 (refer to Figure A.1 for the location of these reference points). The pairs 104-404 and 107-407 have previously been utilized for comparing deflections over time at the side span and midspan, respectively. At midspan, the corrected in-situ measurement is -0.768 m, while the numerical results show a deflection of -0.850 m. The difference is 10.7%. On the side span, the measurements show a deflection of -0.094 m, while the numerical results reach -0.091 m. The difference for the side span is 3.1%.

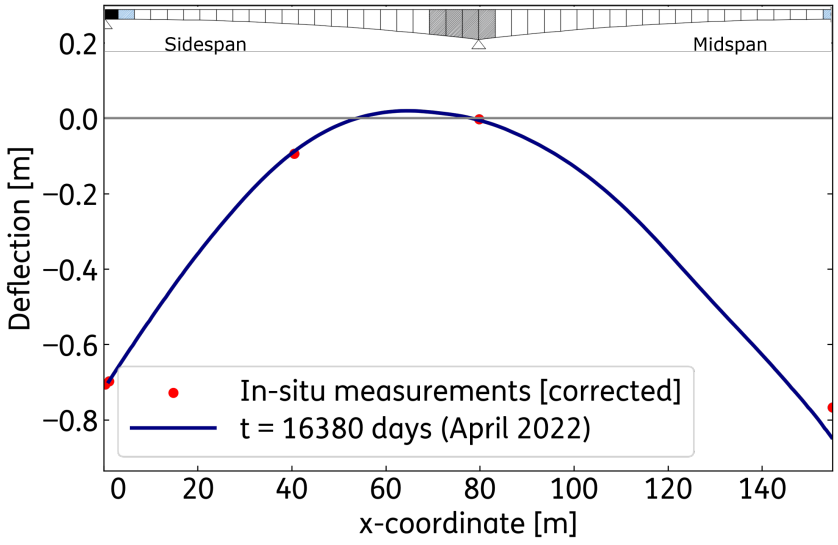

Figure 5.10: Comparison of maximum deflection along the span between the numerical results and the corrected in-situ measurements. The values are from the latest measurement conducted on the Rooyensteinse Brug in April 2022.

5.2.2. Bending moments and stresses in the concrete

As discussed in Chapter 2, a balanced cantilever bridge starts as a statically determined structure, and transitions to a statically indeterminate structure with the stitching at the midspan. In the new static system, creep and shrinkage effects lead to a redistribution of internal forces. This effect can be observed by comparing the bending moment diagrams at different key moments in time. Figure 5.11 shows the moment lines at the beginning and the end of service life. These numerical results come from the composed line elements (see Chapter 4). The sudden drops in the main span are located on the nodes shared by adjacent segments. The FE model is generated with a script that treats the side span and main span in the same way. For that reason, the jumps are likely due to numerical issues with the composed lines and are not considered to be affecting the overall results. Consequently, the values at these shared nodes were filtered out. The post-processed bending moment diagrams are presented in Figure 5.12.

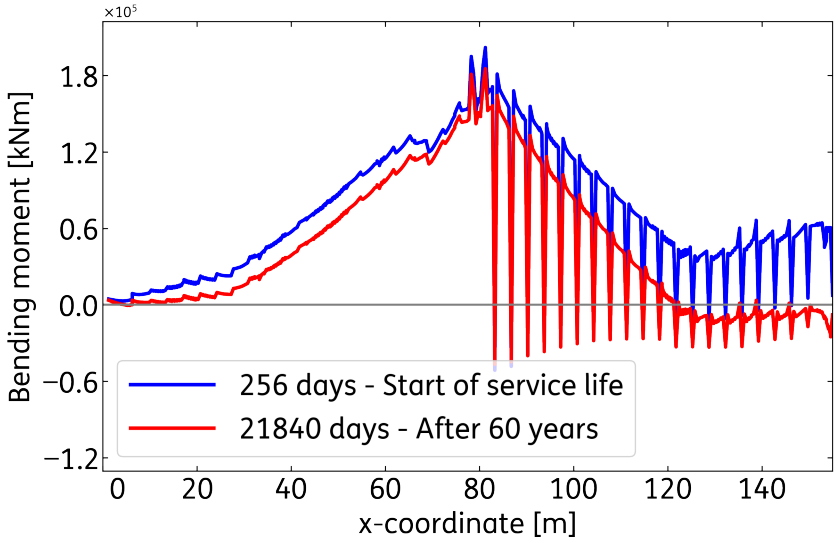

Figure 5.11: Comparison of the bending moment diagram at the end of construction and after 60 years.

The start of service life is marked by the change in the static system. Figure 5.12 shows the different contributions of the prestressing reinforcement to the bending moment. The moment induced by the cantilever tendons reaches its maximum at the hammerhead. The contribution of the continuity tendons to the hogging moment is also present at the extremes of the main span and side span. The effects are more pronounced at the main span, showing a higher number of continuity tendons compared to the side span. The changes in the moment line are noticeable in the results after 60 years. The hogging moment suffers reductions on both sides of the hammerhead. The contribution of the continuity tendons undergoes a significant decrease. Finally, the hogging moment at the midspan is no longer present.

The maximum and minimum principal stresses denoted as σ_1 and σ_3, offer insights into the stress distribution within the model. Furthermore, they help assess the validity of modeling assumptions. Similarly to the bending moment diagrams, two key moments were chosen. Figures 5.13 and 5.14 show the contour plots for the maximum principal stress σ_1 at the beginning and end of service life.

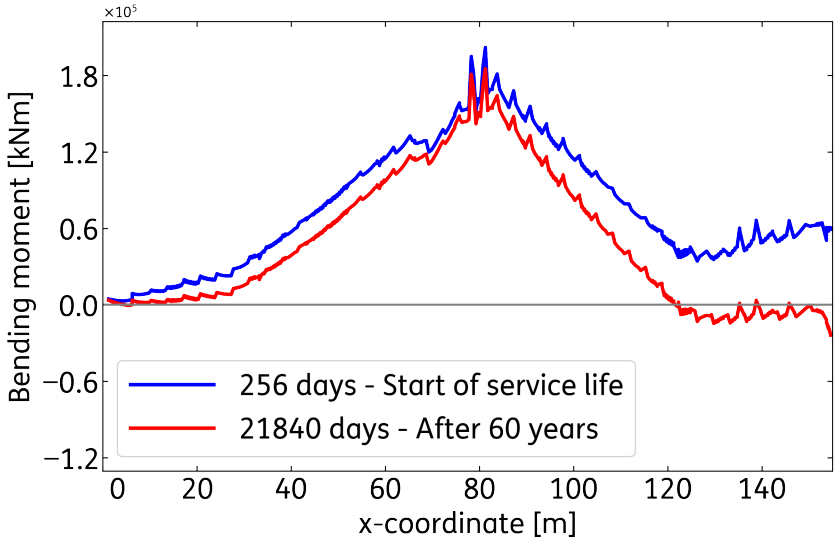

Figure 5.12: Post-processed comparison of the bending moment diagram at the end of construction and after 60 years.

The legend is referenced to the concrete mean tensile strength, equal to 2.55 N/mm^2. This value has been corrected according to Eurocode 2 to account for lightweight aggregate concrete [50].

Figure 5.13 shows that for most of the model, the stresses remain below 50% of f_{ctm}. Nevertheless, at certain locations, the stresses surpass f_{ctm}. The zoom windows in the figure show that at both ends of the bridge, the stresses at the top and bottom slabs surpass three times f_{ctm}. Stress concentrations along the span are evident on the top slab, bottom slab, and to a lesser extent, the webs. These stress concentrations are consistent across all segments and align with the introduction of forces by the cantilever tendons.

Figure 5.14 shows the contour plots for the maximum principal stress σ_1 after 60 years. Similarly to Figure 5.13, the stresses remain below 50% of f_{ctm} for most of the model. Figure shows that at the midspan, the bottom slab presents stresses that surpass three times f_{ctm}. The stress concentrations along the span, noted at the beginning of service life, persist after 60 years, with the majority of values now below f_{ctm}.

Figures 5.15 and 5.16 show the contour plots for the minimum principal stress σ_3 at the beginning and end of service life. The color bar is referenced to the concrete mean compressive strength f_{cm}, equal to 38 N/mm^2. Figure 5.15 shows that, overall, the stresses in the model remain below 40% of the f_{cm}. At the midspan, stresses exceeding twice the value of f_{cm} are present in the bottom slab. Figure 5.16 shows a reduction in compressive stresses in the webs and bottom slab after 60 years in comparison with the beginning of service life. This is noticeable on both sides of the hammerhead, and also at the midspan. The locations exceeding twice the f_{cm} are more concentrated in both extremes of the bottom slab at the midspan, instead of the full width as in Figure 5.15.

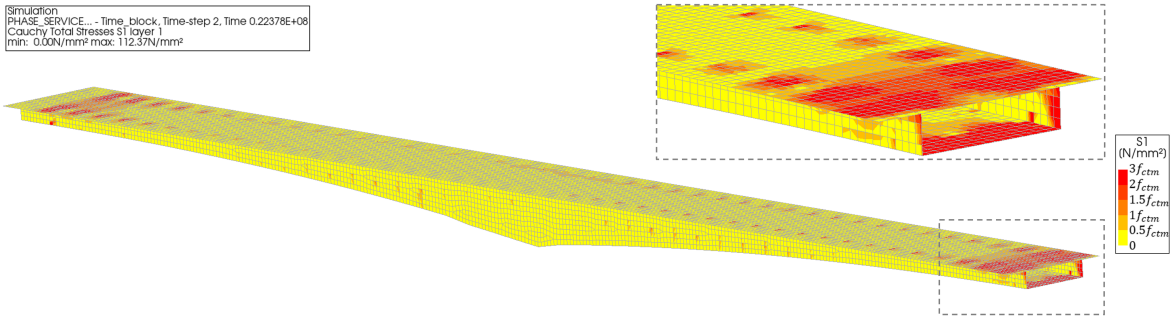

(a) A 3D view with a midspan zoom window.

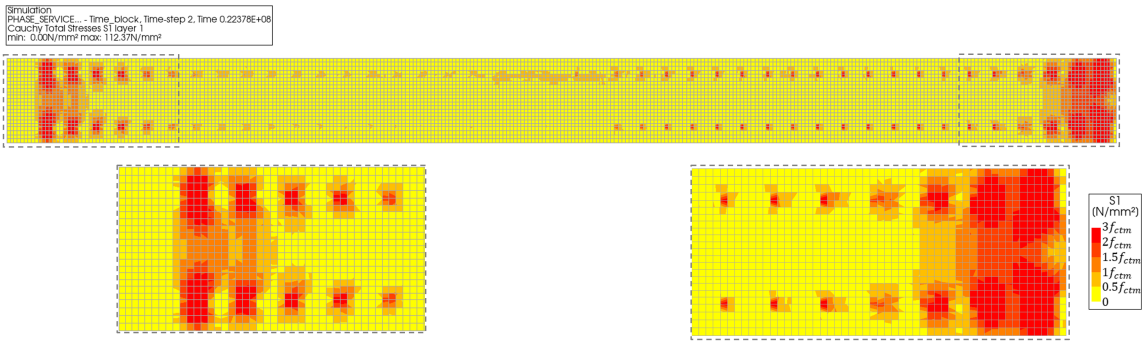

(b) View from the top, with a zoom window on both extremes of the bridge.

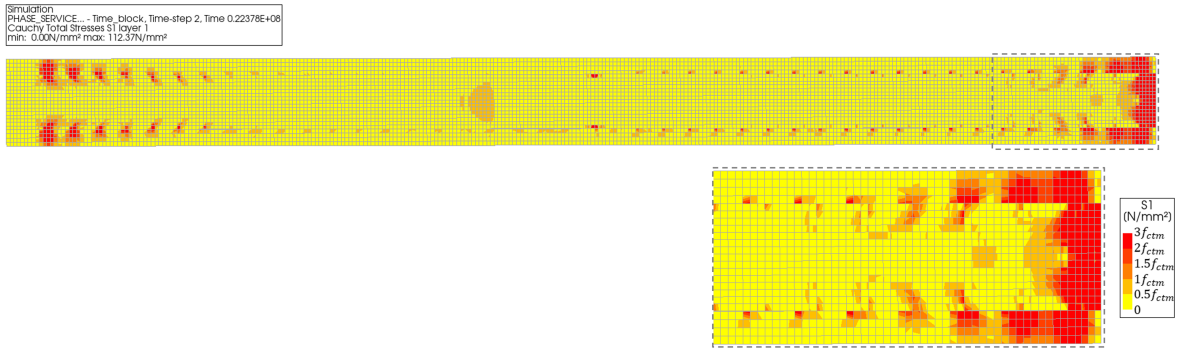

(c) View from the bottom, with a midspan zoom window.

Figure 5.13: Contour plots of the maximum principal stress σ_1 at the beginning of service life. The views presented are 3D, top and bottom. Zoom windows of locations with the highest stresses are included. The color bar is referenced to the concrete mean tensile strength f_{ctm} equal to 2.55 N/mm^2.

5.2.3. Stress level in the tendons and prestress losses

The three factors contributing to time-dependent prestressing losses are creep, shrinkage, and steel relaxation. Therefore, an important part of the study of the long-term effects of creep and shrinkage on the structural behavior of the Rooyensteinse Brug is the analysis of how these phenomena impact prestressing levels over time. Prestressing losses can be evaluated either for a specific tendon or at a cross-sectional level. The first approach provides insights into the impact of immediate and time-dependent losses locally. The second approach allows for a global analysis of the bridge for a specific moment in time. Both approaches will be presented.

The stresses along the tendon are shown in Figures 5.17 and 5.18 for four different prestressing tendons: cantilever tendons 5 and 50, and continuity tendons CA and C16. These selections were made

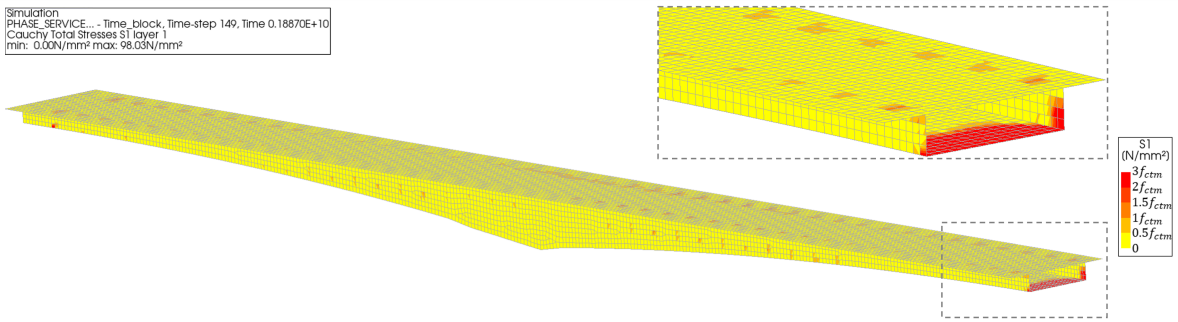

(a) A 3D view with a midspan zoom window.

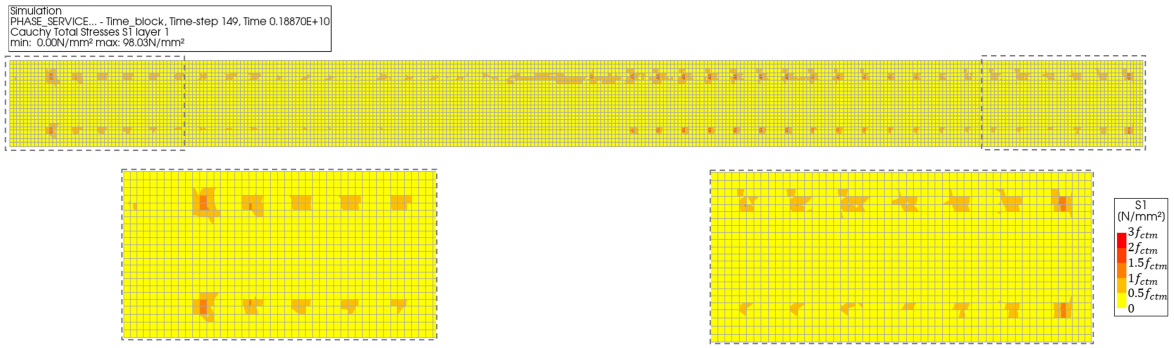

(b) View from the top, with a zoom window on both extremes of the bridge.

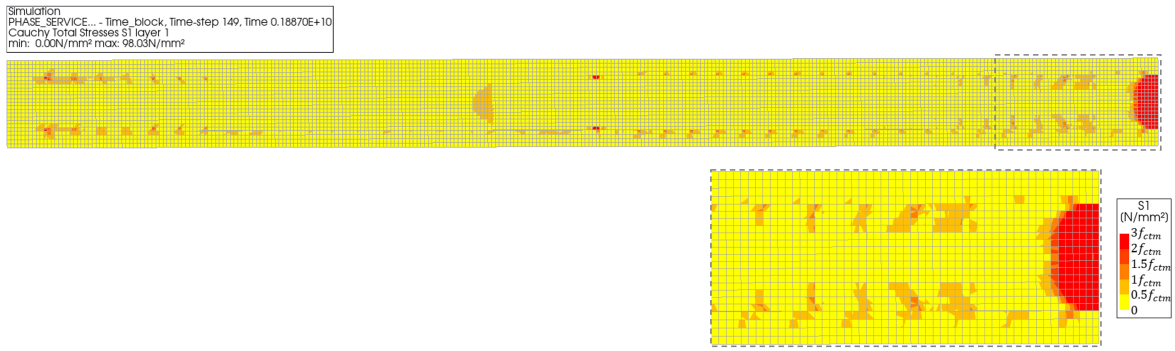

(c) View from the bottom, with a midspan zoom window.

Figure 5.14: Contour plots of the maximum principal stress σ_1 at the end of service life (60 years). The views presented are 3D, top and bottom. Zoom windows of locations with the highest stresses are included. The color bar is referenced to the concrete mean tensile strength f_{ctm} equal to 2.55 N/mm^2.

arbitrarily, aiming to gain insights into scenarios with short and long as well as cantilever and continuity tendons. In Figure 5.17, three key moments were selected: time of prestressing, end of construction, and after 60 years. Additionally, the initial stress σ_{p0} of 1333 N/mm^2 is included for reference. The difference between σ_{p0} and the acting prestressing are the immediate losses due to friction, wobble effect, and anchorage slip. Additionally, the loss due to relaxation is incorporated as a reduction to σ_{p0} (see Chapter 4). The friction and wobble effects are applied as uniform losses over the full length of the tendons. The loss due to anchorage slip is present up to a certain length. This influence length can be visualized in tendon 50, going from 113 to 139 m. For tendons shorter than this required length, the loss due to anchorage slip will be incorporated as a uniform loss along the tendon. This is the case of tendon 5. The second key moment is at the end of construction. At this point, the tendons have been

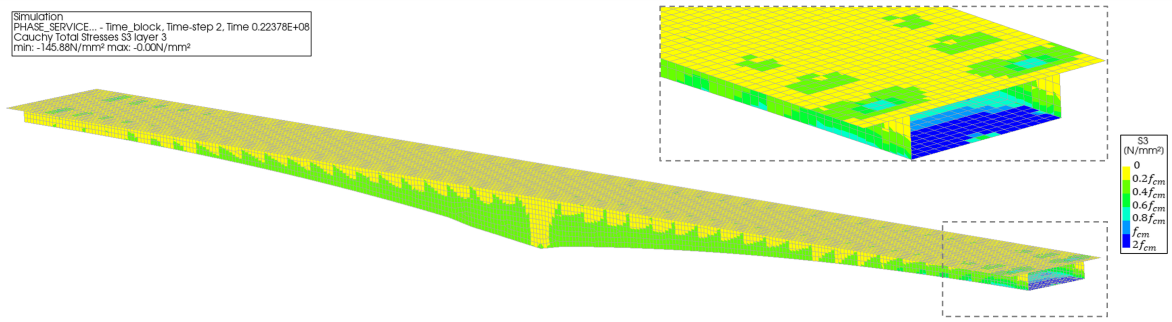

(a) A 3D view with a midspan zoom window.

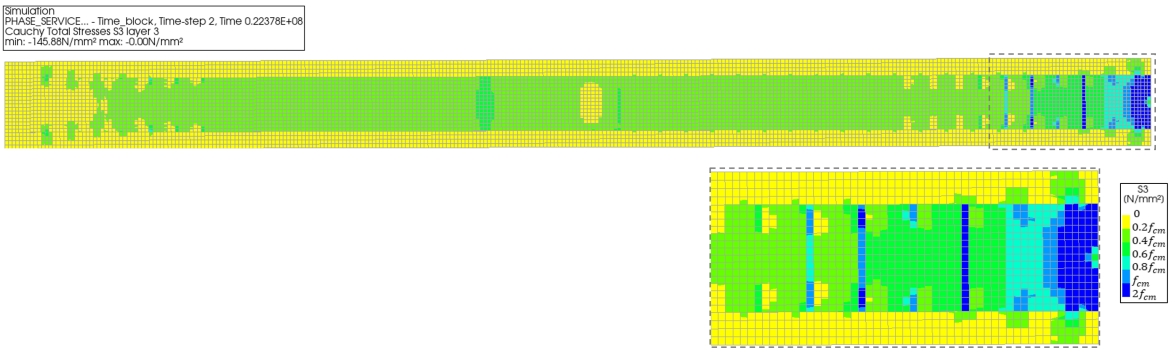

(b) View from the bottom, with a midspan zoom window.

Figure 5.15: Contour plots of the minimum principal stress σ_3 at the beginning of service life. The views presented are 3D and bottom. Zoom windows of locations with the highest stresses are included. The color bar is referenced to the concrete mean compressive strength f_{cm} equal to 38 N/mm^2.

bonded to the concrete for a certain amount of time. This bond means that the stresses applied to concrete segments will also affect the prestressing levels at the tendon level. The difference in prestressing between the time of prestressing and the end of construction is the result of elastic shortening, creep, and shrinkage effects. Elastic shortening results from the compressive stresses introduced during the casting of subsequent segments. The effect is larger toward the extremes of the tendons because the *younger* segments are more susceptible to shortening in comparison to segments cast earlier. These *younger* segments will also be more susceptible to creep and shrinkage due to maturity effects.

Figure 5.18 shows the evolution of the stresses for continuity tendons CA and C16. Given the continuity tendons are activated towards the end of the construction, the second key moment is one week after the end of construction. This timeline captures the transition of loads from construction to service life. Similar to tendons 5 and 50, the blue line shows the immediate prestressing losses due to friction, wobble effect, and anchorage slip. One week after the construction is complete, the stress levels of tendon CA show no significant variation. Contrarily, tendon 16 does show a noticeable loss of prestress close to the midspan, equivalent to 11.4%.

The third moment in Figures 5.17 and 5.18 is after 60 years. The difference in prestressing levels in comparison to the end of construction is the result of creep and shrinkage effects. Overall, the prestressing losses due to creep and shrinkage maintain certain uniformity along the tendons, except for the zones close to the midspan. This can be visualized with tendons 50 and C16 by comparing the prestress levels at the end of construction, and 60 years later. For tendon 50, the loss is 20.0%, and

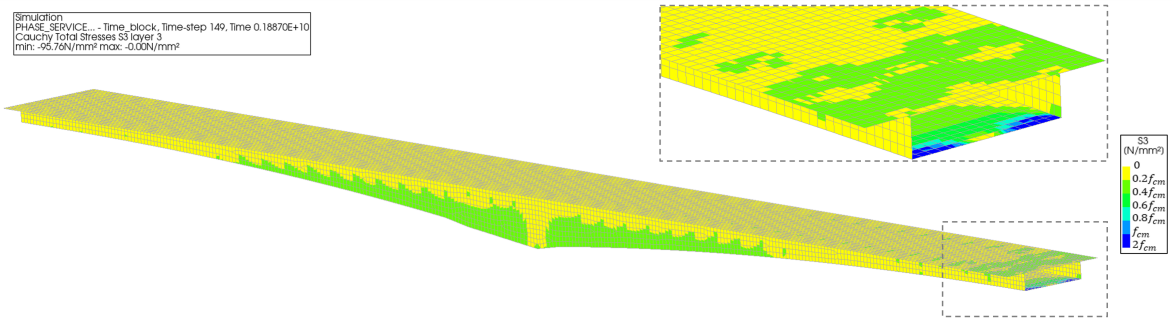

(a) A 3D view with a midspan zoom window.

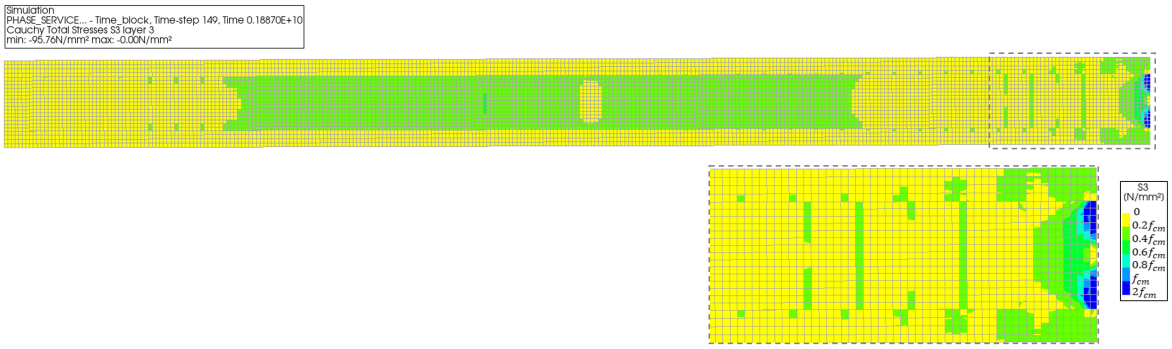

(b) View from the bottom, with a midspan zoom window.

Figure 5.16: Contour plots of the minimum principal stress σ_3 at the end of service life (60 years later). The views presented are 3D and bottom. Zoom windows of locations with the highest stresses are included. The color bar is referenced to the concrete mean compressive strength f_{cm} equal to 38 N/mm^2.

for tendon C16, 37.3%.

The red and green lines in Figures 5.17 and 5.18 show kinks in several locations. Most of these kinks appear in zones where the tendons are curved. The software calculates the stresses along the tendon profile, and a combination of the curvature and a coarse mesh can cause certain jumps in the results. It is expected that a finer mesh improves the results, but for the scale of the model and the type of analysis, the current mesh is considered sufficient. It is then important to mention that these sudden increases and decreases in prestressing do not occur in reality.

With a clear understanding of the evolution of the prestressing losses for a selection of representative tendons, the analysis can be extended to the cross-sectional level. Figure 5.19 shows the prestressing loss after 60 years for four different cross-sections: Segment 2 at the extreme of the side span, Segments 18 and 23 on both sides of the hammerhead, and Segment 42 at the extreme of the main span. For each cross-section, the prestressing loss per tendon is visually represented using a color bar. The average loss displayed in the figure is calculated by considering the loss of all the tendons present at that cross-section. The prestressing loss is calculated relative to the working prestress, defined as the difference between the initial prestress σ_{p0} and the losses due to friction, wobble effect, anchorage slip, and relaxation. Consequently, the prestressing losses shown in Figure 5.19 result primarily from creep and shrinkage effects. The losses due to elastic shortening are also included, but this effect only occurs during the construction stage. The figure shows that Segments 2 and 42 have prestressing losses of 15.8% and 15.9%, respectively. Segments 18 and 23 show smaller losses, with 11.4% and

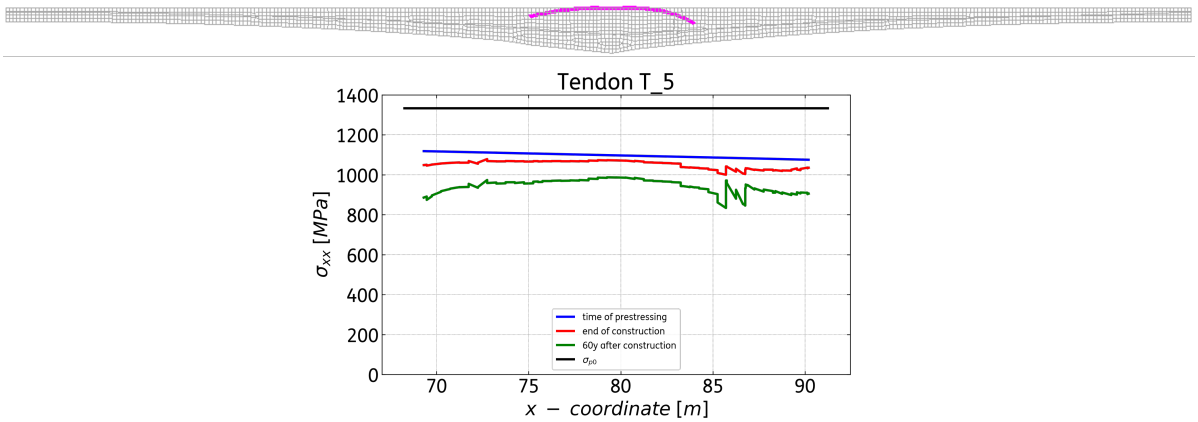

(a) Stresses along the cantilever tendon 5.

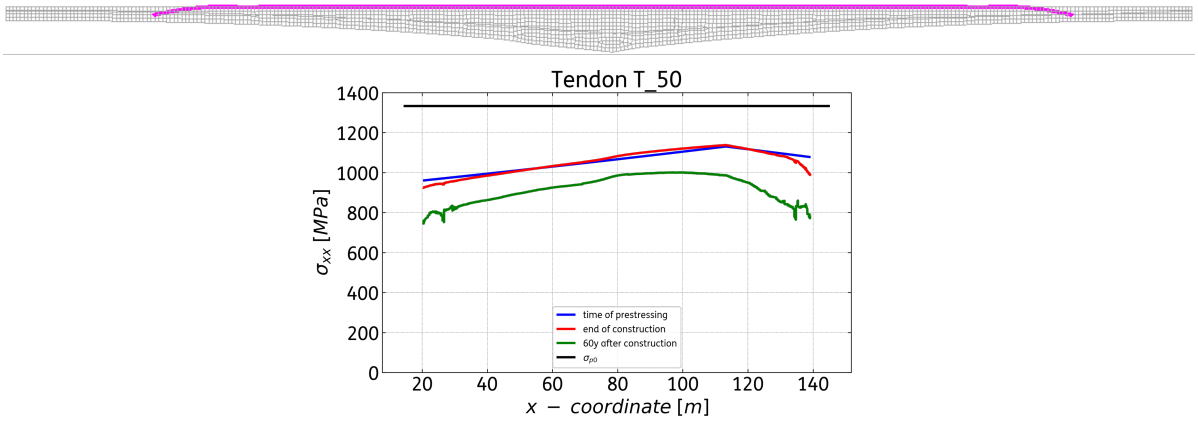

(b) Stresses along the cantilever tendon 50.

Figure 5.17: Evolution of the stresses along the prestressing tendons 5 and 50. Three key moments are selected: at the time of prestressing, at the end of construction, and after 60 years.

9.2% after 60 years. Of all the chosen cross-sections, only Segment 42 has cantilever tendons with individual losses larger than 30%. Nevertheless, the average loss for this cross-section does not grow apart from the others due to the presence of the continuity tendons.

The prestressing losses shown in Figure 5.19 for the selected cross-sections can be computed for all segments. This is illustrated in Figure 5.20. All the segments show an average prestressing loss in the range of 8% to 20%. Segments 9 to 32 remain below 15%, as well as Segments ECB, CSL, and 3 in the side span. The remaining segments, most located close to the midspan, have average losses higher than 15%. Overall, the average prestressing loss for the reference analysis is 14.2%.

The recalculation report of the Rooyensteinse Brug assumed a time-dependent prestressing loss of 20% [18]. This loss accounts for creep, shrinkage, and relaxation of prestressing steel. This value is typically assumed in engineering practice and is consistent with the time-dependent losses of 19.1% from the original calculations [68]. Figure 5.21 compares the average prestressing loss along the span with the 20% typically assumed loss. Four key moments were chosen for this comparison: the end of construction, one month later, after 45 years (2023), and after 60 years. Relaxation was included by adding the assumed loss of 11.2% to the average prestressing loss of all segments. At the end of construction, all segments show a similar average prestressing loss, varying from 11% to 13.8%. The

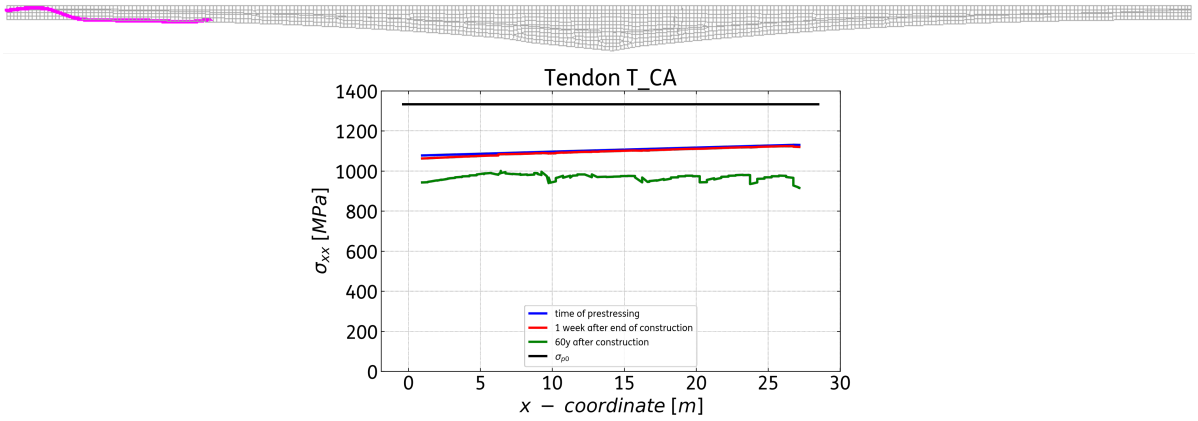

(a) Stresses along the continuity tendon CA.

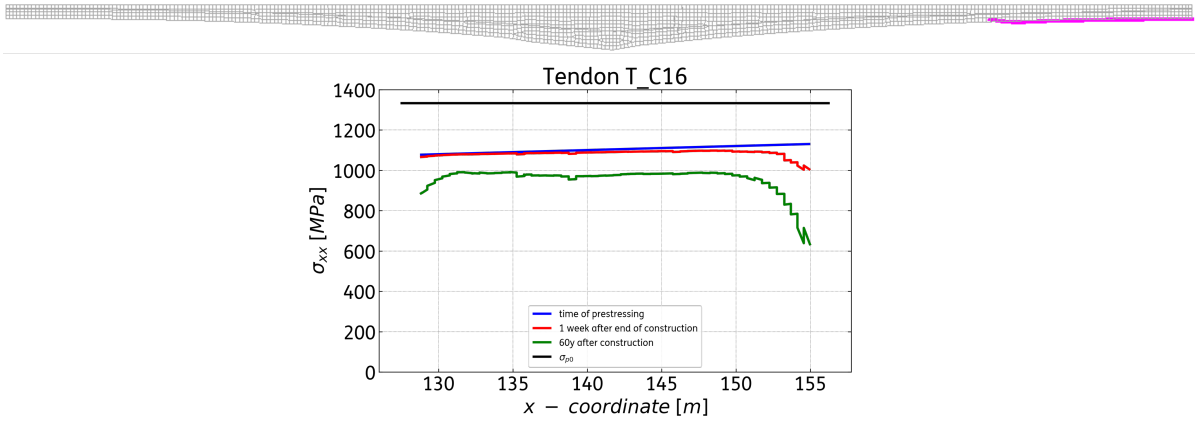

(b) Stresses along the continuity tendon C16.

Figure 5.18: Evolution of the stresses along the prestressing tendons CA and C16. Three key moments are selected: at the time of prestressing, one week after the end of construction, and after 60 years.

main difference one month later is the increase at midspan, and on a smaller scale, at the extreme of the side span. After 45 years, most segments show losses above 20%. The values vary from 19.2% to 30.8%. The difference between the prestressing losses close to the hammerhead and at the extremes is much more marked at this point. While the former shows losses between 20% and 25%, the latter reaches the 30% mark. The differences between the losses after 45 and 60 years are minimal.

5.2.4. Interpretation of results

The relevant results of the Reference Analysis were presented and explained in detail in the previous subsections. The main findings are discussed in this subsection. The analysis of the deflections over time demonstrates that the Reference Analysis can capture the downward trend seen in the in-situ measurements starting from approximately 1988. The slope of the measurements closely resembles the numerical results. It is important to note that the initial two in-situ measurements taken in 1978 and 1980 exhibit a distinct deflection rate compared to the rest of the data. This behavior does not align with the expected time-dependent behavior, which typically involves an initial higher deflection rate followed by a gradual decline over time. The deflections along the span also align with the in-situ measurements, showing both the increase in negative deflection at the midspan and the increase in positive deflection

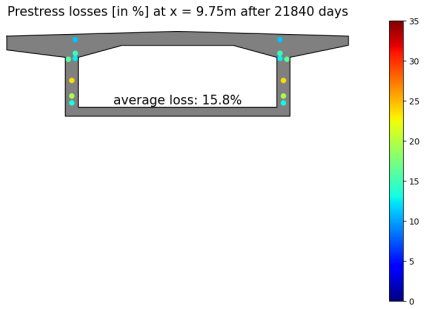

(a) Cross-sectional prestressing loss for Segment 2.

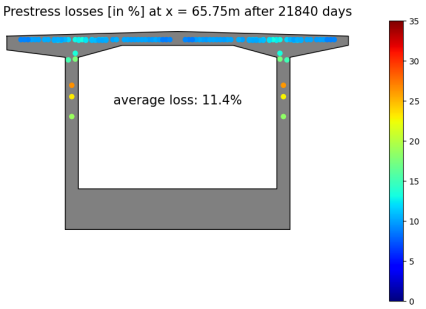

(b) Cross-sectional prestressing loss for Segment 18.

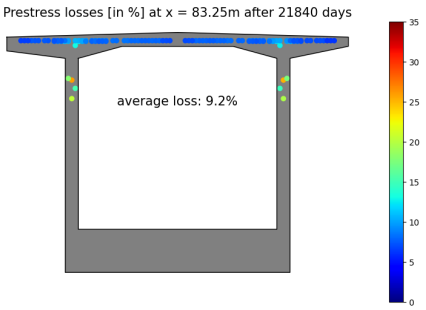

(c) Cross-sectional prestressing loss for Segment 23.

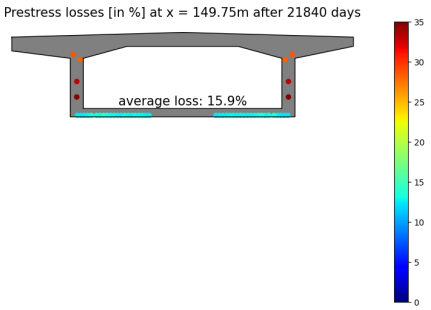

(d) Cross-sectional prestressing loss for Segment 42.

Figure 5.19: Prestressing losses after 60 years for four different cross-sections. The losses account for creep and shrinkage only, and are calculated versus the working prestress, which is the difference between the initial prestress σ_{p0} and the immediate losses.

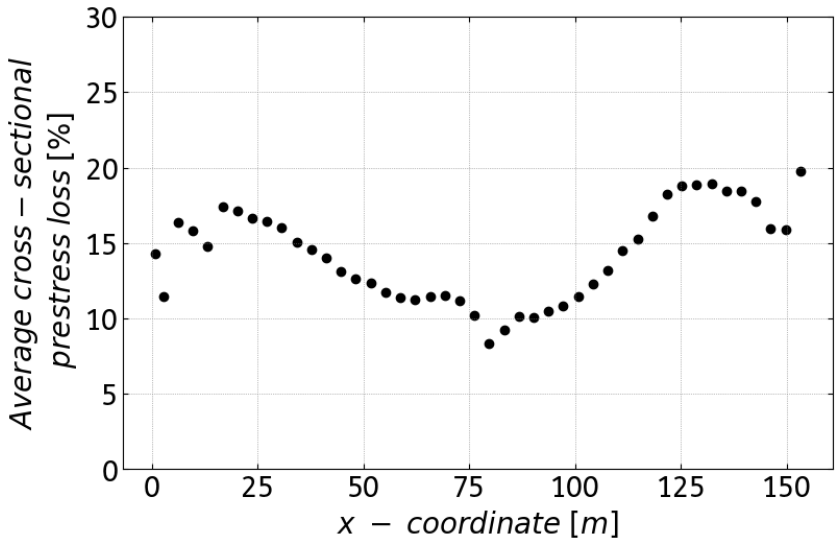

Figure 5.20: Average prestressing loss per cross-section after 60 years. The losses account for creep and shrinkage only, and are calculated versus the working prestress, which is the difference between the initial prestress σ_{p0} and the immediate losses.

at the sidespan. Overall, there is good agreement between the corrected in-situ measurements and the numerical results, seen both visually and quantitatively. The results show the capability of the FE model to capture the real deformed shape of the Rooyensteinse Brug. Another relevant result is the difference in the moment line at the beginning and the end of service life. Figure 5.12 not only shows

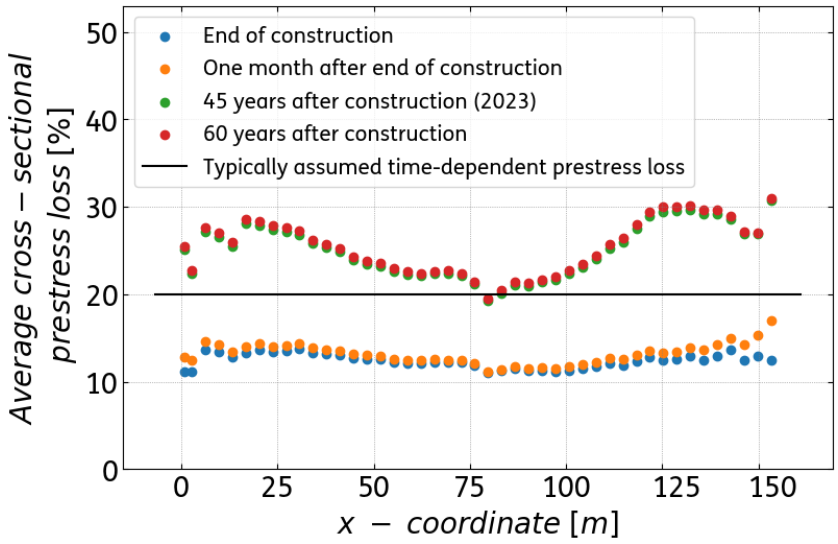

Figure 5.21: Average prestressing loss per cross-section for four key moments. The losses are due to creep, shrinkage, and relaxation, and they are compared with the typically assumed 20% prestress loss.

the redistribution of forces but also the prestressing losses at the end of 60 years. The moment line at the end of service life is consistent with Figure 5.20, which shows higher prestressing losses at the extremes of both spans in comparison to the zone close to the hammerhead.

The maximum principal stress σ_1 provides a means to check the modeling assumption of no cracking. Figure 5.13 shows that at midspan, the stresses at the top and bottom slab surpass three times the concrete mean tensile strength f_{ctm}. Initially, the results suggest that the prestressing of the continuity tendons causes cracking at midspan. Nevertheless, this local effect can also be a consequence of the symmetry conditions applied to the edges of the Segment CS at midspan. The simultaneous application of a constraint with an upward force from the continuity tendons can induce high stresses along all the constrained edges (see Figure 5.13a). Overall, it is expected that the impact of this local effect does not influence significantly the global behavior of the FE model.

Figure 5.14 shows the significant reduction in stresses at the top slab after 60 years. At this stage, tensile stresses predominate at the bottom slab of the Segment CS. Considering the prestressing losses from Figure 5.21 and the bending moment diagram from Figure 5.12, it is apparent that the continuity tendons at midspan have experienced significant losses. Therefore, the tensile stresses are likely a result of the symmetry conditions. The constraints prevent the section from rotating due to the deflection at midspan, consequently inducing tensile forces in the bottom slab.

The minimum principal stress σ_3 serves to check the main assumption behind the principle of superposition, fundamental to the formulation of creep and shrinkage in code-based models. This assumption dictates that the compressive stresses must remain below $0.4 f_{cm}$, equal in this case to -15.2 N/mm^2. The only zone surpassing this limit is the bottom slab at the midspan. The stresses at the bottom slab are likely a result of the compressive stresses introduced by the continuity tendons. The findings in Figure 5.15 are corroborated by the results after 60 years, presented in Figure 5.16. This

figure shows a significant loss of compressive stresses at midspan, consistent with the prestressing loss seen in Figure 5.21. It is important to mention that the values for f_{cm} and f_{tm} used in this analysis are based on the properties at 28 days. In reality, these properties improve over time. According to Eurocode 2, the compressive and tensile strength after 60 years are 46.1 N/mm^2 and 2.9 N/mm^2, respectively [50].

The analysis of prestressing losses in time resulted in several interesting findings. Figure 5.21 shows that after one month of construction, noticeable losses occur at the midspan. Segment CS, with a sudden increase from 12.4% at the end of construction, to 16.9% one month later, suggests important losses in the continuity tendons since early on in the analysis. This segment is the last one to be activated, making it the most sensitive to creep and shrinkage effects. These effects impact the prestressing losses of the continuity tendons from the moment they become bonded to the concrete. The loss at Segment CS keeps increasing to reach 30.8% after 45 years, and 30.9% after 60 years. Nevertheless, the losses at this point are similar to the ones found in other segments of the bridge. As previously mentioned, the prestressing losses resulting from relaxation were included in the FE model as a reduction to the initial force applied to the tendons. Consequently, the stresses in the bridge are lower than they would be in reality. Considering that creep is a stress-dependent phenomenon, the numerical results likely underestimate creep effects.

5.3. Impact of creep and shrinkage models

The effects of different code-based models for creep and shrinkage are assessed through the sensitivity analyses labeled 2, 3, and 4. Sensitivity Analysis 2 employs the MC78 model, Analysis 3 the EC2 model, and Analysis 4 the fprEC2 model. The selection of MC78 in this sensitivity analysis is based on its historical significance: MC78 was used for bridge designs in the ’70s and ’80s. The EC2 reflects the contemporary engineering practice as the current standard for the design of concrete structures. Finally, fprEC2 is presented as an improved version of EC2, motivating a comparative analysis between the two.

5.3.1. Variations in the analysis

As previously outlined in the introduction of this section, the variations in the sensitivity analyses 2, 3, and 4 pertain to the code-based models for creep and shrinkage. Chapter 2 introduced the three considered models: MC78, EC2, and fprEC2. The main equations of each of these models, as well as the additional provisions for lightweight aggregate concrete (LWAC), are presented in Section 2.3.2.

For MC78, the coefficient η_2 with a ρ equal to 1759 kg/m^3, is equal to 0.537 (see Equation 2.3). The multiplying factor for the creep strain was chosen as 1.0 based on the main conclusions found in the study by Wang et. al [62]. For shrinkage, the selected factor is 1.2 to maintain consistency with EC2 and fprEC2. For EC2, η_E is equal to 0.639 (see Equation 2.8). Additionally, η_2 is equal to 1.0 and η_3 is equal to 1.2. Finally, for fprEC2, $\eta_{lw,Ec}$ is equal to 0.639 (see Equation 2.15). Additionally, the factor

for shrinkage strain is equal to 1.2.

The compliance function for LWAC can then be expressed as:

$$\phi(t,t_0) = \frac{1}{\eta \cdot E_c(t_0)} + \frac{\eta \cdot \varphi(t,t_0)}{\eta \cdot E_{c28}} \tag{5.1}$$

where:

η is the code-dependent coefficient for LWAC (i.e. η_2, η_E, $\eta_{lw,Ec}$).

$\varphi_(t,t_0)$ is the creep coefficient for NWC.

$E_c(t_0)$ is the modulus of elasticity of the concrete at the time of loading t_0 for NWC.

E_{c28} is the modulus of elasticity of the concrete at 28 days for NWC.

Based on the above-presented provisions from MC78, EC2, and fprEC2, the influence of LWAC - in comparison to normal weight concrete (NWC) - is only present in the initial elastic response. Figure 5.22 illustrates the difference in the creep compliance and shrinkage strain curves for NWC and LWAC with these three models over 60 years. The curves correspond to the times of loading at 3 and 28 days. It can be observed that the initial response is larger for LWAC, but the slope of the time-dependent response is the same for NWC and LWAC.

Figure 5.23 shows the creep compliance and shrinkage strain curves for these three models in comparison to the Reference Analysis with B4, for 60 years. The creep compliance curves correspond to the times of loading at 3, 7, 14, 28, and 60 days, chosen to better illustrate the differences. This figure highlights significant differences in the creep and shrinkage formulation among B4, MC78, EC2, and fprEC2. The creep compliance functions for MC78 and EC2 reach a final value. For both B4 and fprEC2, creep continues to increase at the end of 60 years but at a different rate. The large differences are also evident in the comparison between shrinkage strain curves. Once more, MC78 and EC2 reach a final value. B4 and fprEC2 continue to increase at the end of 60 years.

5.3.2. Results

The impact of different code-based models is assessed considering the deflections over time and the time-dependent average prestress losses after 60 years. The deflection over time at the midspan and the side span is shown in Figure 5.24. The Reference Analysis with B4 is included for comparison. Figure 5.24a shows the deflections over time at midspan during the construction stage. Overall, the difference between the four models is the most noticeable with the casting of the last four segments (i.e. Segments 41, 42, CSL, and CS). B4 shows a smaller downward deflection throughout the full construction. At the end of construction, the difference in deflection between the Reference Analysis and MC78, EC2, and fprEC2 is 0.178 m (89.1%), 0.145 m (72.7%), and 0.098 m (49.3%), respectively.

The results at midspan during service life, shown in Figure 5.24b, can be analyzed in the short-term (i.e. the first 10 years of service life), and long-term (i.e. multi-decade up to the 60-year analysis endpoint). In the short term, all the sensitivity analyses show a larger downward deflection than the

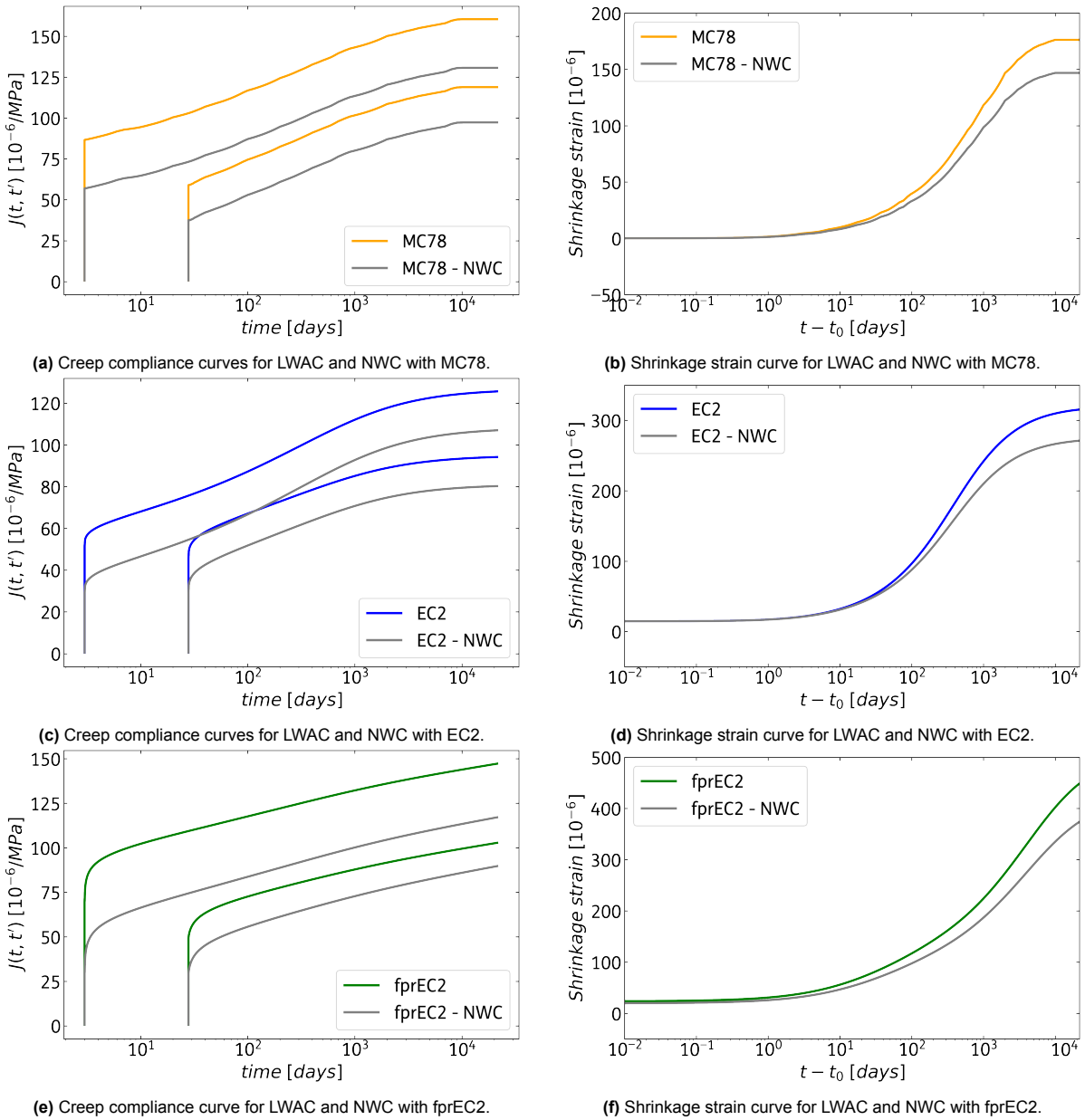

(a) Creep compliance curves for LWAC and NWC with MC78.

(b) Shrinkage strain curve for LWAC and NWC with MC78.

(c) Creep compliance curves for LWAC and NWC with EC2.

(d) Shrinkage strain curve for LWAC and NWC with EC2.

(e) Creep compliance curve for LWAC and NWC with fprEC2.

(f) Shrinkage strain curve for LWAC and NWC with fprEC2.

Figure 5.22: Comparison of creep compliance and shrinkage strain curves for MC78, EC2 and fprEC2 with NWC and LWAC for 60 years (log-scale). The times of loading for the creep compliance curves are 3 and 28 days. According to these code-based models, the impact of using LWAC is only reflected in the initial elastic response.

Reference Analysis. B4 will surpass MC78, EC2, and fprEC2 after approximately 3500 days (9.6 years), 1500 days (4.1 years), and 1000 days (2.7 years), respectively. In the long-term, MC78 and EC2 reach a final deflection value while the decreasing trend shown by fprEC2 continues throughout the 60 years. The difference at the end of the analysis between B4 and MC78, EC2, and fprEC2 is 0.315 m (31.5%), 0.421 m (47.1%), and 0.378 m (42.2%), respectively.

Like Figure 5.24a for the midspan, Figure 5.24c shows the deflections over time at the side span during the construction stage. The results show a minimal difference between the four models during this stage. The Reference Analysis only diverges from the other models at the end of the construction. The difference at the start of service life between B4 and MC78, EC2, and fprEC2 is 0.026 m (12.9%),

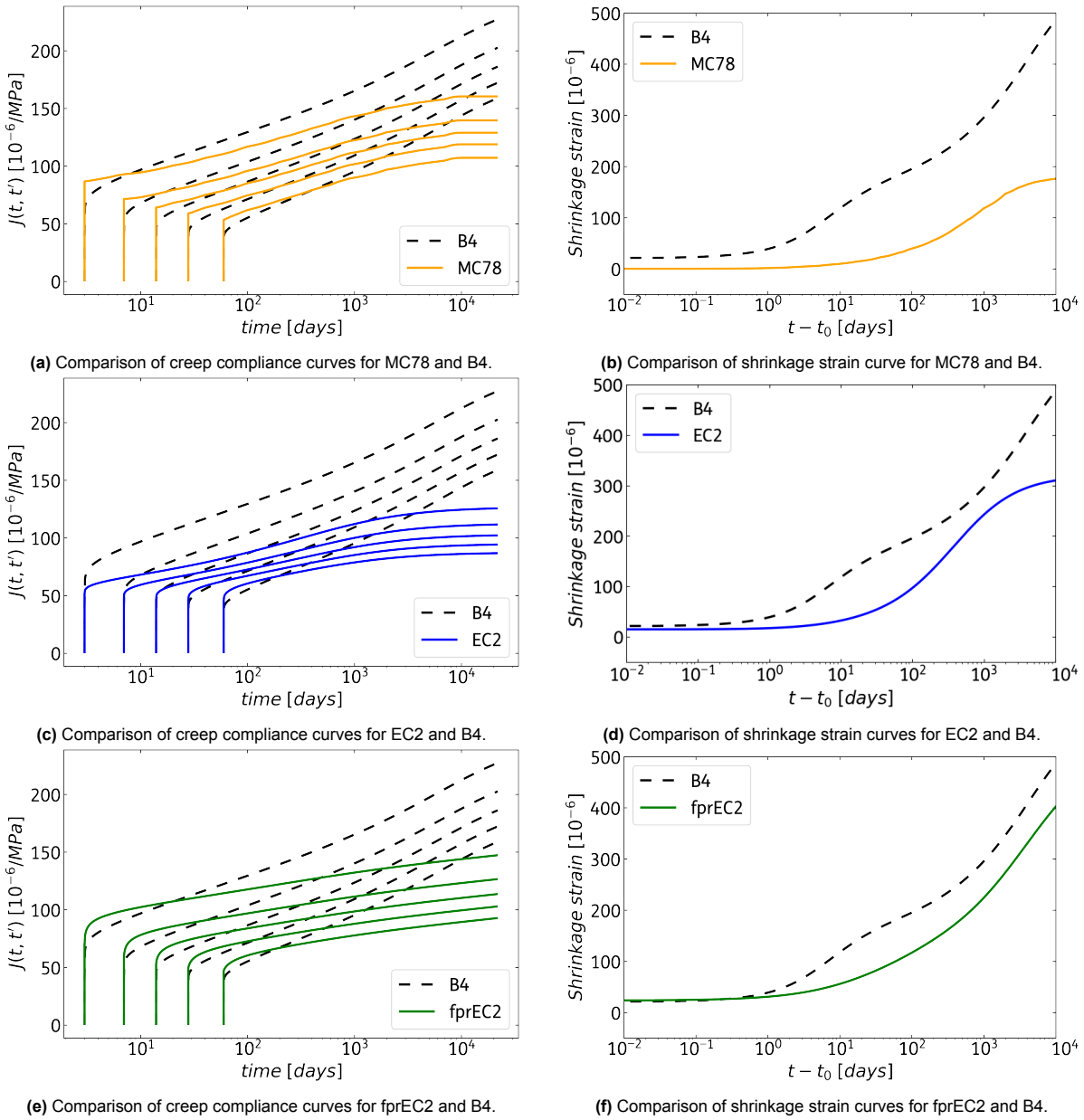

(a) Comparison of creep compliance curves for MC78 and B4.

(b) Comparison of shrinkage strain curve for MC78 and B4.

(c) Comparison of creep compliance curves for EC2 and B4.

(d) Comparison of shrinkage strain curves for EC2 and B4.

(e) Comparison of creep compliance curves for fprEC2 and B4.

(f) Comparison of shrinkage strain curves for fprEC2 and B4.

Figure 5.23: Comparison of creep compliance and shrinkage strain curves for MC78, EC2, and fprEC2 (log-scale). The Reference Analysis using B4 is included for comparison. The times of loading for the creep compliance curves are 3, 7, 14, 28, and 60 days.

0.027 m (13.4%), and 0.027 m (13.4%), respectively.

Figure 5.24d shows that, for both short and long term, B4 exhibits a smaller downward deflection in contrast to MC78, EC2, and fprEC2. The continuously increasing trend from B4 is also seen in fprEC2, while MC78 and EC2 reach a final value. The difference at the end of the analysis between B4 and MC78, EC2, and fprEC2 is 0.097 m (116%), 0.115 m (138%), and 0.109 m (130%), respectively. Overall, MC78 shows the largest downward deflection at the midspan of the three sensitivity analyses, followed by fprEC2. At the side span, MC78 exhibits the largest upward deflection, followed once more by fprEC2.

The sensitivity analyses 2, 3, and 4 are compared with the corrected in-situ measurements in Figure

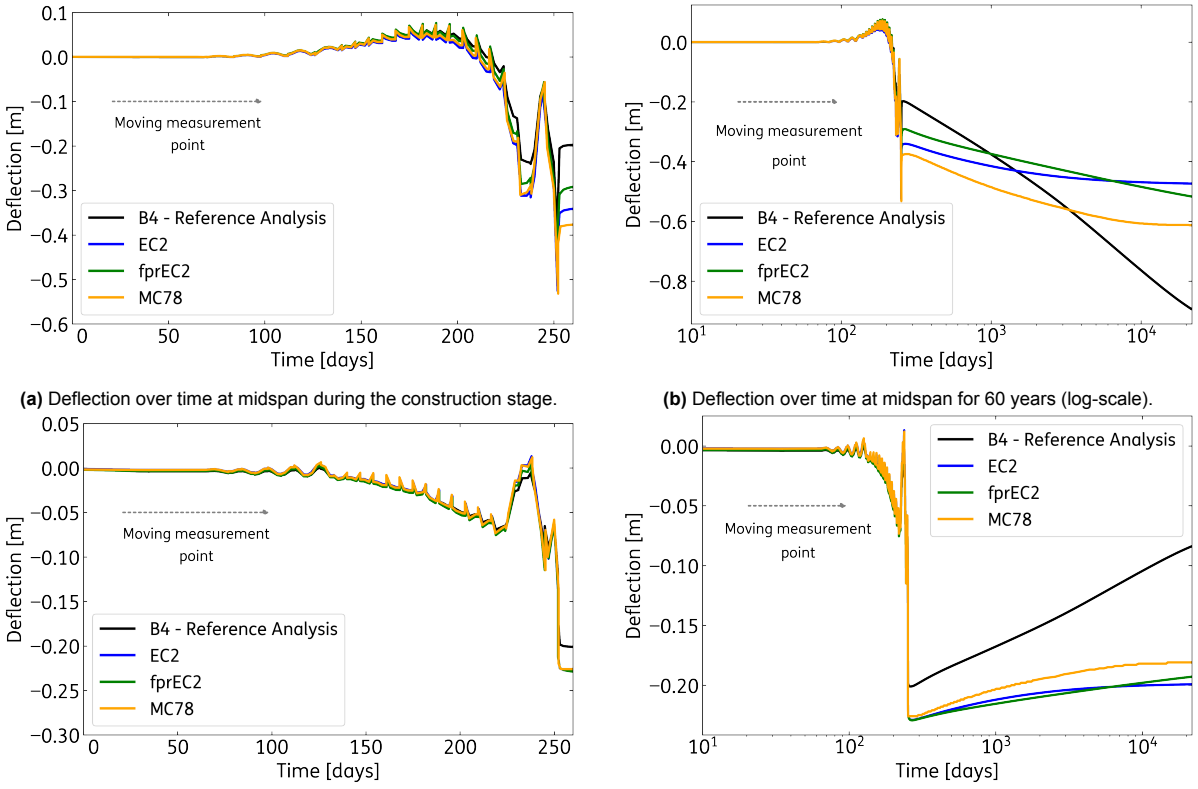

(a) Deflection over time at midspan during the construction stage.

(b) Deflection over time at midspan for 60 years (log-scale).

(c) Deflection over time at the side span during the construction stage.

(d) Deflection over time at the side span for 60 years (log-scale).

Figure 5.24: Deflection over time at midspan and side span with MC78, EC2, and fprEC2. The Reference Analysis with B4 is included for comparison. A zoom window to the construction stage is included for a better visualization of the differences between analyses.

5.25. Similar to Figure 5.24, the results can be examined for the short term (the initial 10 years of service life) and the long term (up to the 60-year analysis endpoint). The in-situ measurements considered for the short-term comparison are from 1980, 1985, 1986, and 1988. The remaining measurements, from 1990, 2012, 2018, and 2022, are used for long-term comparison. At midspan, the difference in average for the first 10 years between the corrected in-situ measurements and MC78, EC2, and fprEC2 is 0.017 m (3.0%), 0.054 m (10.2%), and 0.033 m (6.9%), respectively. The long-term comparison shows an average difference of 0.210 m (24.6%) for MC78, 0.284 m (36.3%) for EC2, and 0.221 m (29.8%) for fprEC2. In comparison with the latest available measurements, in April 2022, the numerical results at midspan exhibit underestimations of 0.284 m (31.7%) for MC78, 0.362 m (43.4%) for EC2, and 0.286 m (36.2%) for fprEC2. Overall, all models mispredict the trend observed in the in-situ measurements.

At the side span, the difference between the corrected in-situ measurements and MC78, EC2, and fprEC2 in the short-term is 0.008 m (4.4%), 0.014 m (7.5%), and 0.013 m (7.1%), respectively. The long-term comparison shows an average difference of 0.042 m (31.9%) for MC78, 0.053 m (37.9%) for EC2, and 0.047 m (32.9%) for fprEC2. In comparison with the latest available measurements, in April 2022, the numerical results at the side span exhibit underestimations of 0.053 m (41.7%) for MC78, 0.065 m (48.2%) for EC2, and 0.057 m (41.6%) for fprEC2. Overall, MC78 is the closest sensitivity analysis to the corrected in-situ measurements, both in the short and long term and for both midspan

and the side span. EC2 shows the largest difference of the three analyses.

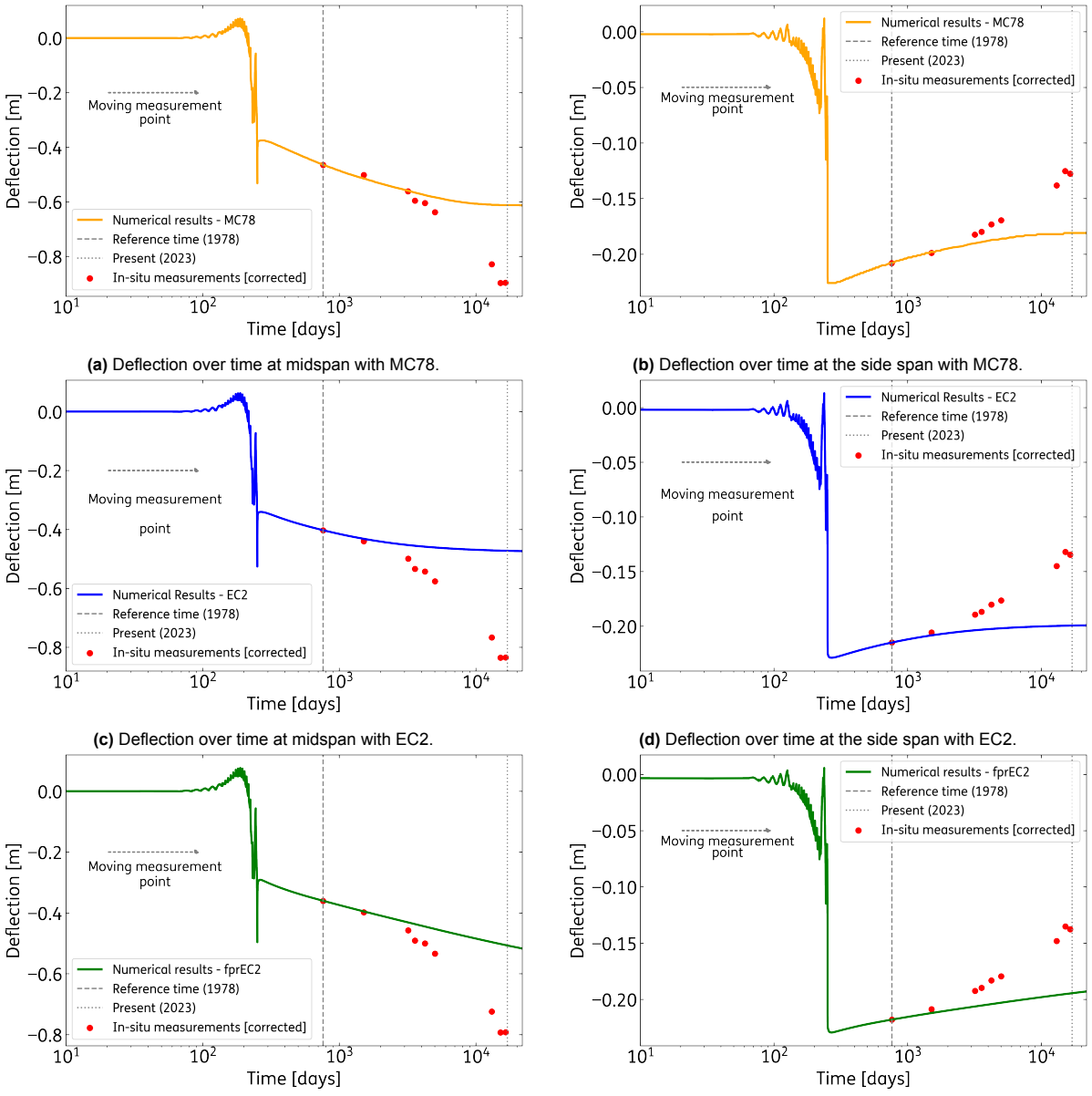

(a) Deflection over time at midspan with MC78.

(b) Deflection over time at the side span with MC78.

(c) Deflection over time at midspan with EC2.

(d) Deflection over time at the side span with EC2.

(e) Deflection over time at midspan with fprEC2.

(f) Deflection over time at the side span with fprEC2.

Figure 5.25: Comparison of the deflection at midspan and side span of MC78, EC2, and fprEC2 with the corrected in-situ measurements (log-scale).

The differences between the Reference Analysis and the sensitivity analyses 2, 3, and 4 are also analyzed in the time-dependent prestressing losses, shown in Figure 5.26. The prestressing losses for the three analyses show a similar distribution as the one observed in the Reference Analysis. The segments near the hammerhead exhibit the lowest prestressing losses, between 15% and 20%. As one moves towards both extremes, the losses increase to a maximum of 25%. Overall, the analysis with fprEC2 results in the highest time-dependent prestressing losses after the Reference Analysis. The differences between MC78 and EC2 are small, except for Segments ECB, SML, 1, 2, and SM.

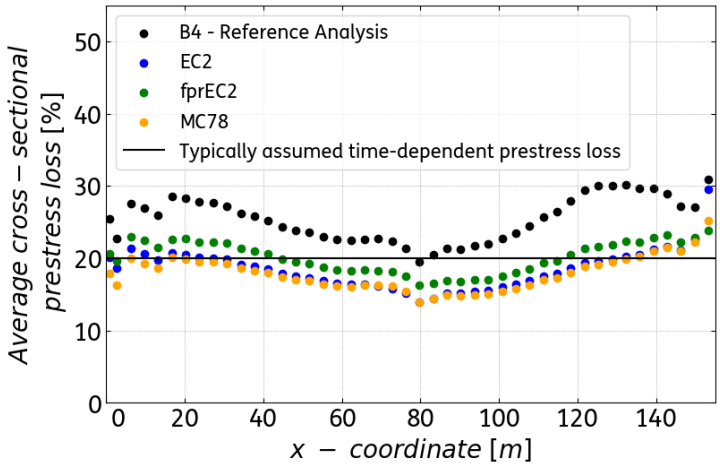

Figure 5.26: Comparison of time-dependent prestress losses after 60 years between the Sensitivity Analyses 2, 3, and 4 and the Reference Analysis. The losses are due to creep, shrinkage, and relaxation, and they are compared with the typically assumed 20% prestress loss.

5.3.3. Interpretation of results

The study on the impact of different code-based models for creep and shrinkage has unveiled several significant findings. Starting at the material level, the creep compliance and shrinkage strain curves for MC78, EC2, and fprEC2 reach values significantly lower than those for B4 at the end of the 60-year analysis. fprEC2 is the only model that as B4, does not converge to an asymptotic final value after 60 years.

The differences in the material models are reflected on the structural level. Differences below 11% between the numerical predictions of the deflections and the corrected in-situ measurements at the midspan and the side span show the capability of MC78, EC2, and fprEC2 to capture the short-term behavior (i.e. within the first 10 years of service life) of the Rooyensteinse Brug. In contrast, these models exhibit a significant underestimation in the long-term behavior (i.e. multi-decade), with differences ranging between 25% and 38%.

The lower deflections over time, in comparison to the Reference Analysis, also seep through the time-dependent prestress losses. MC78, EC2, and fprEC2 predict prestress losses after 60 years that fall below the typically assumed value of 20% for cross-sections near the hammerhead, which are critical for shear capacity. Given their underestimations of the long-term deflections, it is reasonable to assume that the prestressing losses are also underestimated. It should be noted that the Sensitivity Analysis with EC2, being the current standard for the design of concrete structures, resulted in the largest underestimations in deflections over time when compared to the corrected in-situ measurements. The results obtained with fprEC2 indicate a certain degree of improvement compared to EC2. However, the difference with the measured data is still significant.

5.4. Impact of propagation of uncertainty

Sensitivity Analyses 5 and 6 aim to study how the uncertainty in Model B4 propagates into the structural response of the Rooyensteinse Brug. For this, the upper bound (Analysis 5) and lower bound (Analysis 6) from the 90% credible interval are used as the creep compliance and shrinkage strain curves. Note that the Reference Analysis represents the mean creep compliance and shrinkage strain curves.

5.4.1. Variations in the analysis

The upper and lower bound curves are defined based on a 90% credible interval. These curves are determined by considering random variables Ψ_i, i = 1...8, for creep and shrinkage model component uncertainties. These model uncertainties are quantified in [75, 76], and follow lognormal distributions. Based on 10000 drawings from Ψ_i, an equal number of creep compliance and shrinkage curves are generated. Subsequently, a 90% credible interval is computed for each time value. The upper and lower bound values from these 90% credible intervals are connected, which forms the upper and lower bounds seen in Figure 5.27a for creep, and Figure 5.27b for shrinkage.

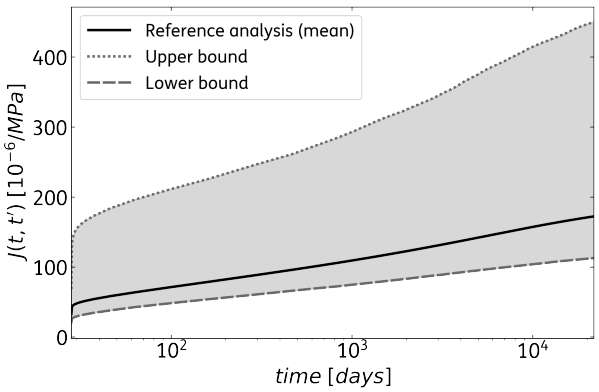

(a) Propagation of uncertainty for creep a time of loading of 28 days.

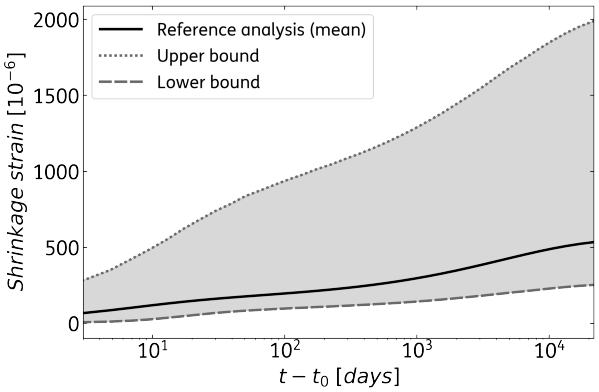

(b) Propagation of uncertainty for shrinkage.

Figure 5.27: The creep compliance and shrinkage strain curves for Sensitivity Analysis 5 (upper bound) and Analysis 6 (lower bound) (log-scale). The Reference Analysis works with the mean creep and shrinkage curves.

5.4.2. Results

Figure 5.28 shows the mean, upper, and lower bounds in comparison to the corrected in-situ measurements. The in-situ measurements were corrected using the Reference Analysis (mean). Throughout the construction stage, shown for the midspan in Figure 5.28a and for the side span in Figure 5.28c, the lower bound response remains in proximity to the mean. This is not observed in the case of the upper bound, which exhibits significantly larger absolute deflections throughout the construction. The difference between the mean and both bounds increases during service life, as illustrated in Figure 5.28b. At the beginning of service life, the difference between the mean and the upper and lower bounds is 0.421 m (210%) and 0.062 m (31.2%), respectively. At the end of service life, the difference increases to 2.01 m (225%) for the upper bound and 0.381 m (42.5%) for the lower bound. The corrected in-situ measurements fall within the range defined by the mean and the lower bounds.

The considerable spread between the mean and the upper bound is also seen at the side span, shown in Figure 5.28c for the construction stage, and Figure 5.28d for service life. However, in this case, the largest difference occurs at the beginning of service life and progressively diminishes towards the end of the 60-year analysis. At the beginning of service life, the difference between the mean and the upper and lower bounds is 0.406 m (202%) and 0.074 m (37.2%), respectively. At the end of service life, the difference is 0.162 m (193%) for the upper bound and 0.023 m (27.5%) for the lower bound. The corrected in-situ measurements fall within the range defined by the mean and the upper bounds.

The differences between the Reference Analysis and the Sensitivity analyses 5 and 6 are also analyzed in the time-dependent prestressing losses, shown in Figure 5.29. In general, the upper and lower bounds mirror the results from the Reference Analysis, displaying smaller losses at the cross-sections near the hammerhead, and a gradual increase towards the extremes of both spans. Specifically, the prestressing losses of the lower bound range between 16% and 28%. In contrast, the upper bound exhibits a broader range, from 26% to 51%. The mean and lower bounds show similar prestressing losses, differing by approximately 5%.

5.4.3. Interpretation of results

The aim of Sensitivity Analyses 5 and 6 is to understand how the uncertainty present in prediction models for creep and shrinkage propagates into the structural response of the Rooyensteinse Brug. The approach used here studies this in an approximate way; a more comprehensive and thorough approach would require a full probabilistic analysis. Nevertheless, the presented results already offer valuable insights regarding the impact of accounting for the inherent and large uncertainties that are present in creep and shrinkage models.

The upper and lower bounds in the B4 creep compliance and shrinkage strain curves reveal significant variability. This substantial uncertainty extends to the structural response predictions, where the deflections at midspan range between 0.514 m and 2.91 m, and at the side span, between -0.061 m and -0.246 m. Attempting to design for such a wide range would be impractical and excessively

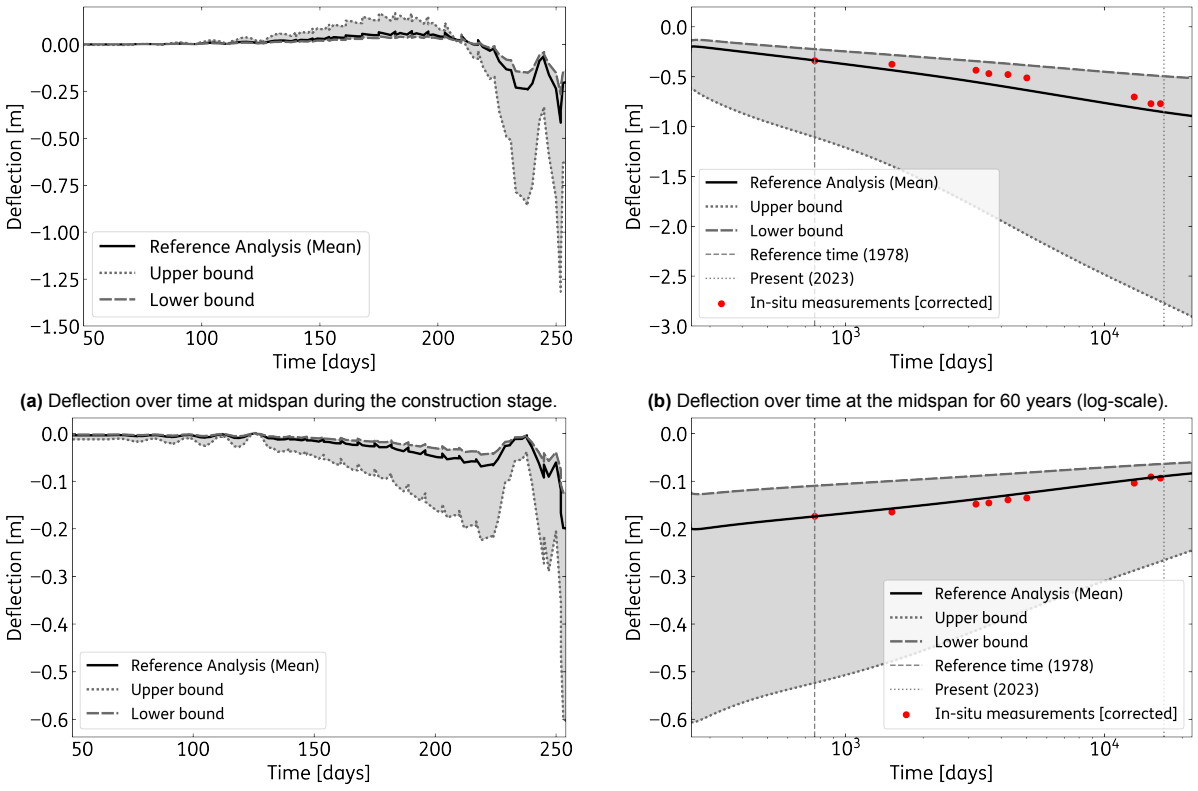

(a) Deflection over time at midspan during the construction stage.

(b) Deflection over time at the midspan for 60 years (log-scale).

(c) Deflection over time at the side span during the construction stage.

(d) Deflection over time at the side span for 60 years (log-scale).

Figure 5.28: Comparison of the deflection over time between the Reference Analysis (mean) Analysis 5 (upper bound), Analysis 6 (lower bound), and the corrected in-situ measurements. The comparison is at the midspan and the side span. The y-axis scale differs in the four plots.

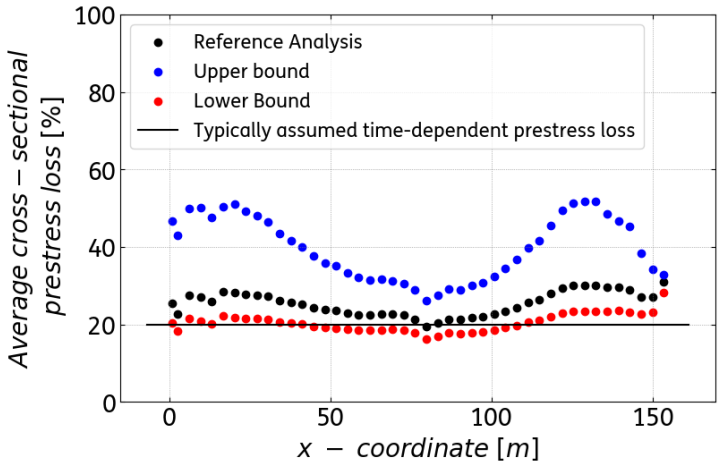

Figure 5.29: Comparison of time-dependent prestress losses between Sensitivity Analyses 5, 6 and the Reference Analysis. The losses are due to creep, shrinkage, and relaxation, and they are compared with the typically assumed 20% prestress loss.

conservative. Nevertheless, these results show that the model uncertainties cannot be neglected.

The results from the Reference Analysis suggest that the typically assumed 20% time-dependent prestressing loss is not conservative for critical shear capacity cross-sections, yet it is also not a substantial underestimation. However, when considering uncertainty, the latter conclusion no longer holds. Moreover, the presence of such a high level of uncertainty, even within theoretically grounded models

like B4, raises pertinent questions regarding the suitability of the EC2 and fprEC2 models.

5.5. Impact of maturity effects

Sensitivity Analysis 7 aims to study the impact of employing a maturity-independent creep model with a fixed age of loading, in contrast to the maturity-based creep model used in the Reference Analysis. Analysis 7 is further divided into Analysis 7.a and 7.b. Analysis 7.a is conducted with a time of loading of 2 days, which corresponds to the age of a newly activated concrete segment when the prestressing force is applied. Analysis 7.b employs a time of loading of 252 days, used for the calculation of the creep coefficient in the recalculation report of the Rooyensteinse Brug [18]. This makes Analysis 7.b a representation of engineering practice nowadays.

5.5.1. Variations in the analysis

While a maturity-based creep model considers the development of concrete properties in time, a maturity-independent creep model will employ a single creep compliance curve for all times of loading. This contrast is demonstrated in Figure 5.30, which compares a set of compliance curves of the Reference Analysis with the single curves from Analyses 7.a and 7.b. The times of loading presented for comparison are 2, 7, 14, and 28 days.

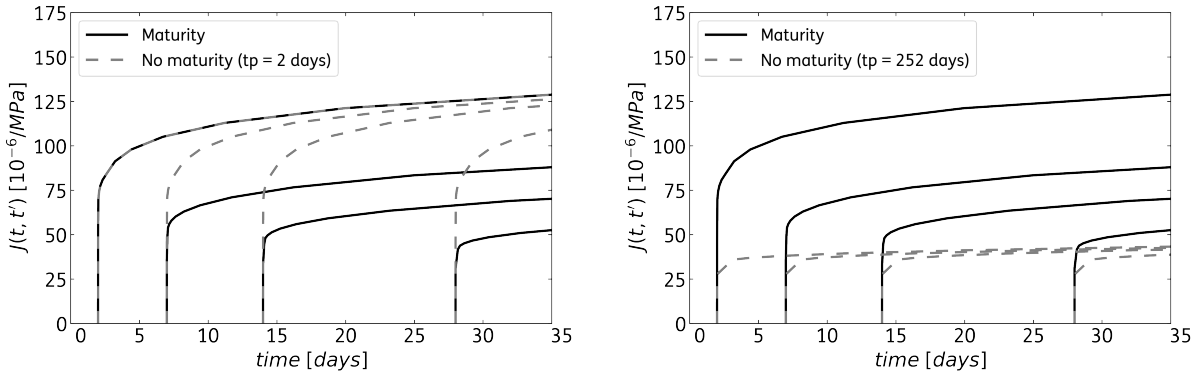

(a) Reference Analysis versus Sensitivity Analysis 7.a.

(b) Reference Analysis versus Sensitivity Analysis 7.b.

Figure 5.30: Comparison of creep compliance curves between the Reference Analysis (maturity) and the sensitivity analyses 7.a and 7.b. For Analysis 7. a, the time of loading is 2 days, and for Analysis 7.b, is 252 days.

5.5.2. Results

The results of the Sensitivity Analyses 7.a and 7.b are evaluated based on the deflections over time and the time-dependent average prestress losses after 60 years. Figure 5.31 presents the deflection over time at the midspan and the side span, with the Reference Analysis included for comparison. During the construction stage, as illustrated in Figure 5.31a, Analysis 7.a shows larger absolute deflections compared to both the Reference Analysis and Analysis 7.b. In contrast, Analysis 7.b closely mirrors the response of the Reference Analysis. The largest difference between Analysis 7.b and the Reference

Analysis occurs at the end of the construction stage. The deloading effect has a smaller impact on Analysis 7.b compared to the Reference analysis, resulting in a difference of 0.051 m (25.6%) at the start of service life. For Analysis 7.a, the difference with the Reference Analysis at this point is 0.407 m (204%).

The difference in midspan deflections between Analysis 7.a and the Reference Analysis remains consistent throughout the 60-year analysis, as shown in Figure 5.31b. In contrast, the initial difference between the Reference Analysis and Analysis 7.b diminishes over time. The gap between the results persists for approximately the first 3000 days (8.2 years). In the long term, the responses are very similar. After 60 years, the difference in midspan deflection between the Reference Analysis and Analyses 7.a and 7.b is 0.565 m (63%) and 0.011 m (1.26%), respectively.

The deflection over time at the side span is shown in Figure 5.31c. Similar to the behavior at the midspan, Analysis 7.a exhibits the largest response, while Analysis 7.b and the Reference Analysis show a similar response. At the beginning of service life, the difference in deflection between the Reference Analysis and Analyses 7.a and 7.b is 0.232 m (116%) and 0.038 m (19.1%), respectively. The 60-year analysis presented in Figure 5.31d illustrates that the difference in deflections remains consistent for all analyses. After 60 years, the difference in the side span deflection between the Reference Analysis and Analyses 7.a and 7.b is 0.219 m (262%) and 0.028 m (33.5%), respectively.

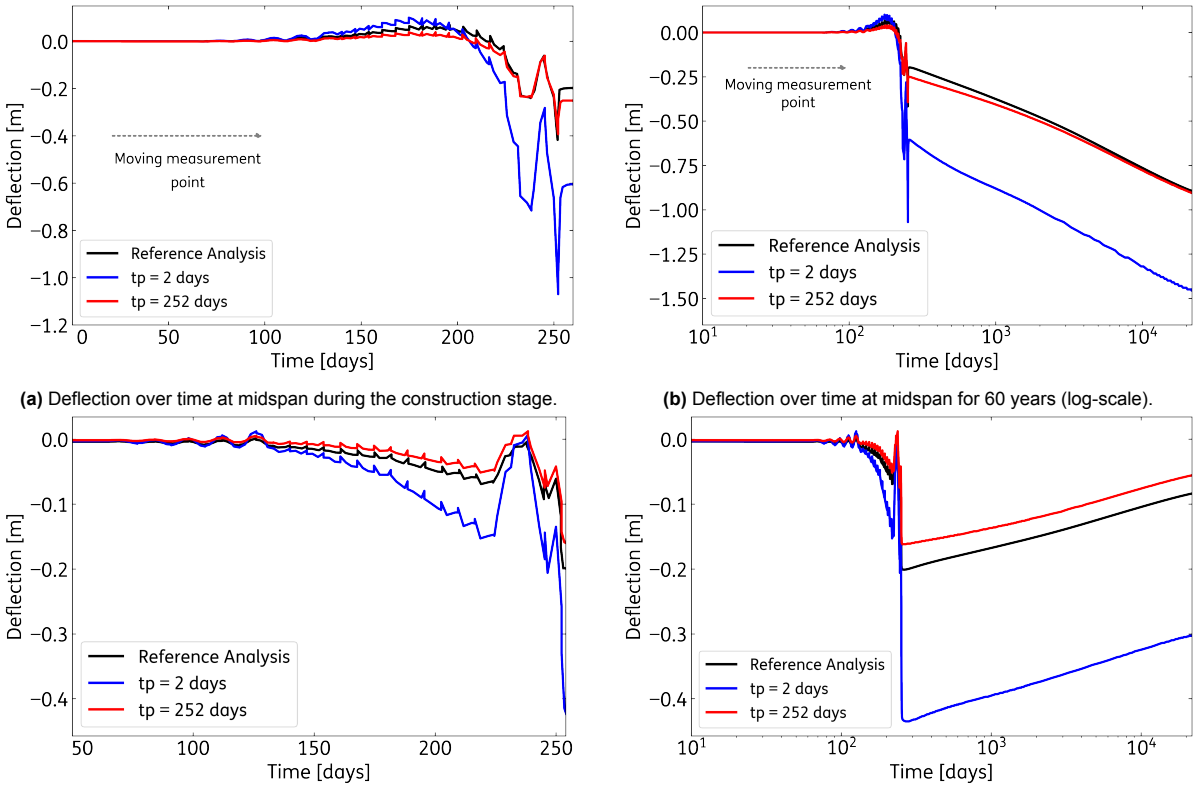

(a) Deflection over time at midspan during the construction stage.

(b) Deflection over time at midspan for 60 years (log-scale).

(c) Deflection over time at the side span during the construction stage.

(d) Deflection over time at midspan for 60 years (log-scale).

Figure 5.31: Deflection over time at midspan and side span for Sensitivity Analyses 7.a (tp = 2 days) and 7.b. (tp = 252 days). The Reference Analysis is included for comparison. A zoom window to the construction stage is included for a better visualization of the differences between analyses.

The comparison between the numerical results from Analyses 7.a and 7.b and the corrected in-situ measurements is shown in Figure 5.32. Overall, both analyses capture the trend of the in-situ data. At the midspan, as shown in Figures 5.32a and 5.32c, the average difference between Analyses 7.a and 7.b and the corrected in-situ measurements is 13.8% and 10.9%, respectively. The difference is smaller at the side span, illustrated in Figures 5.32b and 5.32d, with 3.87% (Analysis 7.a) and 5.7% (Analysis 7.b).

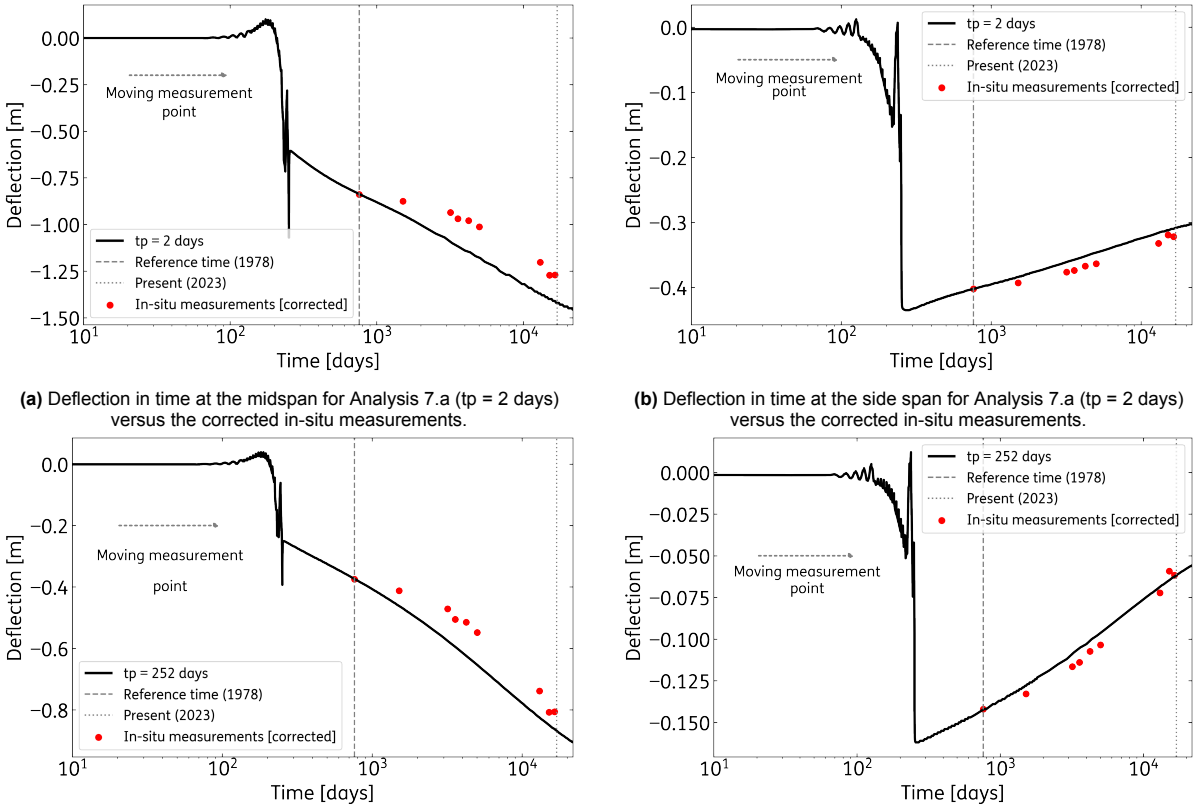

(a) Deflection in time at the midspan for Analysis 7.a (tp = 2 days) versus the corrected in-situ measurements.

(b) Deflection in time at the side span for Analysis 7.a (tp = 2 days) versus the corrected in-situ measurements.

(c) Deflection in time at the midspan for Analysis 7.b (tp = 252 days) versus the corrected in-situ measurements.

(d) Deflection in time at the side span for Analysis 7.b (tp = 252 days) versus the corrected in-situ measurements.

Figure 5.32: Comparison of the deflection for Analysis 7.a (tp = 2 days) and Analysis 7.b (tp = 252 days) with the corrected in-situ measurements (log-scale). The comparison is at the midspan and the side span.

The differences between the Reference Analysis and the Sensitivity Analyses 7.a and 7.b are also analyzed in terms of time-dependent prestressing losses, as shown in Figure 5.33. In general, both Analyses 7.a and 7.b show prestress losses similar to those of the Reference Analysis, falling within a range of 17% to 30%. The smallest losses occur at the cross-sections near the hammerhead, with an increase towards the extremes of both spans.

Analysis 7.b consistently shows lower prestressing losses than the Reference Analysis, with a difference ranging between 1% and 2% in the zone close to the hammerhead, and increasing to 2% - 5% at the extremes. On the other hand. Analysis 7.a displays the largest difference compared to the Reference Analysis in the segments near the hammerhead, approximately 5%. This difference reduces to around 1% for the segments towards the extremes.

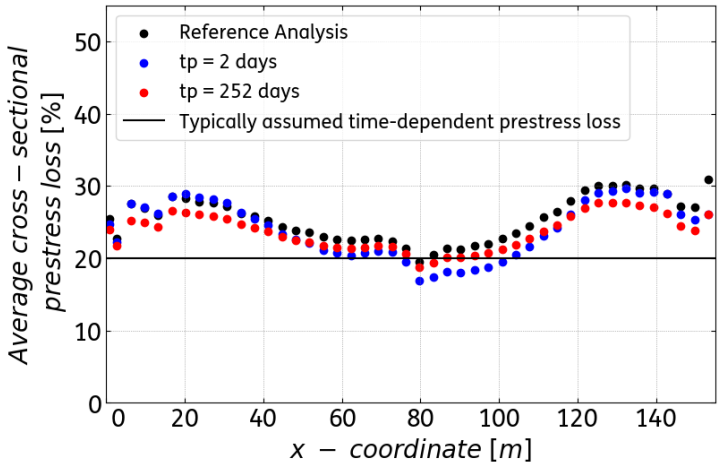

Figure 5.33: Comparison of time-dependent prestress losses between the Sensitivity Analyses and the Reference Analysis. The losses are due to creep, shrinkage, and relaxation, and they are compared with the typically assumed 20% prestress loss.

5.5.3. Interpretation of results

The aim of sensitivity Analysis 7 is to understand the impact of a maturity-independent creep model with a fixed age of loading. The overestimation of deflection by Analysis 7.a is an expected result due to differences in creep compliance compared to the Reference Analysis. However, this overestimation does not significantly translate to prestressing losses, which are lower than the Reference Analysis in the shear-critical zone and comparable to the extremes of both spans.

In contrast to the expected results from Analysis 7.a, Analysis 7.b provides interesting insights. The results from this analysis are rather similar to the Reference Analysis. The difference is only noticeable in the short term (first 10 years of service life) and becomes negligible over time. Overall, the results highlight that the long-term structural behavior of a balanced cantilever box girder bridge can be accurately described by a maturity-independent creep model with a late-age time of loading.

5.6. Impact of cross-sectional variability

Sensitivity Analysis 8 studies the impact of accounting for the variability in drying characteristics among the different segments and cross-sectional components. For this analysis, creep compliance and shrinkage strain curves are defined per cross-sectional component based on their notional size (see Annex E for the calculation of the notional size). In total, this analysis contains 47 concrete material models.

5.6.1. Variations in the analysis

Sensitivity Analysis 8 adopts a creep compliance and shrinkage strain curve per cross-sectional component: top slab, bottom slab, and webs. The top slab has a constant geometry for the full bridge, so only one concrete material model is defined for this component using a notional size of 0.387 m. The height of the webs changes along the bridge, but the variation in volume-to-surface ratio is minimal. Therefore, an average notional size of 0.502 m is used to define one material model for all the webs in the FE

model. On the other hand, the thickness of the bottom slab varies significantly along the bridge, which results in notional sizes ranging from 0.200 m to 1.14 m (see Annex E). This variation motivates the differentiation in material models for the bottom slabs per segment, resulting in 45 material models for the entire bottom slab of the bridge. So, while the Reference Analysis has only one maturity-dependent material model for the whole bridge, Analysis 8 has 47 maturity-dependent material models.

Figure 5.34 illustrates the difference in creep compliance and shrinkage strain curves for the average full cross-section, used for the Reference Analysis, and the structural components. The compliance curves for Segments 1 and 21 were chosen to illustrate the impact of thickness variation in the bottom slab. These are the thinnest and thickest bottom slab thicknesses in the FE model. The loading times chosen for illustrating creep behavior are 3 days and 28 days. The influence of thickness is more evident in the shrinkage strain curves in comparison to the creep compliance, as observed in Figure 5.34. Specifically, the shrinkage curve for the thin bottom slab of Segment 1 indicates early drying in comparison to the average shrinkage curve used in the Reference Analysis. The thick bottom slab of Segment 21 displays the opposite trend. For Segment 1, the final drying shrinkage value is reached after approximately 4000 days (equivalent to 10.9 years). In contrast, the drying rate will start to increase at this point for Segment 21. The following section will analyze the impact of these different drying characteristics on the structural response of the bridge.

5.6.2. Results

The results of the Sensitivity Analysis 8 are evaluated based on the time-dependent deflections and average prestress losses over a period of 60 years. Figure 5.35 shows the deflection in time at midspan and side span for Analysis 8 (denoted as 'non-uniform') and the Reference Analysis (denoted as 'uniform'). During construction, the differences between both analyses are small. At the end of the construction stage, however, a difference in the deloading effect due to the removal of the construction loads is clearly visible, which results in a 17.6% (0.035 m) lower deflection at the beginning of the service life period. Furthermore, the 60-year analysis at midspan shows a considerable difference between the analyses as well, both in magnitude and trend. While the Reference Analysis follows an approximately straight line (in log-scale) throughout the whole service life period, Analysis 8 shows a change in trend after approximately 4000 days (10.9 years) with a smaller deflection rate up to 10.9 years and a higher deflection rate after that. By the end of service life, the difference between the deflections in both analyses is 0.133 m (14.9%). At the side span, the 60-year analysis shows a similar trend for both analyses, with a slightly larger upward deflection for Analysis 8. The difference at the beginning of service life is 0.010 m (5.2%). By the end of service life, it is 0.006 m (7.2%).

Figure 5.36 shows the contrast between Analysis 8 and the corrected in-situ measurements at the midspan and the side span. In general, a surprisingly good agreement between the numerical results and the in-situ data is observed. Analysis 8 captures the two trends of the in-situ measurements: a gradual decrease in the short-term (first 10 years of service life), and a sharper decrease for the long-

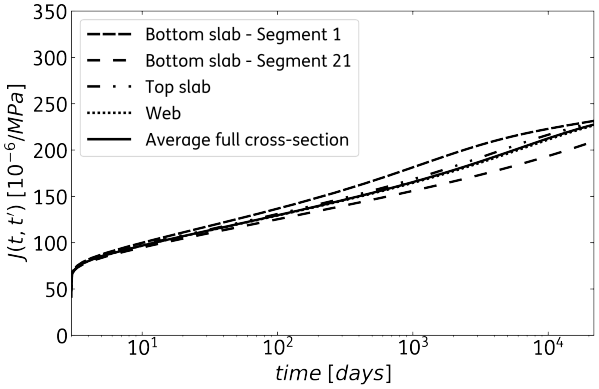

(a) Creep compliance curves for a time of loading of 3 days.

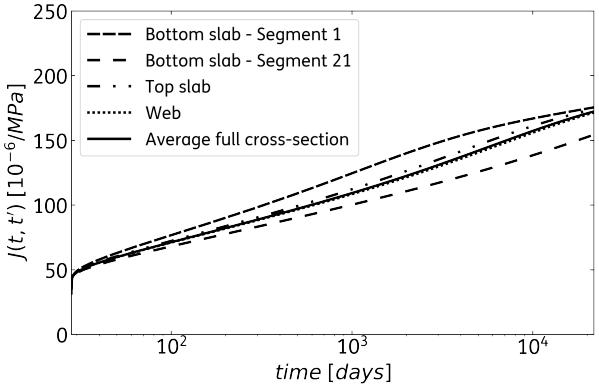

(b) Creep compliance curves for a time of loading of 28 days.

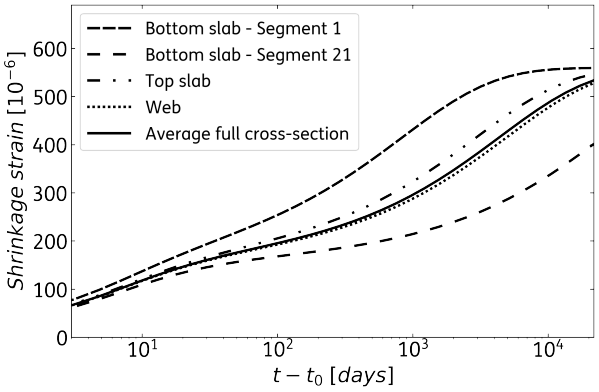

(c) Shrinkage strain curves.

Figure 5.34: Comparison of creep compliance and shrinkage strain curves between Sensitivity Analysis 8 and the Reference Analysis (log-scale). The Reference Analysis considers the full bridge to find an average notional size. Analysis 8 differentiates notional sizes for the top slab, the webs, and the bottom slab of each segment.

term (i.e. multi-decade up to the 60-year analysis endpoint). The results show an average difference of 10.0%, with Analysis 8 overestimating the deflections. At the sidespan, the linear trend of the in-situ measurements is followed closely by Analysis 8, with an average difference of 3.9%. In comparison with the latest available measurements, in April 2022, the numerical results at the midspan and side span exhibit a difference of 0.022 m (3.3%) and 0.086 m (1.2%), respectively.

The differences between the Reference Analysis and the Sensitivity Analysis 8 are analyzed in terms of time-dependent prestressing losses in Figure 5.37. Overall, there are no differences in prestressing losses between the analyses at the side span. This holds true also for the segments close to the

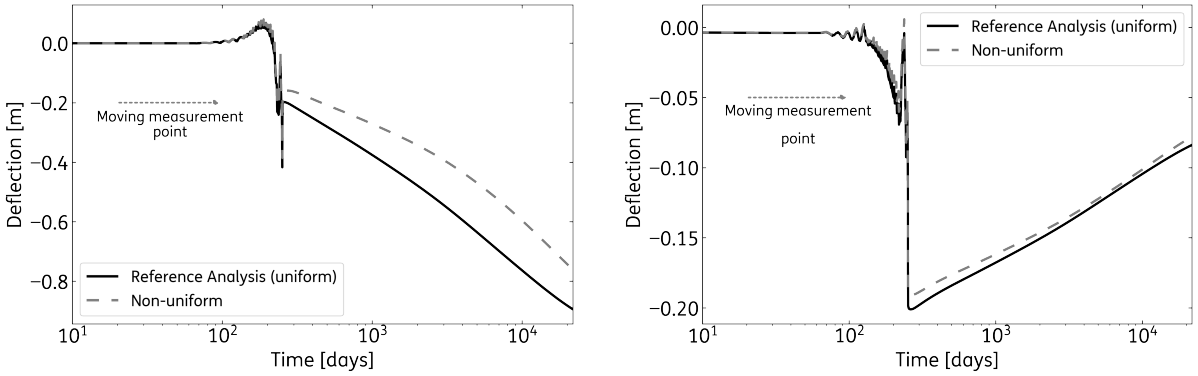

(a) Deflection in time at the midspan during 60 years.

(b) Deflection in time at the side span during 60 years.

Figure 5.35: Comparison of deflection in time between Sensitivity Analysis 8 (non-uniform) and the Reference Analysis (uniform) (log-scale).

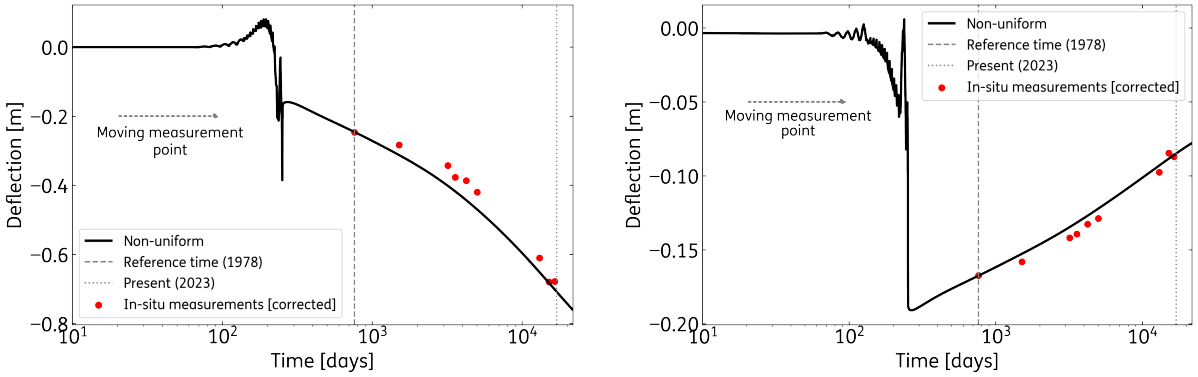

(a) Deflection in time at the midspan during 60 years versus the corrected in-situ measurements.

(b) Deflection in time at the side span during 60 years versus the corrected in-situ measurements.

Figure 5.36: Comparison of deflection in time between Sensitivity Analysis 8 (non-uniform) and the corrected in-situ measurements (log-scale).

hammerhead in the main span. The only visual difference is in the segments near midspan, with larger losses for Analysis 8. Nevertheless, the difference is no larger than 2%.

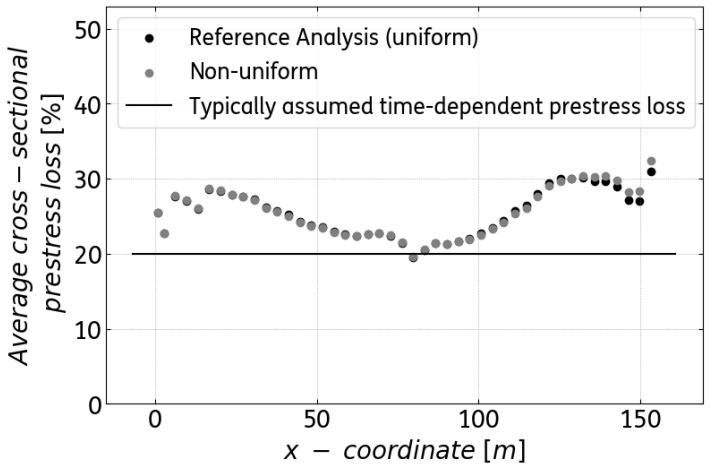

Figure 5.37: Comparison of time-dependent prestress losses between Sensitivity Analysis 8 and the Reference Analysis. The losses are due to creep, shrinkage, and relaxation, and they are compared with the typically assumed 20% prestress loss.

5.6.3. Interpretation of results

The aim of Analysis 8 is to investigate the impact of accounting for cross-sectional variability of drying characteristics in the material model. In comparison to the Reference Analysis, Analysis 8 not only predicts smaller deflections over time at midspan but also exhibits a different trend that aligns with the measured behavior of the Rooyensteinse Brug. The deflection trend at midspan starts the service life period with a gradual decrease, followed by a change in the rate to a steeper decline after approximately 4000 days (10.9 years). This phenomenon can be attributed to the difference in drying shrinkage rates between the top slab and bottom slab: the former experiences an earlier drying shrinkage compared to the latter. This difference is most pronounced in the segments close to the hammerhead, and the change in trend shows their predominant influence on midspan deflection behavior. While drying creep is also present, as seen in Figures 5.34a and 5.34b, its impact is much smaller in comparison to drying shrinkage.

The above phenomenon can be clarified from Figure 5.34c when comparing the top and bottom slab of Segment 21. In the short term (first 10 years of service life), the top slab exhibits a fast drying rate. In contrast, the bottom slab shows a slower drying rate in the form of a lag effect. This behavior causes a positive curvature, which initially reduces the midspan deflection. However, after approximately 10 years, the drying shrinkage at the top slab reaches its final value, while the rate of the bottom slab increases rapidly. Consequently, the cross-sectional drying shrinkage causes a negative curvature which increases the deflection at midspan. Even though the shrinkage strain curves for Segment 21 represent an extreme case, 29 of the 42 segments of the Rooyensteinse Brug have a thicker bottom slab than the average thickness of the top slab, which is approximately 0.4 m.

The good agreement between Analysis 8 and the corrected in-situ measurements gives confidence in its capability to predict the structural behavior in the future. An interesting question that emerges from the deflection measurements in the Rooyensteinse bridge is: how long will the current visible deflection trend continue to decrease linearly (on a logarithmic scale), and will there be a point in time when the trend will diminish? In analysis 8, the considered time period is only 60 years, i.e. up to 2038 (15 years from now). It would require a new analysis with a longer time period to answer this question with certainty, but an estimation can be done with the creep compliance and shrinkage strain curves in Figure 5.38, which cover 100 years. As can be observed in these graphs, the rate of drying creep and shrinkage begins to diminish after 60 to 65 years. This implies that the Rooyensteinse Brug will sustain its current deflection trend for approximately the next two decades.

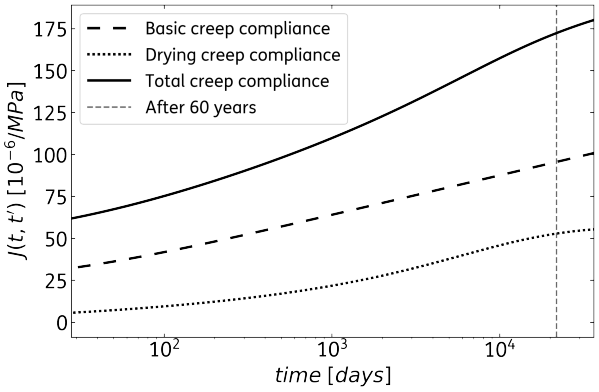

(a) Compliance function for total, basic, and drying creep at time of loading 28 days.

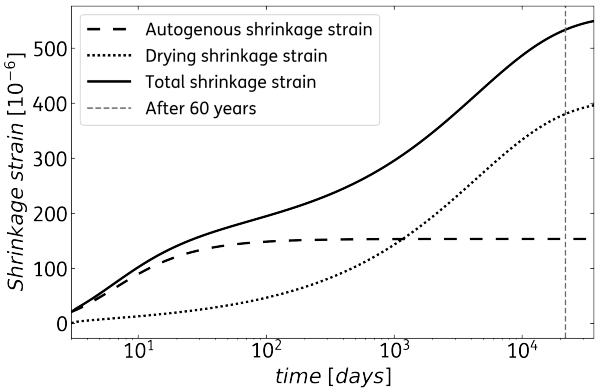

(b) Strain curve for autogenous and drying shrinkage.

Figure 5.38: Contribution of individual components in the creep compliance and shrinkage strain curves for a period of 100 years (log-scale).

6

Discussion

This chapter discusses the main findings from Chapter 5 by contrasting them with findings from existing literature (as presented in Chapter 2) and by placing them in a broader context. The discussion covers three topics: creep and shrinkage models and cross-sectional variability in drying characteristics, the impact of prestress losses in the shear capacity, and propagation of uncertainty.

6.1. Short and long-term deformations in other box girder bridges and the importance of cross-sectional variability in drying characteristics

The deflection measurements at the midspan of the Rooyensteinse Brug reveal a clear change in the trend approximately ten years after construction. This initial gradual deflection that transitions to a sharper trend over time aligns with the in-situ measurements presented in the case studies by Bažant et al. [8], Tong et al. [12], and Louman [15], and is consistently observed in measurement data from various box girder bridges worldwide [5]. The comparison between the Reference Analysis and analysis 8, as discussed in Section 5.6, showed that this change in deflection rate could likely be attributed to the variation in drying characteristics among the different components in the box girder bridge. This is a known phenomenon in literature and has already been documented 20 years ago by Kristek et. al [16].

This observed change in the deflection trend shows the importance of differentiating between short-term (i.e. first 10 years of service life) and long-term (i.e. multi-decade analysis) evaluations when assessing the performance of creep and shrinkage models in the literature. Section 5.3 compared

the deflection predictions derived from Model Code 1978 (MC78), Eurocode 2 (EC2), and the final preliminary release of Eurocode 2 (fprEC2), against the multi-decade in-situ measurements from the Rooyensteinse Brug. The results showed that MC78, EC2, and fprEC2 effectively capture the observed behavior in the short term. However, these results also revealed a significant underestimation by these models in predicting long-term behavior.

The good short-term agreement between commonly used creep and shrinkage models and in-situ measurements observed in this study aligns with findings from previous research. For instance, in the case study by Louman [15], the comparison between numerical results and in-situ measurements at midspan for the Tweede Stichtse Brug revealed that EC2 shows good agreement during the first six years of service life. Similarly, Takács [10] concluded that, for the first 8 years of service life, the numerical results with MC90 exhibited better agreement with the in-situ measurements at midspan in comparison to RILEM B3. In contrast, Tong et al. [12] reported a significant underestimation of midspan deflection for MC10 and B4 in comparison to in-situ data from the first eight years of service life. This discrepancy could be explained by their conclusion on the non-negligible cyclic creep effect induced by vehicle loads. Additionally, Bažant et al. [5] concluded that, although RILEM B3 shows a relatively closer prediction for early deflection history compared to commonly used code-based models, it, too, falls short in capturing the short-term deformations. Their case study was conducted on the Korok-Babeldaob Bridge, which exhibited midspan deflections of -0.600 m after only 1000 days (2.7 years) of service life, indicating the extreme nature of this scenario. These varying results demonstrate that the agreement between short-term in-situ data and the frequently employed code-based models in engineering practice depends on the specific conditions and characteristics of the structure under study.

The underestimation by commonly used creep and shrinkage models in the long-term can also be found in previous research but to a limited extent due to a lack of multi-decade deflection data. Bažant et al. [5] [27] conducted a multi-decade analysis based on the 18 years of deflection data from the Korok-Babeldaob Bridge. Their study showed that models like the modified Model Code 1990, which predict deflections reaching a final horizontal asymptote, underestimate long-term behavior. Additionally, their analysis concluded that the trend of the deflection curve predicted by RILEM B3 aligns with the observed deformations. These main conclusions are in accordance with the results from the Reference Analysis.

The discussion above provides two significant findings. The first one is on the importance of accounting for the cross-sectional variation in drying characteristics in a box girder bridge. This consideration has been shown to improve the accuracy of both short and long-term predictions, and it requires either a two-and-a-half-dimensional model or, if possible, special beam element types [10]. The second finding is on the importance of differentiating between short-term and long-term behavior in the evaluation of creep and shrinkage models. Accurate long-term predictions are particularly important to avoid non-conservative estimations of deflections and the associated prestress losses.

6.2. From prestress losses to their impact on shear capacity

In Chapter 5, the impact of creep and shrinkage on the time-dependent prestress losses is studied. These losses are relevant for Ultimate Limit State (ULS) verification, which includes assessment of the shear capacity. To make the outcomes of this study more tangible, the implications of the additional time-dependent prestress losses on the shear capacity are explored.

In February 2023, TNO evaluated the impact of having prestress losses greater than 20% on the shear capacity of the Rooyensteinse Brug [77]. Figure 6.1 shows the effect of the additional prestress loss on the relative reduction in concrete shear capacity $v_{rd,c,rel}$ for Segment 20 ('hoge doorsnede'). The standards used for this analysis are RBK 1.2.1 (RBK) [78], the current Eurocode 2 (EC2) [50], and a preliminary release of the new Eurocode 2 (prEC2). prEC2 provides two equations for determining the contribution of concrete to the shear capacity: Equation (8.16) (Eq. (8.27) in fprEC2 [51]) and Equation (8.21) (Eq. (8.32) in fprEC2 [51]). Both are included in the analysis.

The results of the Reference Analysis, presented in Section 5.2 and Figure 5.21, show that after 60 years the time-dependent prestress losses of Segment 20 are 22.4%. As shown in Figure 6.1a, this leads to a 4% reduction in concrete shear capacity according to RBK and a 2% reduction as per Eq. (8.16) of prEC2. The remaining two standards show no impact. For the total shear capacity, the reduction according to Figure 6.1b is 1% with RBK, while EC2 and fprEC2 show no impact.

The impact of the additional time-dependent prestress loss can also be calculated using the results of Analysis 5 (upper bound), presented in Section 5.4 and Figure 5.29. For Segment 20, the time-dependent prestress loss with Analysis 5 is 30.5%. This leads to a 9% reduction in the concrete contribution according to RBK, and a 4% reduction based on Eq. 8.16 of prEC2. The total shear capacity is reduced by 4% according to RBK.

The discussion above shows that while the reduction in the shear capacity is limited when using mean values, it may become non-negligible when considering the present large uncertainties in creep and shrinkage models. The current upper bound analysis is a simplified and possibly overly conservative estimate, as it assumes the worst-case scenario of both creep and shrinkage curves simultaneously. Nevertheless, this exploration shows that acknowledging the uncertainties in the creep and shrinkage models will likely result in a reduction in the shear capacity. To determine the extent of this reduction, a more comprehensive probabilistic analysis is required.

6.3. Why uncertainties cannot be neglected

Generally, design codes account for all relevant uncertainties by considering characteristic values and partial factors to ensure safety requirements are met. Remarkably, this practice does not appear to extend to creep and shrinkage. Based on findings from box girder bridge re-assessments and private communications, it is noticed that in practice a time-dependent prestress loss of 20% is commonly assumed for Ultimate Limit State (ULS) verifications; the basis for this assumption remaining unclear. The analyses using mean values with MC78, EC2, and fprEC2 showed that the 20% assumption may

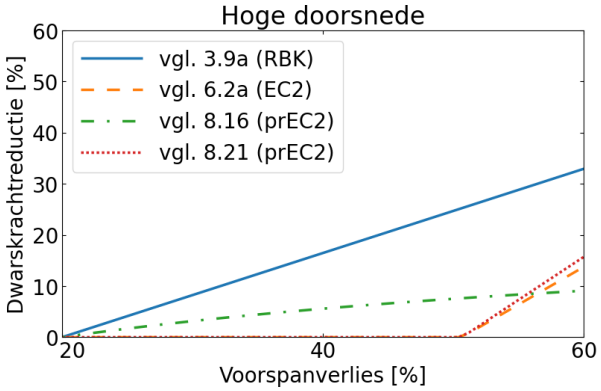

(a) Relative shear capacity reduction in the concrete (*Dwarskrachtreductie*) $v_{rd,c,rel}$ versus the additional prestress loss (*Voorspanverlies*) [77].

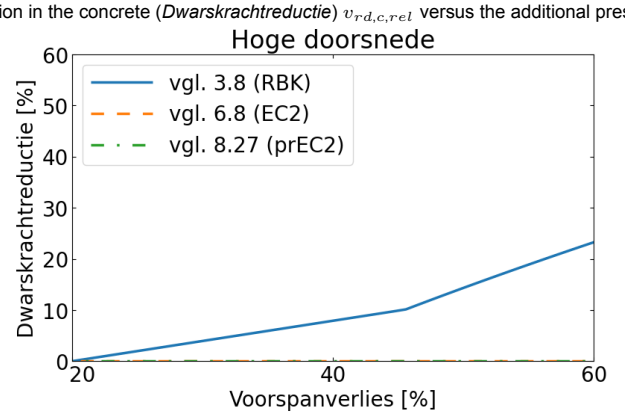

(b) Relative total shear capacity reduction (*Dwarskrachtreductie*) $v_{rd,rel}$ versus the additional prestress loss (*Voorspanverlies*) [77].

Figure 6.1: Relative reduction in shear capacity versus the additional prestressing losses for Segment 20 of the Rooyensteinse Brug.

be indeed a conservative value for long-term prestress losses (see Section 5.3). However, the uncertainties in creep and shrinkage models are large, typically with coefficients of variation above 20% for creep, and above 30% for shrinkage [10].

The results from this case study imply that neglecting the uncertainties in creep and shrinkage is a non-conservative approach. When adopting mean values, the prestress losses with the most accurate model (Analysis 8 using RILEM B4) fall within the range of 20 and 25% for shear-critical zones of the bridge. Moreover, Sections 5.4 and 6.2 show the substantial and non-negligible impact on the structural response of the bridge, the prestress losses, and the shear capacity, when accounting for uncertainties in the B4 Model. In essence, the findings of this case study emphasize the need to re-evaluate the treatment of creep and shrinkage in the re-assessment of creep-sensitive structures, such as box girder bridges. Long-term creep and shrinkage effects should be based on accurate models (e.g. RILEM B4) and should include model uncertainties.

Prior studies have also delved into the implications of incorporating uncertainty into the calculation of the deflection response. For example, Bažant et al. [5] have proposed a simple approach for obtaining upper and lower bounds for the 95% confidence limit, based on the coefficient of variation of the input parameters for the B3 model. Similarly, Takács [10] employed a Monte Carlo simulation to account for uncertainty in various factors, including creep, shrinkage, concrete strength, relative humidity,

temperature, and effective prestressing force with MC90. An interesting way forward is the utilization of Bayesian model updating, as done by Jia et. al. [23]. This study is about updating the prior knowledge on the uncertainties in creep and shrinkage models by considering the deformation measurements of a bridge over time. By propagating the posterior distribution of model uncertainties into the predictions of long-term deformations, a significant reduction in the uncertainty band is achieved. This reduction in uncertainty will also further propagate into the estimation of prestress losses, consequently resulting in a lower impact on shear capacity. In summary, Bayesian model updating is an interesting approach for the re-assessment of existing critical box girder bridges. Furthermore, all these studies agree that designing for a confidence limit instead of a mean value can help minimize the risk of unexpected deflections during service life.

7

Conclusions and Recommendations

7.1. Conclusions

This study aimed to improve the understanding of the long-term time-dependent behavior of balanced cantilever prestressed concrete bridges. The investigation focused on determining whether the long-term effects of creep and shrinkage provide a reasonable explanation for the excessive deformations observed in several bridges worldwide. The research followed a case study approach, working with the Rooyensteinse Brug, a bridge opened in 1977 that exhibits this ongoing trend of excessive deformations. To investigate this behavior, a detailed two-and-a-half-dimensional finite element (FE) model was developed, incorporating a time-dependent phased analysis accounting for the construction phases. The novelty of this FE model lies in its capacity to account for creep and shrinkage effects during the construction phase. Thereby, providing accurate predictions for the deflection and prestress losses at the beginning of service life, and also correctly accounting for the initial effects of creep and shrinkage on the long-term behavior of the bridge. A series of sensitivity analyses were conducted to assess the impact of different creep and shrinkage models, cross-sectional variability, maturity effects, and propagation of uncertainty. The main findings, specific to the Rooyensteinse Brug case study, are presented in Chapter 5, and allow us to go back to the main research question introduced in Chapter 1:

What are the long-term (i.e. multi-decade) effects of creep and shrinkage on the structural behavior of balanced cantilever prestressed concrete bridges?

The main research question is addressed by answering the four sub-questions posed at the start of this research. The conclusions for each sub-question are first summarized in a brief paragraph highlighting the main outcomes, followed by a more detailed explanation.

Which code-based models for creep and shrinkage are suitable to describe the long-term behavior of balanced cantilever prestressed concrete bridges?

The RILEM B4 model, used in the Reference Analysis, was the only creep and shrinkage model able to capture the long-term deflection trend observed in the in-situ measurements of the Rooyensteinse Brug. In contrast, commonly used code-based models, including the current and future Eurocode 2 standards, fail to explain these deflections, displaying notable underestimations.

In the short term (first 10 years of service life), MC78, EC2, and fprEC2 predicted average deflections at midspan and side span of 0.035 m (6.7%) and 0.012 m (6.3%) respectively, when compared to corrected in-situ measurements. In contrast, the B4 model (Reference Analysis) overestimated the deflections at midspan and side span by 0.106 m (23.9%) and 0.010 m (6.8%), respectively. In the long term (multi-decade), MC78, EC2, and fprEC2 underestimated midspan deflections by 0.238 m (30.2%), and side span deflections by 0.048 m (34.3%). Conversely, the long-term prediction with B4 resulted in a difference of 0.096 m (14.9%) and 0.006 m (4.9%) for midspan and side span, respectively.

The limitations of MC78 and EC2 in describing the long-term deflection trend come from the asymptotic behavior of the creep compliance and shrinkage strain curves, which reach a final value. While fprEC2 does not exhibit the same asymptotic behavior, the magnitude of the creep and shrinkage curves remain comparable to MC78 and EC2. In contrast, the non-asymptotic behavior of the creep compliance curve, due to basic creep, and shrinkage strain curve, due to drying shrinkage, makes B4 a model capable of capturing the ongoing trend of excessive deformations.

What are the important aspects to be considered for an accurate modeling of long-term creep and shrinkage effects in balanced cantilever prestressed concrete bridges, and how can they be addressed in a finite element model?

Analysis 8 demonstrated that by accounting for the cross-sectional variability of drying characteristics, both the initial and multi-decade deflections of the Rooyensteinse Brug can be accurately described. Moreover, the results from Analysis 7 showed that for a multi-decade analysis, a maturity-independent creep model with a late age of loading is sufficient to capture the long-term behavior of the bridge.

Accounting for cross-sectional variability in the creep compliance and shrinkage strain curves has proven to be crucial for capturing the initial deflection history of the Rooyensteinse Brug. This consideration has resulted in an improvement in the short-term average deflection prediction at midspan, reducing the difference from 0.106 m (23.9%) to 0.049 m (13.9%) when compared to the corrected in-situ measurements. The improvement is also reflected in the long-term prediction, with a decrease in the difference from 0.096 m (14.9%) to 0.031 m (6.1%). To conduct an analysis accounting for cross-sectional variability, a two-and-a-half-dimensional model where the top slab, bottom slab, and webs are modeled independently for each segment is required.

The difference in midspan deflections between the Reference Analysis and Analysis 7.b is 0.052 m (26.1%) at the beginning of service life, and it reduces to 0.011 m (1.2%) over the 60-year analysis.

This shows that the influence of a maturity-based creep model is the most relevant in the short term (first 10 years of service life). After that period, the response is similar to that of a maturity-independent creep model with a late age of loading. Therefore, for analyzing the trend of multi-decade deflections, a simpler approach involving a single creep compliance curve would suffice.

What is the impact of long-term creep and shrinkage effects on the deformation, prestress losses, and moment redistribution in balanced cantilever prestressed concrete bridges?

The numerical results predict that the current deflection trend will continue to decrease linearly (log-scale) for the next two decades. Additionally, the findings showed that the typically assumed time-dependent prestressing loss of 20% is not a conservative approach. Analyses 5 and 6 showed that the uncertainty inherent in the RILEM B4 model should not be neglected.

Analysis 8, which accounts for the cross-sectional variability, resulted in the most accurate short and long-term deflection prediction when compared to the corrected in-situ measurements. According to this analysis and the creep and shrinkage curves with B4, the current deflection trend will continue to decrease linearly (log-scale) for the next two decades. Beyond this point, B4 predicts a slowing rate of deflection decrease as the drying shrinkage rate diminishes. The results of this analysis predict a negative deflection at midspan of 0.515 m in 15 years from now. Nevertheless, the impact of the deflection increase in the average cross-sectional prestress losses is minimal, with an increase of less than 1%.

The results from Analysis 8 also show that for the shear-critical zone, the prestress losses range between 20% and 25%. This means that the typically assumed time-dependent prestressing loss of 20% is neither a significant underestimation nor a conservative estimate of the losses after 60 years. Furthermore, an exploratory analysis on the impact of prestress losses on the shear capacity showed that for segments in the shear-critical zone, the losses lead to a reduction in shear capacity of less than 5%.

The phenomenon of moment redistribution (Kist-effect) becomes evident when comparing the moment line at the beginning and end of service life. The initial positive moment at midspan, attributed to the continuity tendons, diminishes to zero within the first four years of service life. Beyond this point, it continues to decrease, resulting in a negative bending moment. These results show the potential occurrence of cracking at midspan.

When the uncertainties in the creep and shrinkage model (B4) are acknowledged, a large impact on the predicted deformations and prestress losses can be observed. Using the bounds of the 90% credible interval, the midspan deflections after 60 years range between 0.514 m and 2.91 m, compared to a mean of 0.895 m. The prestress losses range between 18% and 30% in the shear-critical zone, against a mean of 23%. Uncertainty is not commonly considered in design or assessment, but the results show that it cannot be neglected.

To what extent can time-dependent structural finite element analysis help to investigate the hypothesis of long-term effects of creep and shrinkage causing the excessive deformations of balanced cantilever prestressed concrete bridges in the Netherlands?

This thesis demonstrates the capacity of a state-of-the-art creep and shrinkage model (B4) that accounts for cross-sectional variability, in combination with a detailed FE model and a time-dependent phased analysis, to replicate the excessive deformations observed in this case study. The results not only provide insights into this unexpected behavior but also give confidence for future predictions.

Based on the answers given to the research sub-questions above, this study ultimately shows that observed deflections in the Rooyensteinse brug can be reasonably explained by the long-term effects of creep of shrinkage.

7.2. Recommendations

7.2.1. Recommendations for further research

Based on the results and conclusions from this study, the following recommendations for future research are proposed.

- With the current finite element (FE) model, an extension of the sensitivity study conducted in this thesis is recommended. Specifically, it would be beneficial to conduct two separate analyses focusing on the individual contributions of creep and shrinkage to the overall deflection prediction. Additionally, a non-uniform analysis using the fprEC2 is proposed to assess whether the prediction trend changes compared to Analysis 4. Furthermore, an analysis that accounts for prediction error with fprEC2 should be explored to examine how uncertainty propagates with the approach recommended by this standard.
- The FE model presented in this thesis can benefit from two main improvements. First, the effects of relaxation were simplified by assuming a corresponding loss after 60 years and applying it to the initial prestressing force. The next phase should involve implementing relaxation as a time-dependent phenomenon alongside creep and shrinkage. This approach not only offers a more realistic representation but also prevents the underestimation of creep due to the application of reduced prestressing forces. Second, the possibility of concrete crushing and cracking at midspan shown by the maximum and minimum principal stresses σ_1 and σ_3 call for further investigation. To gain more understanding of the stress distribution at midspan and assess the implications of applying symmetry, the subsequent model should incorporate crushing and cracking.
- It is recommended to develop a 1D beam model, commonly used for assessment in practice. A comparison between this model and the detailed 2 1/2D model developed in this thesis can provide insights into the implications of a simpler approach.
- It is recommended to extend the methodology and tools developed in this thesis to another case study, preferably a balanced cantilever bridge exhibiting deflection trends that do not indicate ex-

cessive deformations. This comparative study can provide valuable insights into the applicability of the modeling approach with the B4 model in scenarios where excessive deflections are not a primary concern.

7.2.2. Recommendations for practice

Considering the research outcomes and their practical implications, the following recommendations are suggested for improving the current practices in the assessment and design of balanced cantilever prestressed concrete bridges.

- Commonly used code-based models, including the current standard for the design of concrete structures EC2, underestimate the long-term response of the Rooyensteinse Brug. Therefore, for the assessment of balanced cantilever bridges, it is recommended to use a theoretically grounded model like B4. Furthermore, the cross-sectional variability at a segment-component level should be accounted for in the analysis.
- Uncertainty should be acknowledged in both design and assessment practices. This can involve the use of simple rules, such as adopting an assumption higher than the typical value of 20% for time-dependent prestress losses, or more detailed approaches like those recommended by the B4 Model. While creep and shrinkage are typically considered during the serviceability limit state, it is essential to address their impact on prestress losses in the context of ultimate limit state assessments.
- The high uncertainty on long-term prediction of creep and shrinkage can be reduced by recalibrating the creep compliance and shrinkage strain curves with short-term tests, which is recommended for creep-sensitive structures. Furthermore, a model update approach using bridge deflection data can help reduce the uncertainty further, resulting in upper and lower bounds more practical for design and assessment.

References

[1] G. Sauvageot. “Segmental Concrete Bridges”. In: *Bridge Engineering Handbook*. Ed. by W.-F. Chen and L. Duan. CRC Press, 2000.

[2] C. Menn. *Prestressed Concrete Bridges*. Basel: Birkhauser, 1990.

[3] G. Sauvageot et al. *Bridge Engineering Handbook*. Ed. by W.-F. Chen and L. Duan. CRC Press, 2000.

[4] RILEM Technical Committee TC-242-MDC. “RILEM draft recommendation: TC-242-MDC multi-decade creep and shrinkage of concrete: material model and structural analysis”. In: *Materials and Structures* 48 (2015), pp. 753–770. DOI: https://doi.org/10.1617/s11527-014-0485-2.

[5] Z. P. Bažant, Q. Yu, and G.-H. Li. “Excessive Long-Time Deflections of Prestressed Box Girders: I. Record-Span Bridge in Palau and Other Paradigms”. In: *Journal of Structural Engineering* 138 (2012). DOI: 10.1061/(ASCE)ST.1943-541X.0000487.

[6] Nicky Reybrouck. “Modelling of the Long-Term Behaviour of Reinforced and Prestressed Concrete Beams Based on Extensive Experimental Research”. Faculty of Engineering and Architecture Ghent University, 2020.

[7] C. van der Veen. *Doorgaande deformatie van uitbouwbruggen*. Technische Universiteit Delft, 2022.

[8] Z. Bažant et al. “Pervasive lifetime inadequacy of long-span box girder bridges and lessons for multi-decade creep prediction”. In: 2013.

[9] E. Lantsoght et al. “Long-term material and structural behavior of high-strength concrete cantilever bridge: Results of 20 years monitoring”. In: *Structural Concrete* 19.4 (2018), pp. 1079–1091. DOI: https://doi.org/10.1002/suco.201700214.

[10] P. Takács. “Deformations in Concrete Cantilever Bridges: Observations and Theoretical Modelling”. Department of Structural Engineering Norwegian University of Science and Technology, 2002.

[11] Rijkswaterstaat. *Beeldarchief Rijkswaterstaat: Maasbrug Wessem*. 1963. URL: https://www.archieven.nl/nl/zoeken?mivast=0&miadt=2606&mizig=269&miview=gal&milang=nl&micols=1&mizk_alle=Maasbrug%20Wessem (visited on 09/16/2023).

[12] T. Tong et al. “Long-term performance of prestressed concrete bridges under the intertwined effects of concrete damage, static creep and traffic-induced cyclic creep”. In: *Engineering Structures* 127 (2016), pp. 510–524. DOI: https://doi.org/10.1016/j.engstruct.2016.09.004.

[13] Z. Bažant, M. Hubler, and Q. Yu. “Pervasiveness of Excessive Segmental Bridge Deflections: Wake-up Call for Creep”. In: *ACI Structural Journal* 108 (2011), pp. 766–774.

[14] S. Akbar and M. Carlie. “Long-term deformation of balanced cantilever bridges due to non-uniform creep and shrinkage”. Department of Civil and Architectural Engineering KTH Royal Institute of Technology, 2021.

[15] F.G. Louman. “Realistische simulate vervormingen uitbouwbruggen”. Technische Universiteit Delft, 2005.

[16] V. Křístek et al. “Box Girder Bridge Deflections: Why is the initial trend deceptive?” In: *Concrete International* 28 (2006), pp. 55–63.

[17] R. Wendner, M. Hubler, and Z. Bažant. “The B4 model for multi-decade creep and shrinkage prediction”. In: *Ninth International Conference on Creep, Shrinkage, and Durability Mechanics* (2013). DOI: 10.1061/9780784413111.051.

[18] Wagemaker. “Rooyensteinse Brug Herberekening”. In: (2020).

[19] Comité Euro-International du Béton (CEB). “Evaluation of the Time Dependent Behavior of Concrete”. In: *Comité Euro-International du Béton (CEB)* (1990).

[20] ACI Committee 209. “ACI 209R-92: Prediction of Creep, Shrinkage, and Temperature Effects in Concrete Structures”. In: (1982).

[21] Fédération internationale du béton (fib). *Model Code 2020*. 2020.

[22] Netherlands Organisation for Applied Scientific Research. *DIANA FEA BV*. Version 10.6. Oct. 11, 2022. URL: https://dianafea.com/.

[23] S. Jia B. Han W. Ji H. Xie. “Bayesian inference for predicting the long-term deflection of prestressed concrete bridges by on-site measurements”. In: *Construction and Building Materials* 320 (2022).

[24] N. Hewson. *Prestressed Concrete Bridges - Design and Construction*. 2nd ed. ICE Publishing, 2012.

[25] Y. Yang. *Concrete Bridges: Balanced Cantilever*. Delft University of Technology, 2018.

[26] R. Malm and H. Sundquist. “Time-dependent analyses of segmentally constructed balanced cantilever bridges”. In: *Engineering Structures* 32.4 (2010), pp. 1038–1045. DOI: https://doi.org/10.1016/j.engstruct.2009.12.030.

[27] Z. P. Bažant, Q. Yu, and G.-H. Li. “Excessive Long-Time Deflections of Prestressed Box Girders: II. Numerical Analysis and Lessons Learned”. In: *Journal of Structural Engineering* 138 (2012). DOI: 10.1061/(ASCE)ST.1943-541X.0000375.

[28] J. Crow. “The concrete conundum”. In: *Chemistry World* (2008), pp. 62–66.

[29] Z. Bažant ad F. Wittmann. *Creep and Shrinkage in Concrete Structures*. Ed. by Z. Bažant and F. Wittmann. John Wiley Sons, 1982.

[30] H. Rüsch, D. Jungwirth, and H. Hilsdorf. *Creep and Shrinkage: Their Effect on the Behavior of Concrete Structures*. 1st ed. New York: Springer-Verlag, 1983.

[31] ACI Committee 209. “ACI 209.1R-05: Report on Factors Affecting Shrinkage and Creep of Hardened Concrete”. In: (2005).

[32] Z. P. Bažant and X. Yunping. “Drying creep of concrete: constitutive model and new experiments separating its mechanisms”. In: *Materials and Structures* 27 (1994).

[33] F.H. Wittmann. “Chapter 6: Creep and Shrinkage Mechanisms”. In: *Creep and Shrinkage in Concrete Structures*. Ed. by Z. Bažant and F. Wittmann. John Wiley Sons, 1982.

[34] R. Gilbert A. Castel I. Khan W. South J. Mohammadi. “An Experimental Study of Autogenous and Drying Shrinkage”. In: *High Tech Concrete: Where Technology and Engineering Meet*. Ed. by M. Hordijk D. Luković. CRC Springer, 2018.

[35] W. Lyu. “ffect of micro-cracking and self-healing on long-term creep and strength development of concrete”. Delft University of Technology, 2020. DOI: 10.4233/uuid:8389892d-f54c-4a35-ab18-7809f011c1f6.

[36] Z. Bažant. “Chapter 7: Mathematical Models for Creep and Shrinkage of Concrete”. In: *Creep and Shrinkage in Concrete Structures*. Ed. by Z. Bažant and F. Wittmann. John Wiley Sons, 1982.

[37] ACI Committee 213. “ACI 213R-03: Guide for Structural Lightweight-Aggregate Concrete”. In: (2003).

[38] Mauricio Lopez. “Creep and shrinkage of high-performance lightweight concrete: a multi-scale investigation”. Georgia Institute of Technology, 2005.

[39] A. Neville. *Creep of Concrete: Plain, Reinforced and Prestressed*. 1st ed. Amsterdam: North-Holland Publishing Company - Amsterdam, 1970.

[40] Z. Bažant Y. Xi S. Baweja I. Carol. “Preliminary guidelines and recommendations for characterizing creep and shrinkage in structural design codes”. In: *Proc. 5th International RILEM Symposium on Creep and Shrinkage of Concrete (ConCreep 4)*. Barcelona: E FN Spon, 1993.

[41] R.M. Mors. “Autogenous Shrinkage: Cementitious materials containing BFS”. Delft University of Technology, 2011.

[42] G.L. England. “Creep and temperature effects in concrete structures: reality and prediction”. In: *Applied Mathematics Modelling* (1980).

[43] Comité Euro-International du Béton (CEB). *CEB-FIP Model Code For Concrete Structures*. 1978.

[44] Comité Euro-International du Béton (CEB). *CEB-FIP Model Code 1990 For Concrete Structures*. 1990.

[45] fib. *History*. n.d. URL: https://www.fib-international.org/federation/history.html (visited on 09/17/2023).

[46] Comité Euro-International du Béton (CEB). “CEB Design Manual on Structural Effects of Time-Dependent Behaviour of Concrete”. In: *Comité Euro-International du Béton (CEB)* (1984).

[47] Fédération internationale du béton (fib). *Model Code 2010*. 2010.

[48] fib international. *fib Model Code (2020)*. 2023. URL: https://www.fib-international.org/news/501-fib-model-code-2020.html (visited on 06/23/2023).

[49] European Commission <OR> I. Surname, I. Surname, and I. Surname. *Eurocode 2: Design of concrete structures*. URL: https://eurocodes.jrc.ec.europa.eu/EN-Eurocodes/eurocode-2-design-concrete-structures.

[50] EN. *EN 1992-1-1: Eurocode 2: Design of concrete structures - Part 1-1: General rules and rules for buildings*. 2004.

[51] EN. *Eurocode 2: Design of concrete structures - Part 1-1: General rules and rules for buildings, bridges and civil engineering structures*. 2004.

[52] Z. Bažant and L. [Panula]. “Practical prediction of time-dependent deformations of concrete, Parts I-VI”. In: *Materials and Structures* (1978).

[53] Z. Bažant J. Kim L. Panula. “Improved prediction model for time dependent deformations of concrete, Parts 1-5”. In: *Materials and Structures* (1991).

[54] Z. Bažant and S. Baweja. “Justification and refinements of Model B3 for concrete creep and shrinkage - 1. Statistics and sensitivity”. In: *Materials and Structures* (1995).

[55] M. Wyrzykowski. “MS highlight: Bažant and Baweja (1995), Creep and shrinkage prediction model for analysis and design of concrete structures—model B3”. In: *Materials and Structures* (2022). DOI: https://doi.org/10.1617/s11527-021-01862-z.

[56] Z. Bažant R. Wendner M. Hubler. “NU Database of Multi-Decade Creep Deflections of Bridges”. In: *Northwestern University* (2013).

[57] Z. Bažant and M. Jirásek. *Creep and Hygrothermal effects in concrete structures*. Springer, 2018.

[58] DIANA Finite Element Analysis. *Theory Manual DIANA 10.7*. Oct. 1, 2023. URL: https://manuals.dianafea.com/d107/en/1181807-1181807-theory-107.html.

[59] Z. P. Bažant. “Material Models for Structural Creep Analysis”. In: John Wiley Sons Ltd, 1988. Chap. 2.

[60] C. Best M. Polivka. “Creep of lightweight concrete”. In: *Magazine of Concrete Research* 11 (1959), pp. 129–134.

[61] R. Szydlowski B. Labuzek. “Experimental Evaluation of Shrinkage, Creep and Prestress Losses in Lightweight Aggregate Concrete with Sintered Fly Ash”. In: *Materials* (2021).

[62] Z. Wang X. Li L. Jiang M. Wang Q. Xu K. Harries. “Long-term performance of lightweight aggregate reinforced concrete beams”. In: *Construction and Building Materials* 264 (2022).

[63] A. Akhnoukh. “Internal curing of concrete using lightweight aggregates”. In: *Particulate Science and Technology* 36 (2017). DOI: 10.1080/02726351.2016.1256360.

[64] X. Zheng Y. Zhai S. Zhan S. Song. “Internal relative humidity and drying shrinkage of lightweight aggregate concrete”. In: *Key Engineering Materials* 629-630 (2014).

[65] J. Browning D. Darwin D. Reynolds B. Pendergrass. “Lightweight Aggregate as Internal Curing Agent to Limit Concrete Shrinkage”. In: *ACI Materials Journal* (2011).

[66] S. Hong J. Choi T. Yuan Y. Yoon. “A review on concrete creep characteristics and its evaluation on high-strength lightweight concrete”. In: *Journal of Materials Research and Technology* (2023).

[67] S. Labbé M. Lopez. “Towards a more accurate shrinkage modeling of lightweight and infra-lightweight concrete”. In: *Construction and Building Materials* 246 (2020).

[68] *Berekening Rooyeinsteinse Brug*. 1975.

[69] Ministerie van Verkeer en Waterstaat. “Bestek en Voorwaarden Nr. BR/6994”. In: (1975).

[70] “Kubusdruksterktemetingen Rooyensteinsebrug”. In: (1976).

[71] Witteveen + Bos. “Materiaalonderzoek 39D-103-01 - Rooyensteinsebrug”. In: (2011).

[72] H.J.C. van den Broek U. van den Hoonaard. “De nieuwe brug over de IJssel bij Zutphen”. In: *Cement* (1975).

[73] D. D. Magura M. A. Sozen C. P. Siess. “A Study of Stress Relaxation in Prestressing Reinforcement”. In: *PCI* 9 (1964), pp. 13–57.

[74] Regionaal Archief Rivierenland. *M 4228*. Oct. 10, 2023. URL: https://regionaalarchiefrivierenland.nl/archieven?mizig=293&miadt=102&miaet=14&micode=0670&minr=2804448&miview=ldt.

[75] R. Wendner M. Hubler Z. Bažant. “Statistical justification of model B4 for multi-decade concrete creep using laboratory and bridge databases and comparisons to other models”. In: *Materials and Structures* 48 (2015), pp. 815–833.

[76] M. Hubler R. Wendner Z. Bažant. “Statistical justification of Model B4 for drying and autogenous shrinkage of concrete and comparisons to other models”. In: *Materials and Structures* 48 (2015), pp. 797–814.

[77] B. Brongers H. Burggraaf G. Dieteren G. Eumelen A. Martinez A. Slobbe R. Tai. *Problematiek kokerbruggen*. TNO, 2023.

[78] J. Doorgeest H. Sliedrecht. “RTD1006 - Richtlijn beoordeling kunstwerken (RBK) version 1.2”. In: *Rijkswaterstaat* (2022).

[79] B. Espion P. Halleux. “Long Term Behavior of Prestressed and Partially Prestressed Concrete Beams: Experimental and Numerical Results”. In: *Computer Analysis of the Effects of Creep, Shrinkage, and Temperature Changes on Concrete Structures* (1991).

Appendices

A

Location of reference points

The following annex presents the location of the reference points used for the in-situ measurements of the Rooyensteinse Brug.

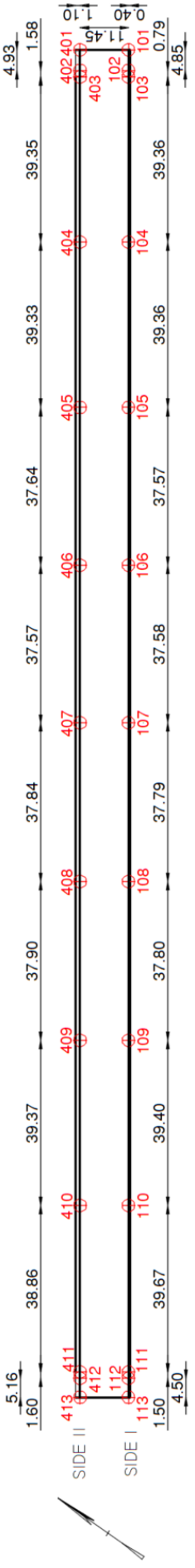

Figure A.1: Reference points on the deck of the Rooyensteinse Brug.

B

Sensitivity study on input parameters for creep and shrinkage

The following annex presents the remaining plots of the sensitivity study presented in Chapter 2 for the creep compliance and shrinkage strain curves.

B.1. Effect of temperature of environment

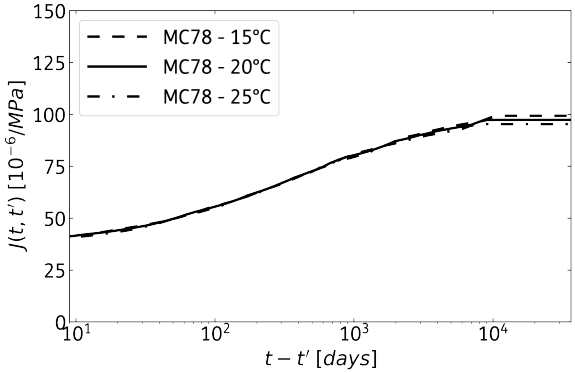

(a) Comparison of creep compliance curves for MC78 at *t'* of 28 days.

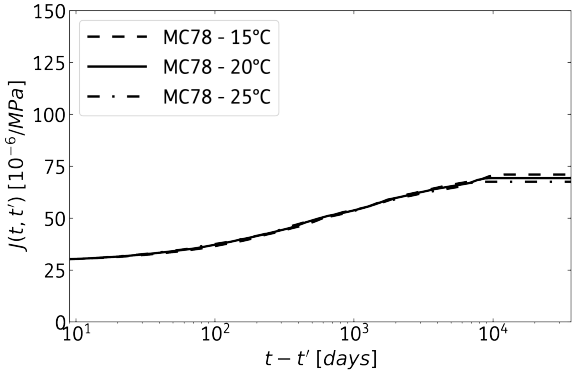

(b) Comparison of creep compliance curves for MC78 at *t'* of 250 days.

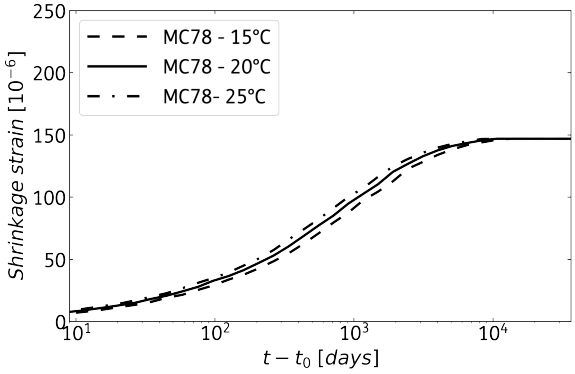

(c) Comparison of shrinkage strain curves for MC78.

Figure B.1: Impact of temperature (*T*) in the creep compliance and shrinkage strain curves of MC78. The chosen values for *T* are 15, 20, and 25°C. The chosen times of loading (*t'*) for creep are 28 and 250 days.

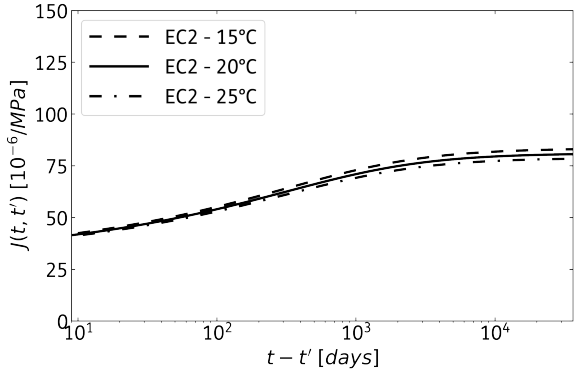

(a) Comparison of creep compliance curves for EC2 at *t'* of 28 days.

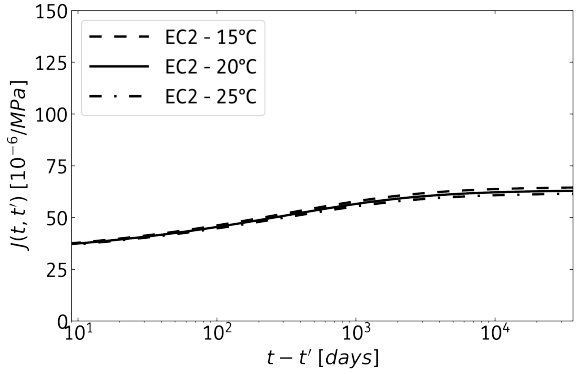

(b) Comparison of creep compliance curves for EC2 at *t'* of 250 days.

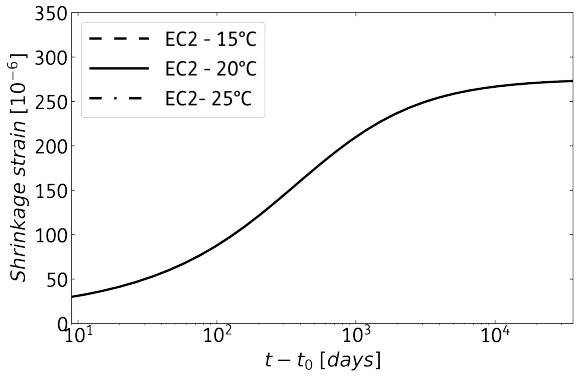

(c) Comparison of shrinkage strain curves for EC2.

Figure B.2: Impact of temperature (*T*) in the creep compliance and shrinkage strain curves of EC2. The chosen values for *T* are 15, 20, and 25°C. The chosen times of loading (*t'*) for creep are 28 and 250 days.

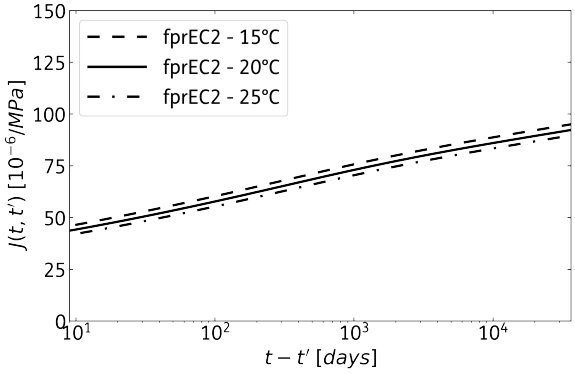

(a) Comparison of creep compliance curves for fprEC2 at *t'* of 28 days.

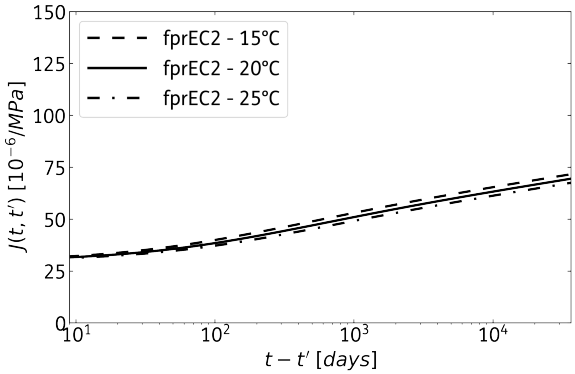

(b) Comparison of creep compliance curves for fprEC2 at *t'* of 250 days.

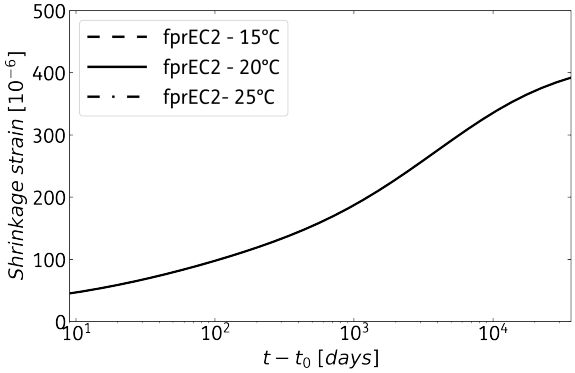

(c) Comparison of shrinkage strain curves for fprEC2.

Figure B.3: Impact of temperature (*T*) in the creep compliance and shrinkage strain curves of fprEC2. The chosen values for *T* are 15, 20, and 25°C. The chosen times of loading (*t'*) for creep are 28 and 250 days.

B.2. Effect of relative humidity

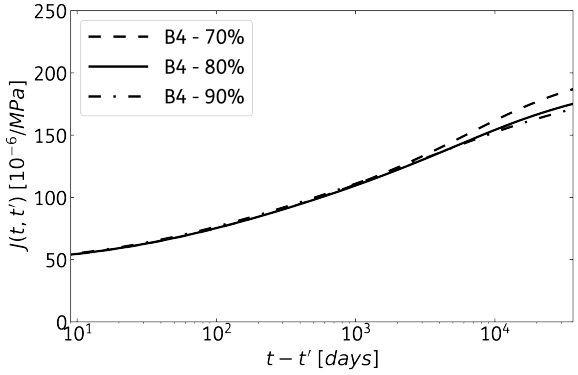

(a) Comparison of creep compliance curves for B4 at *t'* of 28 days.

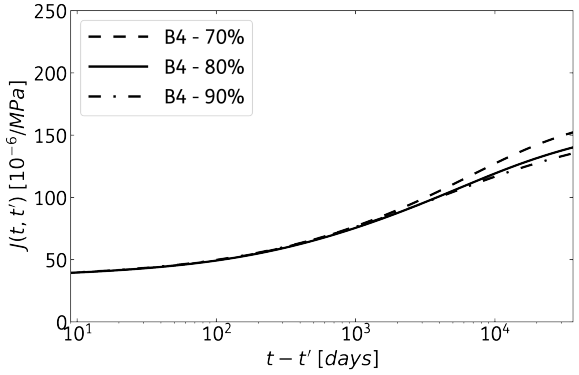

(b) Comparison of creep compliance curves for B4 at *t'* of 250 days.

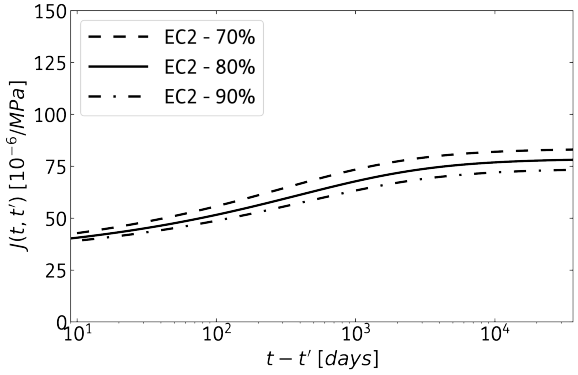

(c) Comparison of creep compliance curves for EC2 at *t'* of 28 days.

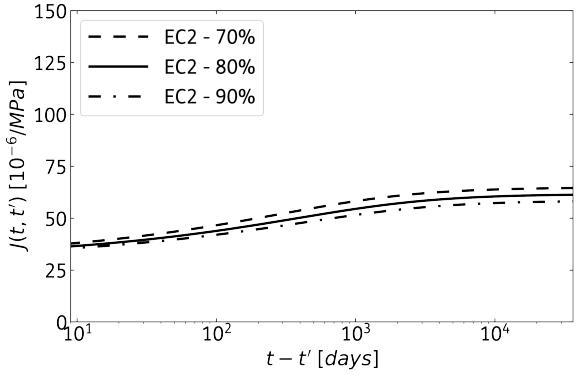

(d) Comparison of creep compliance curves for EC2 at *t'* of 250 days.

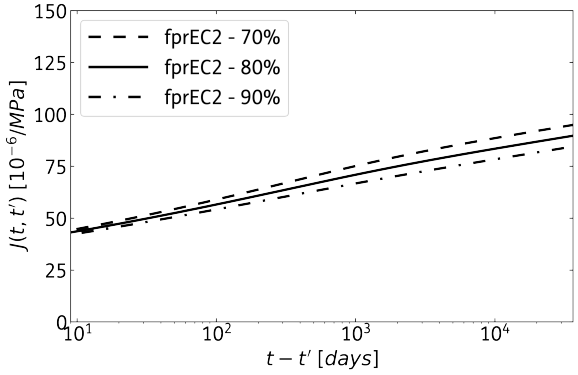

(e) Comparison of creep compliance curves for fprEC2 at *t'* of 28 days.

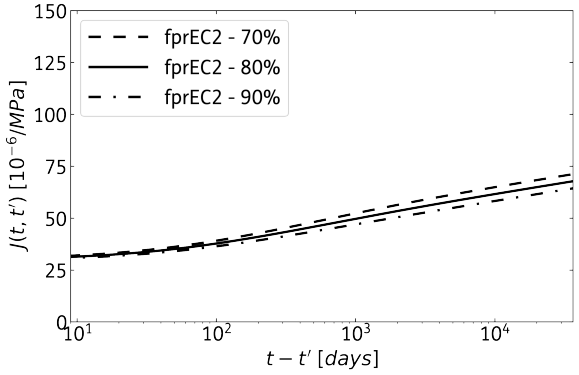

(f) Comparison of creep compliance curves for fprEC2 at *t'* of 250 days.

Figure B.4: Impact of temperature (*T*) in the creep compliance curves of B4, EC2, and fprEC2. The chosen values for *RH* are 70, 80, and 90%. The chosen times of loading (*t'*) for creep are 28 and 250 days.

B.3. Effect of mean compressive strength

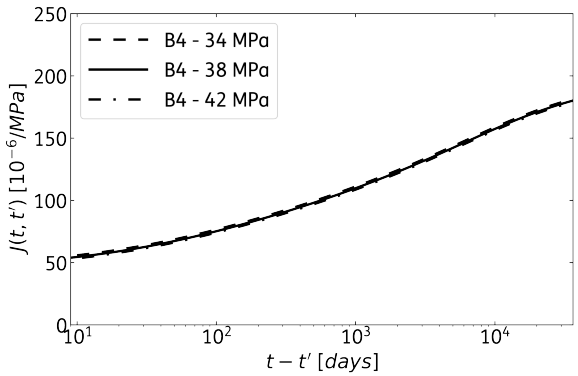

(a) Comparison of creep compliance curves for B4 at *t'* of 28 days.

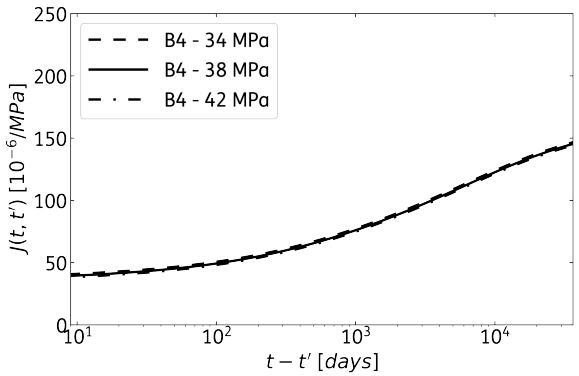

(b) Comparison of creep compliance curves for B4 at *t'* of 250 days.

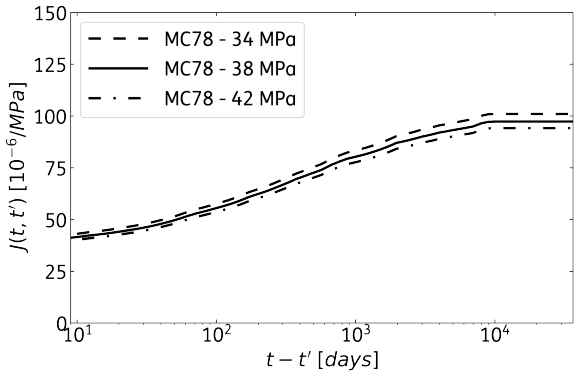

(c) Comparison of creep compliance curves for MC78 at *t'* of 28 days.

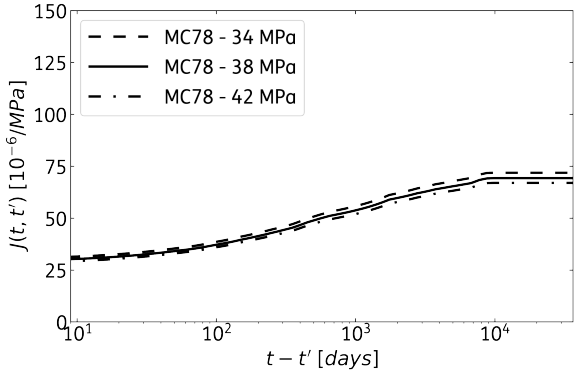

(d) Comparison of creep compliance curves for MC78 at *t'* of 250 days.

Figure B.5: Impact of mean compressive strength (*fcm*) in the creep compliance curves of B4 and MC78. The chosen values for *fcm* are 34, 38, and 42 N/mm^2. The chosen times of loading (*t'*) for creep are 28 and 250 days.

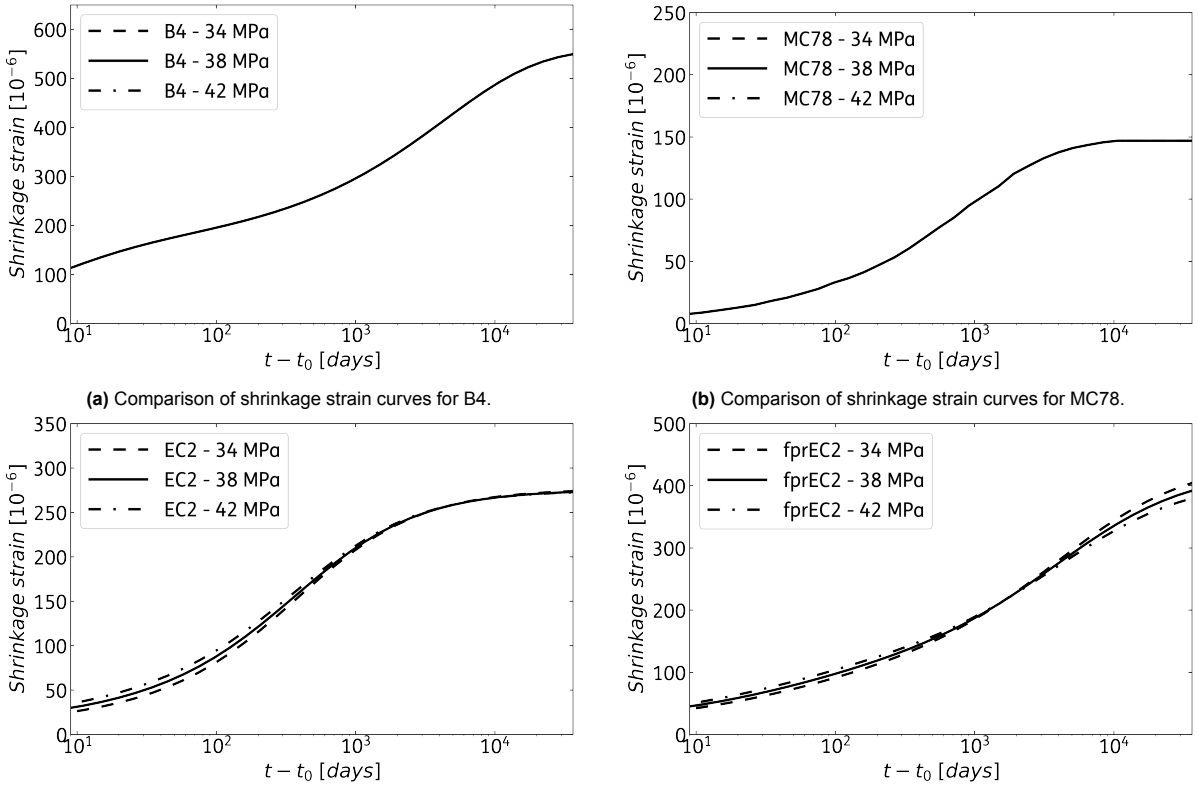

(a) Comparison of shrinkage strain curves for B4.

(b) Comparison of shrinkage strain curves for MC78.

(c) Comparison of shrinkage strain curves for EC2.

(d) Comparison of shrinkage strain curves for fprEC2.

Figure B.6: Impact of mean compressive strength (*fcm*) in the shrinkage strain curves of B4, MC78, EC2, and fprEC2. The chosen values for *fcm* are 34, 38, and 42 N/mm^2.

C

Minimal examples

The finite element model of the Rooyensteinse Brug is complex. The use of hand calculations to verify the output is limited, which means that pin-pointing errors becomes a difficult task. A way to avoid mistakes in the implementation of different procedures is by using minimal examples. A minimal example in finite element modeling is a simplified model that contains only the essential components to demonstrate specific functionalities. By using them, computational efficiency is achieved, and error isolation is possible.

The finite element model presented in this work requires the integration of diverse functionalities. This includes a correct implementation of creep compliance curves within the material models, coupled with the consideration of maturity effects. Additionally, the propagation of uncertainty is also a crucial aspect. The model also includes phasing, which describes the construction method. To ensure the systematic incorporation of these aforementioned concepts, three minimal examples are introduced. Table C.1 concisely summarizes the specific topics addressed in each of these examples.

Topic	Example 1	Example 2	Example 3
Creep Compliance Curves		X	
Propagation of Uncertainty		X	
Maturity Effects	X	X	X
Phasing			X

Table C.1: Topics analyzed on each minimal example.

C.1. Example 1: Single-cell element

With the release of DIANA FEA 10.7, it became possible to incorporate maturity effects into the creep compliance curves for a material model. To test this new functionality, a single-cell element test was proposed. Single-cell tests use only one finite element to validate results.

C.1.1. Model information

The single-cell element was modeled with a four-node quadrilateral isoparametric plane stress element. The height, width, and thickness are 1 m. As per boundary conditions, the element is only restricted for translations. For the upper and lower left corners, the restriction is in *x-direction*, and for the lower left and right in *y-direction*. Per definition, the mesh comprises only one cell. The mesh, boundary conditions, and loading can be observed in Figure C.1.

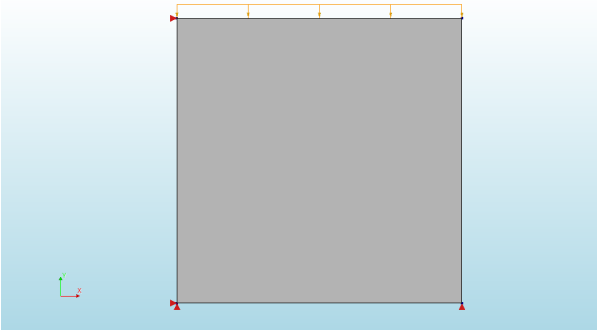

Figure C.1: View of the single-cell element model in DIANA FEA.

This single-cell element is subjected to five different distributed loads, each with a magnitude of -1×10^6 N/m^2. Each load generates a stress $\Delta\sigma$ of 1 N/mm^2 at a different time of loading, as seen in Figure C.2. The analysis is conducted until day number 40.

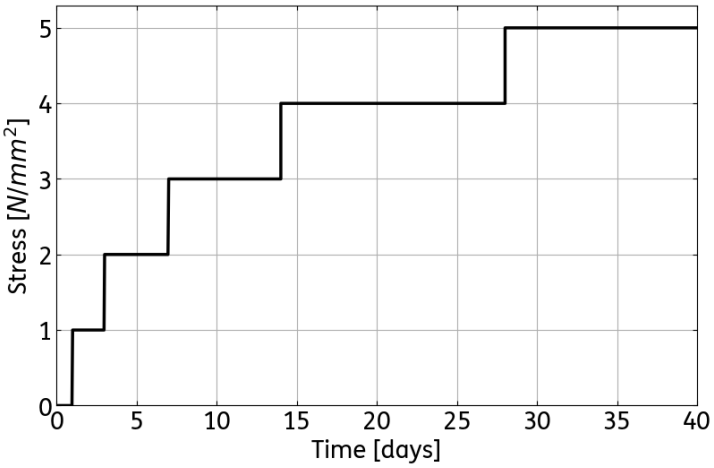

Figure C.2: Applied stress over time.

The compliance curves are constructed based on the creep model outlined in Eurocode 2 [50]. As a benchmark for comparison, the strain over time was initially derived through manual calculations. First,

the creep compliance curve for each time of loading was obtained. Given the stress $\Delta\sigma$ is equal to 1 N/mm^2, each creep compliance curve is equivalent to the Δ strain over time. Finally, superposition is applied to obtain the total response. This result, shown in Figure C.3, is denoted as the ground truth and serves as the reference for validating the implementation of maturity effects within DIANA FEA 10.7.

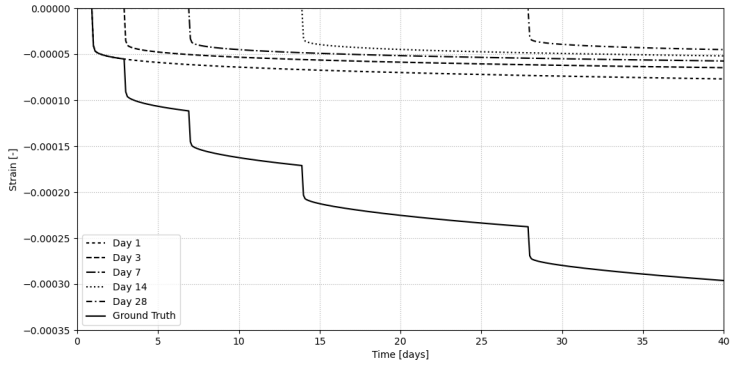

Figure C.3: Δ and total strain (ground truth) over time.

C.1.2. Results

Three scenarios were tested in this minimal example: (i) the treatment of the input, (ii) the interpolation capabilities, and (iii) the impact of accounting for maturity effects. The first scenario is meant to verify that the output, which in this case is the strain over time, corresponds to the input provided to the model. To achieve this, the individual creep compliance curves for all the times of loading were incorporated into the material model. As seen in C.4, the output from the FE model aligns with the ground truth.

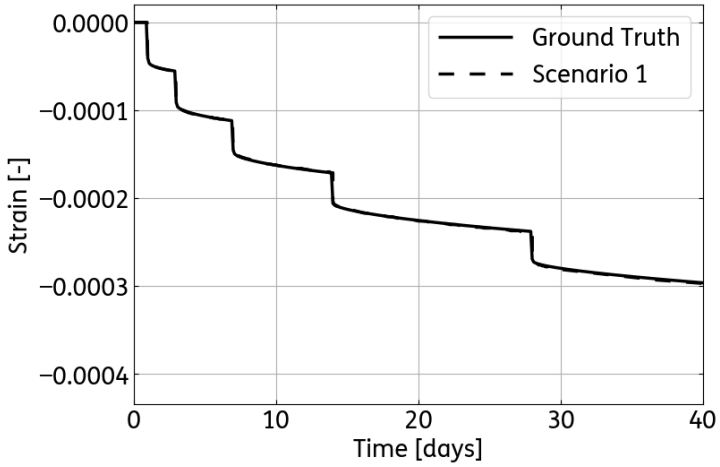

Figure C.4: Strain over time, Scenario 1.

In the Rooyensteinse Brug, every segment is subjected to multiple loads at different concrete ages. This is particularly true for tendon prestressing, which continues to affect segments until the construction

is complete. Incorporating creep compliance curves for all these different times of loading is computationally expensive. Therefore, the objective of Scenario 2 is to evaluate the interpolation capability of DIANA 10.7. For this, two cases are considered, each with a different amount of compliance curves added to the model. The creep compliance curves for each case are indicated in Table C.2. The results for Scenario 2.a and Scenario 2.b are depicted in Figures C.5 and C.6, respectively. Scenario 2 shows the importance of incorporating an adequate number of creep compliance curves at early ages to ensure an accurate interpolation. This can be observed in the significant improvement seen in Figure C.6 compared to C.5 when the compliance curve for loading at 1 day is included. It is also worth noting that inadequate interpolation can result in an underestimation of the strain evolution over time, as evident in the results from Scenario 2.b.

Times of loading [days]	Scenario 2.a	Scenario 2.b
1		X
3		
7	X	X
14	X	X
28	X	X

Table C.2: Compliance curves per case, Scenario 2.

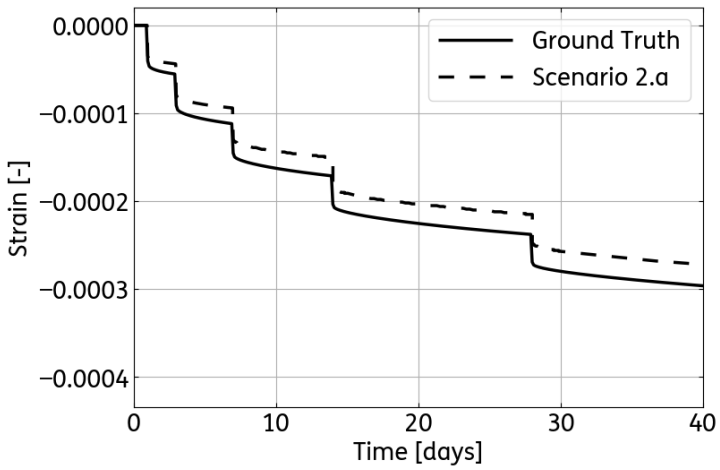

Figure C.5: Strain over time for Scenario 2.a.

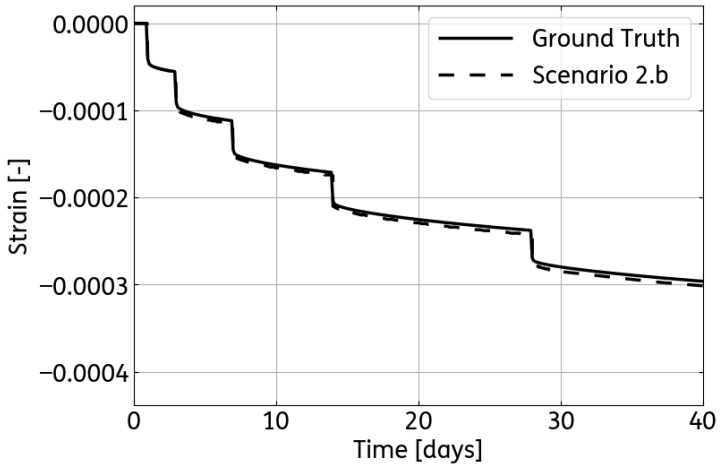

Figure C.6: Strain over time for Scenario 2.b.

Scenario 3 is designed to illustrate the impact of omitting maturity effects from the creep analysis. For this example, only the compliance curve corresponding to a time of loading of 1 day is generated, being shifted for each subsequent loading time. Figure C.7 provides a visual comparison between the ground truth and the strain evolution when maturity effects are not considered. The observed deviation between the curves is approximately 22%. While the overestimation of strain over time when maturity effects are excluded might suggest a conservative prediction, as demonstrated in scenario 2.b, it is evident that overestimation is not a consistent outcome. Furthermore, the primary goal of this project is to develop a detailed finite element model for a balanced cantilever bridge, and disregarding maturity effects fails to capture the actual time-dependent behavior.

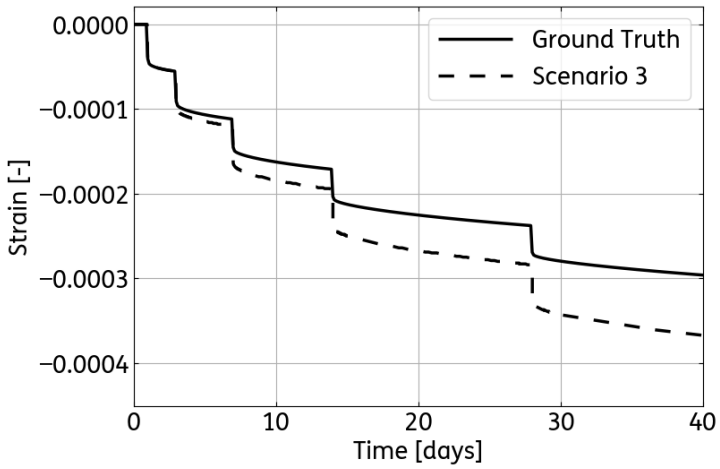

Figure C.7: Strain over time, Scenario 3.

C.2. Example 2: Simply supported prestressed beam

The second minimal example is based on an investigation dedicated to understanding the time-dependent behavior of prestressed beams subjected to long-term sustained loading tests [79]. Previous to this thesis work, TNO developed finite element models of the experiments in DIANA FEA and compared

the results with the experimental data available.

C.2.1. Model information

The full experimental program for these prestressed beams includes a variety of prestressing levels, reinforcement and tendon profiles, and magnitude and time of loading. For this minimal example, two cases were used, referred to in [79] as LT-1.0 and LT-0.5-Q. The details regarding the loading program are presented in Table C.3. The analysis is conducted until day number 2000. Figures C.8 and C.9 show the model of beams LT-1.0 and LT-0.5-Q in the software. The three creep models used for this minimal example are Eurocode 2 (EC2) [50], the *fib* Model Code 2010 (MC10) [47], and the RILEM B4 model (B4) [17].

Beam Case	LT-1.0	LT-0.5-Q
Age at prestressing [days]	14	14
Age at first loading [days]	-	28
Q at first loading [N]	-	16500
Age at second loading [days]	-	84
Q at second loading [N]	-	63750

Table C.3: The loading program [79].

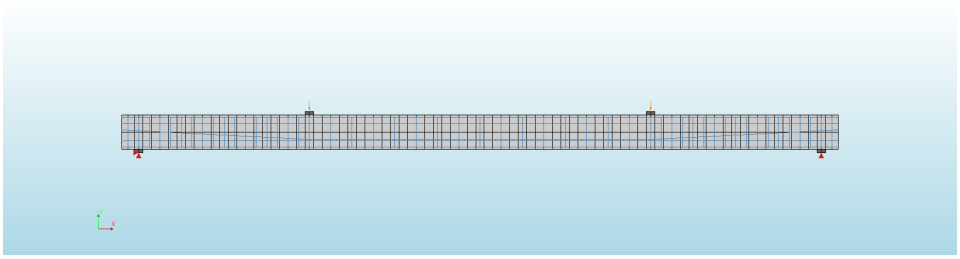

Figure C.8: Beam LT-1.0 in DIANA FEA.

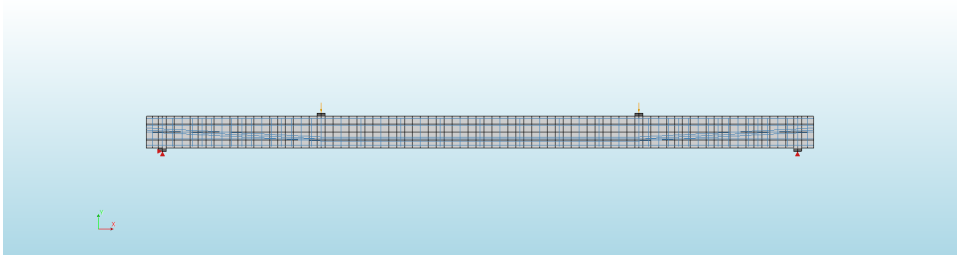

Figure C.9: Beam LT-0.5-Q in DIANA FEA.

C.2.2. Results

Creep compliance curves

The assessment of the response of this structural component primarily focused on the mid-span deflection and the prestress loss. Figures C.10 and C.11 present the outcomes for the three creep models in

the beam LT-1.0. Notably, while EC2 and MC10 show a similar response, B4 displays a faster deflection increase and prestressing loss over time. When using EC2 as the reference, MC10 shows a 0.9% difference in deflection, whereas B4 exhibits a higher difference of 27.6%. Regarding the prestressing level, both EC2 and MC10 show the same loss at the end of the analysis, while B4 displays a 3.7% difference.

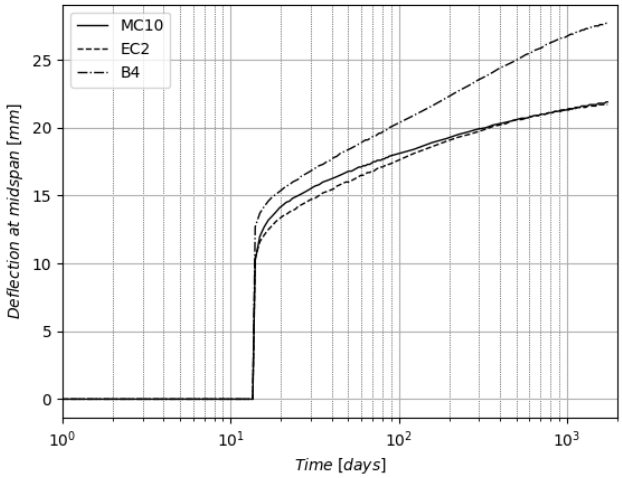

Figure C.10: Comparison of deflection at mid-span over time for beam LT-1.0 with the models EC2, MC10, and B4.

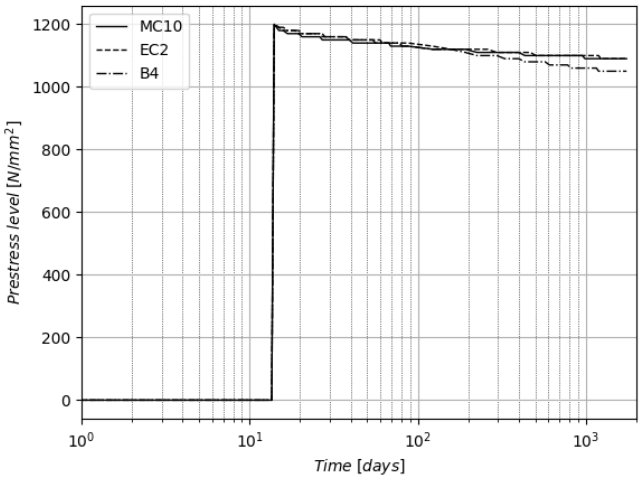

Figure C.11: Comparison of prestress level over time for beam LT-1.0 with the models EC2, MC10, and B4.

Propagation of uncertainty

Recognizing the inherent prediction errors in code-based models, often disregarded in practice, is important. These errors can be accounted for by treating the creep compliance function as a statistical variable rather than a deterministic value. This entails calculating upper and lower bounds in addition to the mean curve. Presenting the expected response within an interval provides a more realistic

representation, particularly considering the substantial uncertainty associated with these models.

In this analysis on the propagation of uncertainty, the upper and lower bounds for B4 were determined, as depicted in Figure C.12). These bounds were then incorporated into the material model for beam LT-1.0, along with the mean compliance curve. Figures C.13 and C.14 illustrate these upper and lower bounds are reflected in the structural response of the beam. In terms of mid-span deflection, the difference between the lower bound and the mean reached 31.6% by the end of the analysis, while for the upper bound, it was even more pronounced at 70.8%. As for prestress loss, the lower bound exhibited a difference was 4.8%, and the upper bound showed a 8.0% variation. These disparities highlight the substantial uncertainty associated with creep models, in this case, the RILEM B4 model. They also emphasize how relying solely on a mean value can result in inaccurate predictions of the response.

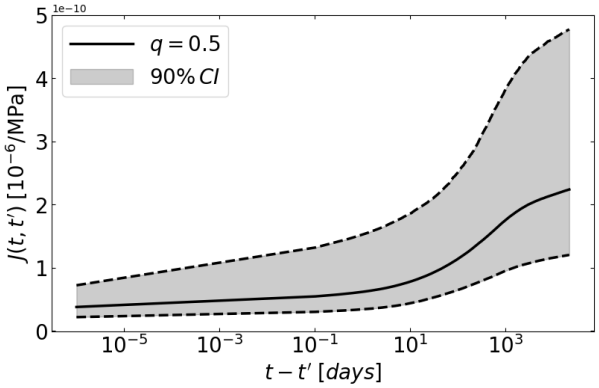

Figure C.12: Propagation of uncertainty with B4.

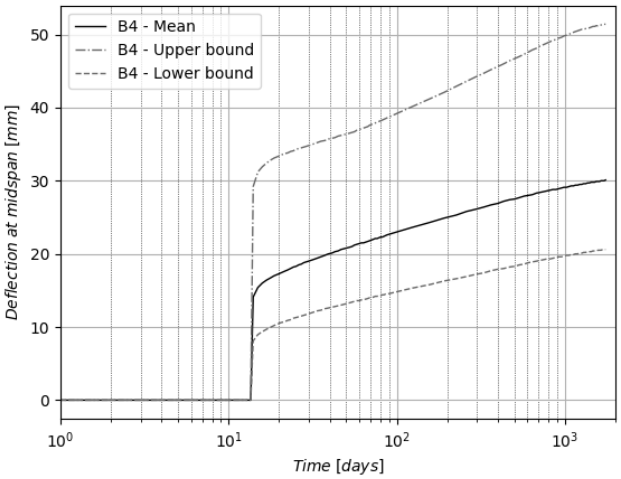

Figure C.13: Comparison of deflection at mid-span over time for beam LT-1.0, with the mean, upper, and lower bounds.

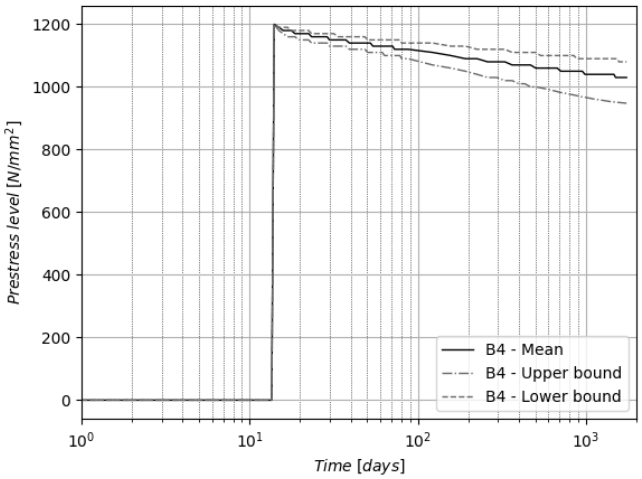

Figure C.14: Comparison of prestress force over time for beam LT-1.0, with the mean, upper, and lower bounds.

Maturity Effects

The validation of functionality of maturity effects in DIANA FEA 10.7 was initially conducted using the single-cell element minimal example. Nevertheless, it is also relevant to explore its impact on the response of a structural component. In this final analysis, the RILEM B4 model (B4) was once more employed, this time with beam LT-0.5-Q. Figure C.15 illustrates the difference in response between the scenario that includes maturity effects and the one that omits them. Consistent with the observations from the single-cell test, the absence of maturity effects leads to a greater deflection. Taking the model with maturity effects as a reference, a difference of 16.4% is observed at the conclusion of the analysis. This overestimation of the response warrants careful consideration, especially given that the time of loading used for the B4 model without maturity effects was 14 days. It is possible that if a later time of loading is chosen for the model, an underestimation of the response might be observed.

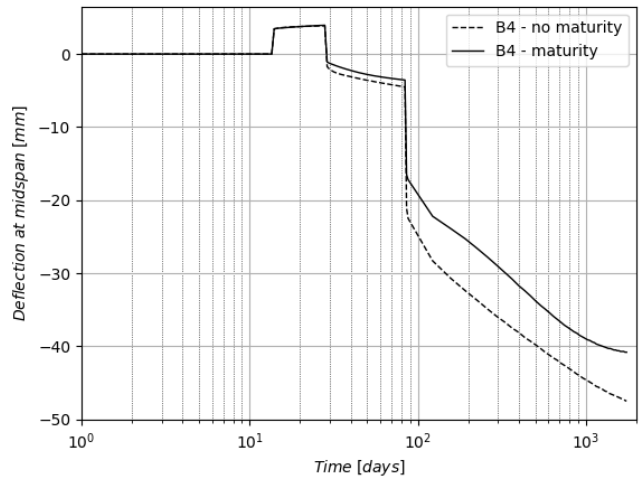

Figure C.15: Comparison of deflection at mid-span over time with beam LT-0.5-Q with and without maturity effects.

C.3. Example 3: Phased prestressed cantilever beam

Accurately representing the phasing process is one of the primary challenges when developing a detailed finite element model of a balanced cantilever bridge. To test the implementation of construction phases in DIANA FEA 10.7, a minimal example of a prestressed cantilever beam is presented. This example was originally created by Louman [15] as part of his research on simulating deformations in balanced cantilever bridges. The results obtained from Louman's work served as a basis for verifying hand calculations and establishing a ground truth. Subsequently, these ground truth was used to validate the model in DIANA FEA 10.7.

C.3.1. Model information

The phased prestressed cantilever beam was modeled with two-node, two-dimensional class-III beam elements. Figure C.16 illustrates the three sections that compose this beam, along with their respective cross-sectional dimensions. At one end, all translations and rotations are restricted. A summary of the relevant data is provided in Table C.4. The term 'fictional notional size' refers to an equivalent I-shaped beam used in the calculation of the creep compliance curves. The prestressing force is applied as an equivalent load to avoid prestressing losses, making the results comparable with the hand calculations. The creep model used for this minimal example is Eurocode 2 [50]. This prestressed cantilever beam is constructed in three primary stages, with each stage involving the addition of a new segment and prestress load. The construction process is outlined in Table C.5.

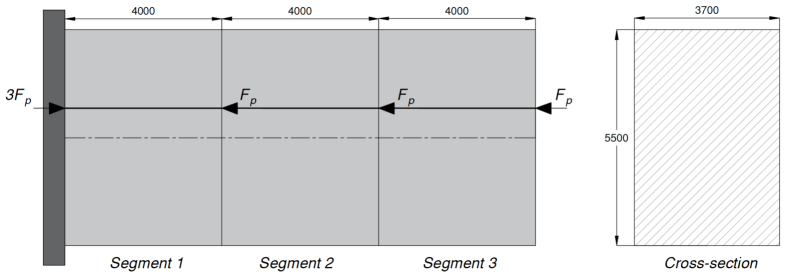

Figure C.16: Segments of phased prestressed cantilever beam

Parameter	Value
Concrete Compressive Strength (f_{cm})	85 N/mm^2
Relative Humidity (RH)	75 %
Fictional Notional Size	2212 mm
Temperature	10 °C
Prestressing Force (P_o)	1×10^8 N
Eccentricity (e)	750 mm

Table C.4: Data for phased prestressed cantilever beam [15].

The timeline presented in Table C.5 is not directly applicable to DIANA FEA 10.7. The implementation of the construction process in the finite element model requires a total of six phases, schematized

Time [days]	Activity
0	Formwork and casting of segment 1
3	Removing formwork and prestressing segment 1
7	Formwork and casting of segment 2
10	Removing formwork and prestressing segment 2
14	Formwork and casting of segment 3
17	Removing formwork and prestressing segment 3

Table C.5: Timeline of construction process.

below.

- Phase 1 [$t = 0$ to $t = 3$]:

  No segments are active.

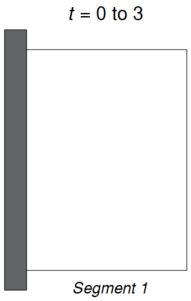

Figure C.17: Phase 1

- Phase 2 [$t = 3$ to $t = 10$]:

  Segment 1 is active.

  At $t = 3$ the self-weight and prestressing for segment 1 are active.

  At $t = 7$ the point load and moment due to the casting of segment 2 are active.

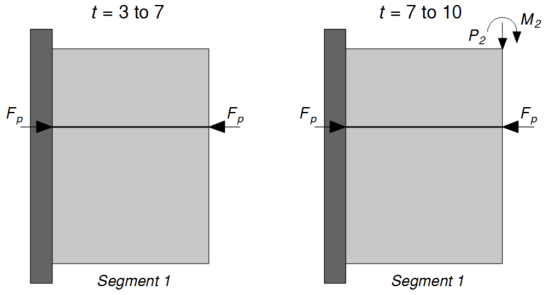

Figure C.18: Phase 2

- Phase 3 [$t = 10$]:

  Intermediate phase to import the deformations from segment 1 to segment 2.

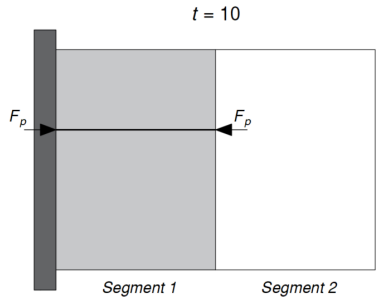

Figure C.19: Phase 3

- Phase 4 [$t = 10$ to $t = 17$]:

  Segment 2 is active.

  At $t = 10$ the self-weight and prestressing for segment 2 are active.

  At $t = 14$ the point load and moment due to the casting of segment 3 are active.

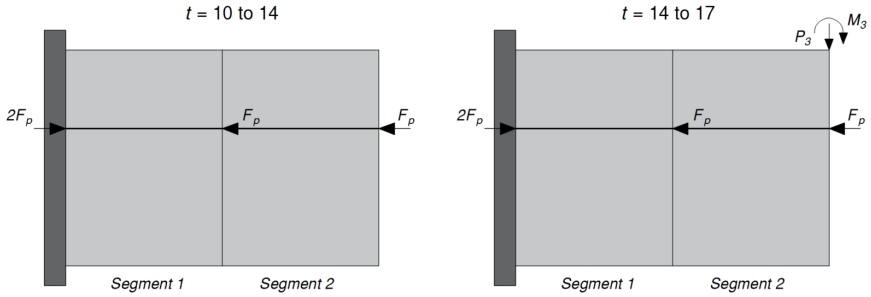

Figure C.20: Phase 4

- Phase 5 [$t = 17$]:

  Intermediate phase to import the deformations from segment 2 to segment 3.

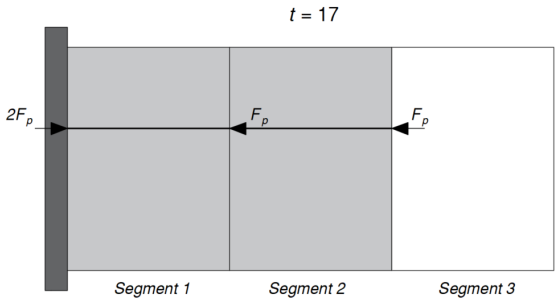

Figure C.21: Phase 5

- Phase 6 [$t = 17$ to $t = 28$]:

  Segment 3 is active.

  At $t = 17$ the self-weight and prestressing for segment 3 are active.

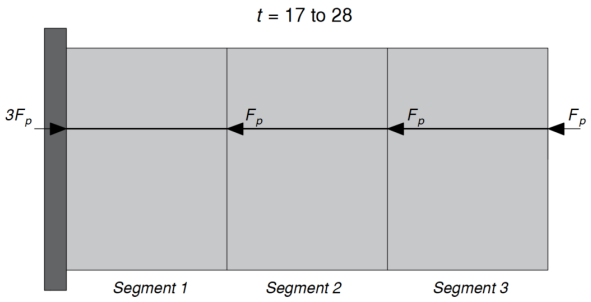

Figure C.22: Phase 6

C.3.2. Results

As a preliminary step, the stresses at the top and the bottom fibers of the prestressed cantilever beam, at the fixed end, were calculated. For this, the following expressions were used:

$$\sigma_{c,top} = -\frac{P_o}{A_b} + \frac{(M_g)(z_t)}{I_c} - \frac{(M_p)(z_t)}{I_c} \tag{C.1}$$

$$\sigma_{c,bottom} = -\frac{P_o}{A_b} - \frac{(M_g)(z_b)}{I_c} + \frac{(M_p)(z_b)}{I_c} \tag{C.2}$$

where:

σ_c = concrete stress
P_o = prestressing force
A_b = area of the section
M_g = moment due to self-weight
M_p = moment due to prestressing force
z = distance between centroid and fiber
I_c = moment of inertia

The stresses for the top and bottom fibers are presented in Table C.6. Additionally, figure C.23 provides a graphical representation of the stress evolution over time. As well as for the single-cell element example, the creep compliance curves for each time of loading were calculated by hand. Then, the strain over time for each increment in stress $\Delta\sigma$ was obtained. Finally, superposition was applied to establish the ground truth. Figure C.24 presents the stress-dependent strains over time for the top and bottom fibers. A comparison with the hand calculations presented by [15] served to validate the results.

Having established and validated the ground truth, the subsequent step involves verifying the implementation of phasing in the finite element (FE) model of the prestressed cantilever beam. Figure C.25 illustrates a comparison between the FE output, accounting for maturity effects, and the hand calculations. This figure demonstrates an agreement in the results, thereby validating the implementation of maturity effects in creep within DIANA FEA 10.7.

To understand the influence of maturity effects on the response of this structural member, Figure C.26

Time Intervals [days]	$\sigma_{c,top}$ [N/mm^2]	$\sigma_{c,bottom}$ [N/mm^2]
3 - 7	-8.721	-1.107
7 - 10	-8.077	-1.751
10 - 14	-17.013	-2.643
14 - 17	-15.941	-3.715
17 - ∞	-24.878	-4.606

Table C.6: Concrete stress at top and bottom.

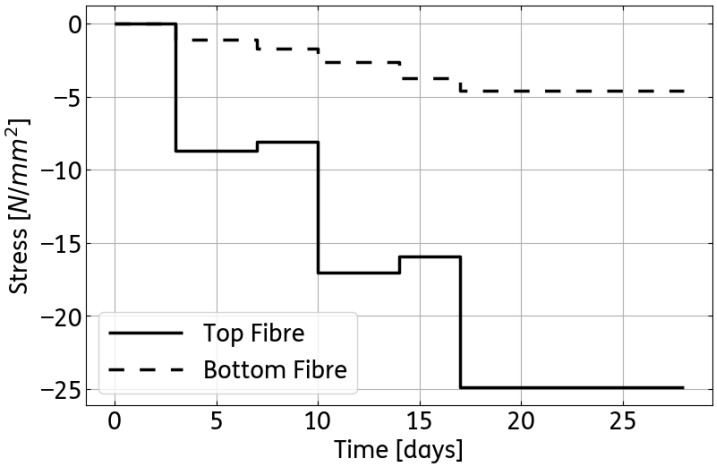

Figure C.23: Applied stresses over time.

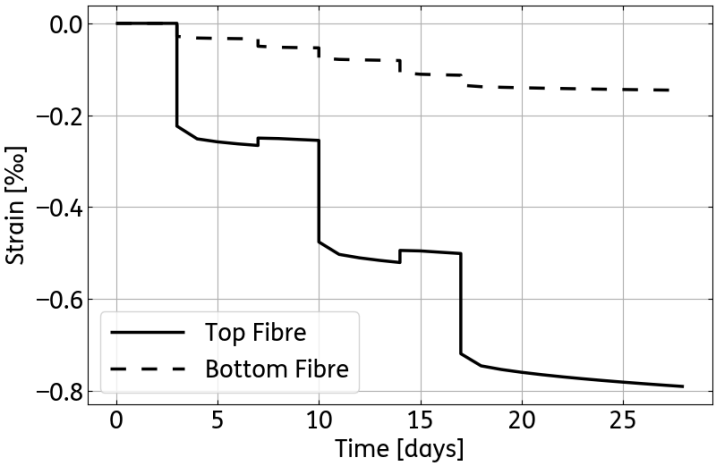

Figure C.24: Stress-dependent strain over time.

presents the FE stress-dependent strain with and without considering maturity effects. The difference, using the model with maturity as a reference, is 4.2% for the top fiber, and 4.6% for the bottom fiber. Similar to the results obtained in the single-cell example, it becomes evident that neglecting maturity effects leads to an inaccurate prediction of the behavior of concrete structures.

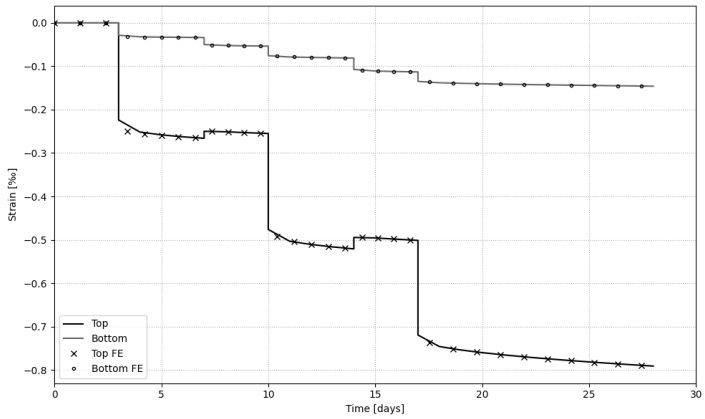

Figure C.25: Comparison of stress-dependent strain over time with maturity effects between the FE model and the hand calculations.

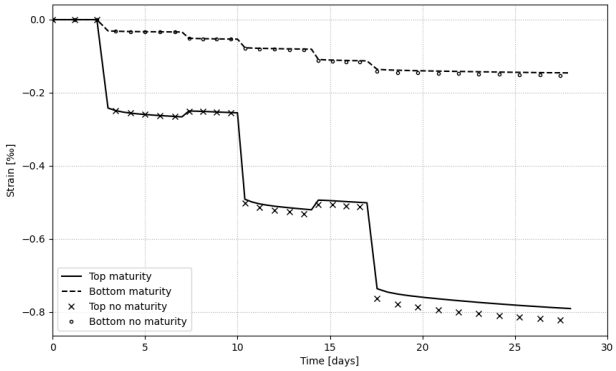

Figure C.26: Stress-dependent strain over time for the FE model.

D

Phasing and load cases overview

Below is an overview of the 58 phases and 186 load cases implemented in the analysis performed in DIANA 10.7. The information includes the phase number, the time in days, the corresponding activated elements, the load increments, and the phase-dependent loads present. For clarification, the abbreviations have the following meanings:

- SW: self-weight
- TOP_SLAB_UDL: construction loads
- ASPHALT_UDL: asphalt layer
- SIDES_QL: over-imposed dead load on both edges of the bridge.
- PH1_TRANSPRESTRESS: transversal prestressing
- PH**XX**_PRESTRESS: longitudinal prestressing in phase **XX**. Refer to table D.2 for the information on the tendons.
- PH**XX**_DP_SEGM**YY**_TF_PM: point load and moment representing the traveling formwork, applied to the corresponding dummy plate in phase **XX**.
- PH**XX**_DP_SEGM**YY**_FC_PM: point load and moment representing the casting of segment **YY**, applied to the corresponding dummy plate in phase **XX**.
- PH**XX**_DP_SEGM**YY**_FC_UDL: distributed load representing the traveling formwork in segment **YY**, applied in phase **XX**.
- PH**XX**_IMP_DEF_segm_**YY_ZZ**: import deformations load, applying the deformations at the end of segment **YY** as constraints for the new segment **ZZ**, in phase **XX**.

Phase	Load/Time dependent	Start time [days]	New activated segments	New activated tendons	New activated load cases
Phase 1	Time	0	19, 20, 21, 22	-	1, 2, 5
Phase 2	Time	35	-	1, 2	6, 7, 8
Phase 3	Load	70	23	-	10
Phase 4	Time	70	-	3, 4	9, 11, 12, 13
Phase 5	Load	77	18	-	15
Phase 6	Time	77	-	8	14, 16, 17, 18
Phase 7	Load	84	24	-	20
Phase 8	Time	84	-	5, 6	19, 21, 22, 23
Phase 9	Load	91	17	-	25
Phase 10	Time	91	-	10	24, 26, 27, 28
Phase 11	Load	98	25	-	30
Phase 12	Time	98	-	7, 9	29, 31, 32, 33
Phase 13	Load	105	16	-	35
Phase 14	Time	105	-	24	34, 36, 37, 38
Phase 15	Load	112	26	-	40
Phase 16	Time	112	-	11, 22	39, 41, 42, 43
Phase 17	Load	119	15	-	45
Phase 18	Time	119	-	26	44, 46, 47, 48
Phase 19	Load	126	27	-	50
Phase 20	Time	126	-	12, 23	49, 51, 52, 53
Phase 21	Load	133	14	-	55
Phase 22	Time	133	-	28	54, 56, 57, 58, 60, 61
Phase 23	Load	140	13, 28	-	63, 64
Phase 24	Time	140	-	13, 30, 32	62, 65, 66, 67, 69, 70
Phase 25	Load	147	12, 29	-	72, 73
Phase 26	Time	147	-	14, 25, 33	68, 71, 74, 75, 76, 78, 79
Phase 27	Load	154	11, 30	-	81, 82
Phase 28	Time	154	-	15, 34, 35	77, 80, 83, 84, 85, 87, 88
Phase 29	Load	161	10, 31		90, 91
Phase 30	Time	161	-	16, 27, 36	86, 89, 92, 93, 94, 96, 97
Phase 31	Load	168	9, 32	-	99, 100
Phase 32	Time	168	-	17, 37, 38	95, 98, 101, 102, 103, 105, 106
Phase 33	Load	175	8, 33	-	108, 109
Phase 34	Time	175	-	18, 29, 40	104, 107, 110, 111, 112, 114, 115
Phase 35	Load	182	7, 34	-	117, 118

Table D.1: Overview of the phased analysis.

Phase	Load/Time dependent	Start time [days]	New activated segments	New activated tendons	New activated load cases
Phase 36	Time	182	-	19, 31, 42	113, 116, 119, 120, 121, 123, 124
Phase 37	Load	189	6, 35	-	126, 127
Phase 38	Time	189	-	20, 39, 44	122, 125, 128, 129, 130, 132, 133
Phase 39	Load	196	5, 36	-	135, 136
Phase 40	Time	196	-	21, 41, 46	131, 134, 137, 138, 139, 141, 142
Phase 41	Load	203	4, 37	-	144, 145
Phase 42	Time	203	-	43, 48, 52	140, 143, 146, 147, 148, 150, 151
Phase 43	Load	210	3, 38	-	153, 154
Phase 44	Time	210	-	45, 50, 54	149, 152, 155, 156, 157, 159, 160
Phase 45	Load	217	2, 39	-	162, 163
Phase 46	Time	217	-	47, 55, 56	158, 161, 164, 165, 166, 168, 169
Phase 47	Load	224	1, 40	-	171, 172
Phase 48	Time	224	-	49, 57	167, 170, 173, 174, 175
Phase 49	Load	231	41	-	177
Phase 50	Time	231	-	51	176, 178, 179, 180
Phase 51	Load	238	42	-	182
Phase 52	Time	238	-	53, 58, 59	181, 183, 184, 185
Phase 53	Load	245	SML, EWD	-	187
Phase 54	Time	245	-	CA, CB, CC	186, 188, 189, 190
Phase 55	Load	252	SM	-	192
Phase 56	None	252	-	C1 - C21	191, 193
Phase 57	Time	252	-	-	3, 4
Service Life	Time	259	-	-	-

Table D.2: Overview of the phased analysis (continued from previous page).

Case	Name	Case	Name
Case 1	SW	Case 46	PH18_PRESTRESS
Case 2	TOP_SLAB_UDL	Case 47	PH18_DP_SEGM_27_TF_PM
Case 3	ASPHALT_UDL	Case 48	PH18_DP_SEGM_27_FC_PM
Case 4	SIDES_QL	Case 49	PH20_DP_SEGM_27_TF_UDL
Case 5	PH1_TRANSPRESTRESS	Case 50	PH19_IMP_DEF_segm_26_27
Case 6	PH2_PRESTRESS	Case 51	PH20_PRESTRESS
Case 7	PH2_DP_SEGM_23_TF_PM	Case 52	PH20_DP_SEGM_14_TF_PM
Case 8	PH2_DP_SEGM_23_FC_PM	Case 53	PH20_DP_SEGM_14_FC_PM
Case 9	PH4_DP_SEGM_23_TF_UDL	Case 54	PH22_DP_SEGM_14_TF_UDL
Case 10	PH3_IMP_DEF_segm_22_23	Case 55	PH21_IMP_DEF_segm_15_14
Case 11	PH4_PRESTRESS	Case 56	PH22_PRESTRESS
Case 12	PH4_DP_SEGM_18_TF_PM	Case 57	PH22_DP_SEGM_13_TF_PM
Case 13	PH4_DP_SEGM_18_FC_PM	Case 58	PH22_DP_SEGM_13_FC_PM
Case 14	PH6_DP_SEGM_18_TF_UDL	Case 59	PH24_DP_SEGM_13_TF_UDL
Case 15	PH5_IMP_DEF_segm_19_18	Case 60	PH22_DP_SEGM_28_TF_PM
Case 16	PH6_PRESTRESS	Case 61	PH22_DP_SEGM_28_FC_PM
Case 17	PH6_DP_SEGM_24_TF_PM	Case 62	PH24_DP_SEGM_28_TF_UDL
Case 18	PH6_DP_SEGM_24_FC_PM	Case 63	PH23_IMP_DEF_segm_14_13
Case 19	PH8_DP_SEGM_24_TF_UDL	Case 64	PH23_IMP_DEF_segm_27_28
Case 20	PH7_IMP_DEF_segm_23_24	Case 65	PH24_PRESTRESS
Case 21	PH8_PRESTRESS	Case 66	PH24_DP_SEGM_12_TF_PM
Case 22	PH8_DP_SEGM_17_TF_PM	Case 67	PH24_DP_SEGM_12_FC_PM
Case 23	PH8_DP_SEGM_17_FC_PM	Case 68	PH26_DP_SEGM_12_TF_UDL
Case 24	PH10_DP_SEGM_17_TF_UDL	Case 69	PH24_DP_SEGM_29_TF_PM
Case 25	PH9_IMP_DEF_segm_18_17	Case 70	PH24_DP_SEGM_29_FC_PM
Case 26	PH10_PRESTRESS	Case 71	PH26_DP_SEGM_29_TF_UDL
Case 27	PH10_DP_SEGM_25_TF_PM	Case 72	PH25_IMP_DEF_segm_13_12
Case 28	PH10_DP_SEGM_25_FC_PM	Case 73	PH25_IMP_DEF_segm_28_29
Case 29	PH12_DP_SEGM_25_TF_UDL	Case 74	PH26_PRESTRESS
Case 30	PH11_IMP_DEF_segm_24_25	Case 75	PH26_DP_SEGM_11_TF_PM
Case 31	PH12_PRESTRESS	Case 76	PH26_DP_SEGM_11_FC_PM
Case 32	PH12_DP_SEGM_16_TF_PM	Case 77	PH28_DP_SEGM_11_TF_UDL
Case 33	PH12_DP_SEGM_16_FC_PM	Case 78	PH26_DP_SEGM_30_TF_PM
Case 34	PH14_DP_SEGM_16_TF_UDL	Case 79	PH26_DP_SEGM_30_FC_PM
Case 35	PH13_IMP_DEF_segm_17_16	Case 80	PH28_DP_SEGM_30_TF_UDL
Case 36	PH14_PRESTRESS	Case 81	PH27_IMP_DEF_segm_12_11
Case 37	PH14_DP_SEGM_26_TF_PM	Case 82	PH27_IMP_DEF_segm_29_30
Case 38	PH14_DP_SEGM_26_FC_PM	Case 83	PH28_PRESTRESS
Case 39	PH16_DP_SEGM_26_TF_UDL	Case 84	PH28_DP_SEGM_10_TF_PM
Case 40	PH15_IMP_DEF_segm_25_26	Case 85	PH28_DP_SEGM_10_FC_PM
Case 41	PH16_PRESTRESS	Case 86	PH30_DP_SEGM_10_TF_UDL
Case 42	PH16_DP_SEGM_15_TF_PM	Case 87	PH28_DP_SEGM_31_TF_PM
Case 43	PH16_DP_SEGM_15_FC_PM	Case 88	PH28_DP_SEGM_31_FC_PM
Case 44	PH18_DP_SEGM_15_TF_UDL	Case 89	PH30_DP_SEGM_31_TF_UDL
Case 45	PH17_IMP_DEF_segm_16_15	Case 90	PH29_IMP_DEF_segm_11_10

Table D.3: Identification of load cases.

Case	Name	Case	Name
Case 91	PH29_IMP_DEF_segm_30_31	Case 137	PH40_PRESTRESS
Case 92	PH30_PRESTRESS	Case 138	PH40_DP_SEGM_4_TF_PM
Case 93	PH30_DP_SEGM_9_TF_PM	Case 139	PH40_DP_SEGM_4_FC_PM
Case 94	PH30_DP_SEGM_9_FC_PM	Case 140	PH42_DP_SEGM_4_TF_UDL
Case 95	PH32_DP_SEGM_9_TF_UDL	Case 141	PH40_DP_SEGM_37_TF_PM
Case 96	PH30_DP_SEGM_32_TF_PM	Case 142	PH40_DP_SEGM_37_FC_PM
Case 97	PH30_DP_SEGM_32_FC_PM	Case 143	PH42_DP_SEGM_37_TF_UDL
Case 98	PH32_DP_SEGM_32_TF_UDL	Case 144	PH41_IMP_DEF_segm_5_4
Case 99	PH31_IMP_DEF_segm_10_9	Case 145	PH41_IMP_DEF_segm_36_37
Case 100	PH31_IMP_DEF_segm_31_32	Case 146	PH42_PRESTRESS
Case 101	PH32_PRESTRESS	Case 147	PH42_DP_SEGM_3_TF_PM
Case 102	PH32_DP_SEGM_8_TF_PM	Case 148	PH42_DP_SEGM_3_FC_PM
Case 103	PH32_DP_SEGM_8_FC_PM	Case 149	PH44_DP_SEGM_3_TF_UDL
Case 104	PH34_DP_SEGM_8_TF_UDL	Case 150	PH42_DP_SEGM_38_TF_PM
Case 105	PH32_DP_SEGM_33_TF_PM	Case 151	PH42_DP_SEGM_38_FC_PM
Case 106	PH32_DP_SEGM_33_FC_PM	Case 152	PH44_DP_SEGM_38_TF_UDL
Case 107	PH34_DP_SEGM_33_TF_UDL	Case 153	PH43_IMP_DEF_segm_4_3
Case 108	PH33_IMP_DEF_segm_9_8	Case 154	PH43_IMP_DEF_segm_37_38
Case 109	PH33_IMP_DEF_segm_32_33	Case 155	PH44_PRESTRESS
Case 110	PH34_PRESTRESS	Case 156	PH44_DP_SEGM_2_TF_PM
Case 111	PH34_DP_SEGM_7_TF_PM	Case 157	PH44_DP_SEGM_2_FC_PM
Case 112	PH34_DP_SEGM_7_FC_PM	Case 158	PH46_DP_SEGM_2_TF_UDL
Case 113	PH36_DP_SEGM_7_TF_UDL	Case 159	PH44_DP_SEGM_39_TF_PM
Case 114	PH34_DP_SEGM_34_TF_PM	Case 160	PH44_DP_SEGM_39_FC_PM
Case 115	PH34_DP_SEGM_34_FC_PM	Case 161	PH46_DP_SEGM_39_TF_UDL
Case 116	PH36_DP_SEGM_34_TF_UDL	Case 162	PH45_IMP_DEF_segm_3_2
Case 117	PH35_IMP_DEF_segm_8_7	Case 163	PH45_IMP_DEF_segm_38_39
Case 118	PH35_IMP_DEF_segm_33_34	Case 164	PH46_PRESTRESS
Case 119	PH36_PRESTRESS	Case 165	PH46_DP_SEGM_1_TF_PM
Case 120	PH36_DP_SEGM_6_TF_PM	Case 165	PH46_DP_SEGM_1_TF_PM
Case 121	PH36_DP_SEGM_6_FC_PM	Case 166	PH46_DP_SEGM_1_FC_PM
Case 122	PH38_DP_SEGM_6_TF_UDL	Case 167	PH48_DP_SEGM_1_TF_UDL
Case 123	PH36_DP_SEGM_35_TF_PM	Case 168	PH46_DP_SEGM_40_TF_PM
Case 124	PH36_DP_SEGM_35_FC_PM	Case 169	PH46_DP_SEGM_40_FC_PM
Case 125	PH38_DP_SEGM_35_TF_UDL	Case 170	PH48_DP_SEGM_40_TF_UDL
Case 126	PH37_IMP_DEF_segm_7_6	Case 171	PH47_IMP_DEF_segm_2_1
Case 127	PH37_IMP_DEF_segm_34_35	Case 172	PH47_IMP_DEF_segm_39_40
Case 128	PH38_PRESTRESS	Case 173	PH48_PRESTRESS
Case 129	PH38_DP_SEGM_5_TF_PM	Case 174	PH48_DP_SEGM_41_TF_PM
Case 130	PH38_DP_SEGM_5_FC_PM	Case 175	PH48_DP_SEGM_41_FC_PM
Case 131	PH40_DP_SEGM_5_TF_UDL	Case 176	PH50_DP_SEGM_41_TF_UDL
Case 132	PH38_DP_SEGM_36_TF_PM	Case 177	PH49_IMP_DEF_segm_40_41
Case 133	PH38_DP_SEGM_36_FC_PM	Case 178	PH50_PRESTRESS
Case 134	PH40_DP_SEGM_36_TF_UDL	Case 179	PH50_DP_SEGM_42_TF_PM
Case 135	PH39_IMP_DEF_segm_6_5	Case 180	PH50_DP_SEGM_42_FC_PM
Case 136	PH39_IMP_DEF_segm_35_36	Case 181	PH52_DP_SEGM_42_TF_UDL

Table D.4: Identification of load cases (continued from previous page).

Case	Name	Case	Name
Case 182	PH51_IMP_DEF_segm_41_42	Case 188	PH54_PRESTRESS
Case 183	PH52_PRESTRESS	Case 189	PH54_DP_SEGM_SM_TF_PM
Case 184	PH52_DP_SEGM_SML_TF_PM	Case 190	PH54_DP_SEGM_SM_FC_PM
Case 185	PH52_DP_SEGM_SML_FC_PM	Case 191	PH56_DP_SEGM_SM_TF_UDL
Case 186	PH54_DP_SEGM_SML_TF_UDL	Case 192	PH55_IMP_DEF_segm_42_SM
Case 187	PH53_IMP_DEF_segm_1_SML	Case 193	PH56_PRESTRESS

Table D.5: Identification of load cases (continued from previous page).

E

Notional size

The following document presents the Excel spreadsheet used for determining the notional size of the box girder and each component separately.

Notional Size Calculation

Top Slab		
Area	4,509	m2
Full Perimeter	24,15	m
Exposed Perimeter	23,25	m
Webs		
Thickness	0,45	m
Bottom Slab		
Width	6,8	m

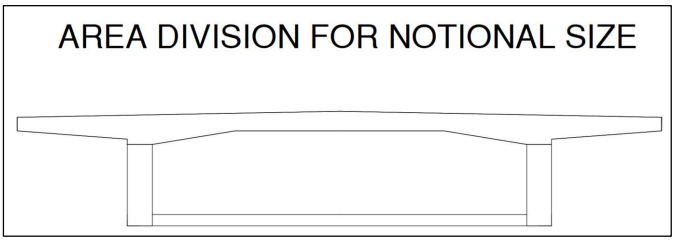

		TOP SLAB			WEBS							BOTTOM SLAB				FULL BOX GIRDER		
Seg.	**Length [m]**	**V [m3]**	**S [m2]**	**D [m]**	**Ex. Height [m]**	**Int. Height [m]**	**Ex. Area [m2]**	**Int. Area [m2]**	**V [m3]**	**S [m2]**	**D [m]**	**t aver. [m]**	**V [m3]**	**S [m2]**	**D [m]**	**V [m3]**	**S [m2]**	**D [m]**
EWD	2,75	12,4	64,0	0,388	1,50	1,30	4,13	3,58	1,86	7,70	0,482	0,200	3,740	37,4	0,200	19,9	116,8	0,340
SML	3,5	15,8	81,4	0,388	1,50	1,30	5,25	4,55	2,36	9,81	0,482	0,201	4,772	47,6	0,201	25,3	148,6	0,340
1	3,5	15,8	81,4	0,388	1,50	1,30	5,29	4,57	2,38	9,86	0,483	0,207	4,915	47,6	0,207	25,5	148,7	0,342
2	3,5	15,8	81,4	0,388	1,52	1,31	5,39	4,61	2,42	10,0	0,485	0,222	5,284	47,6	0,222	25,9	149,0	0,348
3	3,5	15,8	81,4	0,388	1,56	1,33	5,55	4,69	2,50	10,2	0,488	0,246	5,855	47,6	0,246	26,6	149,5	0,356
4	3,5	15,8	81,4	0,388	1,61	1,35	5,78	4,81	2,60	10,6	0,491	0,278	6,616	47,6	0,278	27,6	150,2	0,368
5	3,5	15,8	81,4	0,388	1,69	1,39	6,07	4,96	2,73	11,0	0,495	0,318	7,557	47,6	0,318	28,8	151,1	0,381
6	3,5	15,8	81,4	0,388	1,78	1,44	6,43	5,16	2,89	11,6	0,499	0,363	8,639	47,6	0,363	30,2	152,2	0,397
7	3,5	15,8	81,4	0,388	1,89	1,51	6,85	5,41	3,08	12,3	0,503	0,413	9,829	47,6	0,413	31,8	153,5	0,414
8	3,5	15,8	81,4	0,388	2,02	1,58	7,34	5,71	3,30	13,0	0,506	0,468	11,127	47,6	0,468	33,5	155,1	0,432
9	3,5	15,8	81,4	0,388	2,17	1,68	7,90	6,06	3,55	14,0	0,509	0,525	12,495	47,6	0,525	35,4	156,9	0,451
10	3,5	15,8	81,4	0,388	2,34	1,79	8,52	6,47	3,83	15,0	0,511	0,585	13,911	47,6	0,585	37,4	159,0	0,470
11	3,5	15,8	81,4	0,388	2,53	1,91	9,20	6,94	4,14	16,1	0,513	0,646	15,363	47,6	0,646	39,4	161,3	0,489
12	3,5	15,8	81,4	0,388	2,73	2,05	9,95	7,47	4,48	17,4	0,514	0,706	16,803	47,6	0,706	41,5	163,8	0,507
13	3,5	15,8	81,4	0,388	2,95	2,22	10,76	8,08	4,84	18,8	0,514	0,766	18,219	47,6	0,766	43,7	166,7	0,524
14	3,5	15,8	81,4	0,388	3,20	2,40	11,64	8,76	5,24	20,4	0,514	0,824	19,599	47,6	0,824	45,9	169,8	0,540
15	3,5	15,8	81,4	0,388	3,46	2,60	12,58	9,51	5,66	22,1	0,513	0,879	20,920	47,6	0,879	48,0	173,2	0,555
16	3,5	15,8	81,4	0,388	3,74	2,83	13,59	10,34	6,12	23,9	0,511	0,931	22,146	47,6	0,931	50,2	176,9	0,567
17	3,5	15,8	81,4	0,388	4,03	3,08	14,67	11,25	6,60	25,9	0,509	0,977	23,241	47,6	0,977	52,2	180,8	0,578
18	3,5	15,8	81,4	0,388	4,35	3,35	16,25	12,69	7,31	28,9	0,505	1,017	24,205	47,6	1,017	54,6	186,9	0,585
19	3,5	15,8	81,4	0,388	4,93	3,90	17,89	14,21	8,05	32,1	0,502	1,051	25,014	47,6	1,051	56,9	193,2	0,589
20	3,5	15,8	81,4	0,388	5,29	4,22	19,16	15,39	8,62	34,5	0,499	1,077	25,633	47,6	1,077	58,7	198,1	0,592
21	3,5	15,8	81,4	0,388	5,66	4,57	20,49	16,52	9,22	37,0	0,498	1,136	27,025	47,6	1,136	61,2	203,0	0,603
22	3,5	15,8	81,4	0,388	6,05	4,87	20,05	16,08	9,02	36,1	0,499	1,136	27,025	47,6	1,13550	60,9	201,3	0,605
23	3,5	15,8	81,4	0,388	5,41	4,32	18,28	14,51	8,23	32,8	0,502	1,077	25,633	47,6	1,077	57,9	194,6	0,595
24	3,5	15,8	81,4	0,388	5,04	3,97	17,01	13,33	7,66	30,3	0,505	1,051	25,014	47,6	1,051	56,1	189,7	0,592
25	3,5	15,8	81,4	0,388	4,68	3,65	15,81	12,25	7,11	28,1	0,507	1,017	24,205	47,6	1,017	54,2	185,1	0,586
26	3,5	15,8	81,4	0,388	4,35	3,35	14,67	11,25	6,60	25,9	0,509	0,977	23,241	47,6	0,977	52,2	180,8	0,578
27	3,5	15,8	81,4	0,388	4,03	3,08	13,59	10,34	6,12	23,9	0,511	0,931	22,146	47,6	0,931	50,2	176,9	0,567
28	3,5	15,8	81,4	0,388	3,74	2,83	12,58	9,51	5,66	22,1	0,513	0,879	20,920	47,6	0,879	48,0	173,2	0,555
29	3,5	15,8	81,4	0,388	3,46	2,60	11,64	8,76	5,24	20,4	0,514	0,824	19,599	47,6	0,824	45,9	169,8	0,540
30	3,5	15,8	81,4	0,388	3,20	2,40	10,76	8,08	4,84	18,8	0,514	0,766	18,219	47,6	0,766	43,7	166,7	0,524
31	3,5	15,8	81,4	0,388	2,95	2,22	9,95	7,47	4,48	17,4	0,514	0,706	16,803	47,6	0,706	41,5	163,8	0,507
32	3,5	15,8	81,4	0,388	2,73	2,05	9,20	6,94	4,14	16,1	0,513	0,646	15,363	47,6	0,646	39,4	161,3	0,489
33	3,5	15,8	81,4	0,388	2,53	1,91	8,52	6,47	3,83	15,0	0,511	0,585	13,911	47,6	0,585	37,4	159,0	0,470
34	3,5	15,8	81,4	0,388	2,34	1,79	7,90	6,06	3,55	14,0	0,509	0,525	12,495	47,6	0,525	35,4	156,9	0,451
35	3,5	15,8	81,4	0,388	2,17	1,68	7,34	5,71	3,30	13,0	0,506	0,468	11,127	47,6	0,468	33,5	155,1	0,432
36	3,5	15,8	81,4	0,388	2,02	1,58	6,85	5,41	3,08	12,3	0,503	0,413	9,829	47,6	0,413	31,8	153,5	0,414
37	3,5	15,8	81,4	0,388	1,89	1,51	6,43	5,16	2,89	11,6	0,499	0,363	8,639	47,6	0,363	30,2	152,2	0,397
38	3,5	15,8	81,4	0,388	1,78	1,44	6,07	4,96	2,73	11,0	0,495	0,318	7,557	47,6	0,318	28,8	151,1	0,381
39	3,5	15,8	81,4	0,388	1,69	1,39	5,78	4,81	2,60	10,6	0,491	0,278	6,616	47,6	0,278	27,6	150,2	0,368
40	3,5	15,8	81,4	0,388	1,61	1,35	5,55	4,69	2,50	10,2	0,488	0,246	5,855	47,6	0,246	26,6	149,5	0,356
41	3,5	15,8	81,4	0,388	1,56	1,33	5,39	4,61	2,42	10,0	0,485	0,222	5,284	47,6	0,222	25,9	149,0	0,348
42	3,5	15,8	81,4	0,388	1,52	1,31	5,29	4,57	2,38	9,86	0,483	0,207	4,915	47,6	0,207	25,5	148,7	0,342
SM	1,75	7,9	40,7	0,388	1,50	1,30	1,31	1,14	0,59	2,45	0,482	0,201	2,392	23,8	0,201	11,5	69,4	0,330
			Avg.	**0,388**						**Avg.**	**0,502**			**Avg.**	**0,619**		**Avg.**	**0,471**

F

Reference analysis with new symmetry conditions

The following annex presents the results of the updated Reference Analysis, following the implementation of rotational constraints in the symmetry plane (see section 4.5). This additional simulation aimed to determine the impact of these new boundary conditions on the results. It was found that the influence primarily affects Segment CS at midspan.

In comparison to the original Reference Analysis, the difference in deflection at midspan is 2.5% after 60 years (see Figure F.1). At the side span, the difference after 60 years is 4.0% (see Figure F.2). Regarding prestress losses, the sudden peak previously observed for Segment CS disappeared, and now a more natural trend is seen (see Figure F.14). The maximum principal stress σ_1 at the beginning of service life remains above three times f_{ctm}, suggesting potential cracking (see Figure F.6). But after 60 years, the high stresses at the bottom slab of Segment CS are not present anymore (see Figure F.7). Similarly, the minimum principal stress σ_3 is still above two times f_{cm} at midspan (see Figure F.8); however, after 60 years f_{cm} is not exceeded anymore (see Figure F.9. Overall, the results show improvements with the new symmetry conditions, but the variations are only noticeable in the midspan area.

F.1. Vertical deformations

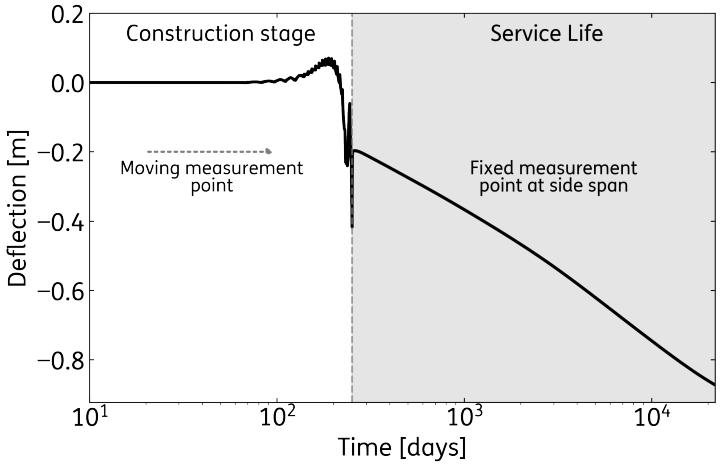

(a) Numerical results with new Reference Analysis.

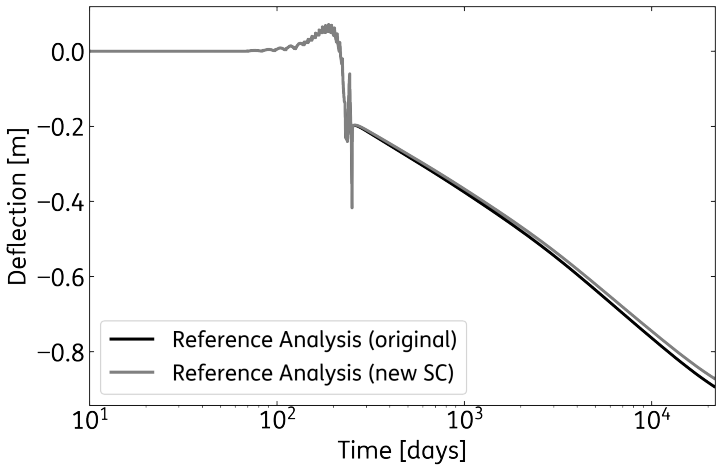

(b) Comparison of results between original and the new symmetry conditions (SC) Reference Analysis.

Figure F.1: Deflection over time at the midspan for a period of 60 years (log-scale).

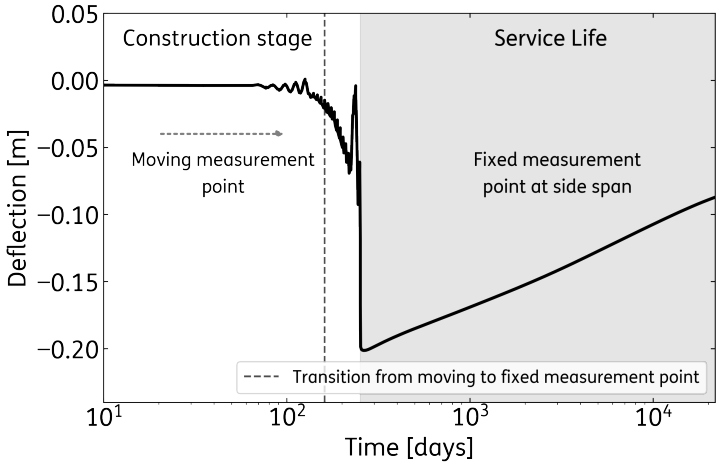

(a) Numerical results with new Reference Analysis.

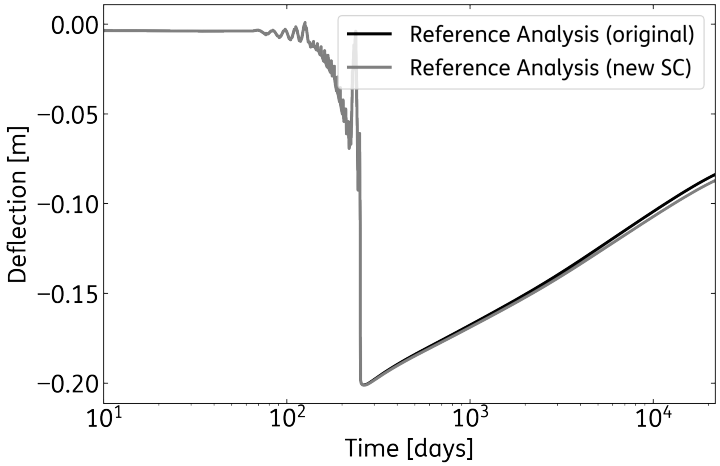

(b) Comparison of results between original and the new symmetry conditions (SC) Reference Analysis.

Figure F.2: Deflection over time at the side span for a period of 60 years (log-scale).

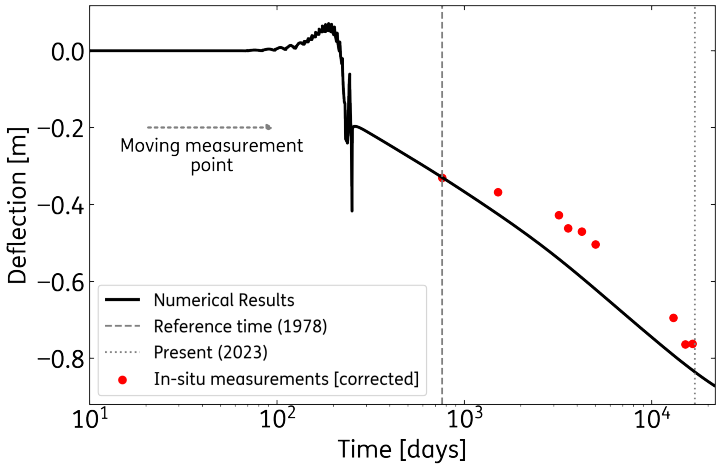

Figure F.3: Comparison of the maximum deflection over time at midspan between the numerical results and the corrected in-situ measurements. The in-situ measurements are corrected for a reference time of 762 days.

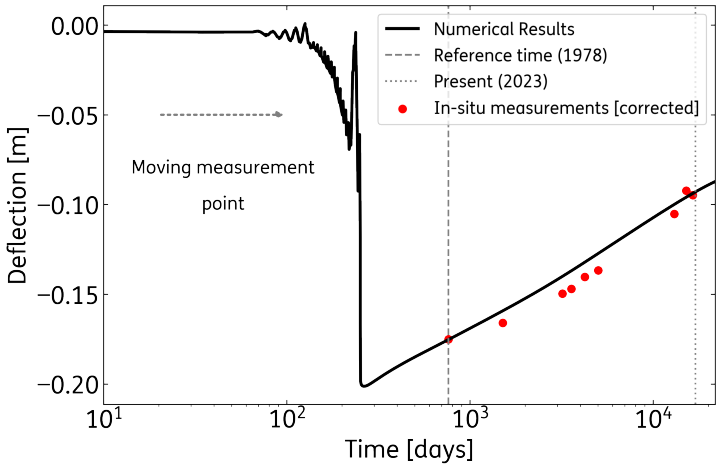

Figure F.4: Comparison of the maximum deflection over time at the side span between the numerical results and the corrected in-situ measurements. The in-situ measurements are corrected for a reference time of 762 days.

F.2. Bending moments and stresses in the concrete

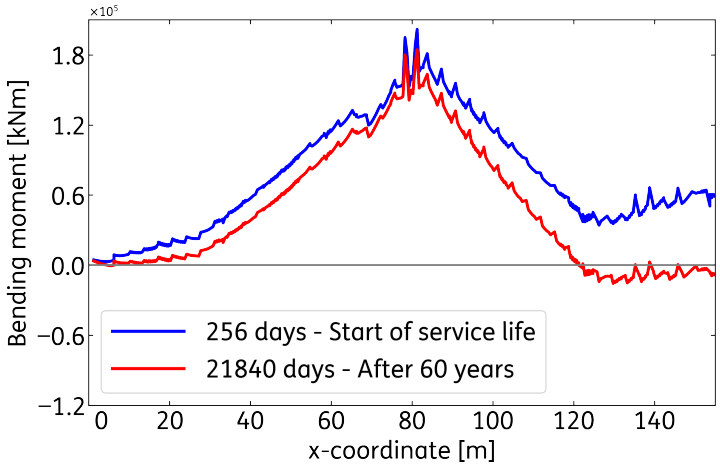

Figure F.5: Post-processed comparison of the bending moment diagram at the end of construction and after 60 years.

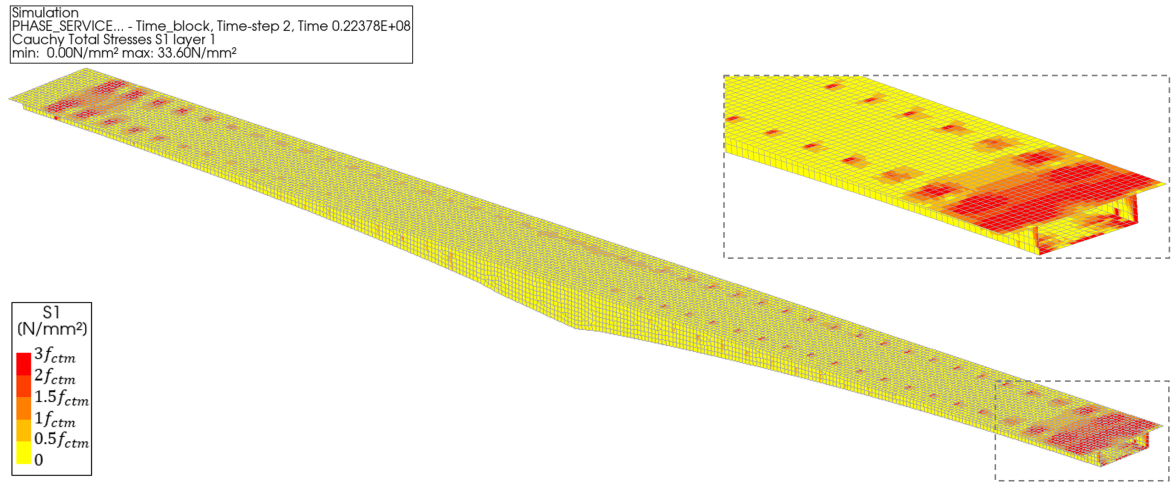

(a) A 3D view with a midspan zoom window.

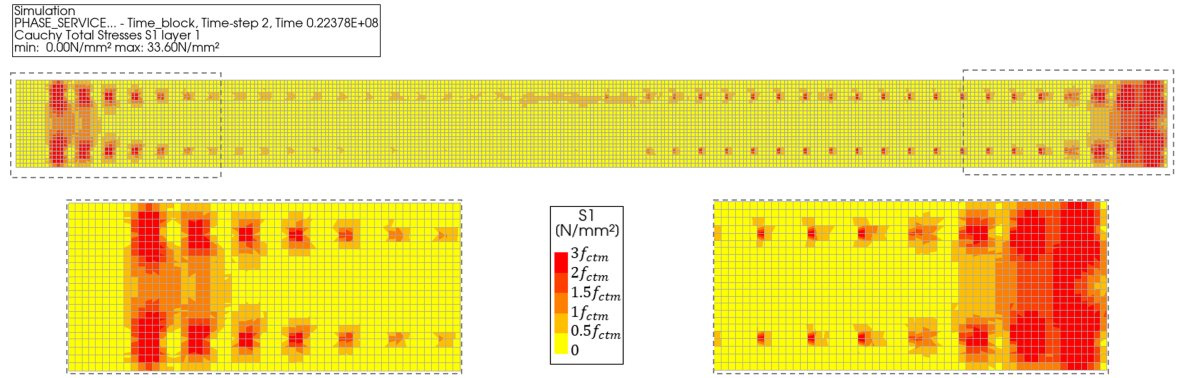

(b) View from the top, with a zoom window on both extremes of the bridge.

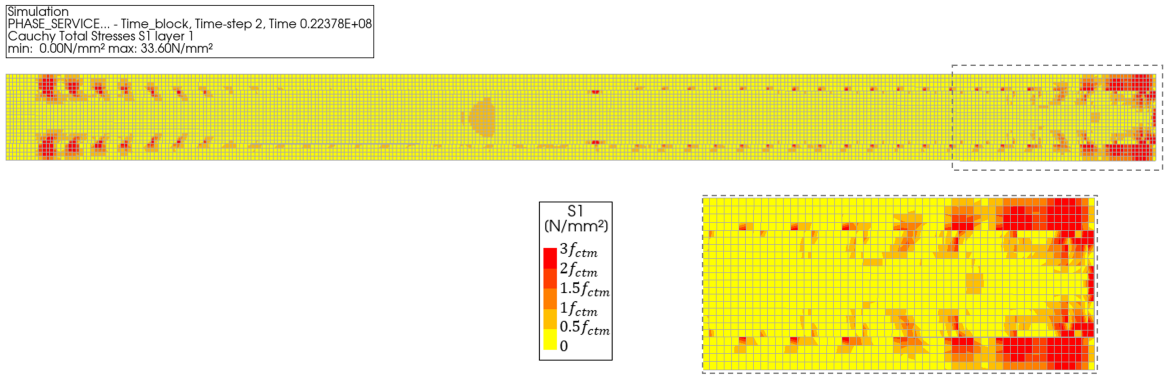

(c) View from the bottom, with a midspan zoom window.

Figure F.6: Contour plots of the maximum principal stress σ_1 at the beginning of service life. The views presented are 3D, top and bottom. Zoom windows of locations with the highest stresses are included. The color bar is referenced to the concrete mean tensile strength f_{ctm} equal to 2.55 N/mm^2.

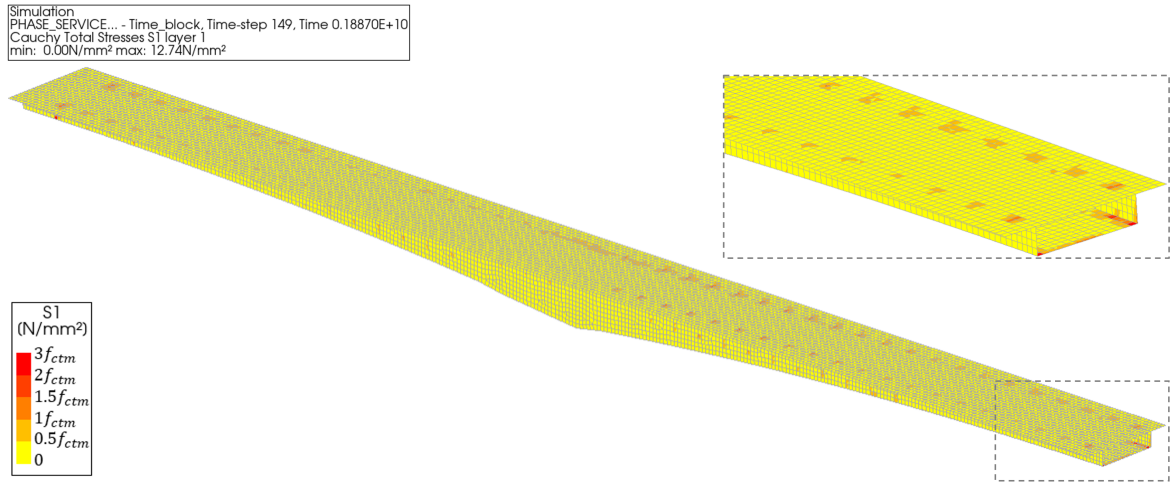

(a) A 3D view with a midspan zoom window.

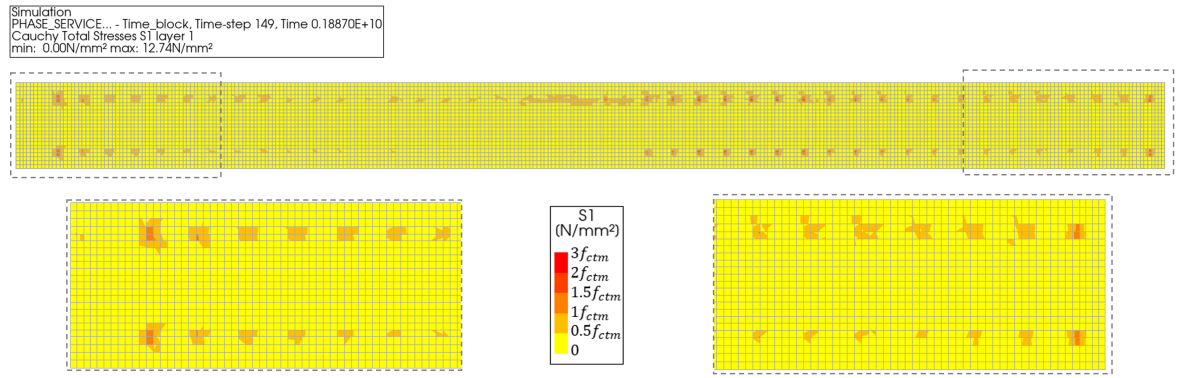

(b) View from the top, with a zoom window on both extremes of the bridge.

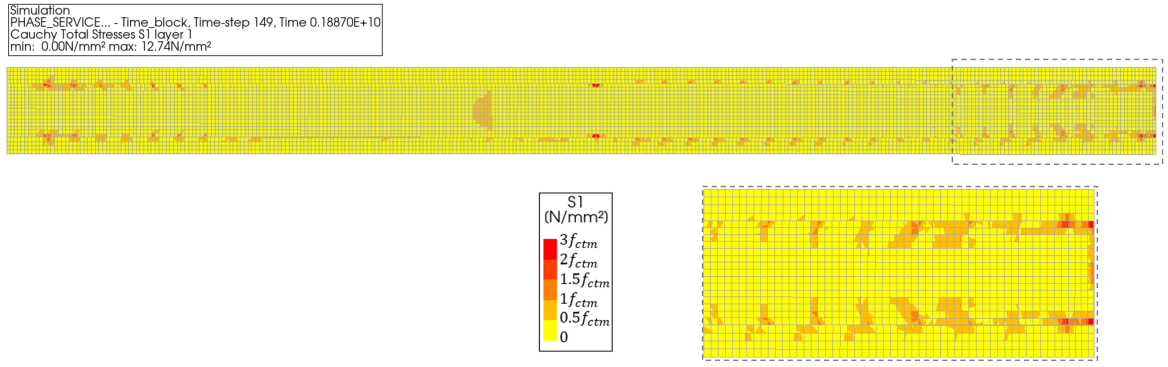

(c) View from the bottom, with a midspan zoom window.

Figure F.7: Contour plots of the maximum principal stress σ_1 at the end of service life (60 years). The views presented are 3D, top and bottom. Zoom windows of locations with the highest stresses are included. The color bar is referenced to the concrete mean tensile strength f_{ctm} equal to 2.55 N/mm^2.

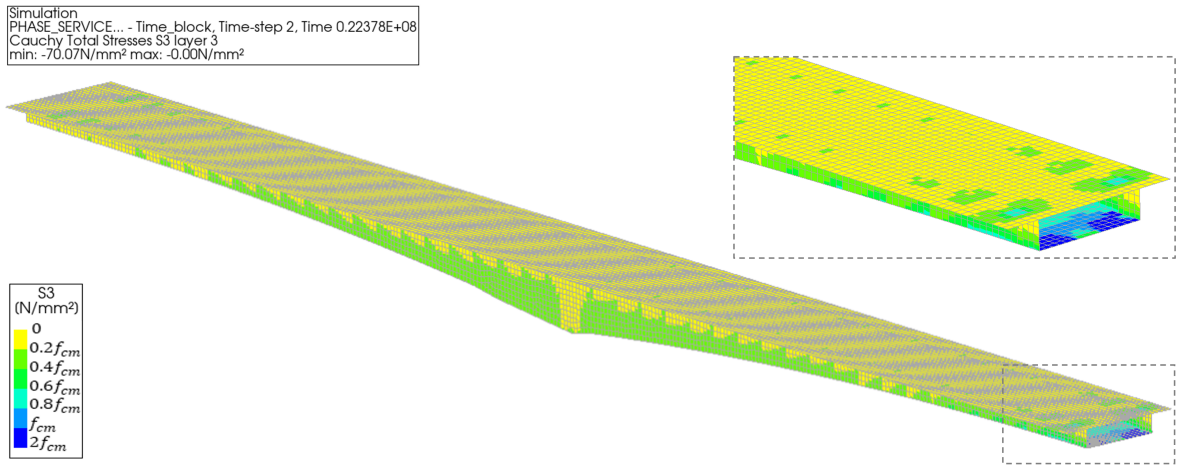

(a) A 3D view with a midspan zoom window.

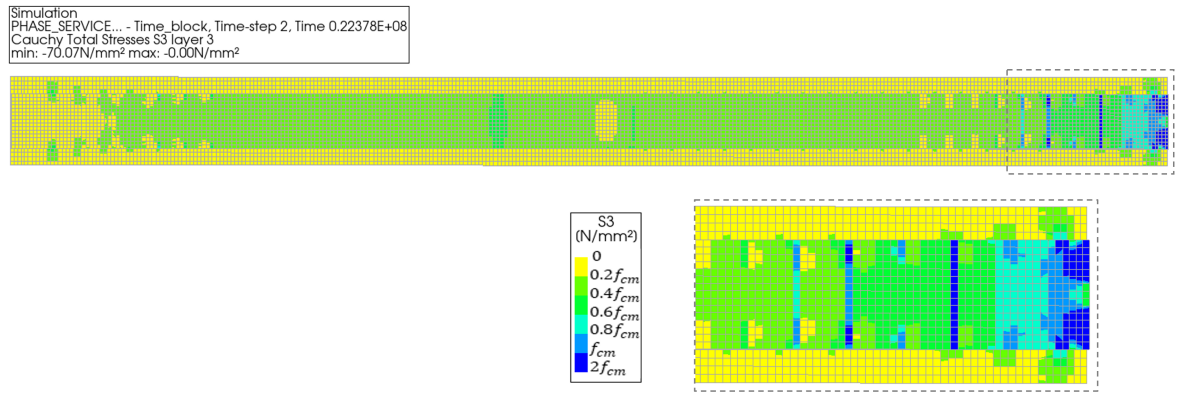

(b) View from the bottom, with a midspan zoom window.

Figure F.8: Contour plots of the minimum principal stress σ_3 at the beginning of service life. The views presented are 3D and bottom. Zoom windows of locations with the highest stresses are included. The color bar is referenced to the concrete mean compressive strength f_{cm} equal to 38 N/mm^2.

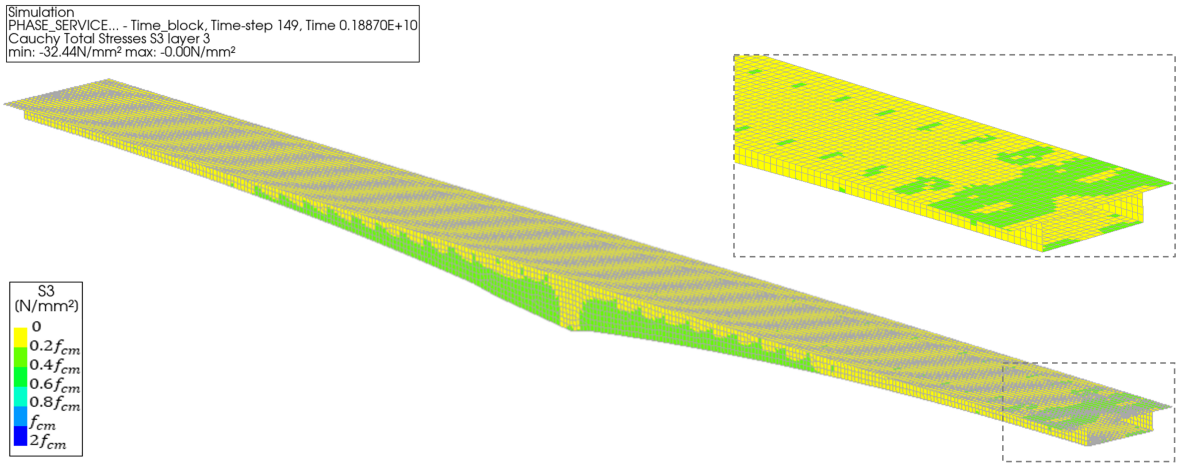

(a) A 3D view with a midspan zoom window.

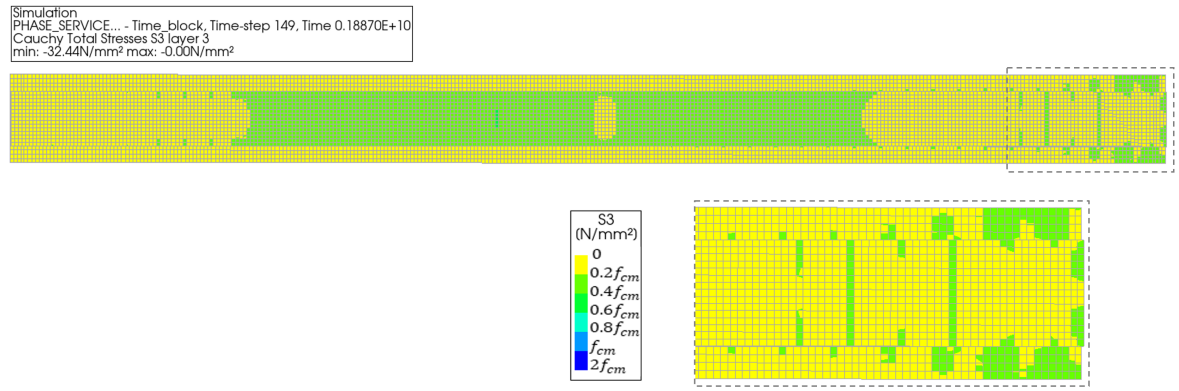

(b) View from the bottom, with a midspan zoom window.

Figure F.9: Contour plots of the minimum principal stress σ_3 at the end of service life (60 years later). The views presented are 3D and bottom. Zoom windows of locations with the highest stresses are included. The color bar is referenced to the concrete mean compressive strength f_{cm} equal to 38 N/mm^2.

F.3. Stress level in the tendons and prestress losses

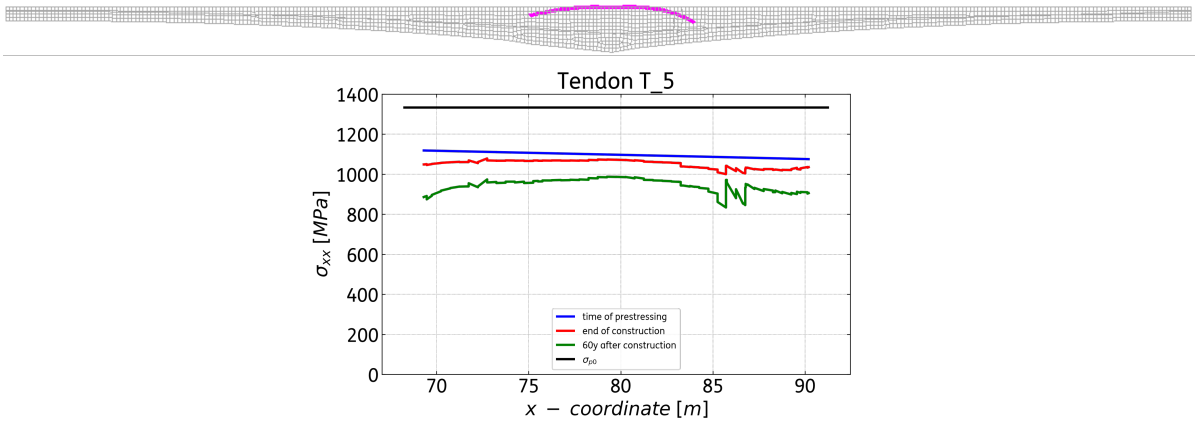

(a) Stresses along the cantilever tendon 5.

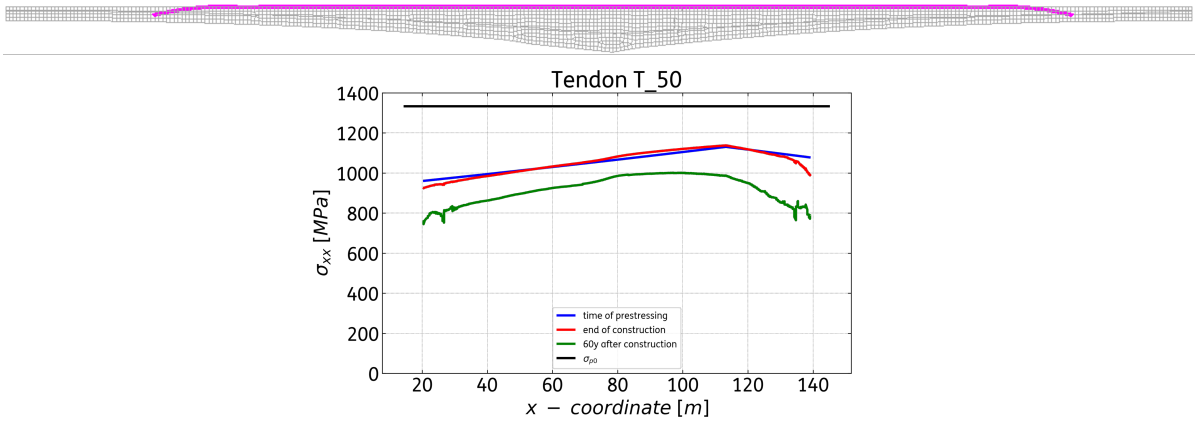

(b) Stresses along the cantilever tendon 50.

Figure F.10: Evolution of the stresses along the prestressing tendons 5 and 50. Three key moments are selected: at the time of prestressing, at the end of construction, and after 60 years.

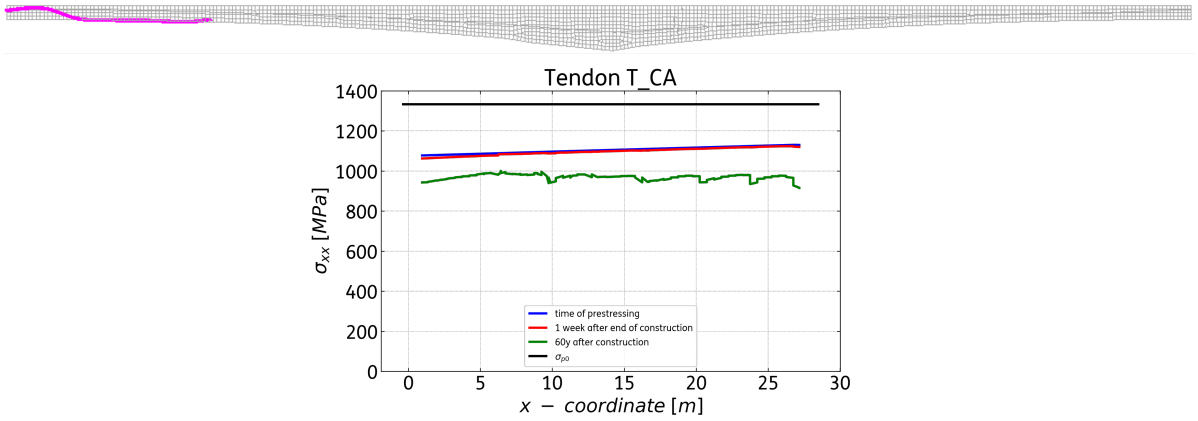

(a) Stresses along the continuity tendon CA.

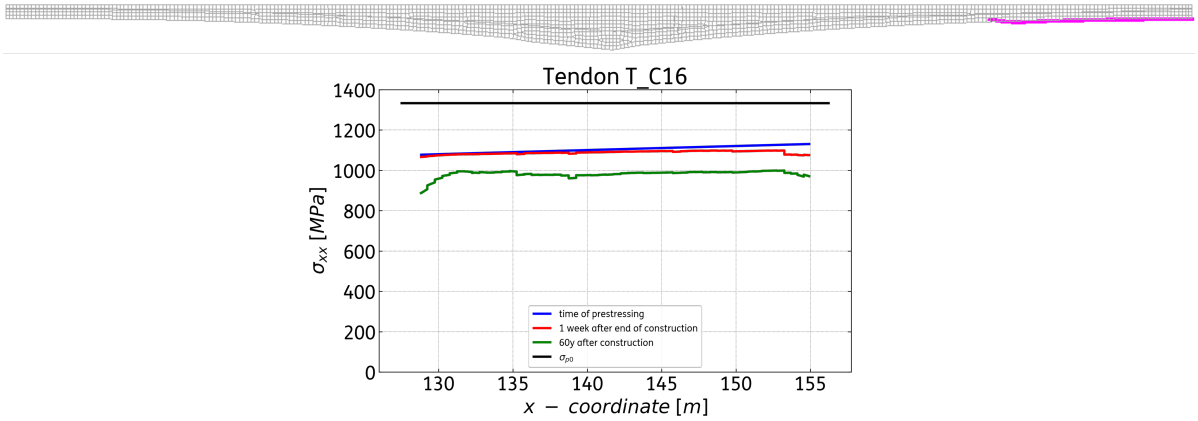

(b) Stresses along the continuity tendon C16.

Figure F.11: Evolution of the stresses along the prestressing tendons CA and C16. Three key moments are selected: at the time of prestressing, one week after the end of construction, and after 60 years.

(a) Cross-sectional prestressing loss for Segment 2.

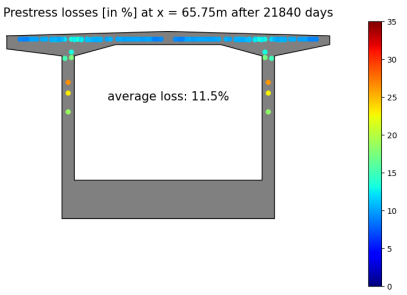

(b) Cross-sectional prestressing loss for Segment 18.

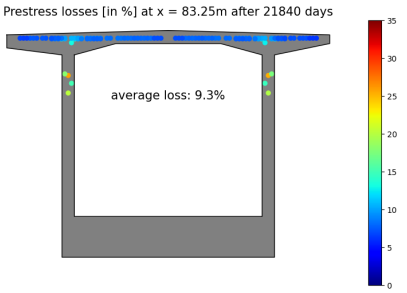

(c) Cross-sectional prestressing loss for Segment 23.

(d) Cross-sectional prestressing loss for Segment 42.

Figure F.12: Prestressing losses after 60 years for four different cross-sections. The losses account for creep and shrinkage only, and are calculated versus the working prestress, which is the difference between the initial prestress σ_{p0} and the immediate losses.

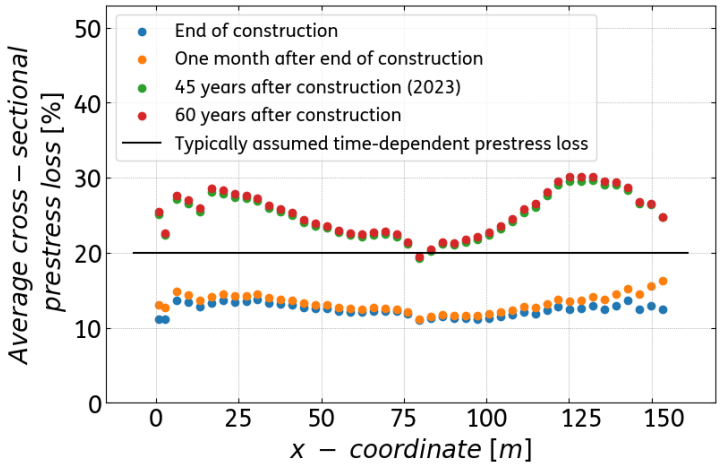

Figure F.13: Average prestressing loss per cross-section for four key moments. The losses are due to creep, shrinkage, and relaxation, and they are compared with the typically assumed 20% prestress loss.

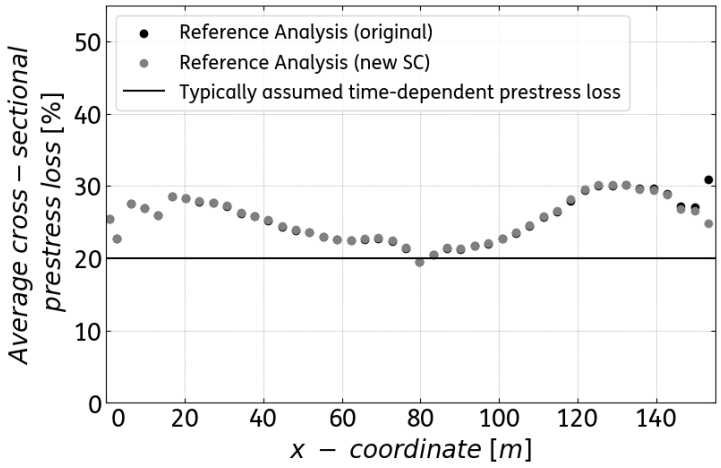

Figure F.14: Comparison of average prestressing loss per cross-section after 60 years for the original Reference Analysis versus the new symmetry conditions (SC). The losses are due to creep, shrinkage, and relaxation, and they are compared with the typically assumed 20% prestress loss.